

NAT'L INST. OF STAND & TECH R.I.C.



A11104 256831





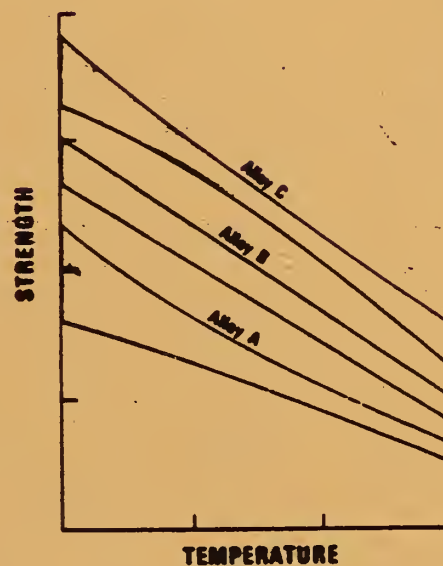
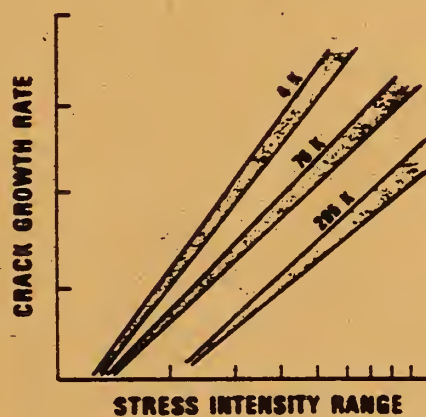
NATIONAL INSTITUTE OF STANDARDS &  
TECHNOLOGY  
Research Information Center  
Gaithersburg, MD 20899





TECHNICAL REPORTS

# MATERIALS STUDIES FOR MAGNETIC FUSION ENERGY APPLICATIONS AT LOW TEMPERATURES - XII



To  
Department of Energy  
Office of Fusion Energy  
Washington, D.C. 20545

Prepared by  
National Institute of Standards  
and Technology  
Boulder, Colorado 80303







TECHNICAL REPORTS

# **MATERIALS STUDIES FOR MAGNETIC FUSION ENERGY APPLICATIONS AT LOW TEMPERATURES - XII**

---

Edited by

**R.P. Reed and R.L. Tobler  
National Institute of Standards and Technology  
Boulder, Colorado 80303**

**November 1989**

Sponsored by

**Department of Energy  
Office of Fusion Energy  
Washington, D.C. 20545**



**UNITED STATES  
DEPARTMENT OF COMMERCE, Robert A. Mosbacher, Secretary  
NATIONAL INSTITUTE OF STANDARDS  
AND TECHNOLOGY, Raymond G. Kammer, Acting Director**







## CONTENTS

SUMMARY . . . . .	v
ORGANIZATIONAL CONTACTS . . . . .	vi
PRORGAM DESCRIPTION . . . . .	vii
STRUCTURAL ALLOYS	
Structural Alloys Program . . . . .	3
Austenitic Stainless Steels with Emphasis on Strength at Low Temperatures . . . . .	9
R.P. Reed	
Nitrogen in Austenitic Stainless Steels . . . . .	45
R.P. Reed	
Effect of Nitrogen and Carbon on FCC-HCP Stability in Austenitic Stainless Steels . . . . .	65
R.P. Reed and M.W. Austin	
Low Temperature Properties of High-Manganese Austenitic Steels . . . .	71
R.P. Reed, P.T. Purtscher, and L.A. Delgado	
Discontinuous Yielding in Austenitic Stainless Steels at Low Temperature . . . . .	93
R.P. Reed and N.J. Simon	
Influence of Interstitial Content on Fracture Toughness . . . . .	107
P.T. Purtscher and R.P. Reed	
Metallographic Study of the Crack-tip Region From Fracture Mechanics Specimens of Austenitic and Ferritic Steels . . . . .	119
P.T. Purtscher, R.P. Reed, and D.K. Matlock	
Tensile, Fracture, and Fatigue Properties of Notched Aluminum Alloy Sheets at Liquid Nitrogen Temperature . . . . .	131
R.L. Tobler, R.P. Walsh, R.P. Reed, J.K. Han, and L. Ma	
Elastic Constants of Four Fe-Cr-Ni-Mn Alloys . . . . .	141
S.A. Kim, H.M. Ledbetter, and Y. Li	
Nickel Effect on Elastic Constants of Fe-Cr-Ni Alloys . . . . .	153
M. Lei and H. Ledbetter	
Nitrogen Effect on Elastic Constants of F.C.C. Fe-18Cr-19Ni Alloys . . . . .	159
S. Lin and H. Ledbetter	

Low-Temperature Magnetic-Elastic Anomalies in F.C.C. Fe-Cr-Ni Alloys . . . . .	169
H. Ledbetter	

Low-Temperature Thermal Expansion of Fe-Cr-Ni Alloys with Various C+N Contents . . . . .	177
M.W. Austin and H.M. Ledbetter	

## WELDING

Welding Program . . . . .	183
The Fracture Toughness of 25Cr-22Ni-4Mn-2Mo Stainless Steel Welds at 4 K . . . . .	187
C.N. McCowan and T.A. Siewert	
The Effect of Inclusions on the Fracture Toughness of 316L Stainless Steel Welds at 4 K . . . . .	199
C.N. McCowan and T.A. Siewert	

## TEST STANDARDS

United States - Japan Development of Test Standards Program . . .	217
U.S. - Japan Cooperative Program for the Development of 4-K Test Standards . . . . .	219
R.L. Tobler	
Memorandum: Trip Report on ASTM D30 Symposium and Technical Committee Meetings Related to the Development of Standards for Mechanical Property Tests of Composites . . . . .	223
R.L. Tobler	
Charpy Tests Near Absolute Zero . . . . .	227
R.L. Tobler and R.P. Reed	
Warm Precracking at 295 K and Its Effects on the 4-K Toughness of Two Austenitic Stainless Steels . . . . .	239
R.L. Tobler and M. Shimada	
Proposed Standard Method for Tensile Testing of Structural Alloys at Liquid Helium Temperature . . . . .	259
R.L. Tobler and R.P. Reed	

## TECHNOLOGY TRANSFER

Technology Transfer Program . . . . .	279
Eleventh Cryogenic Structural Materials Workshop . . . . .	281
N.J. Simon	



## SUMMARY

This report contains the results of a research program to determine the properties of materials that may be used in cryogenic structures for the superconducting magnets of fusion energy power plants and prototypes. Its purpose is to facilitate their design and development. The program was developed jointly by the staffs of the National Institute of Standards and Technology and the Office of Fusion Energy of the Department of Energy; it is managed by NIST and sponsored by DOE. Research is conducted at NIST and at other laboratories through subcontracts with NIST.

Research results for 1988 are presented in technical papers under four headings that reflect the main program areas: Structural Alloys, Welding, Technology Transfer, and United States-Japan Development of Test Standards. Objectives and research highlights are summarized in the introduction to each program area.

NOTE: Certain commercial equipment, instruments, or materials are identified in this report to specify the experimental procedure adequately. In a few instances, company names are used to identify the source of specific research. In no case does such identification imply recommendation or endorsement by the National Institute of Standards and Technology, nor does it imply that the material or equipment identified is necessarily the best available for the purpose.

## ORGANIZATIONAL CONTACTS

Specific technical questions may be directed to the following people, who contributed to major aspects of the program during the fiscal year of 1989.

Department of Energy, Office of Fusion Energy, Washington, D.C. 20545

Program Monitor	D. Beard	(301) 233-4958
-----------------	----------	----------------

National Institute of Standards and Technology, Boulder, CO 80303

Program Manager	R.P. Reed	(303) 497-3870 (FTS) 320-3870
-----------------	-----------	----------------------------------

Structural Alloys	M.W. Austin	(303) 497-3504
	H. Ledbetter	(303) 497-3443
	P.T. Purtscher	(303) 497-5789
	R.P. Reed	(303) 497-3870
	N.J. Simon	(303) 497-3687
	R.L. Tobler	(303) 497-3421
	R.P. Walsh	(303) 497-3818

Welding	C.N. McCowan	(303) 497-3699
	T.A. Siewert	(303) 497-3523

Technology Transfer	N.J. Simon	(303) 497-3687
	E.S. Drexler	(303) 497-5350

United States-Japan	P.T. Purtscher	(303) 497-5789
Development of	R.P. Reed	(303) 497-5789
Test Standards	R.L. Tobler	(303) 497-3421
	R.P. Walsh	(303) 497-3818



## PROGRAM DESCRIPTION

The objective of the program is to assist in the design, construction, and safe operation of magnetic fusion energy (MFE) systems that use cryogenic components, especially superconducting magnets. The specific steps taken to achieve this objective are: (1) evaluation of the materials research needs specific to MFE devices; (2) research programs to acquire the necessary data; and (3) effective materials technology transfer by rapid dissemination of the data to potential users through personal contacts, publications, and workshops.

Efforts directed at the first objective began with the publication of the "Survey of Low Temperature Materials for Magnetic Fusion Energy" in March 1977. A publication updating part of this survey, "Structural Alloys for Superconducting Magnets in Fusion Energy Systems," was included in Volume IV (1981) of this series. In Volume VI (1983), reviews of the properties of austenitic stainless steels and of their elastic constants also contributed to this objective. Through interactions with low-temperature design, construction, and measurement programs, such as the Large Coil Project, CIT, and ITER (International Thermonuclear Experimental Reactor), we learn of new problems as they arise. This year's report contains results of continued research in support of Compact Ignition Tokamak designs by the Princeton Plasma Physics Laboratory and the Massachusetts Institute of Technology. Research projects contributing to the second objective are described in the technical papers. Again, research toward the establishment of test standards was emphasized. The third objective is satisfied, in part, by these annual reports and by the series of workshops on Cryogenic Structural Materials. Since 1982, handbook pages presenting the available data for specific materials have been distributed to members of the magnetic fusion energy community who are involved with low-temperature materials.





# **STRUCTURAL ALLOYS**





## STRUCTURAL ALLOYS PROGRAM

LEADER: R.P. Reed

CONTRIBUTORS: M.W. Austin, L.A. Delgado, S.A. Kim, H. Ledbetter,  
P.T. Purtscher, N.J. Simon, R.L. Tobler, R.P. Walsh

### OBJECTIVES

- o Development of strong, tough structural alloys for use in superconducting magnets
- o Development of strong, fatigue-resistant structural alloys for use in pulsed superconducting magnets
- o Development of effective codes and standards for low-temperature property measurements and structural design

### RESEARCH HIGHLIGHTS

- o Two new reviews have been written:

Austenitic Stainless Steels with Emphasis on Their Low-Temperature Behavior. Austenite, ferrite, body-centered cubic and hexagonal close-packed martensite, stacking-fault energy, carbides, and sigma phase were described. Recent international development of higher strength, tougher austenitic stainless steels was summarized. Discussions of the effect of martensite phase transformations on the stress-strain characteristics, nitrogen strengthening, and strengthening theory based on lattice-parameter and elastic-property data, all at low temperatures, were included.

Low-Temperature Properties of High-Manganese Austenitic Steels. Emphasis was placed on strength, toughness, elastic properties, thermal expansion, and magnetic properties, those properties most critical for materials used in cryogenic structures. Strength and toughness parameters and mechanisms were discussed, including alloying, martensitic transformations, twinning, and grain size. Information was included from many recent studies, particularly Japanese studies, of alloy development for superconducting-magnet applications at 4 K.

- o Regression analysis for significant design parameters has been carried out on a matrix of 99 recent NBS measurements at 4 K on a variety of 316, 316 LN, and 316 LHN alloys. This matrix includes alloying, refining, and processing data on alloys obtained from suppliers in Japan, Europe, and the United States. For structural use in 4 K superconducting magnet applications, alloy 316 LN offers higher strength than 304 LN with equivalent toughness. Nitrogen additions permit the attainment of high yield-strength levels with little added cost.

- o The fracture process at low temperatures in tension and from fatigue precracking has been better characterized. Cleavage-like facets along slip planes in austenite have been identified. Ductile dimples in the fracture of tensile specimens have been related to inclusion parameters. A new model has been developed for better understanding of void nucleation, which sometimes controls the fracture of austenitic steels.

# SUMMARY OF MECHANICAL PROPERTY MEASUREMENTS OF STRUCTURAL ALLOYS

Alloy [Designation]	Country of Supplier	Tensile 295-4 K	Elastic 295-4 K	Fracture Toughness 295, 76, 4 K	Fatigue Crack Growth Rate 295, 76, 4 K	Fatigue S-N 4 K	Report, Volume (page)
<b>AUSTENITIC STEELS</b>							
Fe-5Cr-25Mn-0.2C	Japan	VII					VII (65)
Fe-5Cr-26Mn	Japan		VI				VI (181)
Fe-13Cr-19Mn	USSR		III		VI		III (79) VI (41)
Fe-13Cr-22Mn-0.2N	Japan	VI					VII (65)
Fe-16Cr-8Ni-8Mn	U.S.	VIII		VIII			VIII (151,181)
Fe-17Cr-18Mn-0.5N	U.S.	VII, VIII		VIII			VII (65) VIII (181)
Fe-17Cr-9Ni-8Mn	U.S.		III				III (91)
Fe-17Cr-13Ni-2Mo [316]	U.S.	I,II, III,IV, VI,VIII, IX,X,XI	VI	I,II, VIII, IX,X,XI	II,VIII, IX	I	I (15,71) II (79) III (49,105,117) IV (147) V (185) VI (157) VIII (181,209,251) IX (15,27,43) X (77) XI (71)
Fe-17Cr-13Ni-2Mo [316LN]	U.S.	II,IX,XI		II,IX,XI	II		II (79) IX (15,27,53) XI (71,103)
Fe-18Cr-(11-14)Ni- (0-4)Mo [316LN]	U.S.	X	X	X			X (9,31,43,55)
Fe-18Cr-3Ni-13Mn	U.S.	I,VI, VIII,XI	III	I,VIII,XI	I,VI,VII		I (93) III (91) VI (53) VII (85) VIII (167,219) XI (89)
Fe-18Cr-8Ni- (0-6)Mn	U.S.		X				X (67)
Fe-19Cr-(6-15)Ni- 4Mn-(0.1-0.3)N	USSR	VIII,XI		VIII,IX,XI			VIII (123) IX (53) XI (113)
Fe-19Cr-9Ni [304] (cont'd on next page)	U.S.	I,II, III,	I,II, III,	I,II, III,	II,III,IV		I (15,71,213) II (79,149,175) III (15,91,105,117)

\* MATERIALS STUDIES FOR MAGNETIC FUSION ENERGY APPLICATIONS AT LOW TEMPERATURES: NBSIR 78-884 (I); NBSIR 79-1609 (II); NBSIR 80-1627 (III); NBSIR 81-1645 (IV); NBSIR 82-1667 (V); NBSIR 83-1690 (VI); NBSIR 84-3000 (VII); NBSIR 85-3025 (VIII); NBSIR 86-3050 (IX); NBSIR 87-3067 (X); NBSIR 88-3082 (XI)



# SUMMARY OF MECHANICAL PROPERTY MEASUREMENTS OF STRUTURAL ALLOYS, continued

Alloy [Designation]	Country of Supplier	Tensile 295-4 K	Elastic 295-4 K	Fracture Toughness 295, 76, 4 K	Fatigue Crack Growth Rate 295, 76, 4 K	Fatigue S-N 4 K	Report, Volume (page)
Fe-19Cr-9Ni [304], cont'd	U.S.	IV,VI, VII,IX,X	IV,VIII	IV,IX, X	IV		IV (37,101,203, 215,227) V (71) VI (73) VII (13,47,75,15) IX (27) X (77)
Fe-19Cr-9Ni [304L]	U.S.	II,III, IV,VIII, IX, X	I,II,IV	II,IV VIII,IX	III,IV, VIII		I (213) II (79,123,175) IV (37,101,131, 215,302) VIII (181,229,251) IX (27,141) X (9)
Fe-19Cr-9Ni- (1-10)Mn	U.S.	IV,V, VIII	V	IV,V,VIII, IX			IV (77) V (15,59,189) VIII (181) IX (53)
Fe-19Cr-9Ni-N [304N]	U.S.	I,III, IV,IX	IV	I,III,IV, IX	I,III,IV		I (93) III (15) IV (37,101,203, 215) IX (27)
Fe-19Cr-9Ni-N [304LN]	U.S.	II,III, IV,V,VI VIII,IX	IV,VIII	II,III,IV, VIII,IX	II,III,IV, VIII		II (35,79) III (15) IV (37,101,203) V (29) VI (113) VIII (181,207,229) IX (159)
Fe-19Cr-10Ni- (0.03-0.29)N- (0.03-0.09)C	U.S.	III,VIII	VIII,IX, XI	III,VIII	III		III (15) VIII (145,181) IX (159) XI (131)
Fe-20Cr-7Ni-8Mn [216]	U.S.	VIII		VIII			VIII (151,181)
Fe-20Cr-8Ni-2Mn [304HN]	U.S.	VIII		VIII			VIII (151,181)
Fe-20Cr-16Ni-6Mn	USSR	V,VI	V				V (29,213) VI (113)
Fe-21Cr-6Ni-9Mn	U.S.	I,VIII	III,VI	I,VIII		I	I (15,71) III (91) VI (157) VIII (151,31)  VIII (181) IX (93) X (9)

\* MATERIALS STUDIES FOR MAGNETIC FUSION ENERGY APPLICATIONS AT LOW TEMPERATURES: NBSIR 78-884 (I); NBSIR 79-1609 (II); NBSIR 80-1627 (III); NBSIR 81-1645 (IV); NBSIR 82-1667 (V); NBSIR 83-1690 (VI); NBSIR 84-3000 (VII); NBSIR 85-3025 (VIII); NBSIR 86-3050 (IX); NBSIR 87-3067 (X); NBSIR 88-3082 (XI)

SUMMARY OF MECHANICAL PROPERTY MEASUREMENTS OF STRUCTURAL ALLOYS, continued

Alloy [Designation]	Country of Supplier	Tensile 295-4 K	Elastic 295-4 K	Fracture Toughness 295, 76, 4 K	Fatigue Crack Growth Rate 295, 76, 4 K	Fatigue S-N 295, 4 K	Report, Volume (page)
Fe-21Cr-12Ni-5Mn	U.S.	I,II	III	I,II	I,II		I (93) II (79) III (91)
Fe-25Cr-21Ni [310]	U.S.	V,VI, VII, VIII, IX, X	III,VI	V,VIII			III (105,117) V (71,145) VI (73) VII (65)
Fe-19Ni-9Co [200-300 grades]	U.S.		IV				IV (237)
Reviews of austenitic steels		IV,V,VI, XI	IV,V,VI, XI	IV,V,VI, XI	IV,V,VI,VII	IV, VI	IV (17,257), V (171) VI (11,127,157) VII (103) XI (3,47)
<b>ALUMINUM ALLOYS</b>							
Al-2.7Cu-2.2Li- 0.12Zr	U.S.		X				X (163)
Al-6Cu-0.2Mn-0.1Fe [5083-0]	U.S.		II	II	II	II	II (19)
Al-0.6Fe-0.2Cu- 0.1Si [1100]	U.S.	IX					IX (107)
Al-4Mg [5083-0]	U.S.	IV				II	II (35) IV (185)
<b>COPPER ALLOYS</b>							
99.99Cu-Ag [C10100, C10200]	U.S.	IX,XI					IX (95,107) XI (147)
99.5Cu-Ag [C10400]	U.S.	X	X			X	X (83,127,139)
99.75Cu-Ag [C15500]	U.S.	X	X			X	X (83,127,139, 151)
97.6Cu-Ag-0.38Be [C17510]	U.S.	X					X (83)
99.95(Cu+Fe)-18Cr- 13Mn-3Ni-0.37N [laminate]	U.S.	XI					XI (159)
<b>SUPERCONDUCTORS</b>							
Nb-45Ti	U.S.		III				III (133)

\* MATERIALS STUDIES FOR MAGNETIC FUSION ENERGY APPLICATIONS AT LOW TEMPERATURES: NBSIR 78-884 (I); NBSIR 79-1609 (II); NBSIR 80-1627 (III); NBSIR 81-1645 (IV); NBSIR 82-1667 (V); NBSIR 83-1690 (VI); NBSIR 84-3000 (VII); NBSIR 85-3025 (VIII); NBSIR 86-3050 (IX); NBSIR 87-3067 (X); NBSIR 88-3082 (XI)





AUSTENITIC STAINLESS STEELS  
WITH EMPHASIS ON STRENGTH AT LOW TEMPERATURES

Richard P. Reed

National Institute of Standards and Technology  
Boulder, Colorado

The structure and properties of austenitic stainless steels are reviewed, with emphasis on their low-temperature behavior. Austenite, ferrite, body-centered cubic and hexagonal closed-packed martensite, stacking-fault energy, carbides, and sigma phase are described. Recent international development of higher strength, tougher austenitic stainless steels is summarized. This chapter discusses the effect of martensite phase transformations on the stress-strain characteristics, as well as nitrogen strengthening and strengthening theory based on lattice-parameter and elastic-property data, all at low temperatures.

## INTRODUCTION

Rustproof steels, with increased passivity, were discovered at the turn of the century. These new steels, called stainless steels, are characterized by high Cr ( $> 10\%$ \*) and low C ( $< 0.3\%$ ). Research beginning in 1904 by Guillet (1904-1914, France),<sup>1</sup> followed by Portevin (1909-1912, France),<sup>2</sup> Giesen (1909, England),<sup>3</sup> and Monnartz (1911, Germany)<sup>4</sup> led to an understanding of the corrosion behavior of Fe-Cr-C alloys. During the same period, Guillet (1906)<sup>5</sup> and Giesen (1909)<sup>3</sup> published studies of Fe-Cr-Ni austenitic stainless steels. Clearly, the objective of these early studies was to develop a rustproof or corrosion-resistant alloy.

Since then, an enormous amount of research has been directed toward understanding and improving the properties of Fe-Cr-Ni alloys. From their initial use as cutlery, the applications of these steels have broadened considerably, along with their compositions. Only two criteria determine whether steels are classified as stainless (or rustproof or pitless): Fe base element and about 11Cr or more. This broad classification is divided into six principal subclasses:

---

\*Weight percent is used, unless otherwise specified.

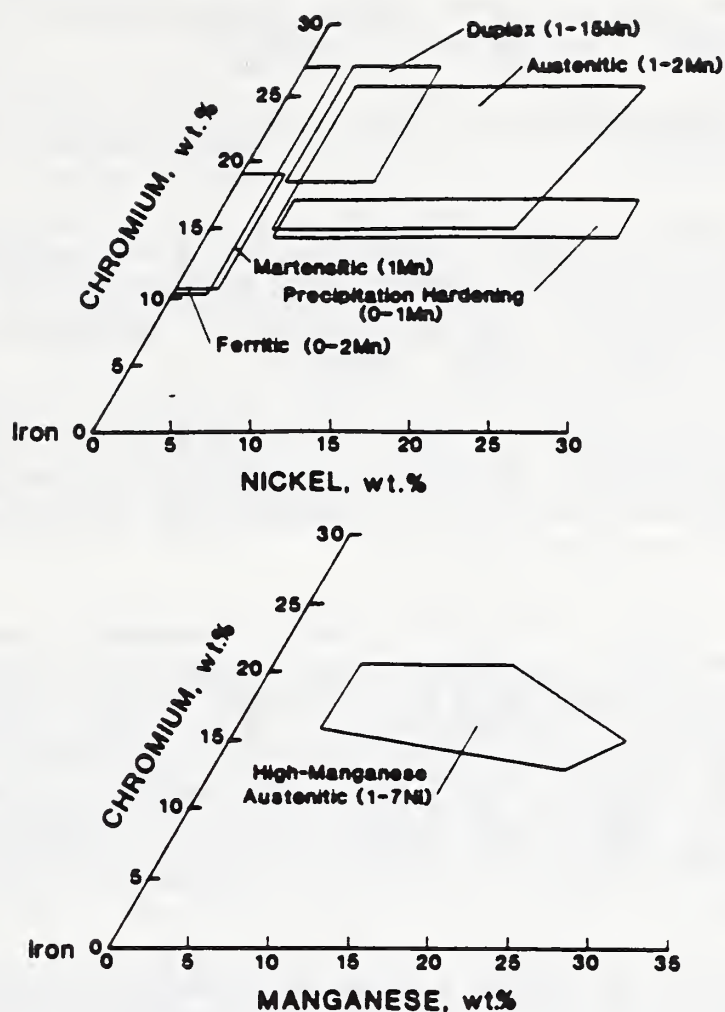
1. Ferritic steels contain 11 to 30Cr, have little or no Ni, and low C. Ferritic structure is body-centered cubic (bcc) and ferromagnetic; it is usually obtained by slow cooling from the hot forming temperature.
2. Martensitic steels typically have high Cr and low C and Ni contents. Martensitic structure is bcc; its greater hardness and strength are obtained by quenching.
3. Austenitic steels typically contain 18Cr and 8Ni. The face-centered cubic (fcc) austenitic structure is stabilized by the Ni content.
4. High-manganese, austenitic steels typically contain 24Mn, instead of 8Ni, to stabilize the austenitic structure. Their development was driven by the relative scarcity and high costs of Cr and Ni.
5. Duplex steels contain varying amounts of Ni (4-8%) to adjust the relative amounts of ferrite and austenite and, thus, to achieve high strength (from the ferrite) and adequate toughness (from the austenite).
6. Precipitation-hardened steels contain Al, Nb, and Ti, which form carbides during aging at high temperatures. The carbides precipitate in either martensitic or austenitic structures, increasing the strength at the higher temperatures.

The ternary Fe-Cr-Ni and Fe-Cr-Mn diagrams in Fig. 1 show the chemical boundaries of these elements for the six types of stainless steels. Often these steels are strengthened by adding interstitial C or N or the solid-solution alloying element Mo.

The earliest book (1935) on stainless steels that has come to our attention is a series of technical papers on production and fabrication, properties, test techniques, and applications edited by Thum.<sup>6</sup> Then in 1949 Zapffe produced a simplified book<sup>7</sup> that emphasized the three structures (ferritic, martensitic, and austenitic) of stainless steels. This book also contains the fascinating history of the development and industrial manufacture of these steels. Two volumes devoted to stainless steel applications, production, corrosion resistance, properties, and alloying effects were written by Monypenny in 1951 and 1954.<sup>8,9</sup> In 1956, Keating wrote a user-oriented book<sup>10</sup> on Cr-Ni austenitic steels that focused on properties and fabrication techniques.

The American Society for Metals published Source Book on Stainless Steels (1976)<sup>11</sup> that includes property, fabrication, corrosion, forging and heat-treatment, phase-diagram, and other information central to the use of stainless steels. To date, the exhaustive handbook assembled by Peckner and Bernstein in 1977<sup>12</sup> represents the most comprehensive review of these alloys; it documents stainless steel melting, fabrication, metallurgy, corrosion resistance, properties, and applications. Lula recently (1986) revised a general introductory book by Parr and Hanson,<sup>13</sup> in which they discuss metallurgy, properties, corrosion, and fabrication of stainless steels. In the same year, he also wrote a careful review of the metallurgy, properties, and applications of high-Mn stainless steels.





(Top) Fe-Cr-Ni ternary alloys.  
 (Bottom) Fe-Cr-Mo ternary alloys.

Figure 1. Composition ranges of various types of stainless steels.

From the 1950s into the 1980s, several major international conferences have been held on stainless steels in general or specific aspects of these alloys. Those of which we are aware are:

1. Symposium on  $\sigma$ -phase formation and verification; 1950; sponsored by the American Society for Testing and Materials.<sup>15</sup>
2. Symposium on the residual element effects on properties; 1966; sponsored by the American Society for Testing and Materials.<sup>16</sup>
3. Conference, Stainless Steels for the Fabrication and User; 1969; proceedings published by the Iron and Steel Institute, London.<sup>17</sup> At this conference, some of the first reports of dual-phase stainless steels were presented.



4. Conference on stainless steels in general, with emphasis on new applications; 1977; sponsored by Climax Molybdenum Company and held in London.<sup>18</sup>
5. Symposium on stainless steel castings; 1980; sponsored by ASTM.<sup>19</sup>
6. Conference on stainless steels with emphasis on properties and alloy development for cryogenic applications; 1982; sponsored by the International Cryogenic Materials Conference and held in Kobe, Japan.<sup>20</sup>
7. Conference on stainless steels with emphasis on fabrication techniques, selection criteria, new developments, and new applications; 1985; proceedings published by the American Society for Metals.<sup>21</sup>

Thus, notable stainless steel development, applications, and associated research have been significant for about fifty years. During this time, stainless steels have been used in many applications with material requirements far exceeding the definitive rustproof property of the steels. They are versatile because they have high toughness, variable strength, high elastic moduli, excellent weldability, and other practical properties. Their stainless nature, of course, ensures low maintenance costs in most applications.

Austenitic stainless steels are usually chosen for cryogenic applications by virtue of their low thermal conductivity, good weldability, and excellent toughness. They are well suited for applications that require unusual safety considerations, such as storage of some liquefied gases. Currently, stronger, tougher austenitic steels are needed for use at very low temperature, 4 K. Nitrogen-strengthened Fe-Cr-Ni and Fe-Cr-Mn steels are being studied and developed, especially in Japan.

Subsequent sections review how alloying affects the general structural characteristics and properties of stainless steels. The first section discusses their solidification, precipitation, and transformation structures; the second section presents the effects of alloying on their cryogenic properties.

## STRUCTURES

Stainless steels are complex. They solidify as either an austenitic (fcc) or a ferritic (bcc) structure. At intermediate temperatures, an intermetallic compound ( $\sigma$ -phase), carbide precipitates, or both may form. During cooling or plastic deformation, two martensitic transformation products with bcc and hexagonal close-packed (hcp) structures may form. At least three magnetic phases are possible: austenite is typically paramagnetic at high temperatures and antiferromagnetic at very low temperatures; ferrite is ferromagnetic.

## Austenite

Austenite is naturally the dominant phase of austenite stainless steels at ambient temperatures. Austenite is sometimes called  $\gamma$  and is always designated  $\gamma$  in phase diagrams. Solid-solution alloying elements, such as Cr, Ni, and Mn, assume normal lattice sites in the Fe-base, fcc structure; there is no convincing evidence of ordering of these elements in the austenitic steels. Smaller atoms, such as C, N, P, and S, are thought to be located interstitially in fcc octahedral lattice sites. For these elements (especially N), electronic bonding or short-range ordering may be present, but so far the evidence is circumstantial. Austenite remains paramagnetic on cooling until about 50 K; then it usually becomes antiferromagnetic. The magnetic structure of alloys with high-Ni content may become mictomagnetic or spin-glass at low temperatures. The Néel temperatures, or temperatures of transition to mixed ferromagnetic states, are strongly dependent on alloying.

## Ferrite

Ferrite may form during solidification or high-temperature treatment, depending on alloy content. It is occasionally present in small amounts (usually less than 10%) in alloys that are rapidly cooled, such as weldments. This bcc phase is conventionally called  $\delta$ -ferrite when it forms at temperatures above the  $\gamma$ -loop or range and  $\alpha$ -ferrite when it forms at lower temperatures. Most austenitic stainless steels have sufficient stabilizing elements, such as Ni, Mn, C, and N, to lower the temperature of the  $\gamma$ -loop or range sufficiently to prevent the diffusion-controlled  $\gamma \rightarrow \alpha$  transformation. In wrought alloys, the retained  $\delta$ -ferrite is typically transformed to austenite during forging or hot rolling. However, since the solubilities of many elements differ between the two phases, the solidification structure affects the location of these elements. This is especially significant for elements, such as P and S, that are more soluble in ferrite; therefore, they are less prone to precipitate along grain boundaries during solidification when  $\delta$ -ferrite is present. For this reason,  $\delta$ -ferrite is thought to avert hot cracking in austenitic stainless steel weldments.

The relative amounts of austenite and ferrite that form during solidification are critically dependent on alloying. The liquidus and solidus surfaces of the Fe-Cu-Ni ternary have been presented by Speich<sup>22</sup> and Schurmann and Brauckman.<sup>23</sup> The eutectic trough extends from near the Fe corner (76Fe-10Ni-14Cr) to a ternary eutectic (about 8Fe-43Ni-49Cr). Primary austenite solidifies if the composition is on the Ni side of the eutectic liquidus. Nearer the eutectic liquidus on the Ni side, limited ferrite forms, mainly in the dendritic cell boundaries. On the Cr-rich side of the liquidus line, primary ferrite solidifies.<sup>24</sup> Upon cooling, however, ferrite transforms to austenite in compositions typical of austenitic stainless steels. The ternary isothermal sections at 1350°C and 1100°C are shown in Fig. 2. At lower temperatures, the  $\delta + \gamma$  region increases with attendant decreases in both  $\delta$  and  $\gamma$  single regions.



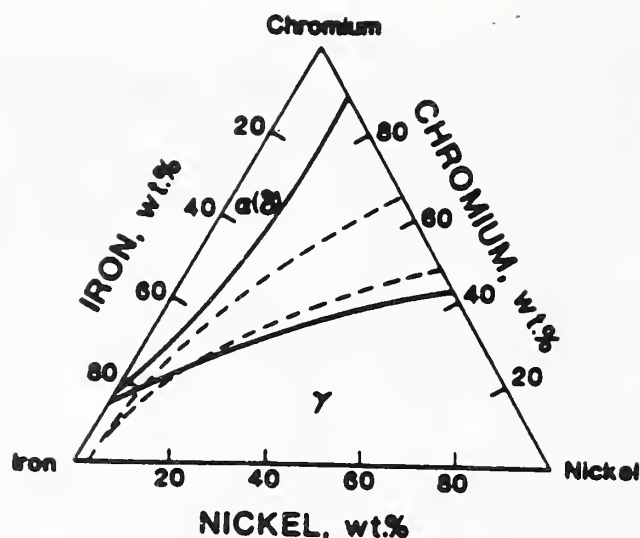


Figure 2. Isothermal sections at 1359°C (dashed lines) and 1100°C (solid lines) for Fe-Cr-Ni ternary system.

The tendency to transform from  $\delta$ -ferrite to  $\gamma$  is illustrated by the phase diagrams at constant Fe content but varying Ni and Cr content (Fig. 3). Notice that the minimum Ni content for stable  $\gamma$  at 70Fe is about 8% (22Cr) and at 60Fe, about 14.5% (25.5Cr). In practice, these limits are adjusted by small additions of C, N, Mn, Si, and, sometimes, Mo.

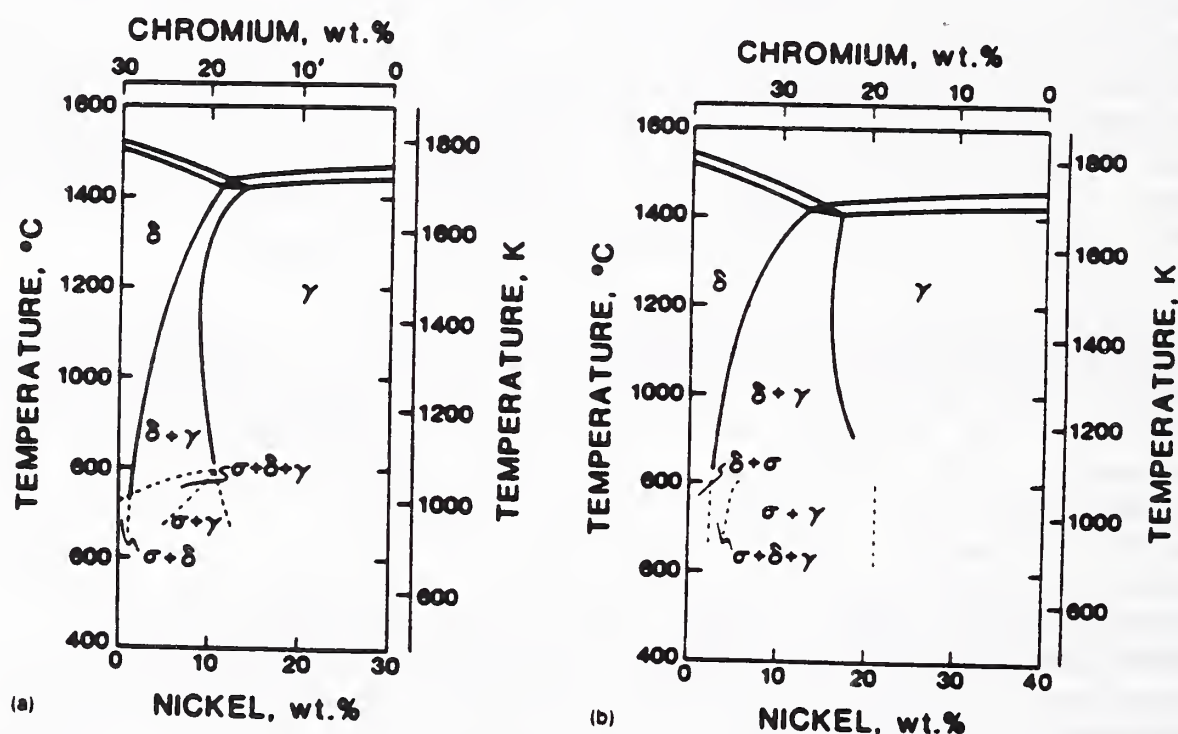


Figure 3. Binary  $\text{Fe-Cr}_x\text{Ni}_{30}$  (a) and  $\text{Fe-Cr}_y\text{Ni}_{40-y}$  (b) phase diagrams depicting dependence on Cr and Ni at constant Fe contents of (a) 30 and (b) 40 wt. %.



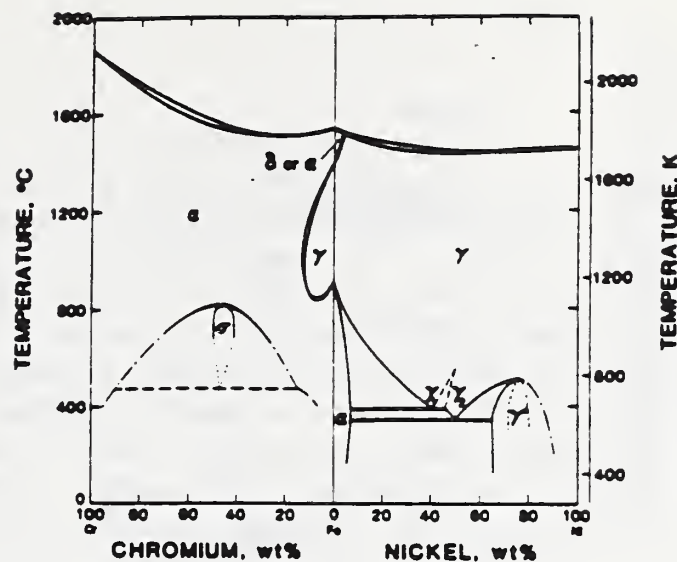


Figure 4. Binary Fe-Cr and Fe-Ni phase diagrams.

The binary Fe-Cr and Fe-Ni phase diagrams are shown in Fig. 4. Whereas adding Cr encourages ferrite, adding Ni stabilizes the austenite. Indeed, in both binaries, there is an extensive solid-solution range (>85% alloy contents) at temperatures above 800°C (below 800°C,  $\sigma$ -phase forms in Fe-Cr alloys, and below 500°C, Fe-high-Ni alloys tend to order). Binary Fe-alloy phase diagrams for Mo, Si, and Mn are reviewed by Novak.<sup>25</sup> Like Cr, Mo and Si have extensive ferrite ranges; the  $\gamma$ -loop extends to only about 2Mo and 2Si. Austenite is encouraged by alloying Fe with Mn; at 1000°C, the  $\gamma$ -loop extends to 70Mn.

For welding, the amount of  $\delta$ -ferrite present is normally estimated from a Schaeffler<sup>26</sup> or DeLong<sup>27</sup> diagram. The ferrite portion of this type of diagram is shown in Fig. 5; the lines representing zero ferrite, or the demarcation between pure austenite (above) or small amounts of ferrite (below), are plotted. Tie lines depicting constant ferrite amounts have been developed empirically in terms of the Ni equivalent (austenite-forming tendency) and Cr equivalent (ferrite-forming tendency). These equivalents serve to identify the austenite-martensite and austenite-ferrite boundaries at ambient temperatures, where many alloying elements are present.

The proposed Ni- and Cr-equivalent equations are summarized in Table 1. Presumably, the Suutala formulations,<sup>28</sup> are the most reliable equations because they are the most recent and were developed from the most data. Manganese additions up to 2 to 4% have been found to promote austenite formation; greater amounts tend to promote ferrite formation.<sup>29</sup> Nitrogen additions result in greater austenite stability. Notice in Table 1 that the more recent Hammar<sup>30</sup> equivalents emphasize C more than N. Suutala concludes that at low (normal) contents, Mn additions stabilize austenite, but at higher contents (> 5%), Mn additions enhance ferrite formation. Thus Hull's formulation,<sup>29</sup> which includes a negative  $Mn^2$  term, provides the best representation of Mn effects.

Ferrite is ferromagnetic at temperatures below about 600°C and paramagnetic at higher temperatures.

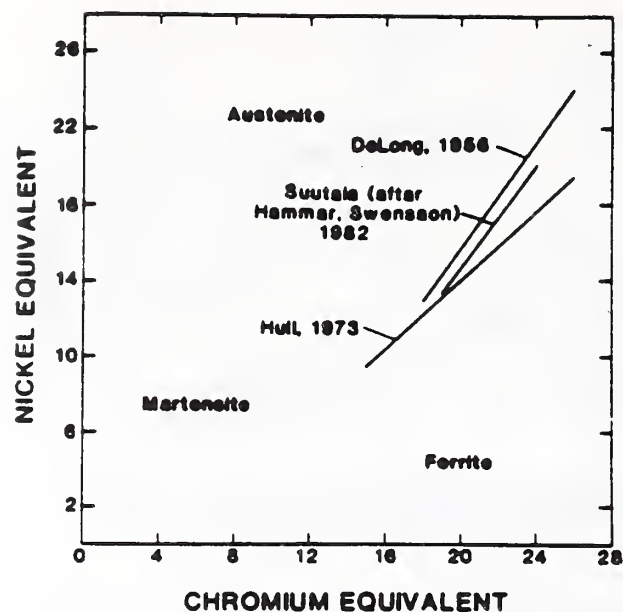


Figure 5. Ferrite portion of Schaeffler diagram depicting lines that estimate the first solidification of ferrite during cooling to room temperature after welding.

Table 1. Ferrite Solidification Equivalent Coefficients.

Investigator (year)	Cr Equivalent Coefficient (per wt.%)					
	Cr	Mo	Si	Nb	Ti	Al
DeLong et al. (1956)	1	1	1.5	0.5	—	—
Hull (1973)	1	1.21	0.48	0.14	2.2	2.48
Hammar, Svensson (1979)	1	1.37	1.5	2	3	—

Investigator (year)	Ni Equivalent Coefficient (per wt.%)						
	Ni	Mn	C	N	Cu	Co	Mn <sup>2</sup>
DeLong et al. (1956)	1	0.5	30	30	—	—	—
Hull (1973)	1	0.11	24.5	18.4	0.44	0.41	-0.0086
Hammar, Svensson (1979)	1	0.31	22.5	14.2	1	—	—



## Martensite

The use of austenitic stainless steels is complicated by the metastability of the austenitic structure of most alloys. The metastability leads to martensitic transformation, which is a significant design consideration in applications requiring fracture control planning, close dimensional tolerances, the absence of a ferromagnetic phase, and high toughness of weldment, heat-affected zone, and base metal. Either upon cooling, under applied elastic stresses, or during plastic deformation, the austenitic phase of Fe-Cr-Ni alloys may transform to bcc ( $\alpha'$ ) and hcp ( $\epsilon$ ) martensite phases. The alloy composition affects the chemical free-energy difference between the two phases.

Kaufman<sup>31</sup> derived free-energy relationships between  $\gamma$  and  $\alpha'$  for the Fe-Cr-Ni ternary system. Reed<sup>32</sup> reviewed the Fe-Cr-Ni ternary free-energy relations between fcc and bcc and suggested a relationship for the free-energy differences between fcc and hcp structures based on the earlier binary Fe-Cr- and Fe-Ni-alloy work of Kaufman.<sup>31</sup>

Other alloying elements, such as C, N, Mn, Mo, and Si, contribute to austenitic stability in austenitic stainless steels. The complexity of the final structure has led to many studies to characterize the effects of alloying on the stability of the austenitic structure with respect to  $\alpha'$ -martensite.

Expressions relating the stability of the austenite and the temperatures of transformation during cooling ( $T_{ms}$ ) or during deformation ( $T_{md}$ ) have been developed empirically and are summarized in Table 2. Eichelman and Hull,<sup>33</sup> working with austenitic alloys with compositions of 10 to 18Cr, 6 to 12Ni, 0.6 to 5Mn, 0.3 to 2.6Si, 0.004 to 0.129C, and 0.01 to 0.06N, established that all these alloying elements stabilize the austenite and thus lower  $T_{ms}$ . Monkman et al.,<sup>34</sup> using a larger number of specimens with compositions of 5 to 13Ni, 11 to 19Cr, and 0.035 to 0.126(C + N), produced a similar analysis and concluded that  $T_{ms}$  was linearly dependent on composition only to a first approximation. The dependence of  $T_{ms}$  on the C and N concentration seemed to be influenced by the Cr and Ni concentration.

Hull<sup>29</sup> studied the effects of Ni, Cr, Mn, C, N, Si, and Co (Al, Th, V, and W sometimes were added) on  $\alpha'$ -martensite formation during low-temperature cooling-and-deformation experiments and on ferrite retention after cooling to room temperature from the melt. Hull's study confirmed that all the above elements suppress low-temperature  $\alpha'$  formation during either cooling or deformation. To predict the effect of elemental additions on  $T_{ms}$ , Hull assumed that the Ni contribution was the average of the Monkman et al. and Eichelman and Hull results and then compared all the effects of alloying additions with that of Ni. The formulation of Andrews<sup>35</sup> applies to lower Cr and Ni concentrations, and thus higher  $T_{ms}$ ; his results are included in Table 2 to indicate the disparity between the high- and low-temperature empirical results. In all studies, specimens of various



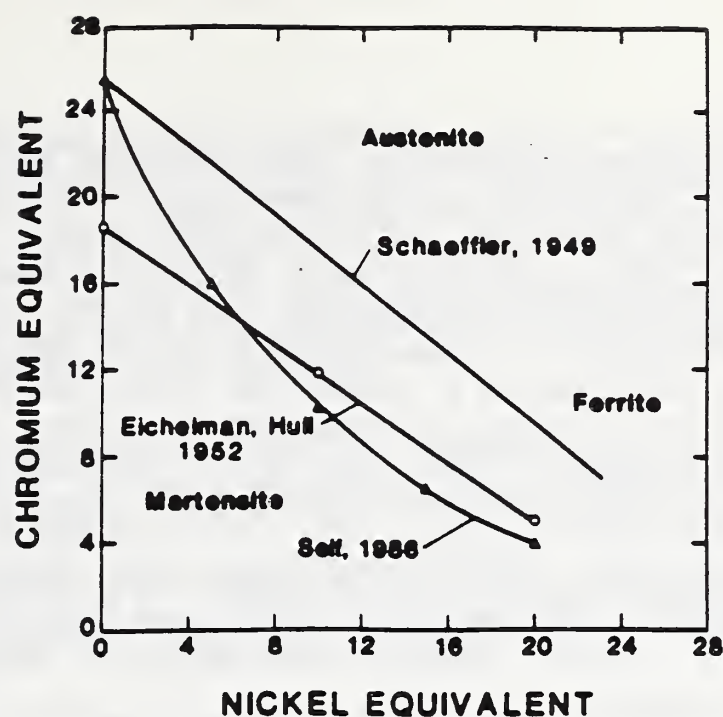
compositions were prepared and cooled, and their  $T_{ms}$  values were measured. Regression analyses were used to obtain the empirical dependence of  $T_{ms}$  on alloy concentration. Self<sup>36</sup> recently studied a wide range of compositions of weld deposits. For analyses, he assumed nonideal behavior, and with regression analysis, he derived a predictive equation containing interactive Cr-Ni and (Cr + Mo)-C terms (Table 2).

From Tables 1 and 2, it is apparent that the roles of Cr, Mo, and Si are reversed in the stabilization of the bcc structure (ferrite and  $\alpha'$ -martensite) between high and low temperatures. Binary Fe-Cr free-energy derivations<sup>31,32</sup> do not suggest this trend. Perhaps the explanation for the stabilizing effect at lower temperatures is the contribution of these elements to the increase in austenite flow strength. The effect of Mo on flow strength is discussed later in this paper.

The analytic expressions of Schaeffler, Eichelmann and Hull, and Self are plotted in terms of Ni and Cr equivalents in Fig. 6. The less conservative analysis of Self implies that at room temperature, considerably less than 18Cr is required to achieve the complete austenite stability of an 8Ni-equivalent alloy. Also, the nonlinear nature of the Self equivalent indicates the possibility of martensite control by means of alloy optimization rather than alloy "trade-offs," as offered by the linear trend lines.

Table 2. Temperature equivalent coefficients for calculation of  $T_{ms}$

Element	Equivalent coefficient, K/wt. %				
	Investigator (year)				
	Eichelmann, Hull (1953)	Monkman, Cuff, Grant (1957)	Andrews (1965)	Hull (1973)	Self (1975)
Base.....	1578	1455	273	1755	794
Cr.....	-41.7	-36.7	-12.1	-47	-14.3
Ni.....	-61.1	-56.7	-17.7	-59	-17.3
Mn.....	-33.3	-	-30.4	-54	-28.9
Si.....	-27.8	-	-	-37	-37.6
C.....	-1670	-1460	-	-2390	-350
N.....	-1670	-1460	-423	-3720	-
Mo.....	-	-	-7.5	-56	-29.6
Other.....	-	-	-	-180(Ti)	-1.19 (CrNi) +23.1 (Cr+Mo)C



For constant amounts of 1 Mn, 0.03 C, and 0.5 Si.

Figure 6. Martensite portion of Schaeffler diagram depicting lines that estimate the first formation of martensite during cooling to room temperature after welding.

Experiments have been conducted to assess the influence of cold work (either tensile or compressive) on  $T_{md}$ . Results are contained in Table 3. The experimental definition of  $T_{md}$  varied in each study: Angel<sup>37</sup> used 50%  $\alpha'$  at 30% tensile elongation; Williams et al.<sup>38</sup> used 2.5%  $\alpha'$  at 45% compressive elongation; and Hull<sup>29</sup> used the minimum detection level (probably about 1%  $\alpha'$ ) at 50% compressive elongation. There are subtle distinctions among the coefficients for  $T_{ms}$  and  $T_{md}$  calculations. After cooling, the Cr and Ni coefficients are nearly equal, Mn is higher, C and N are a factor of 50 higher; after deformation, Cr and Mn are decidedly less than Ni, and C and N are about a factor of 10 higher. Careful research to delineate the dependence of composition on free energy, stacking-fault energy, and deformation parameters is needed to understand these distinctions.

Table 3. Temperature Equivalents for Calculation of  $T_{md}$

Investigator (Year)	Equivalent Coefficients (kelvins per wt.%)								
	Base	Cr	Ni	Mn	Si	C	N	Mo	Other
Angel (1954)	686	-14	-9.5	-8.1	-9.2	-46.2	-46.2	-18.5	
Hull (1973)	1655	-23	-59	-41	-20	-777	-315	-24	-12 (Co)
Williams et al. (1976)	686	-6	-25	-16	+21	-222	-222	-11	



Upon cooling or during deformation, fcc austenite may transform to two martensitic products. The hcp phase is associated with extended stacking faults and forms as thin sheets on (111) austenite planes. In most austenitic stainless steels, the  $\alpha'$  product forms as laths. Breedis<sup>39</sup> reported a lath  $\alpha'$  morphology for compositions ranging from Fe-19Cr-11Ni to Fe-10Cr-16Ni; at lower Cr and higher Ni concentrations the  $\alpha'$  morphology changed to surface martensite and then to a plate-like structure (Fig. 7). From Reed,<sup>40</sup> the  $\alpha'$  lath-like structure is parallel to  $\langle 110 \rangle_\gamma$ , with  $(225)_\gamma$ ,  $(112)_\gamma$ , or both habit planes.<sup>41</sup> The laths are restricted within  $(111)_\gamma$  bands, and usually three sets of habit planes form within the band.

There is a considerable amount of accommodation deformation in the austenite after transformation during cooling, particularly within the (111) bands containing the  $\alpha'$  laths. Either  $\epsilon$ -martensite or large amounts of stacking faults are present.

The orientation relationships between the  $\gamma$ -,  $\epsilon$ -, and  $\alpha'$ -phases<sup>41</sup> are

$$\begin{aligned} (111)_\gamma &\parallel (0001)_\epsilon \parallel (101)_{\alpha'} \\ [110]_\gamma &\parallel [\bar{1}210]_\epsilon \parallel [111]_{\alpha'} \end{aligned} \quad (1)$$

These relationships are apparently retained regardless of the manner of  $\epsilon$  or  $\alpha'$  formation.

Transformation during plastic deformation initially results in  $\alpha'$ -martensite at intersections of active (111) deformation bands. The  $\alpha'$  assumes the shape of laths along  $\langle 110 \rangle$  common to the two active (111) systems. Evidence of dislocation pileups at  $\alpha'$  laths has been observed.<sup>32</sup> Also, more than one lath forms at each transformation site, and in contrast to the  $\alpha'$ -phase that forms on cooling, all laths have the same habit-plane variant.

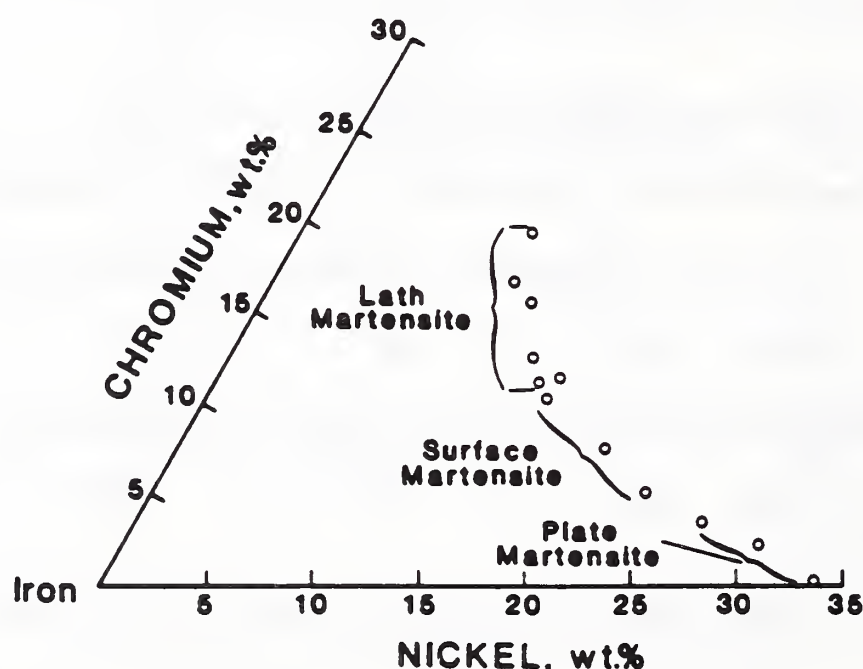


Figure 7. Compositional dependence of  $\alpha'$ -martensite morphology in Fe-Cr-Ni ternary alloys.



The internal defect structure of the  $\alpha'$ -phase in Fe-Cr-Ni steels consists predominantly of dislocations. As Cr is replaced by Ni, Breedis<sup>39</sup> reports that the cellular, irregular distributions of dislocations that are typical of  $\alpha'$  laths change to the planar, regular arrays that are typical of  $\alpha'$  plates. Also, as Ni replaces Cr, the amount of  $\epsilon$  transformation decreases, the sharpness of the hcp reflections decreases, and the fcc twin reflections become more diffuse.

Many metallurgists have been concerned with the role of the  $\epsilon$  transformation: does  $\epsilon$  act as a precursor transformation ( $\gamma \rightarrow \epsilon \rightarrow \alpha'$ ), or is the  $\epsilon$  an accommodation effect ( $\gamma \rightarrow \alpha'$ ,  $\gamma \rightarrow \epsilon$ )? Both effects have been observed. The stainless steels with low stacking-fault energy tend to form  $\epsilon$ , and the  $\alpha'$  tends to form from  $\epsilon$ . Higher stacking-fault-energy alloys require transformation stresses for observable  $\epsilon$  formation.

Several characteristics of the austenite-bcc-martensite transformation in stainless steels cause problems in many applications. The martensitic bcc has a specific volume 1.7% larger than the parent austenite; therefore, these steels expand during transformation. The martensite forms as individual crystals, and the shear stress and volume expansion associated with transformation disrupt localized regions. For example,  $\alpha'$  formation near or at the surface results in localized surface upheavals. For service that requires close tolerances, such as valves or bearings, these local surface fluctuations are disastrous.

Another concern, mostly in the presence of magnetic fields or pulsed currents, is that the bcc martensitic product is ferromagnetic, whereas the parent austenite is paramagnetic. A simple rule is that each percent of bcc martensite results in a permeability increase of 0.01. Therefore, if time-dependent field changes corresponding to material changes of the order of 0.10 are significant, than alloy selection is important.

### Stacking-Fault Energy

The stacking-fault energy is related to the free-energy difference between the fcc principal structure and the hcp structure. Lower stacking-fault energy leads to wider partial-dislocation separation (larger fault ribbons), and hence, more planar dislocation slip structures and reduced cross slip.

Schramm and Reed<sup>42</sup> used x-ray peak-shift measurements, coupled with previous stacking-fault energy measurements, to estimate the dependence of the stacking-fault energy on chemical composition. This dependence should correspond to the dependence of the  $\gamma \rightarrow \epsilon$  transformation on composition, because a stacking fault represents a local planar area of  $\epsilon$ . Rhodes and Thompson<sup>43</sup> suggested that the stacking-fault energy values of the Schramm and Reed analysis were too large, considering additional weak-beam electron-microscopy data. Weak-beam electron microscopy measurements by Bampton, Jones, and Loretto<sup>44</sup> confirmed that the least-square analysis of Schramm and Reed produced stacking-fault energies that were too large. From measurements of individual nodes, they estimated a data spread of  $\pm 25\%$ . Brofman and Ansell<sup>45</sup> added C content to the factors affecting stacking-fault energy. The stacking-fault energy composition dependencies are contained in Table 4.

Table 4. Stacking-fault energy at room temperature.

Investigator (Year)	Energy Equivalent, mJ/(m <sup>2</sup> ·wt.%)							
	Base	Cr	Ni	Mn	Si	C	Mo	Other
Dulieu, Nutting (1964)	0	-	0.5	1.4	-	3.4	0.1	3.6 (Ti), 3.2 (Cu), -0.55 (Co)
Schramm, Reed (1975)	-53	0.7	6.2	3.2	-	-	9.3	
Rhodes, Thompson (1977)	1.2	0.6	1.4	17.7	-4.7	-	-	
Brofman, Ansell (1978)	16.7	0.9	2.1	-	-	26	-	

Ledbetter and Austin<sup>46</sup> recently examined with x-rays the effects of additions of C and N ( $C + N \leq 0.325$  wt.%,  $N \leq 0.21$  wt.%) on the stacking-fault energy of an Fe-8Cr-10Ni alloy. They reported an increase of about 10% in the stacking-fault energy per at.% C + N. Earlier, Stoltz and VanderSande<sup>47</sup> determined with weak-beam microscopy that N in excess of about 0.24 wt.% dramatically decreased the stacking-fault energy of an Fe-19Cr-7Ni-8Mn-0.03C alloy. Fujikuma et al.<sup>48</sup> measured stacking-fault probabilities for an Fe-18Cr-10Ni-8Mn alloy. They reported a minimum at about 0.15N; a slight increase at lower N contents, and a rapid increase at higher N. Thus, all three sets of measurements appear to be consistent: the stacking-fault energy increased slightly with N contents up to about 0.20 wt.%; it decreased substantially for higher N contents.

### Carbides

The solid-solution solubility of the mobile interstitials C and N in austenitic alloys is very temperature dependent (Fig. 8).<sup>49,50</sup> At temperatures less than about 950°C, C begins to precipitate as a carbide in practically all austenitic steels, since the solubility limit is about 0.035. Using electron microscopy, the solubility of C in type 316 steel (Fe-19Cr-14Ni-2Mo) has been represented by the expression<sup>51</sup>:

$$\log [C \text{ (ppm)}] = 7.771 - 6272/T(K) \quad (1)$$



The solubility limits determined from Eq. (1) are considerably less than those given in Fig. 8, which reflects the higher sensitivity of electron microscopy for detection of carbides. Carbides precipitate in the range 500 to 1000°C; below 500°C the atom mobility is too low, and above 1000°C the solubility of C and N is sufficient. The most common carbide is  $M_{23}C_6$ , where M represents a metal, normally Cr. However, Fe, Mo, Ti, and Nb also may assume the position of the metallic element, and N and B may assume the position of C in the  $M_{23}C_6$  structure.

The solubility limits of both C and N are reduced by the presence of Ni (see Fig. 8 for C). On the basis of binary Fe-Ni data,<sup>52</sup> Fig. 9 shows that this reduction is about 0.014N from the addition of 20Ni. The data of Sakamoto et al.,<sup>53</sup> obtained from observations of bubbling vacuum-induction melts, are quite consistent and represent the practical limits of maximum N contents (Fig. 9). These limits are particularly important to define the N-strengthening limitations that are discussed under Strength. Consistent with the binary alloy solubility limits, these data show that both Cr and Mn increase the ingot capacity for N.

Carbides precipitate primarily at ferrite-austenite interfaces, followed by grain boundaries, noncoherent and coherent twin boundaries, and, finally, within grains. This is depicted schematically in Fig. 10.<sup>54,55</sup> The temperature decreases and the time for nucleation increases as the precipitation site changes from high- to low-energy boundaries. Increased C content increases precipitation temperature and decreases time; increased N content has the reverse effect, suppressing carbide formation.<sup>12</sup>

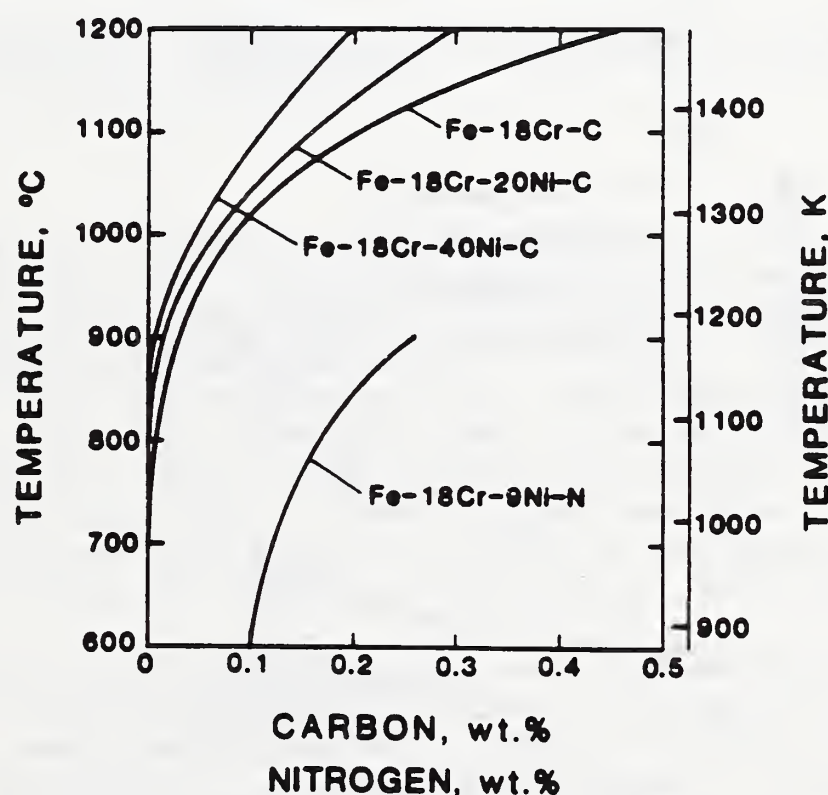


Figure 8. Solubility limits for carbon<sup>(49)</sup> and nitrogen<sup>(50)</sup> as functions of temperature for various alloys.



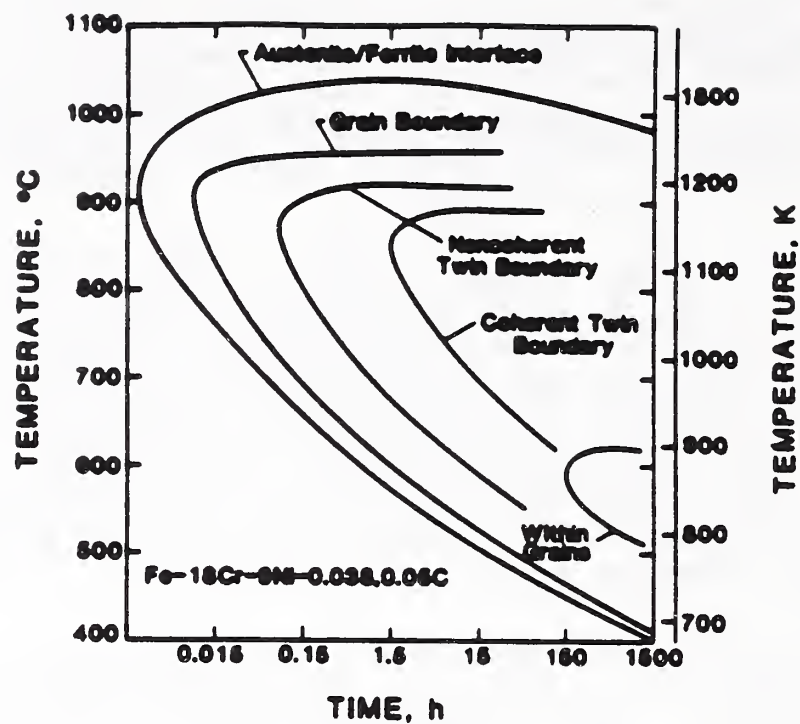


Figure 9. Solubility limits for nitrogen in Fe-Cr, Fe-Ni, and Fe-Mn binary alloys at 1473 K<sup>(52)</sup> and in Fe-15Ni-Mn-Cr alloy liquids<sup>(53)</sup>.

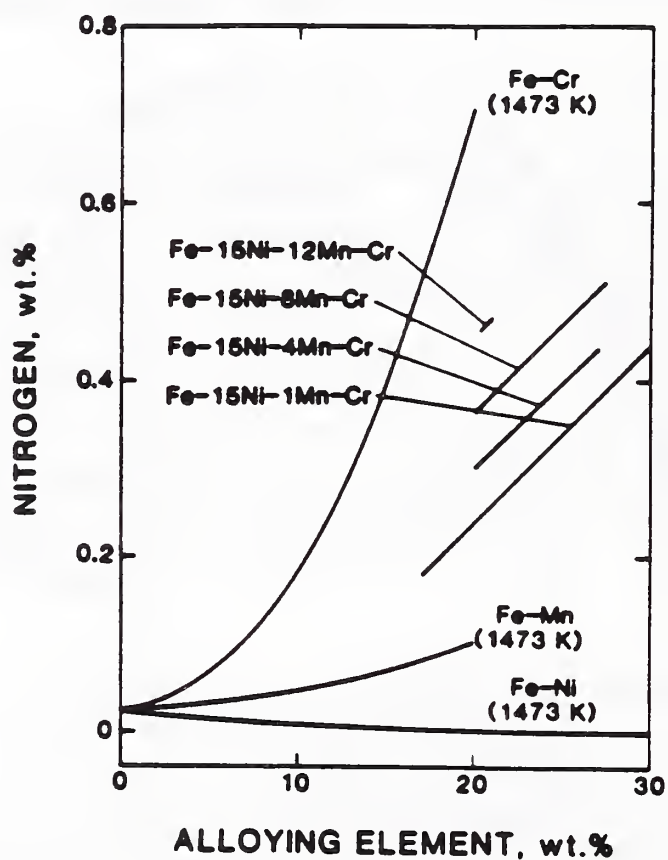


Figure 10. Time-temperature carbide precipitation kinetics, with specific sites identified<sup>54, 55</sup>.

The  $M_{23}C_6$  carbide has a complex fcc structure with 92 metallic atoms and 24 smaller (C, N, or B) atoms and a lattice parameter of 10.61 to 10.64 Å.<sup>12</sup> But there is only minor mismatch between the (111)  $M_{23}C_6$  and (111) austenite, estimated at 1.3% by Lewis and Hattersley.<sup>56</sup> Thus, the common plane of the interface between the two structures has been identified as (111).<sup>55,56</sup> Alloy additions to the  $M_{23}C_6$  structure, such as N, tend to decrease its lattice parameter and to increase the amount of interface mismatch. This should retard the growth kinetics.

Carbide precipitates normally have a sheet-like morphology at lower temperatures (480–730°C) and dendritic shapes at intermediate temperatures (600–875°C); particles form at the higher temperatures (> 850°C).<sup>55</sup> Higher temperatures, as well as longer aging times, promote coarsened structures.

Carbide precipitation in austenitic steels has long been associated with increased sensitivity to intergranular corrosion, termed sensitization. For many applications, suppression of sensitization is achieved by rapid cooling from solution-treatment temperature. During welding, however, the heat-affected zone unavoidably enters the temperature range of carbide formation. To prevent severe sensitization during welding, two courses have been followed: (1) low-carbon ( $\leq 0.03$ ) grades, designated by AISI with the "L" nomenclature, have been provided and (2) alloys with Ti (AISI 321) and Nb (AISI 347) have been developed to achieve more random TiC or NbC precipitation within grains, rather than  $M_{23}C_6$  precipitation at grain boundaries. These alloys are often called stabilized grades of stainless steel, since the C, taken out of solution, is unavailable for carbide formation and precipitation at grain boundaries.

More thorough reviews of carbide formation in austenitic steels are provided by Novak<sup>25</sup> and Lai.<sup>57</sup>

### Sigma Phase

Notice the Fe–Cr part of the phase diagram in Fig. 4: at Cr contents greater than about 15%, the  $\sigma$ -phase may form when the alloy is exposed to temperatures between 400 to 800°C. The  $\sigma$ -phase extends into the Fe–Cr–Ni ternary diagram, as indicated by Fig. 3. Alloys rich in Cr and lean in Ni tend toward  $\sigma$ -phase formation at lower temperatures. Maehara et al.<sup>58</sup> studied the effects of alloy additions on the amounts and aging times for  $\sigma$ -phase formation. They found that Ni decreases the amount of  $\sigma$ -phase formation, but increases the rate of formation in an Fe–25Cr–2.8Mo-base alloy. Additions of Cr and Mo increase both the aging kinetics and amount of  $\sigma$ -phase in Fe–6.5Ni–2.8Mo and Fe–25Cr–6.5Ni-base alloys, respectively.

In Fe–Cr, the highest temperature of  $\sigma$ -phase formation is 821°C (Fig. 4); Ni additions gradually increase this temperature (Fig. 3). The constant-Fe vertical sections of the Fe–Cr–Ni ternary of Fig. 3 are consistent with the liquidus, solidus, 1100°C, and 650°C isotherms of Speich<sup>22</sup> and the 802°C and 648°C isotherms of Talbot and Furman.<sup>59</sup> Like carbides, the  $\sigma$ -phase forms preferentially at high-energy surfaces. Also, when ferrite is present, there is a strong tendency for  $\sigma$ -phase to form initially within the ferrite or at the ferrite side of the  $\gamma$ – $\delta$  boundary.



The  $\sigma$ -phase has a tetragonal structure, 30 atoms per unit cell, an  $a_0$  lattice parameter range of  $-8.29$  to  $9.21$  Å, and  $c_0$  lattice parameter range of  $-4.60$  to  $4.78$  Å.<sup>12</sup> Sigma-phase alloy constituents do not have fixed stoichiometric ratios; they may range from  $B_4A$  to  $BA_4$ . Alloy additions, such as Cr, Mo, V, and Si, promote  $\sigma$ -phase formation.

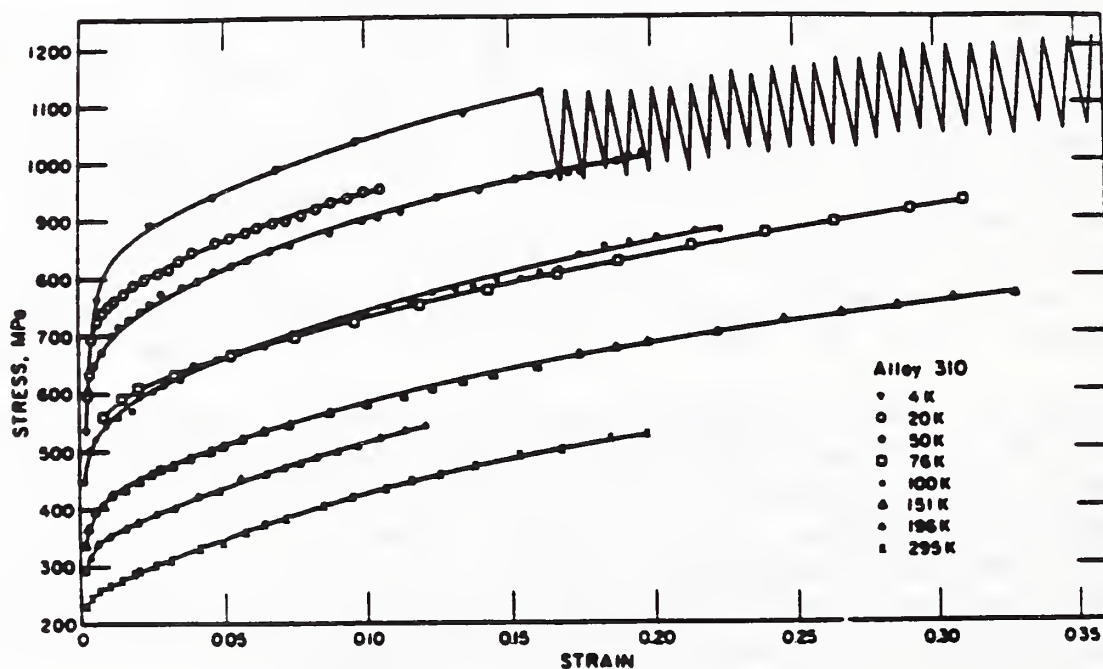
For a more extensive review, see Novak<sup>25</sup> and Lai.<sup>57</sup>

## PROPERTIES

### Stress-Strain Characteristics

The AISI 300 series stainless steels used in cryogenic applications range from metastable to stable austenites. Alloys such as 304, containing 18Cr and 8Ni, are metastable, whereas 310, containing 26Cr and 20Ni, is stable with respect to martensitic transformation. The stress-strain behavior and temperature dependence of the flow strength of these alloys differ and depend on the austenite stability. In the less stable alloys, both  $\epsilon$ - and  $\alpha'$ -martensite form; in the slightly metastable alloys, such as 316, only  $\alpha'$ -martensite forms; and in the stable alloys, neither  $\epsilon$ - nor  $\alpha'$ -martensite forms during deformation to fracture at any temperature.

At low temperatures, the tensile stress-strain characteristics of austenitic stainless steels depend on the stability of the austenitic structure. Consider the engineering stress-strain curves of a stable austenitic steel, alloy 310 (Fig. 11a) and a metastable alloy 304 (Fig. 11b) at low temperatures. As the temperature decreases, the yield strength of alloy 310 increases significantly, and the work-hardening rates, reflecting only dislocation interactions, remain relatively constant.





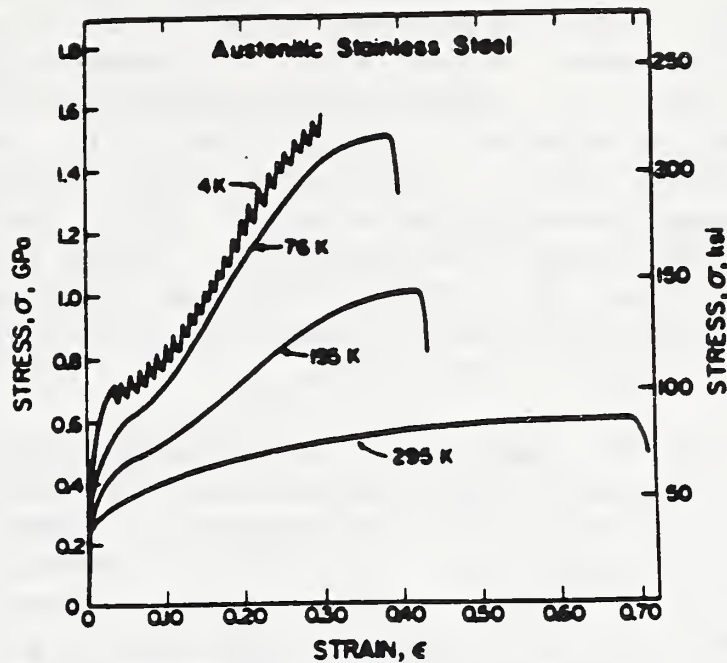


Figure 11. Low-temperature stress-strain curves for (top) a stable austenitic alloy 310 (Fe-23Cr-20Ni) and (bottom) a metastable austenitic alloy 304 (Fe-19Cr-9Ni).

In a metastable austenitic, polycrystalline alloy at low temperatures, three distinct stages are present in the stress-strain curves. The contours of their stress-strain curves (Fig. 12) are remarkably similar to single-crystal shear-stress-strain curves. Stage I represents the microstrain and early macrostrain behavior. The formation of  $\alpha'$ -martensite is not thought to occur in this range; stacking-fault clusters, or  $\epsilon$ -martensite, or both are most likely to complement dislocation interactions to reduce the rate of work hardening.

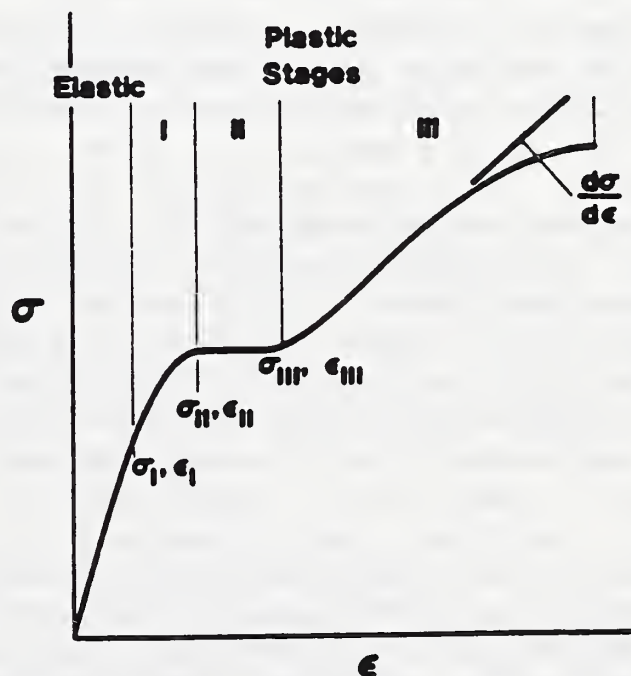


Figure 12. Schematic depiction and characterization of three stages associated with the stress-strain curves for polycrystalline metastable austenitic stainless steels at low temperatures.

Stage II, the "easy glide" range, is associated with increasing  $\epsilon$ -martensite formation and the formation of  $\alpha'$ -martensite laths at cross-slip intersections. Suzuki et al.<sup>60</sup> proposed that such  $\alpha'$  laths, with the long  $\langle 110 \rangle$  direction representing the intersection of two active slip systems, act as windows to assist cross slip. Another possible explanation is that strain-induced  $\epsilon$ -martensite (whose formation increases prevalent in this stage), contributes a larger strain component (or, alternatively, exhibits lower work-hardening rates). Stage II is most prevalent in the temperature range 76 to 200 K. In this temperature region, the range of strain at which the stress remains relatively constant is large, usually from 0.04 to 0.10.

In stage III, the rate of work hardening increases and then becomes constant over a relatively large amount of plastic deformation (20 to 40%). The volume percentage of  $\alpha'$ -martensite is linearly related to plastic deformation in stage III. The nature of the transition in the roles of  $\alpha'$ -martensite formation — from possibly promoting easy glide in stage II to being associated with a linear, high rate of work hardening in stage III — is not clear. Perhaps in stage III essentially all active cross-slip sites have been transformed to  $\alpha'$ -martensite, and subsequent  $\alpha'$ -martensite formation occurs within active glide bands. Such  $\alpha'$ -martensite formation would not be expected to promote stacking-fault glide. There is a hint from the x-ray data of Reed and Guntner<sup>61</sup> that the following sequence may occur: A maximum value of the volume concentration of  $\epsilon$ -martensite occurs at about the transition from stage II to stage III. There is apparently no  $\epsilon$ -martensite formation during stage III; the amount of  $\epsilon$ -martensite decreases with strain, presumably transforming to  $\alpha'$ -martensite.

Stages I and II decrease in significance in more stable austenites, but stage III is retained. For instance, AISI 316 exhibits neither stage I nor stage II, but does begin to transform to  $\alpha'$ -martensite at strains of about 0.02 below 190 K. No  $\epsilon$ -martensite was detected in 316LN alloys.

Alloying of austenitic stainless steels affects the stress and strain parameters of the three stages of low-temperature deformation. The effects of Mn alloying on these parameters at 4 K have been studied by Reed and Tobler.<sup>62</sup> The yield strength,  $\sigma_y$  (flow strength at 0.002 plastic strain) is within stage I. As shown in Fig. 13,  $\sigma_y$  is linearly dependent on Mn content, increasing with increasing Mn. The linear dependence is similar to that of  $\sigma_{II}$ , the stress at which stage II begins. The increase of  $\sigma_y$  with Mn is considerable, about 33 MPa per wt.% Mn. The addition of Mn to austenite solid solution does not alter the lattice parameter nor the shear modulus significantly (see later discussion), therefore traditional solid-solution strengthening should not result from Mn addition. But, Mn increases the stacking-fault energy and suppresses  $\alpha'$ - and  $\epsilon$ -martensite transformation; these phase transformations influence the stress and strain parameters. Therefore, the increases in strength that occur when Mn is added are due to Mn's contribution to austenite stability. Figure 13 shows that an addition of 0.1N increases  $\sigma_y$  about 290 MPa. Nitrogen has the same strengthening effect in stable alloys, which implies that N has little effect on hcp or bcc stability within the composition range 0.1 to 0.2 wt. %



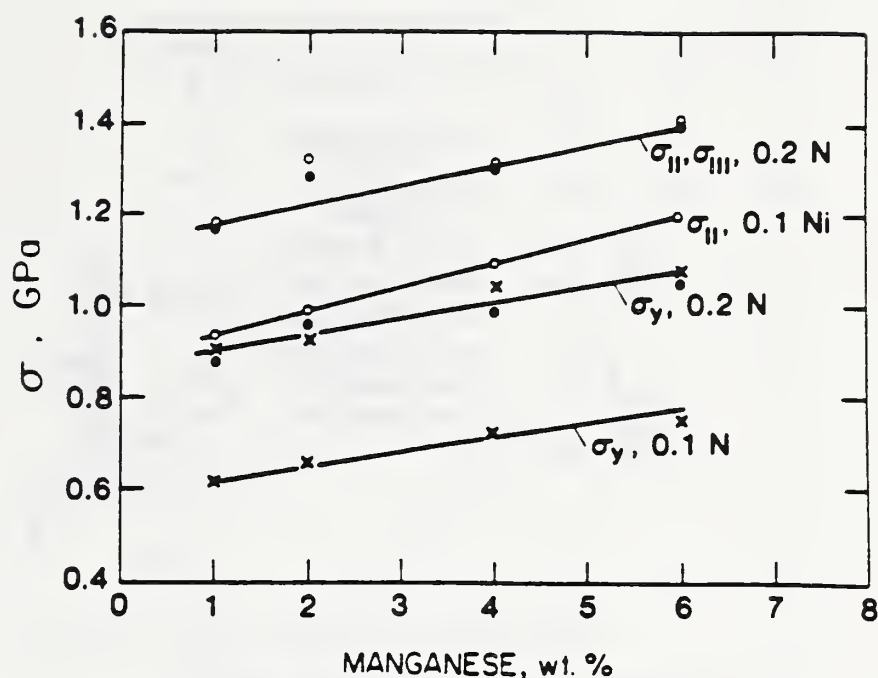


Figure 13. Dependence of stages I and II strength parameters on Mn and N contents at 4 K.

The stress denoting transition to the region of high work-hardening rates,  $\sigma_{III}$ , tracks very closely with  $\sigma_{II}$ . The rate of work hardening (from engineering stress-strain curves) of stage III decreases with increasing Mn and N, as shown in Fig. 14. The addition of N slightly affects the dependence of Mn content; N contributes to the reduction of  $d\sigma/d\epsilon$  about ten times more strongly (on the basis of wt.% addition) than Mn. The dependence of the work-hardening rate in stage III on the percent  $\alpha'$ -martensite per unit elongation is shown in Fig. 15. Clearly, there is a strong linear correlation, and the rate of work hardening can be regarded as a function of austenite stability with respect to  $\alpha'$ -martensite formation, as determined by composition.

We have performed numerous correlations between the normalized amount of strain-induced  $\alpha'$ -martensite at final elongation at 4 K and the alloy composition. Our best correlation for this normalized strain-induced martensite was obtained by using the Williams et al.<sup>38</sup> regression analysis for  $T_{md}$ . In Fig. 16 their expression is plotted versus percent  $\alpha'$ /percent tensile elongation at 4 K for a series of modified 316LN alloys. Correlation is excellent for these alloys with a calculated  $T_{md}$  ranging from 120 to 240 K.

Therefore, the deformation characteristics of austenitic stainless steels can be significantly controlled by alloying. Sufficient alloy additions to stabilize the austenite result in typical solid-solution-strengthened, fcc stress-strain characteristics. The shape of the stress-strain curves of metastable austenites during strain-induced  $\alpha'$ - and  $\epsilon$ -martensite transformations is affected by alloying.



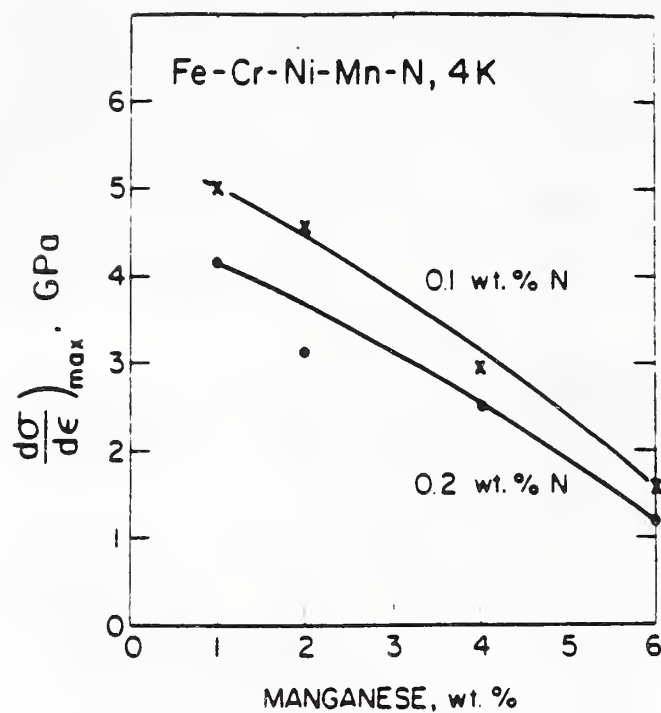


Figure 14. Dependence of stage III work-hardening rate on Mn and N contents at 4 K.

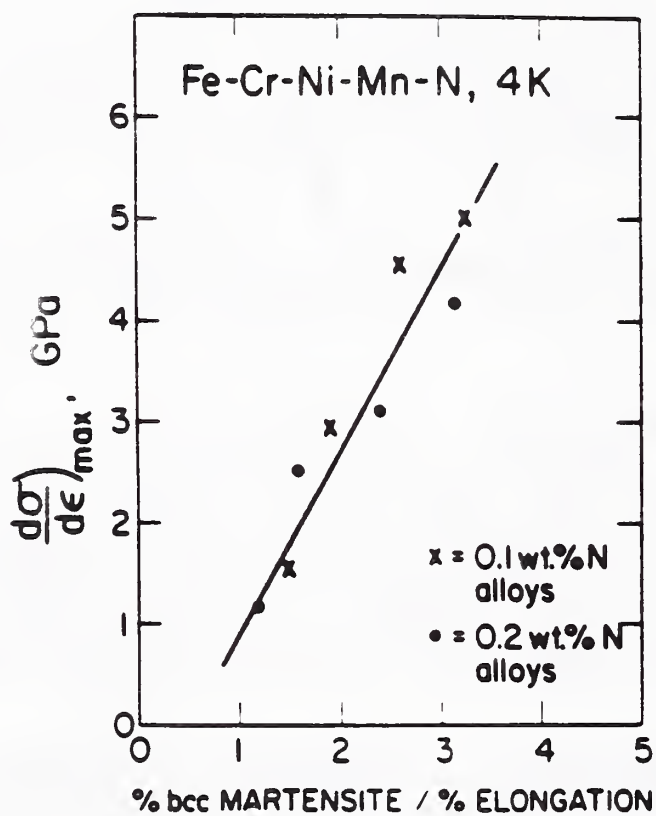


Figure 15. Dependence of stage III work-hardening rate on normalized amount of  $\alpha'$ -martensite formed during uniform elongation at 4 K.

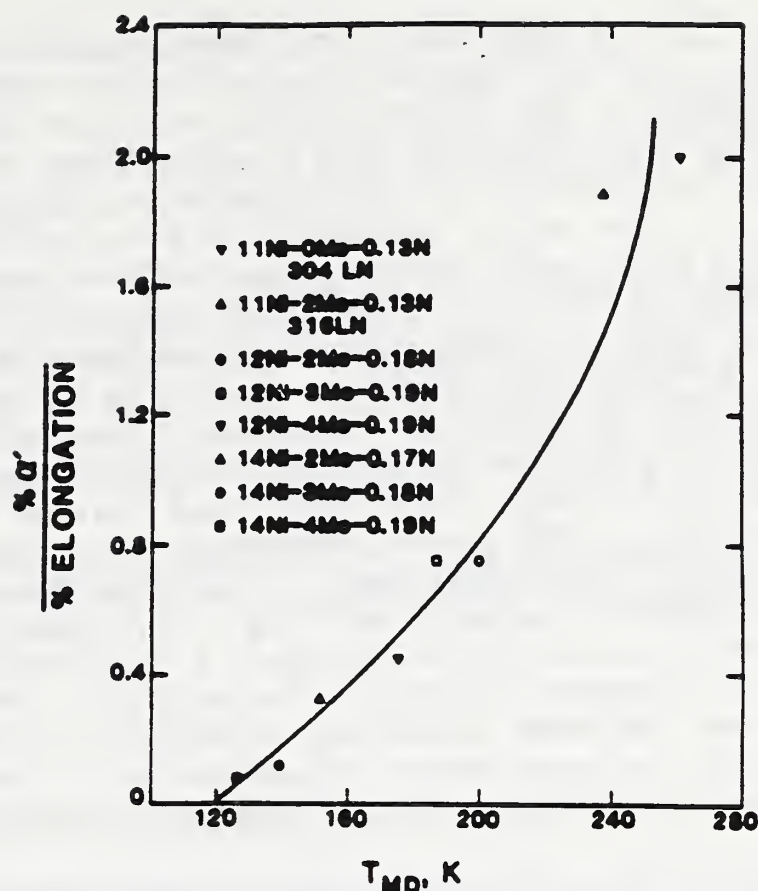


Figure 16. Correlation between normalized  $\alpha'$ -martensite formation in stage III with alloying, as characterized by the  $T_{md}$  calculations of Williams et al.<sup>37</sup>

### Strength

In addition to austenite stability, the strength of austenitic stainless steels is influenced by temperature, grain size, cold and hot working, and interstitial and solid-solution alloying. Temperature and grain-size effects have been discussed previously.<sup>63-66</sup> We focus here on the effects of alloy strengthening on stable austenitic steels at low temperatures.

At very low temperatures, the variation of tensile yield strength ( $\sigma_y$ ) with N, C, Mo, Mn, and Ni additions to Fe-Cr-Ni austenitic steels has been recently and extensively studied. In Japan a program to develop an alloy with  $\sigma_y$  of 1200 MPa and a toughness of 200 MPa·m<sup>1/2</sup> has now been completed.<sup>67-69</sup> At NBS we have tested at low temperatures some of the new Japanese alloys, the European 316LN alloys, and selected laboratory heats from U.S. suppliers in which N, C, Mo, Mn, and Ni alloy additions were systematically varied. A summary of these test results follows.

The interstitial additions substantially strengthen the alloys at low temperatures.<sup>64,65,70-83</sup> In Fig. 17, the effect of C + N on  $\sigma_y$  at 4 K for an Fe-18Cr-10Ni steel is presented.<sup>72</sup> The break in the linear dependencies at about 0.15(C + N) is related to martensitic transformation; at lower C + N contents, the strain-induced martensite reduces the lower flow strength, as discussed in the Stress-Strain Characteristics section. Regression analysis of 99 data points for alloy 316LN (and alloys with similar compositions) at 4 K indicated that  $\sigma_y$  increased 237 MPa per 0.1N;<sup>77</sup> an earlier analysis of 30 data points of 304LN-type alloys at 4 K found that  $\sigma_y$  increased 319 MPa per 0.1N.<sup>70</sup> Strengthening from C is about half that

of N at 4 K.<sup>70</sup> Thus, N additions strengthen considerably more than equivalent C additions at low temperatures. Alloying with N instead of C also reduces the tendency toward sensitization, as discussed under Carbides. Furthermore, N is less expensive than C. For these reasons, N is now usually selected to increase the low-temperature strength of austenitic stainless steels. Many recent studies have measured the strengthening contribution from N for both Fe-Cr-Ni and Fe-Cr-Mn base austenitic structures at 4 K.<sup>64,65,70-75,77-83</sup> Studies of Reed and Simon<sup>70,77</sup> found a smaller standard deviation from regression analyses using the power of one to express the [N] dependence compared to 1/2 or 2/3 power dependence. Fundamental theories for solid-solution strengthening<sup>84-86</sup> predict dependence of the flow strength on concentration to the power 1/2 or 2/3 from dislocations cutting through the stress field created by individual atoms of this concentration. The linear dependence of  $\sigma_y$  on C + N shown in Fig. 17 also supports this assessment. This dependence of  $\sigma_y$  on N alloying is strongly dependent on temperature (Fig. 17). Reed and Simon<sup>70</sup> found that the N coefficient increased by a factor of 6 from 295 to 4 K, while the coefficient for C increased by only a factor of 2. This strong temperature dependence implies increased N bonding strength, or clustering, below room temperature, since the temperature dependence of C (the larger atom), should reflect the modulus and size effects (see later discussion).

The dependence of  $\sigma_y$  on solid-solution alloying additions, such as Mo, Mn, and Ni, is not as great. Molybdenum increases strength most effectively, about 50 MPa per wt.% at 4 K.<sup>74,87-89</sup> There is evidence that at higher Ni contents the strengthening effects of Mo are reduced.<sup>89</sup> Mn, when not affecting austenite stability, increases  $\sigma_y$  by about 10 MPa per wt.% at 4 K.<sup>53,73,75,89,90</sup> Nickel does not contribute directly to solid-solution strengthening, but does affect strength through its strong contribution to austenite stability. The temperature dependence of the solid-solution strengthening additions has not been assessed.

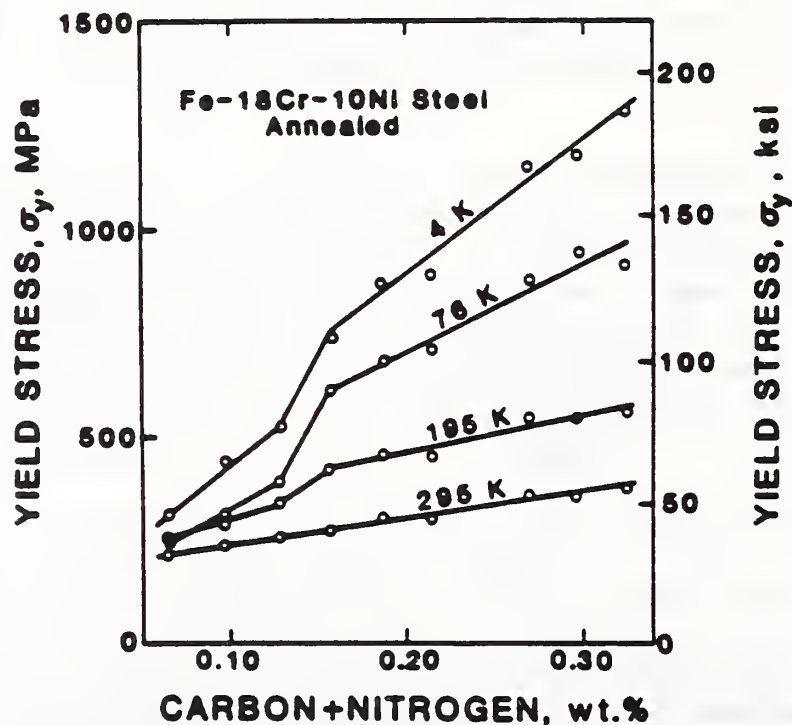


Figure 17. Dependence of yield strength on C and N contents in Fe-18Cr-10Ni austenitic stainless steel at low temperatures.



In Table 5, the strengthening contributions from substitutional and interstitial alloying additions in fcc elements<sup>92-97</sup> and in austenitic stainless steels<sup>62-91</sup> are listed in terms of a fraction of the shear modulus. This refers to the increase of  $\sigma_y$  from adding 100% (by atoms) of the solute, found by extrapolating from available data that usually range from 1 for interstitials to 5 to 20 at.%.

Adding C to Ni<sup>96</sup> or C to austenite produces roughly the same increases in strength at low temperatures. The addition of Mo to Ni or to Fe-Cr-Ni is also approximately equivalent. Galligan and Goldman<sup>92</sup> have achieved much stronger strengthening effects from alloying by quenching-in Ag into probable split-interstitial sites in Pb. In their work, strength increases are linearly proportional to Ag content, not to a fractional power of it.

From the theory of solid-solution strengthening,<sup>84-86</sup> the shear strength,  $\tau$ , resulting from a random array of single atoms interacting with mobile dislocations is

$$\tau = A[C_F^{2/3}] [f_o^{4/3}], \quad (2)$$

Table 5. Strengthening Contributions in fcc Alloys.

Solvent	Solute	Temperature (K)	Amount ( $\Delta\sigma/100\%$ )
Ag	Al	4	G/30
	Sb	294	G/100
		76	G/30
Ni	Mo	295	G/45
	C	4	G/7
		295	G/30
Cu	Ni	76	G/120
	Au	76	G/100
Pb	Ag*	4	2G
	Sn	4	0
Fe-Cr-Ni (Austenite)	N	4	G/2.5
		295	G/15
	C	4	G/5.5
		295	G/10
	Mo	4	G/60
		295	0
	Mn	4	G/200
		295	0
	Ni	4	0
		295	0

\*Quenched from 300 K

where  $C_F$  is the concentration of a solute species, and  $A$  is considered to be a constant for this discussion. The maximum interaction force,

$$f_0^2 = \eta^2 + \alpha^2 \delta^2, \quad (3)$$

where the modulus misfit,

$$\delta = \frac{1}{G} \frac{dG}{dc}. \quad (4)$$

In Eq. (4),  $G$  is the shear modulus,  $c$  is the concentration, and the size misfit,

$$\delta = \frac{1}{a} \frac{da}{dc},$$

where  $a$  is the lattice parameter. The constant  $\alpha$  is typically about 20.<sup>84</sup> Thus, the relative magnitudes of the strengthening contributions of various solutes may be estimated by comparing the modulus and size misfit parameters, assuming that other possible strengthening effects (e.g., electrostatic, stacking-fault interactions) are small.

Ledbetter and Austin<sup>98</sup> studied the elastic properties of austenitic stainless steel alloy series and measured their lattice parameters. Their measurements are summarized in Table 6, where  $E$  is Young's modulus,  $G$  is shear modulus,  $B$  is bulk modulus,  $\nu$  is Poisson's ratio, and  $V$  is atomic volume. Lattice parameter measurements at 4 K are planned in the near future.

Table 6. Effect of Alloying on Volume and Elastic Constants.

Alloying Element	$\frac{1}{a} \frac{da}{dc}$	$\frac{1}{E} \frac{dE}{dc}$		$\frac{1}{G} \frac{dG}{dc}$		$\frac{1}{B} \frac{dB}{dc}$		$\frac{1}{\nu} \frac{d\nu}{dc}$		$V(X)/V(Fe)$
	295 K	295 K	4 K	295 K	4 K	295 K	4 K	295 K	4 K	
C	0.218	-0.78	0.61	-0.76	0.81	-0.93	-0.52	-0.11	-0.90	0.34
N	0.240									0.30
Ni	-0.003	0.07	—	0.09	—	-0.01	—	-0.06	—	0.93
Mn	0.022	-0.30	-0.38	-0.27	-0.37	-0.45	-0.48	-0.12	-0.08	1.04
Mo	0.150	-0.91	-0.14	-1.18	-0.38	0.79	1.30	1.22	1.13	1.32
Cr	0.075	—	—	—	—	—	—	—	—	1.02



At room temperature both C and N show a large size misfit despite their small atom size [signified by the  $V(X)/V(Fe)$  ratio]; obviously they must occupy interstitial lattice sites to achieve this increase. This size misfit is larger for N than C, although the atom size of N is less than C. The divergence of E and G trends from B and  $\nu$  trends implies electronic bonding effects that alter shear modes differently than dilatational modes; this divergence is found for N and C at 4 K and for Mo at both temperatures. Furthermore, the change of the sign of the Young's and shear moduli parameters of N and C on cooling from 295 to 4 K implies a low-temperature transition toward increased covalent bonding.

The maximum interaction forces, assuming  $\alpha = 20$ , for each solute are summarized in Table 7. The order of ratios of the interaction forces is nearly correct when compared to the strengthening contribution listed in Table 5; only C and N are reversed. However, the relative magnitudes of the interaction forces of C and N show greater disparity compared to the relative magnitudes of the solute contributions. The interstitial element interaction forces are smaller than would be expected if one considered their strengthening contributions. This disparity undoubtedly will be increased at 4 K when the lattice parameter measurements at 4 K are obtained: the ratio of strengthening contributions from interstitials increases relative to substitutional solid-solution elements at 4 K.

This leads to the suggestion that, particularly at low temperatures, the dislocation-interstitial interaction is distinct from that of the dislocation-solid-solution interaction. The interaction force ratios could be brought more in line with the strengthening contributions by increasing  $\alpha$ , the parameter related to the curvature of the interaction potential of the solvent with the moving dislocations,<sup>8,9</sup> since the size-misfit parameters relate directly to the relative strengthening contributions for each type of atom. These disparities, combined with the linear dependence of strength on solute interstitial content, lead to the consideration of interstitial clustering.

Galligan and Goldman<sup>9,2</sup> measured strengthening factors of 2G at room temperature for presumably split interstitials of Ag in Pb, where Ag has only slightly lower specific volume than Pb. It is not difficult to envision that the much smaller C and N interstitials, in similar lattice positions strengthen by factors of G/10 to G/15 at room temperature and that this strong, short-range interaction force is strongly temperature dependent.

Table 7. Maximum Interaction Forces\* for Solutes in Austenitic Stainless Steel.

T(K)	C	N	Ni	Mn	Mo
295	4.43	4.86	0.26	0.52	3.22

$$*f_0^2 = \eta^2 + \alpha^2 \delta^2, \text{ where } \alpha \text{ is assumed to equal } 20$$



## SUMMARY

Austenitic stainless steel structures and strengths have been reviewed. Emphasis was placed on low-temperature characteristics to include recent studies that have led to stronger alloys for cryogenic applications. The stress-strain characteristics of austenitic stainless steels depend on austenite stability. A region of low work hardening, following initial plastic deformation, is associated with hcp martensite formation and bcc martensite formation at cross-slip sites. The final work-hardening stage is associated with bcc martensite formation. All stages are related to alloying effects on austenite stability.

The interstitials C and N have been shown to contribute more to strength than that predicted by solution-hardening dislocation theories. It is argued that C and N must act in clusters to increase solution hardening. Nitrogen has proven to be the most effective alloying element for increasing strength at low temperatures.

## REFERENCES

1. L. Guillet, "Chromium Steels," Rev. Metall. 1, 155 (1904).
2. A. M. Portevin, "Contribution to the Study of the Special Ternary Steels," Iron and Steel Institute, Carnegie Sch. Mem. 1, 230 (1909).
3. W. Giesen, "The Special Steels in Theory and Practice," Iron and Steel Institute, Carnegie Sch. Mem. 1 (1909).
4. P. Monnartz, "The Study of Iron-Chromium Alloys with Special Consideration of their Resistance to Acids," Metallurgie 8, 161 (1911).
5. L. Guillet, "Nickel-Chrome Steels," Rev. Metall. 3, 332 (1906).
6. The Book of Stainless Steels, Ed. E. E. Thum, American Society for Metals, Metals Park, Ohio (1935), 787 pp.
7. C. A. Zapffe, Stainless Steels, American Society for Metals, Metals Park, Ohio (1949), 368 pp.
8. J. H. G. Monypenny, Stainless Iron and Steel, vol. 1, Chapman and Hall, London (1951), 524 pp.
9. J. H. G. Monypenny, Stainless Iron and Steel, vol. 2, Chapman and Hall, London (1954), 330 pp.
10. F. H. Keating, Chromium Nickel Austenitic Steels, Butterworths Scientific, London (1956), 138 pp.
11. Source Book on Stainless Steels, American Society for Metals, Metals Park, Ohio (1976), 408 pp.
12. Handbook of Stainless Steels, Eds. D. Peckner and I. M. Bernstein, McGraw-Hill, New York (1977).

13. J. G. Parr and A. Hanson, revised by R. A. Lula, Stainless Steel, American Society for Metals, Metals Park, Ohio (1986), 173 pp.
14. R. A. Lula, Manganese Stainless Steels, The Manganese Centre, Paris (1986), 83 pp.
15. Symposium on the Nature, Occurrence, and Effects of Sigma Phase, STP 110, American Society for Testing and Materials, Philadelphia (1951), 181 pp.
16. Effects of Residual Elements on Properties of Austenitic Stainless Steels, STP 418, American Society for Testing and Materials, Philadelphia (1967), 136 pp.
17. Stainless Steels, The Iron and Steel Institute, London (1969), 214 pp.
18. Stainless Steel '77, Climax Molybdenum Company (1977), Climax, Colorado, 256 pp.
19. Stainless Steel Castings, Eds. V. G. Behal and A. S. Melilli, STP 756, American Society for Testing and Materials, Philadelphia (1982), 444 pp.
20. Austenitic Steels at Low Temperatures, Eds. R. P. Reed and T. Horiuchi, Plenum Press, New York (1983), 388 pp.
21. New Developments in Stainless Steel Technology Conference Proceedings, Ed. R. A. Lula, American Society for Metals, Metals Park, Ohio (1985), 391 pp.
22. G. R. Speich in: Source Book on Stainless Steels, American Society for Metals, Metals Park, Ohio (1976), pp. 424-426.
23. E. Schurmann and S. Brauckman, "Untersuchungen über die Schmelzgleichgewichte in der Eisenecke des Dreistoffsystems Eisen-Chrom-Nickel," Arch. Eisenhüttenw. 48, 3-8 (1977).
24. J. A. Brooks, J. C. Williams, and A. W. Thompson, "STEM Analysis of Primary Austenite Solidified Stainless Steel Welds," Metall. Trans. 14A, 23-31 (1983).
25. C. J. Novak in: Handbook of Stainless Steels, Eds. D. Peckner and I. M. Bernstein, McGraw-Hill, New York (1977), pp. 401-478.
26. A. Schaeffler, "Constitution Diagram for Stainless Steel Weld Metal," Met. Prog., p. 680B.
27. W. T. DeLong, G. A. Ostrom, and E. R. Szumachowski, "Measure and Calculation of Ferrite in Stainless Steel Weld Metal," Weld. J. 35, 521s-528s (1956).
28. N. Suutala, "Effects of Manganese and Nitrogen on the Solidification Mode in Austenitic Stainless Steel Welds," Metall. Trans. 13A, 2121-2130 (1982).



29. F. C. Hull, "Delta Ferrite and Martensite Formation in Stainless Steels," Weld. J. 52, 193s-203s (1973).
30. O. Hammar and U. Svensson in: Solidification and Casting of Metals, The Metals Society, London (1979), pp. 401-410.
31. L. Kaufman, "The Lattice Stability of the Transition Metals," in: Phase Stability in Metals and Alloys, Eds. P. S. Rudman, J. Stringer, and R. I. Jaffee, McGraw-Hill, New York (1967), pp. 125-150.
32. R. P. Reed, "Martensitic Phase Transformations," in: Materials at Low Temperatures, Eds. R. P. Reed and A. F. Clark, American Society for Metals, Metals Park, Ohio (1983), pp. 295-341.
33. G. H. Eichelman and F. C. Hull, "The Effect of Composition on the Temperature of Spontaneous Transformation of Austenite to Martensite in 18-8 Type Stainless Steel," Trans. Amer. Soc. Met. 45, 77-104 (1953).
34. F. C. Monkman, F. B. Cuff, and N. J. Grant, "Computation of  $M_s$  for Stainless Steels," Met. Prog. 71, 94-96 (1957).
35. K. W. Andrews, "Empirical Formulae for the Calculation of Some Transformation Temperatures," J. Iron Steel Inst. 203, 721-727 (1965).
36. J. A. Self, "Effects of Compositions upon the Martensite Transformation Temperature of Austenitic Steel Welds," Center for Welding Research, MT-CWR-086-037, Colorado School of Mines, Golden, Colorado (1986).
37. T. Angel, "Formation of Martensite in Austenitic Stainless Steels," J. Iron Steel Inst. 177, 165-174 (1954).
38. I. Williams, R. G. Williams, and R. C. Capellano, "Stability of Austenitic Stainless Steels between 4 K and 373 K," in: Proceedings of the Sixth International Cryogenic Engineering Conference, IPC Science and Technology Press, Guildford, Surrey, England (1976), pp. 337-341.
39. J. G. Breedis, "Martensitic Transformation Iron-Chromium-Nickel Alloys," Trans. AIME 230, 1583-1596 (1964).
40. R. P. Reed, "The Spontaneous Martensitic Transformations in 18% Cr, 8% Ni Steels," Acta Metall. 10, 865-887 (1962).
41. R. M. Kelly, "The Martensite Transformation in Steels with Low Stacking Fault Energy," Acta Metall. 13, 635-646 (1965).
42. R. E. Schramm and R. P. Reed, "Stacking Fault Energies of Seven Commercial Austenitic Stainless Steels," Metall. Trans. 6A, 1345-1351 (1975).
43. C. G. Rhodes and A. W. Thompson, "The Composition Dependence of Stacking Fault Energy in Austenitic Stainless Steels," Metall. Trans. 8A, 1901-1906 (1977).



44. C. C. Bampton, L. P. Jones, and M. H. Loretto, "Stacking Fault Energy Measurements in Some Austenitic Stainless Steels," *Acta Metall.* 26, 39-51 (1978).
45. P. J. Brofman and G. S. Ansell, "On the Effect of Carbon on the Stacking Fault Energy of Austenitic Stainless Steels," *Metall. Trans.* 9A, 879-880 (1978).
46. H. M. Ledbetter and M. W. Austin, "Stacking-Fault Energies in 304-Type Stainless Steels: Effects of Interstitial Carbon and Nitrogen" in: Materials Studies for Magnetic Fusion Energy Applications at Low Temperatures—VIII, Ed. R. P. Reed, National Bureau of Standards, NBSIR 85-3025, Boulder, Colorado (1985), pp. 271-294.
47. R. E. Stoltz and J. B. VanderSande, "The Effect of Nitrogen on Stacking Fault Energy of Fe-Ni-Cr-Mn Steels," SAND 79-8735, Sandia Laboratories, Albuquerque, New Mexico (1979).
48. M. Fujikuma, K. Takada, and K. Ishida, "Effect of Manganese and Nitrogen on the Mechanical Properties of Fe18%Cr10%Ni Stainless Steels," *Trans. Iron Steel Inst. Jap.* 15, 464-469 (1975).
49. H. Tuma, M. Vyklicky, and K. Lobl, "Activity and Solubility of C in Austenitic 18 Percent Cr-Ni Steels," *Arch. Eisenhüttenw.* 41, 983-988 (1970).
50. T. Masumoto and Y. Imai, "Structural Diagrams and Tensile Properties of the 18 Percent Cr-Fe-Ni-N Quarternary System Alloys," *J. Jpn. Inst. Met.* 33, 1364-1371 (1969).
51. M. Deighton, "Solubility of  $M_{23}C_6$  in Type 316 Stainless Steel," *J. Iron Steel Inst.* 208, 1012-1014 (1970).
52. D. Kumar, A. D. King, and T. Bell, "Mass Transfer of Nitrogen from  $N_2-H_2$  Atmospheres into Fe-18Cr-Ni-Mn Alloys," *Met. Sci.* 17, 32-40 (1983).
53. T. Sakamoto, Y. Nakagawa, and I. Yamauchi, "Effect of Mn on the Cryogenic Properties of High Nitrogen Austenitic Stainless Steels in: Advances in Cryogenic Engineering—Materials, Vol. 32, Eds. R. P. Reed and A. F. Clark, Plenum Press, New York (1986), pp. 65-71.
54. S. J. Rosenberg and C. R. Irish, "Solubility of Carbon in 18 Percent Chromium - 10 percent Nickel Austenite," *J. Res. Nat. Bur. Stand.* 48, 40-48 (1952).
55. R. Stickler and A. Vinckier, "Morphology of Grain-Boundary Carbides and Its Influence on Intergranular Corrosion of 304 Stainless Steel," *Trans. Amer. Soc. Met.* 54, 362-380 (1961).
56. M. H. Lewis and B. Hattersley, "Precipitation of  $M_{23}C_6$  in Austenitic Steels," *Acta Metall.* 13, 1159-1168 (1965).
57. J. K. L. Lai, "A Review of Precipitation Behavior in AISI Type 316 Stainless Steel," *Mater. Sci. Eng.* 61, 101-109 (1983).

58. Y. Maehara, Y. Ohmori, J. Murayama, N. Fujino, and T. Kunitake, "Effects of Alloying Elements on  $\sigma$  Phase Precipitation in  $\delta\gamma$  Duplex Phase Stainless Steels," *Met. Sci.* 17, 541-547 (1983).
59. A. M. Talbot and D. E. Furman, "Sigma Formation and Its Effect on the Impact Properties of Iron-Nickel-Chromium Alloys," *Trans. Amer. Soc. Met.* 45, 429-442 (1953).
60. T. Suzuki, H. Kojama, K. Suzuki, T. Hashimoto, and M. Ichihara, "An Experimental Study on the Martensite Nucleation and Growth in 18/8 Stainless Steel," *Acta Metall.* 25, 1151-1162 (1977).
61. R. P. Reed and C. J. Guntner, "Stress-Induced Martensitic Transformations in 18Cr-8Ni Steel," *Trans. AIME* 230, 1713-1720 (1964).
62. R. P. Reed and R. L. Tobler, "Deformation of Metastable Austenitic Steels at Low Temperatures," in: Advances in Cryogenic Engineering—Materials, vol. 28, Eds. R. P. Reed and A. F. Clark, Plenum Press, New York (1982), pp. 49-56.
63. R. P. Reed, and J. M. Arvidson, "The Temperature Dependence of the Tensile Yield Strength of Selected Austenitic Steels," in: Advances in Cryogenic Engineering—Materials, vol. 30, Eds. A. F. Clark and R. P. Reed, Plenum Press, New York (1984), pp. 263-270.
64. N. J. Simon and R. P. Reed, "Strength and Toughness of AISI 304 and 316 at 4 K," *J. Nucl. Mater.* 141-143, 44-48 (1986).
65. R. P. Reed, N. J. Simon, P. T. Purtscher, and R. L. Tobler, "Alloy 316LN for Low Temperature Structures: A Summary of Tensile and Fracture Data, in: Proceedings, Eleventh International Cryogenic Engineering Conference, Eds. G. Klipping and I. Klipping, Butterworths, Guildford, Surrey, England (1986), pp. 786-790.
66. R. L. Tobler, R. P. Reed, and D. S. Burkhalter, "Temperature Dependence of Yielding in Austenitic Stainless Steels," in: Advances in Cryogenic Engineering—Materials, vol. 26, Eds. A. F. Clark and R. P. Reed, Plenum Press, New York (1980), pp. 107-110.
67. H. Nakajima, K. Yoshida, Y. Takahashi, E. Tada, M. Oshikiri, K. Koizumi, S. Shimamoto, R. Mira, M. Shimara, S. Tone, "Development of the New Cryogenic Structural Material for Fusion Experimental Reactors," in: Advances in Cryogenic Engineering—Materials, vol. 32, Eds. R. P. Reed and A. F. Clark, Plenum Press, New York (1984), pp. 219-226.
68. K. Yoshida, N. Nakajima, K. Koizumi, M. Shimada, Y. Sanda, Y. Takahashi, E. Tada, H. Tsuji, and S. Shimamoto, "Development of Cryogenic Structural Materials for Tokamak Reactor," in: Austenitic Steels at Low Temperatures, Eds. R. P. Reed and T. Horiuchi, Plenum Press, New York (1983) pp. 29-39.



69. S. Shimamoto, H. Nakajima, K. Yoshida, and E. Tada, "Requirements for Structural and Alloys for Superconducting Magnet Cases," in: Advances in Cryogenic Engineering—Materials, vol. 32, Eds. R. P. Reed and A. F. Clark, Plenum Press, New York (1986), pp. 23-32.
70. R. P. Reed and N. J. Simon, "Low Temperature Strengthening of Austenitic Stainless Steels with Nitrogen and Carbon," in: Advances in Cryogenic Engineering—Materials, vol. 30, Eds. A. F. Clark and R. P. Reed, Plenum Press, New York (1984), pp. 127-136.
71. K. Nohara, T. Kato, T. Sasaki, S. Suzuki, and A. Ejima, "Strengthening and Serrated Flow of High-Manganese Nonmagnetic Steel at Cryogenic Temperature," in: Advances in Cryogenic Engineering—Materials, vol. 30, Eds. R. P. Reed and A. F. Clark, Plenum Press, New York (1984), pp. 193-201.
72. R. L. Tobler and R. P. Reed, "Tensile and Fracture Properties of Manganese-Modified AISI 304 Type Stainless Steel," in: Advances in Cryogenic in Engineering—Materials, vol. 28, Eds. R. P. Reed and A. F. Clark, Plenum Press, New York (1982), pp. 83-92.
73. T. Horiuchi, R. Ogawa, M. Shimada, S. Tone, M. Yamaga, and Y. Kasamatsu, "Mechanical Properties of High Manganese Steels at Cryogenic Temperatures," in: Advances in Cryogenic Engineering—Materials, vol. 28, Eds. R. P. Reed and A. F. Clark, Plenum Press, New York (1982), pp. 93-103.
74. S. Yamamoto, N. Yamagami, and C. Ouchi, "Effect of Metallurgical Variables on Strength and Toughness of Mn-Cr and Ni-Cr Stainless Steels at 4.2 K," in: Advances in Cryogenic Engineering—Materials, vol. 32, Eds. R. P. Reed and A. F. Clark, Plenum Press, New York (1986), pp. 57-64.
75. T. Horiuchi, R. Ogawa, and M. Shimada, "Cryogenic Fe-Mn Austenitic Steels," in: Advances in Cryogenic Engineering—Materials, vol. 32, Eds. R. P. Reed and A. F. Clark, Plenum Press, New York (1986), pp. 33-42.
76. R. L. Tobler, D. H. Beekman, and R. P. Reed, "Factors Influencing the Low Temperature Dependence of Yielding in AISI 316 Stainless Steels," in: Austenitic Steels at Low Temperatures, Eds. R. P. Reed and T. Horiuchi, Plenum Press, New York (1983), pp. 135-157.
77. N. J. Simon and R. P. Reed, "Design of 316LN-Type Alloys," in: Advances in Cryogenic Engineering—Materials, vol. 34, Eds. A. F. Clark and R. P. Reed, Plenum Press, New York (1987), to be published.
78. R. P. Reed, P. T. Purtscher, K. A. Yushchenko, "Nickel and Nitrogen Alloying Effects on the Strength and Toughness of Austenitic Stainless at 4 K," in: Advances in Cryogenic Engineering—Materials, vol. 32, Eds. R. P. Reed and A. F. Clark, Plenum Press, New York (1986), pp. 33-42.



79. T. Sakamoto, Y. Nakagawa, and I. Yamauchi." Effect of Mn on the Cryogenic Properties of High Nitrogen Austenitic Stainless Steels," in: Advances in Cryogenic Engineering—Materials, vol. 32, Eds. R. P. Reed and A. F. Clark, Plenum Press, New York (1986), pp. 65-71.
80. Y. Takahashi, K. Yoshida, M. Shimada, E. Tada, R. Miura, and S. Shimamoto, "Mechanical Evaluation of Nitrogen-Strengthened Stainless Steels at 4 K," in: Advances in Cryogenic Engineering—Materials, vol. 28, Eds. R. P. Reed and A. F. Clark, Plenum Press, New York (1986), pp. 73-81.
81. H. Masumoto, K. Suemune, H. Nakajima, and S. Shimamoto, "Development of High-Strength, High-Manganese Steels for Cryogenic Use," in: Advances in Cryogenic Engineering—Materials, vol. 30, Eds. A. F. Clark and R. P. Reed, Plenum Press, New York (1984), pp. 169-176.
82. K. Shibata, Y. Kobiti, Y. Kishimoto, and T. Fujita, "Mechanical Properties of High Yield Strength High Manganese Steels at Cryogenic Temperatures," in: Advances in Cryogenic Engineering—Materials, Vol. 30, Eds. R. P. Reed and A. F. Clark, Plenum Press, New York (1984), pp. 169-176.
83. T. Sakamoto, Y. Nakagawa, I. Yamauchi, T. Zaizen, H. Nakajima, and S. Shimamoto, "Nitrogen-Containing 25Cr-13Ni Stainless Steel as a Cryogenic Structural Material," in: Advances in Cryogenic Engineering—Materials, vol. 30, Eds. A. F. Clark and R. P. Reed, Plenum Press, New York (1984), pp. 145-152.
84. P. Haasen, "Solution Hardening in f.c.c. Metals," in: Dislocations in Solids, Chapter 15, Ed. F. R. N. Nabarro, North-Holland, New York (1976), pp. 155-189.
85. F. R. N. Nabarro, "The Theory of Solution Hardening," Philos. Mag. 35, 613-622 (1977).
86. R. Labusch, "Statistische Theorien der Mischkristallhärte," Acta Metall. 20, 917-927 (1972).
87. K. Suemune, K. Sugino, H. Matsumoto, H. Nakajima, and S. Shimamoto, "Improvement of Toughness of a High-Strength, High-Manganese Stainless Steel for Cryogenic Use," in: Advances in Cryogenic Engineering—Materials, vol. 32, Eds. R. P. Reed and A. F. Clark, Plenum Press, New York (1986), pp. 51-56.
88. K. Ishikawa, K. Hiraga, T. Ogata, and K. Nagai, "Low Temperature Properties of High-Manganese-Molybdenum Austenitic Iron Alloys," in: Austenitic Steels at Low Temperatures, Eds. R. P. Reed and T. Horiuchi, Plenum Press, New York (1983), pp. 295-309.
89. P. T. Purtscher and R. P. Reed, "Effect of Chemical Composition on the 4 K Mechanical Properties of 316LN-Type Alloys," in: Advances in Cryogenic Engineering—Materials, vol. 34, Eds. A. F. Clark and R. P. Reed, Plenum Press, New York (1987), to be published.

90. R. Muira, H. Nakajima, Y. Takahashi, and K. Yoshida, "32Mn-7Cr Austenitic Steel for Cryogenic Applications," in: Advances in Cryogenic Engineering—Materials, vol. 30, Eds. A. F. Clark and R. P. Reed, Plenum Press, New York (1984), pp. 245-252.
91. K. Hiraga, K. Ishikawa, K. Nagai, and T. Ogata, "Mechanical Properties of Cold-Rolled and Aged Fe-Ni-Cr-Ti-Austenitic Alloys for Low Temperature Use," in: Advances in Cryogenic Engineering—Materials, vol. 30, Eds. R. P. Reed and A. F. Clark, Plenum Press, New York (1984), pp. 203-210.
92. J. M. Galligan and P. D. Goldman, "Metal Interstitial Solid-Solution Strengthening," in: Strength of Metals and Alloys. Proceedings of the Fifth International Conference, Pt. II (1980), pp. 983-988.
93. A. A. Hendrickson and M. E. Fine, "Solid Solution Strengthening of Ag by Al," Trans. AIME 221, 967-974 (1961).
94. T. A. Bloom, U. F. Kocks, and P. Nash, "Deformation Behavior of Ni-Mo Alloys," Acta Metall. 33, 265-277 (1985).
95. Y. Nakada and A. S. Keh, "Solid-Solution Strengthening in Ni-C Alloys," Metall. Trans. 2, 441-447 (1971).
96. G. J. denOtter and A. Van den Beukel, "Flow Stress and Activation Volume of Some Cold-Worked Copper-Based Solid Solutions," Phys. Status Solidi(a) 55, 785-792 (1975).
97. J. H. Tregilgas and J. M. Galligan, "Hardening from Metal Interstitials in a Face-Centered Cubic Lattice—Pb-Ag," Scr. Metall. 9, (1975) pp. 1225-1227.
98. H. M. Ledbetter and M. W. Austin, unpublished measurements, National Bureau of Standards, Boulder, Colorado (1987).





## NITROGEN IN AUSTENITIC STAINLESS STEELS

R.P. Reed

National Institute of Standards and Technology  
Boulder, Colorado

Nitrogen alloyed in austenitic stainless steels improves austenite stability, mechanical properties, and corrosion resistance. Research on super-N steels (steels supersaturated with nitrogen), including processing and properties, is presented. These new steels rival the latest ferritic steels in strength but have potentially greater toughness.

### INTRODUCTION

For many years nitrogen has been added to austenitic stainless steels because (1) it stabilizes austenite, thus reducing the tendency for ferrite formation at high temperatures and martensitic transformation at low temperatures; (2) it increases flow strength more than additions of C or solid-solution alloying elements; (3) it is more soluble than C at intermediate and high temperatures, thus reducing precipitates; (4) it retards carbide formation and growth, thus reducing sensitization; (5) it is abundant and therefore inexpensive. In summary, N imparts to austenitic stainless steels their serviceable attributes: improved strength and corrosion resistance and slower high-temperature reactions.

Perhaps the first study of the effects of N additions to steels was by Adcock<sup>1</sup> on Cr and Fe-Cr alloys in 1926. In the 1930s, studies on N additions to Fe-Cr documented their increased strength. In the late 1930s and early 1940s, the shortage of Ni during the war inspired research on the possible replacement of Ni with N to stabilize austenite. Replacing Ni with a combination of N and Mn, another possibility, had the additional advantage of increasing N solubility. This research in the United States resulted in new alloys, the AISI-200 series. Gunia and Woodrow<sup>2</sup> wrote an excellent review of the early progress in using N to increase strength, substitute for Ni, and increase corrosion resistance in austenitic stainless steels.

Zackay used centrifugal casting and pressurized-ingot-solidification techniques to achieve N contents up to 0.75 wt.% in Fe-Cr-Mn austenitic steels.<sup>3,4</sup> The high-temperature tensile and creep properties of these alloys were better than those of the current (AISI-300-series) austenitic stainless steels. Thus, N-strengthened alloys began to be considered and developed for high-temperature applications.

High-N austenitic steels now in use include the AISI-200 series, N and HN grades of the AISI-300 series, and specialty steels containing more Cr, Ni, Mn, or Mo than specified under current AISI designations.

## STABILITY

Austenitic steels may solidify as austenite [face-centered cubic (fcc),  $\gamma$ ], ferrite [body-centered cubic (bcc)  $\delta$  or  $\alpha$ ], or a combination of these structures. The stability of the austenite structure is complicated. During cooling or deformation, one or two martensitic products [bcc,  $\alpha'$ ; hexagonal close-packed (hcp),  $\epsilon'$ ] may form. Their formation depends on the amount of Cr, Ni, Mn, and interstitials (primarily C and N) in the alloy. When N additions exceed the solubility limits at high temperatures,  $\text{Cr}_2\text{N}$  precipitates (with a hcp structure) form. Stacking-fault energy depends primarily on the relative free energies of the  $\gamma$  and  $\epsilon'$  structures. The effects of N addition on these structures are considered.

## Solubility

Since high-N contents are usually introduced into austenitic stainless steels as a gas, it is useful to know the solubility limits of gaseous N at high temperatures. Solubility depends on pressure; at 1600°C (2900°F), almost 3 wt.% N has been measured in a molten Fe-20Cr-15Mn alloy at a pressure of 10 MPa (100 bar). At the same temperature and pressure, about 1 wt.% N can be dissolved in Fe-20Cr-Ni alloys. Results of early work<sup>5</sup> at low nitrogen pressures (< 0.1 MPa or 1 bar) supported Sievert's law: N solubility is proportional to pressure to the 1/2 power. Sievert's law breaks down at high pressures: then solubility is proportional to pressure to a power less than 1/2.<sup>6</sup> The effects of alloying on N solubility in a liquid Fe-18Cr-8Ni base at 0.1 MPa (1 bar) and 1600°C (2900°F) are summarized in Figure 1.<sup>6</sup> Most alloying elements increase N solubility, but the important element, Ni (as well as W, Cu, Sn, Si, and Co), decreases N solubility. Gaseous-N solubility in austenitic steels is increased by adding Cr and decreased by adding Ni (see Kikuchi et al.<sup>7</sup> for review).

In the solid, the first N-containing phase to begin precipitating is usually  $\text{Cr}_2\text{N}$ . Austenite- $\text{Cr}_2\text{N}$  phase-boundary measurements<sup>8</sup> compiled for both Fe-Cr-Ni and Fe-Cr-Mn austenites and new measurements<sup>7</sup> of the phase boundaries for two austenitic steels, Fe-25Cr-28Ni and Fe-25Cr-20Ni, are shown in Figure 2. As in the liquid, adding Ni decreases N solubility, and adding Cr increases N solubility. The austenite- $\text{Cr}_2\text{N}$  phase boundary in the Fe-Cr-Mn-N system extends to larger values of N, indicating that N is more soluble when Ni is replaced by Mn. The quaternary Fe-Cr-Ni-N system has been evaluated thermodynamically.<sup>9</sup>

A representative curve for carbide formation in Fe-Cr-Ni-C alloys<sup>10</sup> is also included in Figure 2. At intermediate temperatures (800-1000°C; 1400-1800°F), the solubility of C in solid solution is nearly one-tenth that of N.



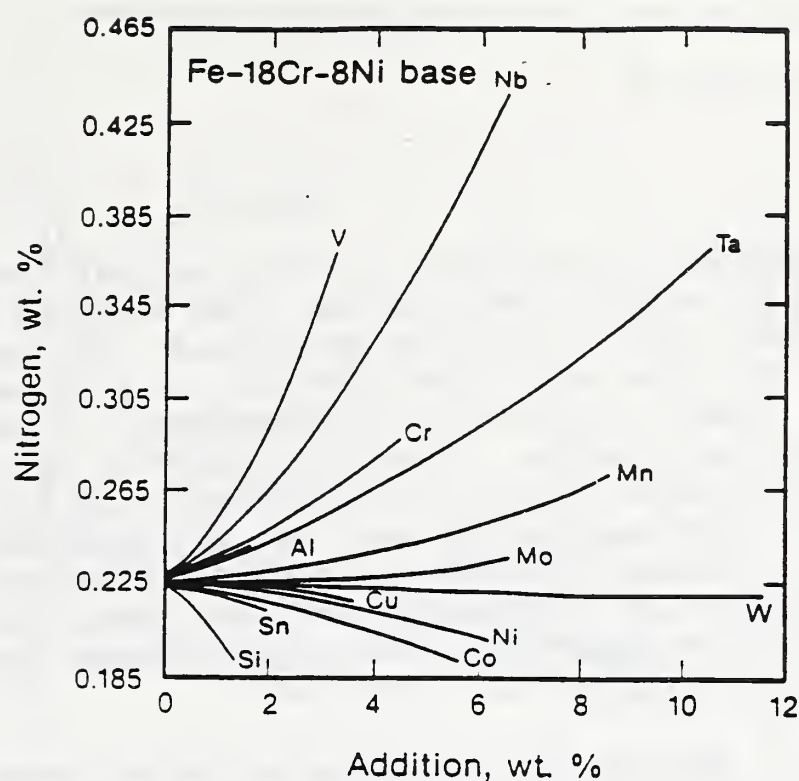


Figure 1. Solubility of various alloying elements in Fe-18Cr-8Ni liquid at 0.1 MPa (1 bar) and 1600°C (2900°F).<sup>5</sup>

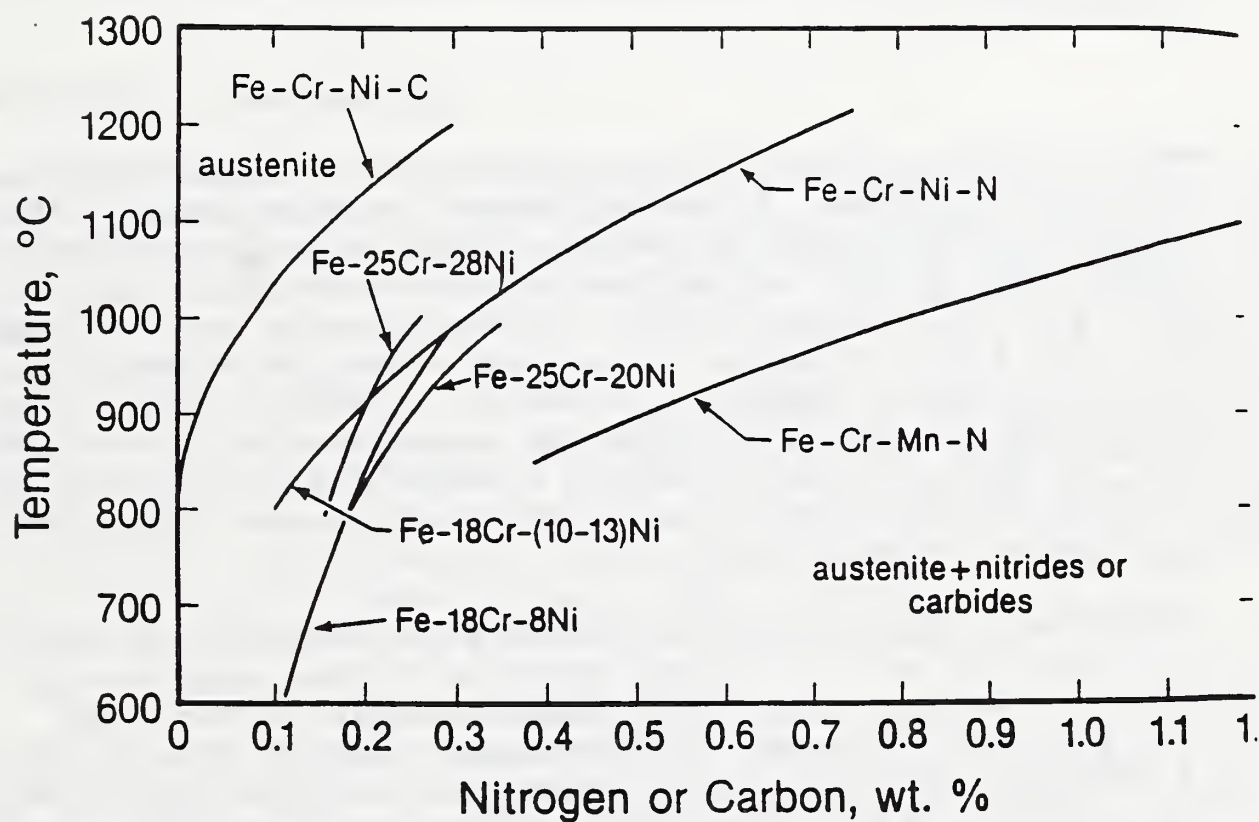


Figure 2. Phase boundaries between austenite and  $\text{Cr}_2\text{N}$  or carbides (for Fe-Cr-Ni-C alloys) with addition of N or C.<sup>7,9,10]</sup>



## Solidification

The relative amounts of austenite and ferrite that form during solidification are critically dependent on alloying. The liquidus and solidus surfaces of the Fe-Cr-Ni ternary have been determined: The eutectic trough extends from near the Fe corner (76Fe-10Ni-14Cr) to a ternary eutectic (about 8Fe-43Ni-49Cr).<sup>11</sup> Primary austenite solidifies when the composition is on the Ni side of the eutectic liquidus. Nearer the eutectic liquidus on the Ni side, limited ferrite forms, mainly in the dendritic cell boundaries. On the Cr-rich side of the liquidus line, primary ferrite solidifies. Upon cooling, however, ferrite transforms to austenite in compositions typical of austenitic stainless steels. Although few quantitative experimental studies of N effects on primary solidification modes have been reported, the stabilization of austenitic structure by N addition is recognized.

For estimates of ferrite and austenite in the weldments of austenitic stainless steels, solidification equivalent coefficients for Cr and Ni have been empirically developed (see Reed<sup>10</sup> for review). Expressions relating these coefficients to chemical composition are plotted on a diagram similar to the one originally developed by Schaeffler.<sup>12</sup> The N contribution is included as part of the Ni (austenite stability) term. Currently, on a weight-percent basis, N is considered to be 20 times more effective than Ni in stabilizing austenite; that is, the solidification equivalent coefficient for N is 20 times the Ni coefficient.<sup>13</sup>

## Ferrite

Ferrite may form during either solidification or high-temperature treatment, depending on alloy content. Occasionally small amounts (usually <10%) are present in rapidly cooled, lean, austenitic (AISI-300-series) stainless steel alloys (those whose primary solidification mode is ferrite), such as weldments. This bcc phase is conventionally called  $\delta$ -ferrite when it forms at temperatures above the  $\gamma$ -loop or range, and  $\alpha$ -ferrite when it forms at lower temperatures. Most austenitic stainless steels have sufficient stabilizing elements (such as Ni, Mn, C, and N) to lower the temperature of the  $\gamma$ -loop enough to prevent the diffusion-controlled  $\gamma \rightarrow \alpha$  transformation. In wrought alloys, the  $\alpha$ -ferrite retained from solidification is typically transformed to austenite during forging or hot rolling.

Figure 3 shows the effect of N on the boundary of the austenite and austenite + ferrite phases for an Fe-18Cr-base alloy at various temperatures.<sup>14</sup> Below 1200°C (2200°F), adding N only mildly suppresses ferrite formation (1 wt.% N  $\approx$  20 wt.% Ni when the slope of the phase boundary is considered). Above 1200°C, N strongly stabilizes the austenitic structure in alloys containing  $\geq$  7.5 wt.% Ni (1 wt.% N  $\approx$  200 wt.% Ni). Thus, the lower temperature N:Ni equivalency ratio (1:20) corresponds to the weld-metal ratio discussed above, indicating sufficient time and solute mobility below 1200°C to establish near-equilibrium conditions during weld-metal solidification.

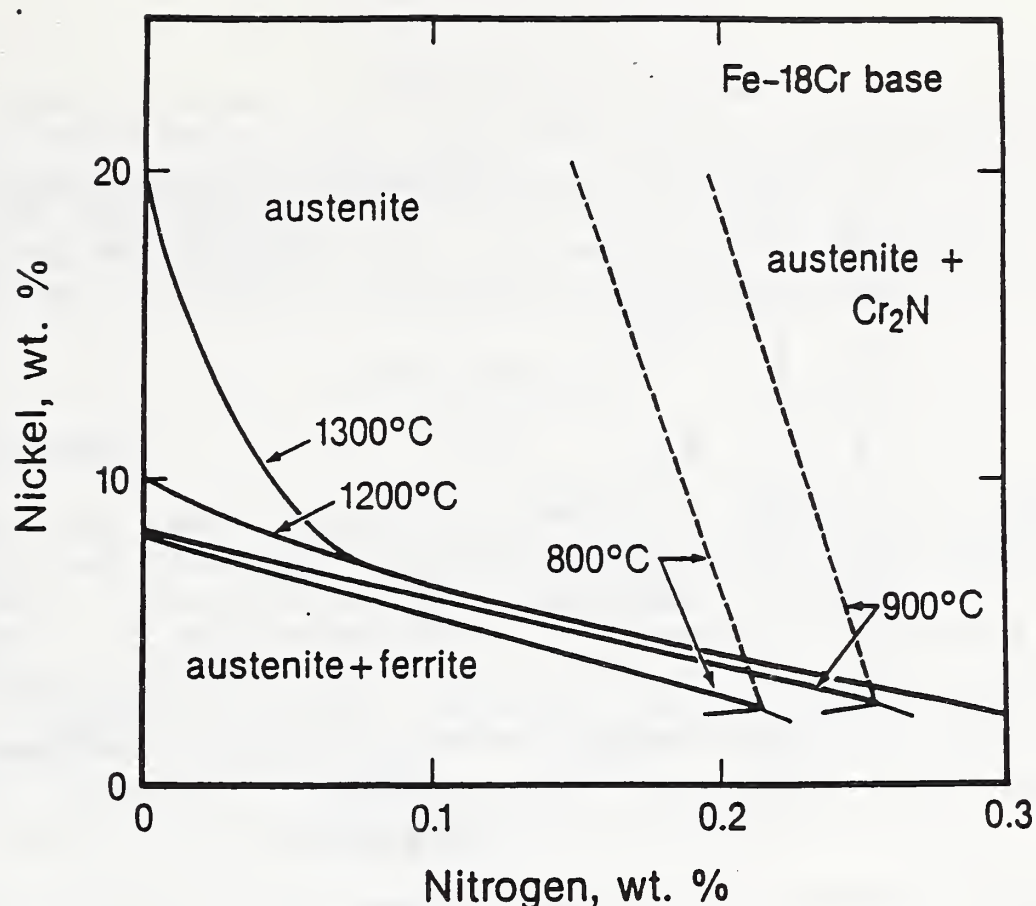


Figure 3. Phase boundaries separating austenite, austenite + ferrite, and austenite +  $\text{Cr}_2\text{N}$  regions as a function of N and Ni additions to an Fe-18Cr base alloy, plotted for various temperatures.<sup>14</sup>

### Martensitic Transformation

The addition of N increases austenite stability with respect to martensitic transformation in both bcc and hcp structures. The suppression of  $\alpha'$  martensite by N on cooling has long been recognized, and expressions to calculate the martensite start temperature,  $T_{\text{ms}}$ , were developed (see, for example, the review by Reed<sup>10</sup>). In these expressions, the contributions of N and C have usually been found to be the same: 1 wt.% N or C lowers  $T_{\text{ms}}$  by roughly 1500°C (2700°F). In most  $T_{\text{ms}}$  expressions, N contributes about 25 times more than Ni, close to the ratios of 20 for equilibrium and weldment-ferrite formation below 1200°C (2200°F), which were discussed earlier. In expressions for calculation of the highest temperature for strain-induced  $\alpha'$  martensite,  $T_{\text{md}}$ ,<sup>10</sup> the contributions of N and C are also equivalent: 1 wt.% of interstitial increases  $T_{\text{md}}$  about 250°C (450°F), approximately 10 times that of the common metal alloying elements (Cr, Ni, Mn).

The effect of N addition on  $\epsilon'$ -martensite formation in austenitic steels has not been previously characterized. Our recent room-temperature measurements<sup>15</sup> of Fe-18Cr-10Ni alloy specimens plastically deformed to strains of 0.05 and 0.10 at 76 K (-323°F), shown in Figure 4, were obtained by using integrated x-ray diffraction peaks of  $\epsilon'$  martensite. Adding both C (0.038 - 0.112 wt.%) and N (0.042 - 0.264 wt.%) increases austenite stability with respect to strain-induced  $\epsilon'$  martensite.



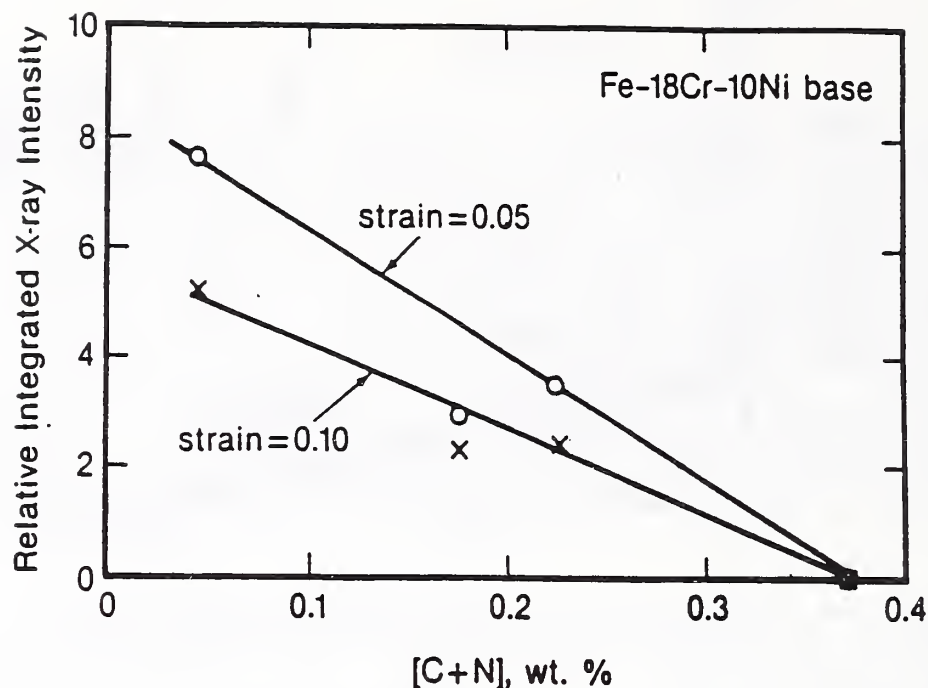


Figure 4. Relative integrated peak intensity, averaged from the (100) and (101) hcp structure peaks, following plastic deformation to strains of 0.05 and 0.10 at 76 K ( $-321^{\circ}\text{F}$ ); x-ray analysis at 295 K ( $72^{\circ}\text{F}$ ).<sup>15</sup>

### Stacking-Fault Energy

Stacking-fault energy is related to the free-energy difference between the fcc principal structure and the hcp structure. Lower stacking-fault energy leads to wider partial-dislocation separation, more planar dislocation arrays, and reduced cross slip.

The effects of additions of C and N ( $C + N \leq 0.364$  wt.%,  $N \leq 0.264$  wt.%) on the stacking-fault energy of an Fe-18Cr-10Ni alloy were examined with x-rays.<sup>16</sup> Within data scatter, the stacking-fault energy can be considered to be independent of C + N content. Using transmission electron microscopy, values of the stacking-fault energy of  $24 \pm 3$  mJ/m<sup>2</sup> and  $23 \pm 5$  mJ/m<sup>2</sup> were measured for a Fe-17Cr-12Ni-2Mo-0.02C alloy with N contents of 0.08 and 0.25 wt.%, respectively.<sup>17</sup> Weak-beam microscopy measurements showed that N in excess of 0.24 wt.% (to 0.52 wt.%) had little effect on the stacking-fault energy of an Fe-19Cr-7Ni-8Mn-0.03C alloy, but that at 0.21 wt.% N, the stacking-fault energy was considerably higher.<sup>18</sup> All three sets of measurements may be consistent with either of the following possibilities: (1) The stacking-fault energy is independent of N contents in Fe-Cr-Ni alloys; in Fe-Cr-Ni-Mn alloys, there is a transition. (2) Both alloy systems undergo a transition in the stacking-fault energy with N content, but in the Fe-Cr-Ni alloys, the transition occurs at higher N content, and the N-solubility limits may preclude measurement. However, it is discomforting to realize that these



"transition" premises depend exclusively on one measurement (of the Fe-19Cr-7Ni-8Mn-0.03C-0.21N alloy<sup>18</sup>); all other results indicate no N-composition dependence of the stacking-fault energy. The constant (or reduced) stacking-fault energy and the suppression of the  $\gamma \rightarrow \epsilon'$  transformation with increased N content are conflicting trends since both are expected to reflect the dependence of the free-energy difference between the fcc and hcp structures on N content.

## CORROSION RESISTANCE

The increasing demands of the petrochemical industry for higher strength, corrosion-resistant alloys have led to consideration of N-alloyed austenitic stainless steels. Additions to high-Cr ( $\geq 20$  wt.%) austenitic steels containing Mo and about 0.2 wt.% N significantly increase the resistance to corrosion from acids (Figure 5).<sup>19,20</sup> Nitrogen actively assists in the formation of a preliminary film, and apparently, subsequent passive films contain more Cr and Mo if N is present.<sup>21</sup> When N is added to common austenitic steels (such as AISI 304, 316, and 347), it has less effect on corrosion resistance to acids—and sometimes even a slightly adverse effect.<sup>22</sup>

Pitting corrosion, which usually occurs in the presence of halide (Cl, Br) ions, represents localized breakdown of the passive film. Figure 5 shows that adding N decreases the pitting corrosion rate from FeCl<sub>3</sub>-HCl attack. With these reduced rates, an increase in the effective potential is needed to initiate pitting corrosion. The resistance to pitting corresponds to  $1[\text{Cr}] + 3.3[\text{Mo}] + x[\text{N}]$ , where [Cr], [Mo], and [N] represent the total wt.% of each element and values of x range from 13 to 30.<sup>22,23</sup> Plots of this expression versus effective pitting potential<sup>22</sup> reach a plateau maximum at about a value of 33 when x is 16.

Truman<sup>22</sup> summarized various studies relating N content to stress corrosion and corrosion fatigue. Most authors concluded that increased N levels reduce the effects of stress-enhanced corrosion, but a few disagreed.

Nitrogen content usually reduces the deleterious effects of sensitization (precipitation or microstructural solute segregation) on corrosion resistance. However, when the N content exceeds its solubility limits, Cr<sub>2</sub>N will precipitate and deplete the matrix of Cr; this results in reduced passivity.

Carbides precipitate at ferrite-austenite interfaces, at grain boundaries, at noncoherent and coherent twin boundaries, and finally, within grains (in order of probability). As the precipitation site changes from high- to low-energy boundaries, the temperature decreases and the time for nucleation increases. Increased C content increases precipitation temperature and decreases time; increased N content has the reverse effect, suppressing carbide formation.<sup>19,24</sup> The M<sub>23</sub>C<sub>6</sub> carbide has a complex fcc structure with 92 metallic atoms and 24 smaller (C, N, or B) atoms. The common plane of the carbide-austenite interface has been identified as (111).<sup>25</sup> Alloy additions to the M<sub>23</sub>C<sub>6</sub> structure, such as N, tend to decrease its lattice parameter and to increase the amount of interface mismatch. This should retard the growth kinetics.

## STRENGTH

Because N provides excellent strength with very little increase in production cost, it has been used in the development of strong, tough, low-temperature alloys. Table I summarizes the strength increases calculated (in most cases using regression analyses) from controlled experimental data sets of many studies;<sup>26-35</sup> various techniques or assumptions were used to determine the dependence of the power of the N content ([N]) for calculating the yield strength. Some analyses assumed a linear fit,<sup>29-31,34,35</sup> some used  $[N]^{\frac{1}{2}}$ ,<sup>28,32,33</sup> and some compared various powers of the N content.<sup>26,27</sup> From comparisons for the same data, powers less than 1 usually result in slightly better data fits, but these trends are usually within 2 standard deviations of each other. Therefore, there is no conclusive evidence of the dependence of the yield strength on the power of [N].

Table I. Nitrogen Contribution to Yield Strength from Various Reports

Authors (Date)	Base Alloy	N Contribution to Yield Strength, MPa/wt.% (ksi/wt.%)	
		4 K (-452°F)	295 K (72°F)
Reed, Simon (1989) <sup>26</sup>	Fe-19Cr-10Ni	2400 (348)	500 (73)
Reed, Purtscher, Delgado (1988) <sup>27</sup>	Fe-Cr-Mn	2140 (311)	680 (99)
Werner, Uggowitzer, Speidel (1987) <sup>28</sup>	Fe-Cr-Mn		580 (84)*
Simon, Reed (1986) <sup>27</sup>	Fe-Cr-Ni	3190 (463)	
	Fe-Cr-Ni-Mo	2780 (403)	
Yamamoto, Yamagami, <sup>29</sup> Ouchi (1986)	Fe-Cr-Mn	2940 (427)	570 (83)
Reed, Simon (1984) <sup>27</sup>	Fe-Cr-Ni	3400 (493)	420 (61)
Sakamoto et al. (1984) <sup>30</sup>	Fe-Cr-Ni	2500 (363)	690 (100)
Takahashi et al. (1982) <sup>31</sup>	Fe-Cr-Ni-Mo	2910 (422)	
Fujikura, Kato (1978) <sup>32</sup>	Fe-Cr-Mn		510 (74)
Norström (1977) <sup>33</sup>	Fe-18Cr-14Ni-3Mo		310 (45)*
Irvine, Gladman, Pickering (1969) <sup>34</sup>	Fe-Cr-Ni		440 (64)
Irvine, Llewellyn, Pickering (1961) <sup>35</sup>	Fe-18Cr-10Ni		710 (103)

\*An interactive contribution from N grain size was also found.



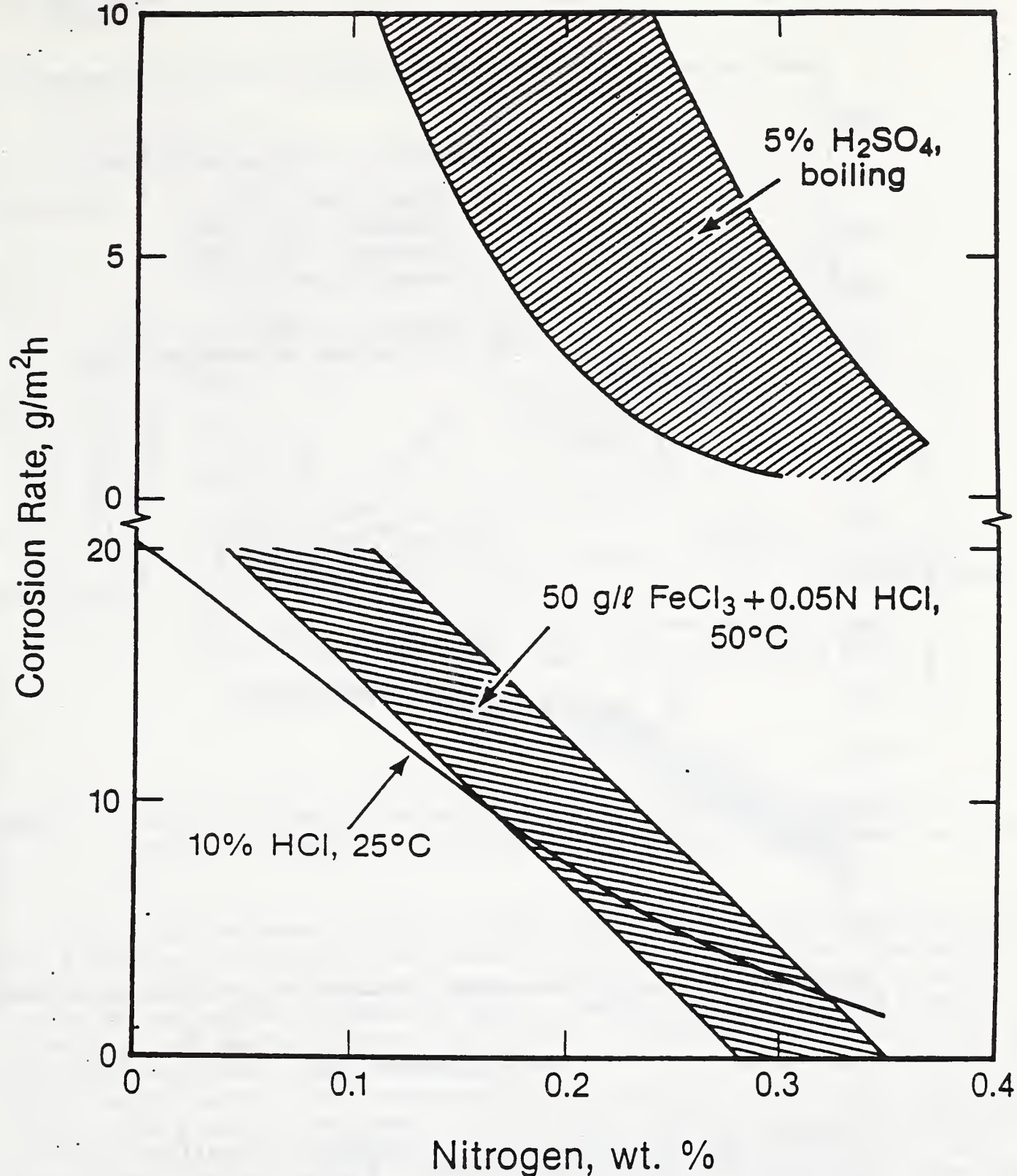


Figure 5. Dependence of corrosion rate on N content for both an acidic (H<sub>2</sub>SO<sub>4</sub>, HCl) and crevice (FeCl<sub>3</sub>) environment at different temperatures.<sup>19</sup>

The strengthening contribution from interstitial N addition is very dependent on temperature. Figure 6 presents average measurements at 295, 77, and 4 K (72, -321, and -452°F) for Fe-Cr-Ni alloys with N contents within the solubility limits. At 295 K, the increase in yield strength is approximately 50 MPa (7.3 ksi)/0.1 wt.% N addition. At 4 K, this strengthening has increased to about 250 MPa (36 ksi)/0.1 wt.% N—a factor of 5.



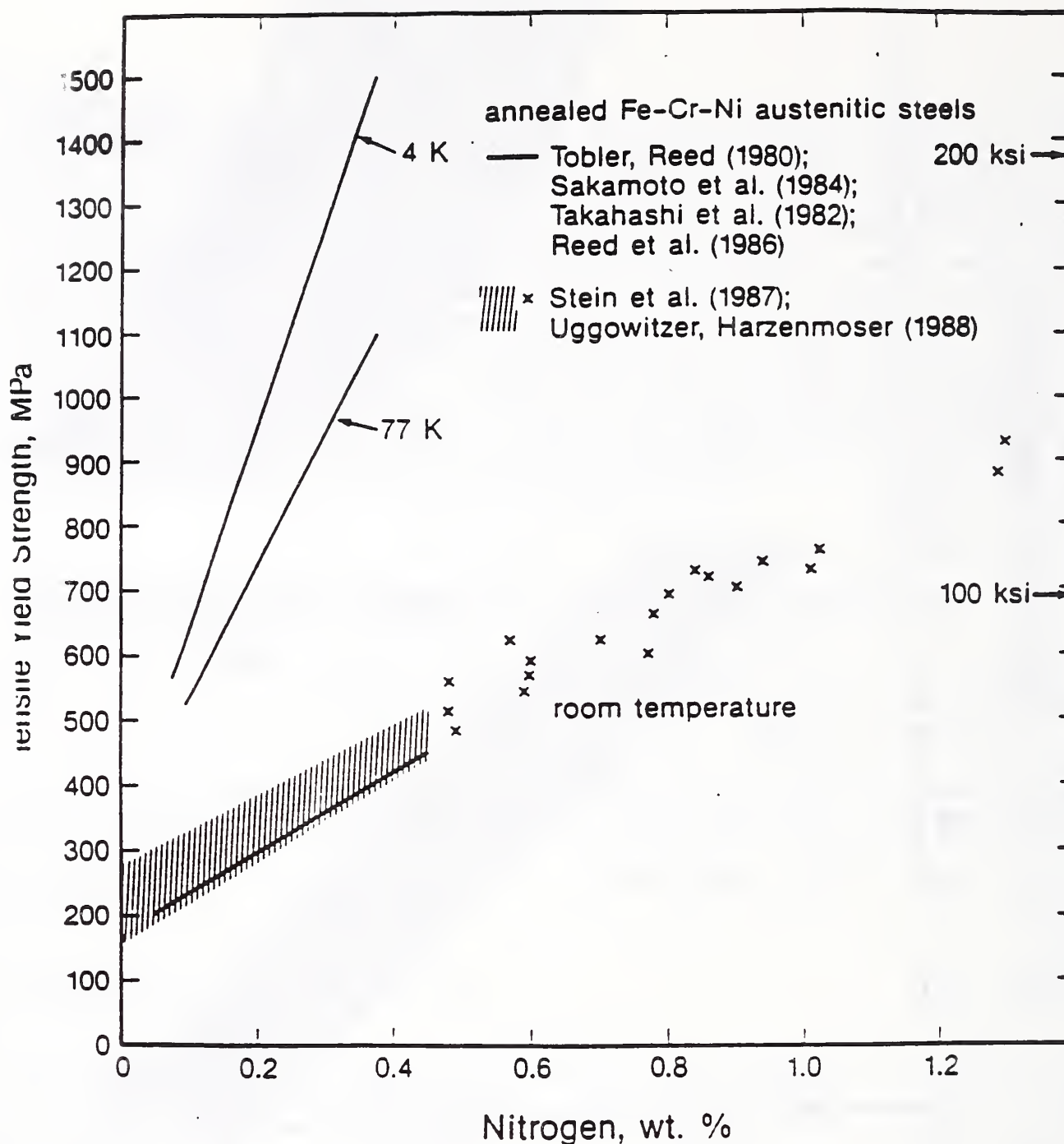


Figure 6. Dependence of the tensile yield strength (0.2% offset) on N content of Fe-Cr-Ni-base austenitic alloys for selected low temperatures.<sup>26,30,31,36,37</sup>

Figure 7 shows the effects of common alloying elements on the yield strength of Fe-Cr-Ni-base austenitic stainless steels at 295 K.<sup>35</sup> The largest increases in yield strength are supplied by the smallest elements (N, C, and B) that occupy interstitial sites. Nitrogen strengthens steel more than C: At 295 K, N increases strength about 20% more than C, but at 4 K, N increases strength 300% more than C.<sup>26</sup> Ferrite-forming elements, elements whose atomic sizes are much different from those of the Fe-Cr-Ni solvent, are next in order of strengthening contributions. Elements whose atomic sizes closely match the average size of the Fe-Cr-Ni matrix contribute the least.

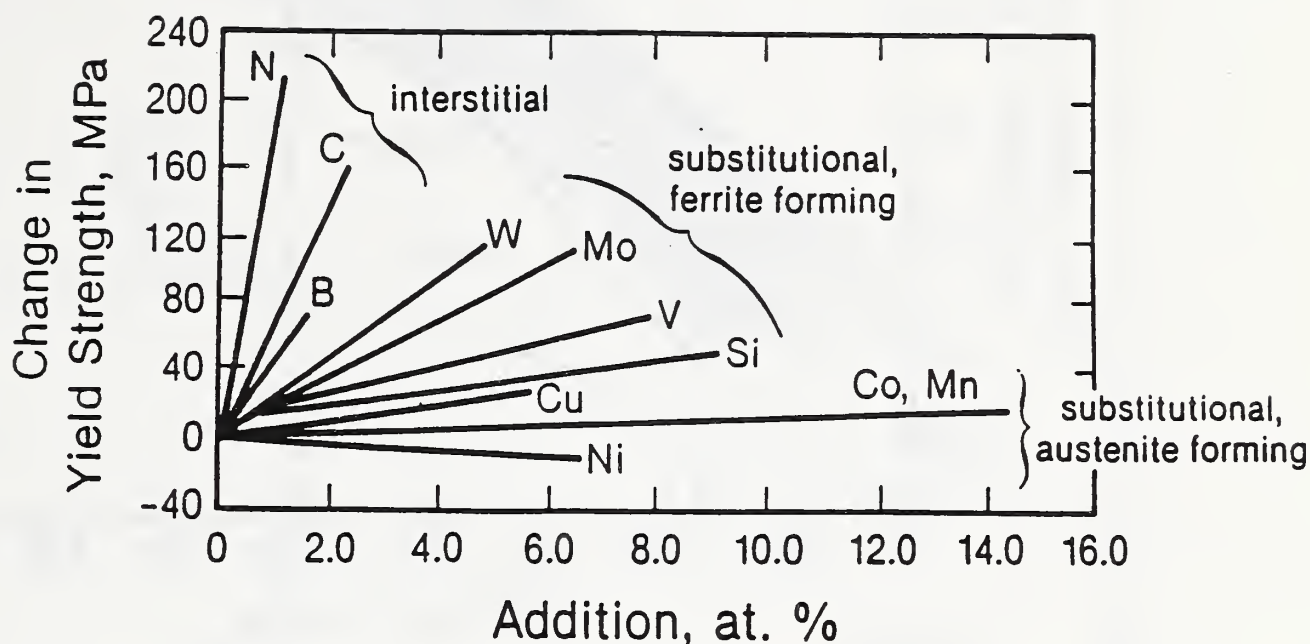


Figure 7. Contributions of selected alloying elements to 295-K tensile yield strength for Fe-Cr-Ni-base austenitic stainless steels.<sup>35</sup>

The large increases in flow strength that result from N alloying remain a puzzle. Proposals that account for the discrepancies from solution-hardening theories include long-range ordering; local ordering between N and Cr, Mn, or Mo; split interstitial sites; "microprecipitates" of nitrides; clustering; and Mn-N effective "molecules." Therefore, identification of the actual occupancy sites and randomness of distribution for N atoms will significantly improve our understanding of interstitial strengthening in fcc alloys. One piece of evidence is the frequent observation that dislocations tend toward a linear alignment at high-N contents and toward a cellular structure at low-N contents. The relative insensitivity to stacking-fault energy at compositions below about 0.24 wt.% N (see discussion of stacking-fault energy) implies that ordering may explain the change of dislocation geometry.

## CREEP AND FATIGUE

For high-temperature applications, such as in steam and nuclear power plants, N alloying of austenitic stainless steels usually prolongs operational lifetime. As Figure 8 illustrates, adding N also enables the attainment of higher stress for a desired operational lifetime.<sup>38-40</sup> Creep ductility is not sacrificed,<sup>41</sup> and at times, is improved.<sup>42,43</sup> In contrast, adding C lowers creep ductility.<sup>41</sup> Figure 8 shows that very small changes in interstitial content substantially improve creep resistance.



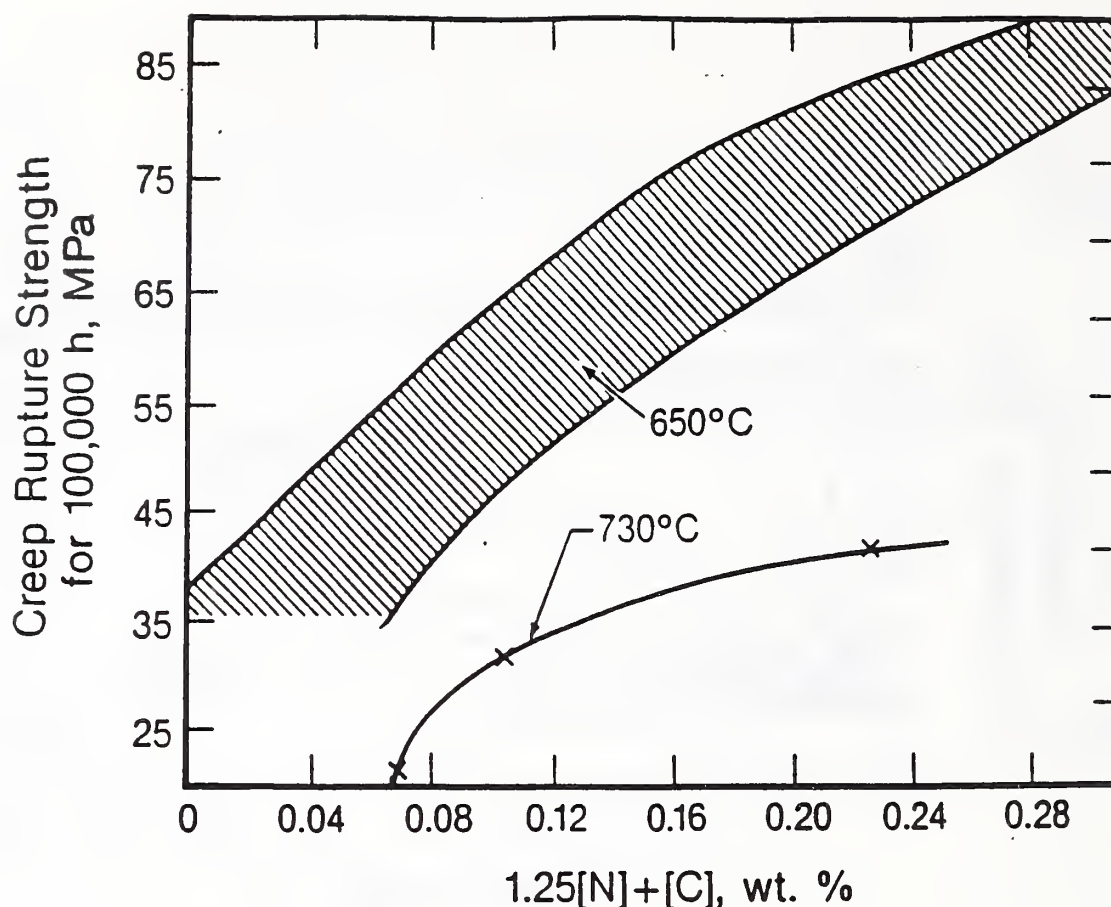


Figure 8. Effect of N and C content on creep strength to achieve a 100,000-h lifetime for Fe-19Cr-10Ni base alloys (with N contents from 0.03 to 0.14, C contents from 0.02 to 0.10) at holding temperatures of 650°C (1200°F) and 730°C (1350°F). Band represents more than 40 data points (650°C data from Goodell, Cullen, and Freeman;<sup>38</sup> 730°C data from Hoke review<sup>39</sup>).

There is evidence that the improved creep properties resulting from N addition are associated with N solid-solution strengthening.<sup>44</sup> When a series of alloys with very low C was used to preclude the influence of carbide formation, the minimum creep rates decreased with increasing N content from 800 to 1000°C (1500 to 1850°F) (Figure 9). Also, the decrease of minimum creep rate at 800°C was independent of C content, as illustrated by the dashed curve in Figure 9. In this study, intergranular  $\text{Cr}_2\text{N}$  precipitates at lower temperatures and at long times to rupture were observed. The minimum creep rate decreased with increasing N content in all cases where the N remained in solid solution.

At temperatures higher than about 800°C (1500°F), the distinctions between C and N become less. In fact, at 900°C (1650°F), the creep properties of AISI 316 were reported to be superior to those of AISI 316LN.<sup>42</sup> At lower temperatures (< 800°C), the reduced amount of N in solid solution seems to be dependent on the precipitation of  $\text{Cr}_2\text{N}$ . At higher temperatures (900; 1000°C), the more similar creep behavior of low- and high-N austenitic steels may be attributed to the participation of N in carbide formation. The coarse carbonitrides would, of course, remove N from solid solution and reduce its strengthening effect.

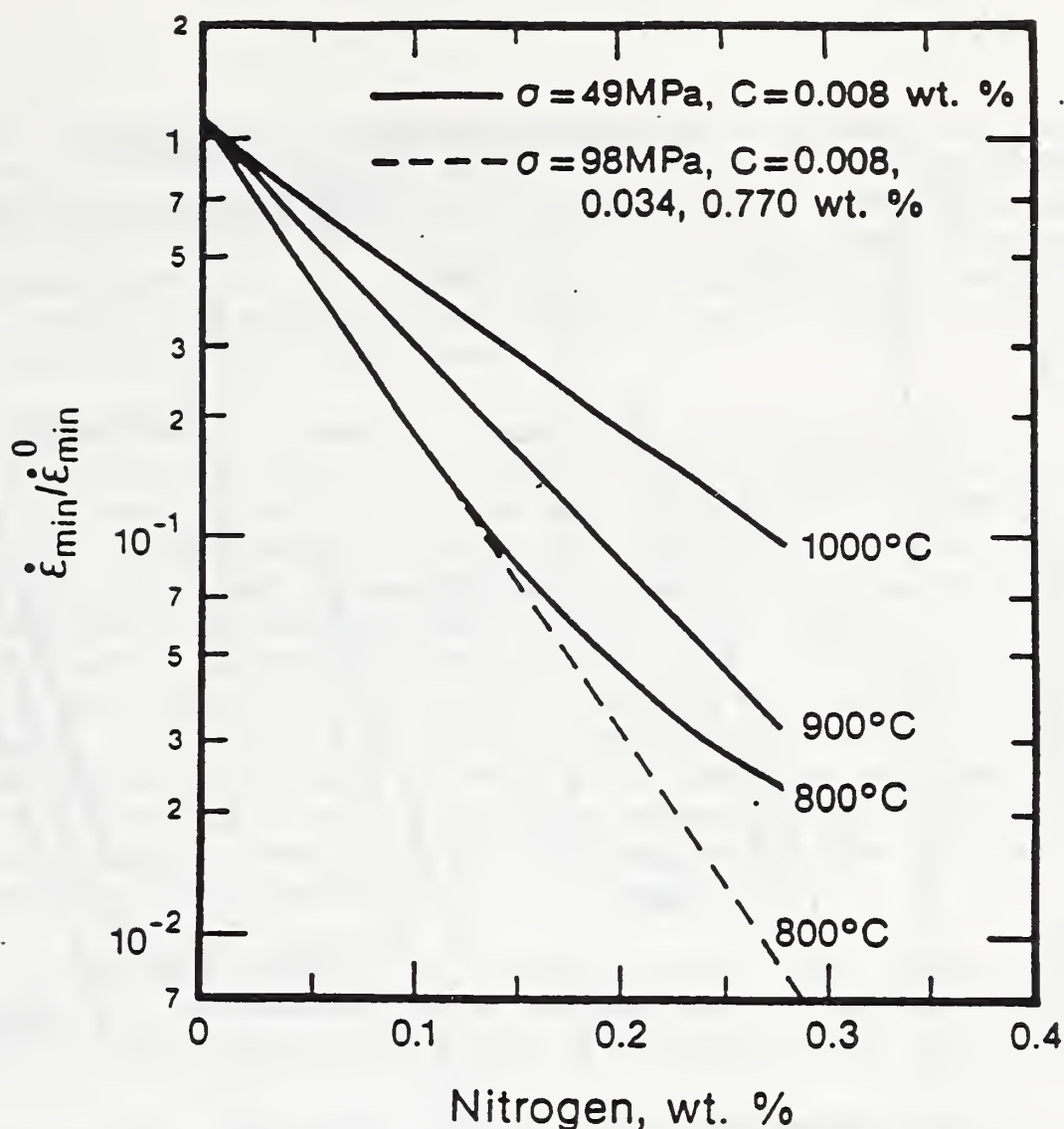


Figure 9. Ratio of minimum creep rate,  $\dot{\epsilon}_{min}$  to a N-free alloy and a 0.005-wt. % N alloy with 0.008 wt. % C as a function of N content at a stress level of 48 MPa (7 ksi); solid lines. The dashed line represents data at 800°C (1500°F) and a stress level of 98 MPa (14 ksi) for all alloys with varying C + N content.<sup>44</sup>

The fatigue-crack-growth rates are affected by strain-induced martensite. Martensite formation in the plastic zone about the crack tip shields the crack, lowering the stress intensity at the tip of the crack. This is illustrated by the low-temperature values<sup>45</sup> for a series of AISI 304 alloys with varying N and C contents (Figure 10). At 295 K, high-strength alloys (those with high C + N contents) had lower fatigue-crack-growth rates. At low temperatures, the crack-growth rates of the high-strength alloys were the same or higher than the 295-K rates, but the crack-growth rates of the low-strength steels (low C + N content) were considerably lower. This reduction correlates very well with the increase of strain-induced  $\alpha'$  martensite in the process zone at the crack tip.

The effects of N on fatigue behavior were recently reviewed.<sup>46</sup> Nitrogen improves the fatigue life of austenitic steels; most studies attributed this improvement to increased resistance to strain localization from increased planar slip. Resistance to strain localization reduces the formation of persistent slip bands and increases slip reversibility.



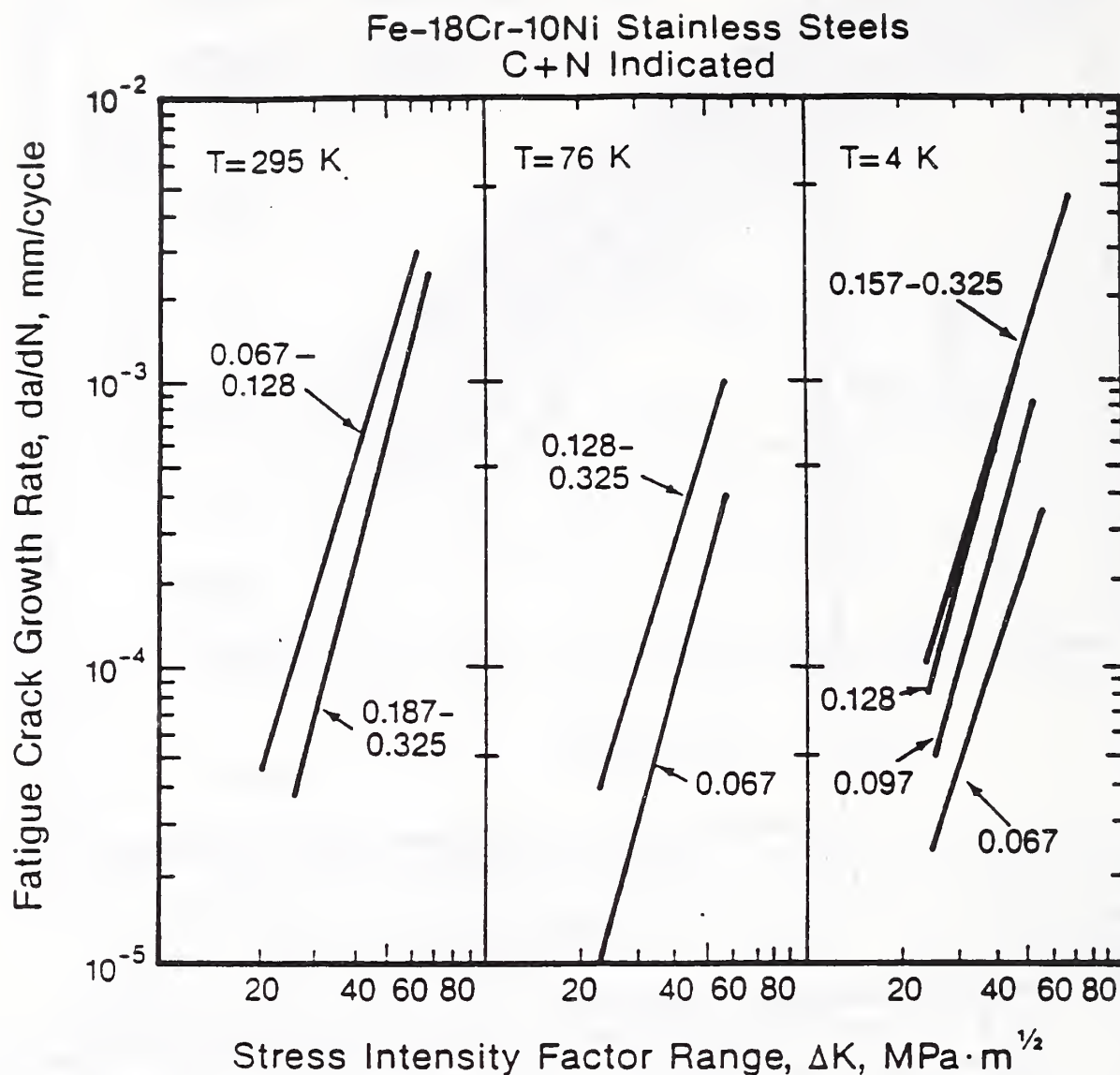


Figure 10. Fatigue-crack-growth rates at low temperatures for Fe-18Cr-10Ni base alloy with varying C + N contents that are specified in wt.% with each curve.<sup>45</sup>

## SUPER-NITROGEN STEELS

### Processing

The development of pressurized electroslag remelting as an industrial process has enabled the production of super-N austenitic stainless steels (steels supersaturated with N). These new steels contain up to 1 wt.% N, in excess of the N solubility at atmospheric pressure. Super-N steels are now being produced for generator retaining rings, and they are expected to be used in power generation, ship building, chemical and cryogenic processes, and pressure vessels. Processes that were proposed previously for producing super-N steels have not been amenable to large-scale industrial production (pressurized induction furnaces,<sup>6</sup> centrifugal casting<sup>4</sup>), have tended to produce inhomogeneous ingots (plasma-arc remelting<sup>47</sup>), or have not been able to achieve high enough N levels (ingot gasification<sup>4</sup>).

The use of pressurized electroslag remelting is extensively discussed by Stein et al. in their review of some of the super-N-steel processes.<sup>48</sup> In both plasma-arc remelting and pressurized induction melting, N is introduced as a gas, but in the pressurized electroslag remelting process, the N is introduced to the liquid-phase alloy in granulated form within the slag system. Granulated additives with high N contents must be used; currently, silicon nitrides are favored.<sup>48</sup>

To obtain the desired chemical composition and homogeneity, it is necessary to consider electrode and additive chemistry, speed of motion through the slag and liquid, bath convection, temperature, and N pressure. Double remelting is sometimes necessary to obtain adequate chemical homogeneity. Currently, the most advanced pressurized-electroslag-remelting facility is capable of producing 20-ton ingots up to 1000 mm (39 in) in diameter.<sup>48</sup> It uses a stationary copper mold that is cooled with pressurized water, has a movable hood, and is capable of a maximum pressure of 4.2 MPa (42 bar). In contrast to normal electroslag-remelting practice, the pressurized system requires more automation because the progress of the remelting is not visible. Thus, a reliable sensor system and knowledge of the effects of pressure, temperature, and speed variations are necessary for efficient industrial application.

Super-N steels are more difficult to hot-work. The range of hot-working temperatures and amount of hot working are restricted, limiting the size and shape of the forgings that can be achieved within given mill facilities.

Holzgruber<sup>49</sup> maintains that super-N steels are best produced on a large scale by using N-gas purging of liquid metal. In this process, electroslag heating with either a consumable or nonconsumable electrode produces a liquid-metal alloy with a constant chemical composition that is unaffected when N is added. Gaseous N is added to this base metal from the bottom; the liquid metal and slag pools are held under pressure to control the N content. An important advantage of this system is that any normal casting technique can be used, since the entire process can be performed in a ladle-like container. For large-scale production of ingots, a pressurized casting chamber, featuring a porous bottom plug in the liquid-metal container and a launder with pressure-gate valves through which the molten metal pours into the ingot mold, is suggested.

## SUPER-NITROGEN STEELS

### Properties

A completely new set of property data is being developed from super-N steels produced by the pressurized-electroslag-remelting process. In Figure 6, the Fe-Cr-Ni-base data have been extended to N contents from 0.4 to 1.0 wt.%.<sup>36,37</sup> The linear trend of tensile yield strength versus N content at room temperature to approximately 1 wt.% encourages the use of alloys with N contents in excess of their solubility limits. Yield strengths to almost 1000 MPa (145 ksi) at room temperature are attainable in alloys with no cold or hot working and with a single phase.



The most significant information, though, is that super-N steels are comparable to, if not better than, contemporary ferritic steels in terms of strength and toughness (Figure 11).<sup>36,50,51</sup> The higher strength was attained by cold-working at room temperature. The success of acquiring very high strengths in austenitic steels is particularly encouraging because, in contrast to the maraging and dual-phase steels and 9Ni-Co alloys, the development of super-N steels did not have the benefit of extensive research programs to optimize strength-toughness behavior through chemical composition and thermomechanical processing.

Other property data on super-N austenitic steels have resulted from studies of welding,<sup>48</sup> effects of grain size on tensile yield strength,<sup>28</sup> the temperature dependence of the tensile flow strength,<sup>8,37</sup> strain hardening,<sup>8,37</sup> effects of annealing time and temperature on fracture toughness and Cr<sub>2</sub>N precipitation,<sup>8</sup> corrosion resistance,<sup>36,52</sup> effects of cold work on tensile yield strength,<sup>36,50,52</sup> and reversed-cycle fatigue at room temperature.<sup>53</sup>

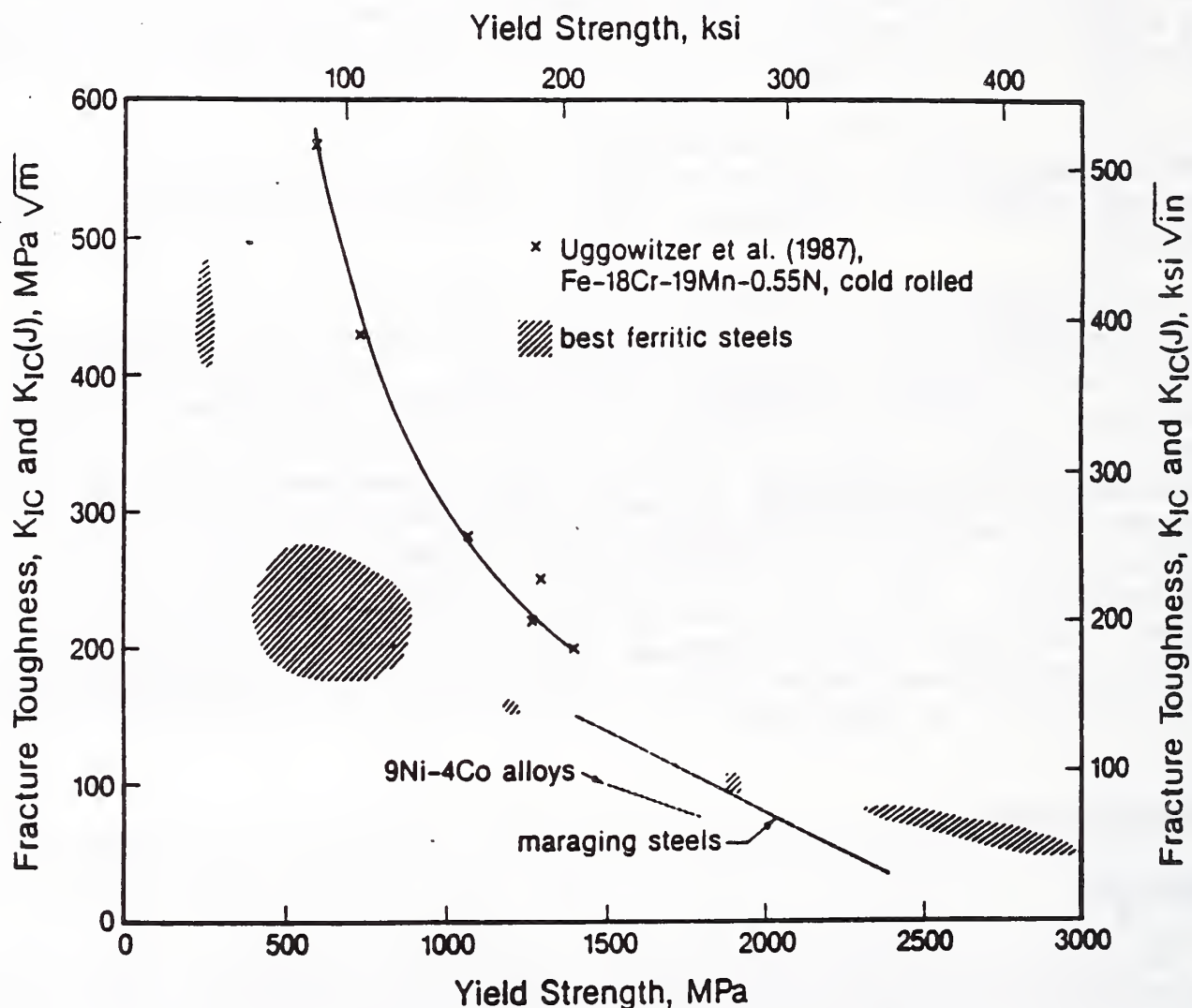


Figure 11. Room-temperature fracture toughness and yield strength data to compare super-N steels with ferritic steels. Fracture toughness data either from linear elastic tests or from J-Integral tests, converted to linear elastic.<sup>36,50,51</sup>

## CONCLUSIONS

Additions of N to austenitic stainless steels increase austenite stability, strength, and corrosion resistance and improve performance. These improvements enable more extensive use of high-N steels at both low and high temperatures. The very recently developed super-N austenitic steels have potential for applications where very high performance steels are required.

## REFERENCES

1. F. Adcock, "The Effect of Nitrogen on Chromium and Some Iron-Chromium Alloys," *J. Iron Steel Inst.* 114 (1926) 119-126.
2. R.B. Gunia and G.R. Woodrow, "Nitrogen Improves Engineering Properties of Chromium-Nickel Stainless Steels," *J. Mater.* 5 (1970) 413-430.
3. V.F. Zackay, J.F. Carlson, and P.L. Jackson, "High Nitrogen Austenitic Steels," *Trans. Amer. Soc. Met.* 48 (1956) 509-525.
4. V.F. Zackay, E.R. Morgan, and J.C. Shyne, "Production of High Nitrogen Steels," *J. Met.* 8 (1956) 216.
5. W.M. Small and R.D. Pehlke, "The Effect of Alloying Elements on the Solubility of Nitrogen in Liquid Iron-Chromium-Nickel Alloys," *Trans. AIME* 242 (1968) 2501-2505.
6. H. Feichtinger, A. Satir-Kolorz, and Z. Xiao-Hong, "Solubility of Nitrogen in Solid and Liquid Iron Alloys with Special Regard to the Melting Range," accepted for publication in Proc. "HNS-88" (Lille, France) ed. J. Foct and A. Hendry (London: Institute of Metals, 1989).
7. M. Kikuchi, M. Kajihara, and K. Frisk, "Solubility of Nitrogen in Austenitic Stainless Steels," accepted for publication in Proc. "HNS-88" (Lille, France) ed. J. Foct and A. Hendry (London: Institute of Metals, 1989).
8. M.A. Harzenmoser and P.J. Uggowitzer, "Neue aufgesteckte austenitisch-rostfreie Stähle und Duplexstähle," *Modern Stähle*, vol. 1, ed. P.J. Uggowitzer and M.O. Speidel (Zurich: Schweizerischen Akademie der Werkstoffwissenschaften, ETH, 1987), 219-247.
9. K. Frisk and M. Hillert, "Thermodynamics of the Fe-Cr-Ni-N System," accepted for publication in Proc. "HNS-88" (Lille, France) ed. J. Foct and A. Hendry (London: Institute of Metals, 1989).
10. R.P. Reed, "Austenitic Stainless Steels with Emphasis on Strength at Low Temperatures," *Alloying* (Metals Park, OH: ASM International, 1988), 225-256.
11. G.R. Speich, *Source Book on Stainless Steels* (Metals Park, OH: ASM International, 1976), 424-426.
12. A.L. Schaeffler, "Constitution Diagram for Stainless Steel Weld Metals," *Met. Prog.* 56 (1949) 680.
13. T.A. Siewert, C.N. McCowan, and D.L. Olson, "Ferrite Number Prediction to 100 FN in Stainless Steel Weld Metal," *Weld. J.* 67 (1988) 289s-298s.
14. T. Masumoto and Y. Imai, "Structural Diagrams and Tensile Properties of the 18%Cr-Fe-Ni-N Quaternary System Alloys," *J. Jap. Inst. Met.* 33 (1969) 1364-1371.
15. R.P. Reed, unpublished data, National Institute of Standards and Technology, Boulder, Colorado (1988).



16. H.M. Ledbetter and M.W. Austin, "Stacking-Fault Energies in 304-Type Stainless Steels: Effects of Interstitial Carbon and Nitrogen," in *Materials Studies for Magnetic Fusion Energy Applications at Low Temperatures - VIII*, ed. R.P. Reed (NBSIR 85-3025, National Institute of Standards and Technology, 1985), 271-294.
17. R. Taillard and J. Foct, "Mechanisms of the Action of Nitrogen Interstitials upon the Low Cycle Fatigue Behavior of 316 Stainless Steel," accepted for publication in Proc. "HNS-88" (Lille, France) ed. J. Foct and A. Hendry (London: Institute of Metals, 1989).
18. R.E. Stoltz and J.B. VanderSande, "The Effect of Nitrogen on Stacking Fault Energy of Fe-Ni-Cr-Mn Steels," *Metall. Trans.* 11, (A)(1980) 1033-1037.
19. T. Sakamoto et al., "High Corrosion Resistent Nitrogen-Containing Stainless Steels for Use by the Chemical Industry," *Alloys for the Eighties*, ed. R.Q. Barr (Greenwich, CT: AMAX, 1980), 269-279.
20. J.R. Kerns, "The Effect of Nitrogen on the Corrosion Resistance of Austenitic Stainless Alloys Containing Molybdenum," *New Developments in Stainless Steel Technology*, ed. R.A. Lula (Metals Park, OH: ASM International, 1985), 117-127.
21. C.R. Clayton and K.G. Martin, "Evidence of Anodic Segregation of Nitrogen in High Nitrogen Stainless Steels and Its Influence on Passivity," accepted for publication in Proc. "HNS-88" (Lille, France) ed. J. Foct and A. Hendry (London: Institute of Metals, 1989).
22. J.E. Truman, "Effects of Nitrogen Alloying on Corrosion Behavior of High Alloy Steels," accepted for publication in Proc. "HNS-88" (Lille, France) ed. J. Foct and A. Hendry (London: Institute of Metals, 1989).
23. P. Gumpel and T. Ladwein, "The Effect of Nitrogen on Mechanical-Technological and Corrosion Properties of Stainless Steels," accepted for publication in Proc. "HNS-88" (Lille, France) ed. J. Foct and A. Hendry (London: Institute of Metals, 1989).
24. H. Their, A. Baumel, and E. Schmidtman, "Einfluss von Stickstoff auf des Ausscheidungsverhalten des Stahles x5CrNiMo1713," *Arch. Eisenhüttenw.* 40 (1969) 333-339.
25. M.H. Lewis and B. Hattersley, "Precipitation of  $M_{23}C_6$  in Austenitic Steels," *Acta Metall.* 13 (1965) 1159-1168.
26. R.P. Reed and N.J. Simon, "Nitrogen Strengthening of Austenitic Stainless Steels at Low Temperatures," accepted for publication in Proc. "HNS-88" (Lille, France) ed. J. Foct and A. Hendry (London: Institute of Metals, 1989).
27. R.P. Reed, P.T. Purtscher, and L.A. Delgado, "Low-Temperature Properties of High-Manganese Austenitic Steels," *High-Manganese Austenitic Steels*, ed. R.A. Lula (Metals Park, OH: ASM International, 1988), 13-22.
28. E. Werner, P. J. Uggowitzer, and M. O. Speidel, "Mechanical Properties and Aging Behavior of Nitrogen Alloyed Austenitic Steels," *Mechanical Behaviour of Materials - V*, (New York: Pergamon, 1987).
29. S. Yamamoto, N. Yamagami, and C. Ouchi, "Effect of Metallurgical Variables on Strength and Toughness of Mn-Cr and Ni-Cr Stainless Steels at 4.2 K," *Advances in Cryogenic Engineering - Materials*, vol. 32, ed. R.P. Reed and A.F. Clark (New York, NY: Plenum, 1986), 57-64.
30. T. Sakamoto et al., "Nitrogen-Containing 25Cr-13Ni Stainless Steel as

- a Cryogenic Structural Material," *Advances in Cryogenic Engineering - Materials*, vol. 30, ed. A.F. Clark and R.P. Reed (New York, NY: Plenum, 1984), 137-144.
31. Y. Takahashi et al., "Mechanical Evaluation of Nitrogen-Strengthened Stainless Steels at 4 K," *Advances in Cryogenic Engineering - Materials*, vol. 28, ed. R.P. Reed and A.F. Clark (New York, NY: Plenum, 1982), 73-81.
  32. M. Fujikura and T. Kato, "Effects of Carbon, Nitrogen and Nickel Content on the Low Temperature Impact Value of High Manganese Austenitic Steel," *J. Iron Steel Inst. Jap.* 64 (1978) 97-106.
  33. L.A. Norström, "The Influence of Nitrogen and Grain Size on Yield Strength in Type AISI 316L Austenitic Stainless Steel," *Met. Sci.* 11 (1977) 208-212.
  34. K.J. Irvine, T. Gladman, and F.B. Pickering, "The Strength of Austenitic Steels," *J. Iron Steel Inst.* 207 (1969) 1017-1028.
  35. K.J. Irvine, D.T. Llewellyn, and F.B. Pickering, "High-Strength Austenitic Stainless Steels," *J. Iron Steel Inst.* 199 (1961) 153-175.
  36. G. Stein, J. Menzel, and H. Dörr, "Möglichkeiten zur Herstellung von Schmiedestücken mit hohen Stickstoffgehalten in der Desu-Anlage," *Moderne Stähle, Ergebnisse der Werkstoff-Forschung*, vol. 1 (Zurich: Schweizerische Akademie der Werkstoffwissenschaften, 1987), 181-193.
  37. P.J. Uggowitzer and M. Harzenmoser, "Strengthening of Austenitic Stainless Steels by Nitrogen, accepted for publication in Proc. "HNS-88" (Lille, France) ed. J. Foct and A. Hendry (London: Institute of Metals, 1989).
  38. P.D. Goodell, T.M. Cullen, and J.W. Freeman, "The Influence of Nitrogen and Certain Other Elements on the Creep-Rupture Properties of Wholly Austenitic Type 304 Steel," *J. Basic Eng. (Trans. Amer. Soc. Met. E)* 89 (1967) 517-524.
  39. J.H. Hoke, "Mechanical Properties of Stainless Steel at Elevated Temperatures," *Handbook of Stainless Steels*, ed. D. Peckner and I.M. Bernstein (New York, NY: McGraw-Hill, 1977), 21.1-21.20.
  40. Y. Kawabe, R. Nakagawa, and T. Makoyama, "Effect of Nitrogen and Molybdenum on the High Temperature Strength of 18Cr-12Ni-0.02C Austenitic Steel," *Trans Iron Steel Inst. Jap.* 8 (1968) 353-362.
  41. T. Nakazawa et al., "Effects of Nitrogen and Carbon on Creep Properties of Type 316 Stainless Steels," accepted for publication in Proc. "HNS-88" (Lille, France) ed. J. Foct and A. Hendry (London: Institute of Metals, 1989).
  42. J.K. Solberg, "The Influence of Carbon and Nitrogen on the High Temperature Creep Properties of AISI 316 Austenitic Stainless Steel," *Mater. Sci. Eng.* 55 (1982) 39-44.
  43. J. Sobotka et al., "Creep Ductility and Creep Fracture of Non-Stabilized CrNiMo Steels with Nitrogen Additions," accepted for publication in Proc. "HNS-88" (Lille, France) ed. J. Foct and A. Hendry (London: Institute of Metals, 1989).
  44. T. Matsuo et al., "Effect of Nitrogen on Creep Deformation of 25Cr-28Ni Austenitic steels - Solid Solution Strengthening Due to Nitrogen, accepted for publication in Proc. "HNS-88" (Lille, France) ed. J. Foct and A. Hendry (London: Institute of Metals, 1989).
  45. R.L. Tobler and R.P. Reed, "Interstitial Carbon and Nitrogen Effects on



- the Cryogenic Fatigue Crack Growth of AISI 304 Stainless Steel," *J. Test. Eval.* 12 (1984) 364-370.
46. S. Degallaix, J. I. Dickson, and J. Foot, "The Effect of Nitrogen on the Fatigue and Creep-Fatigue Behavior of Austenitic Stainless Steels," accepted for publication in Proc. "HNS-88" (Lille, France) ed. J. Foot and A. Hendry (London: Institute of Metals, 1989).
  47. G. Torkhov et al., "Development of Melting and Thermomechanical Processing Parameters for a High-Nitrogen Stainless Steel Prepared by Plasma-Arc Remelting," *J. Met.* 30 (1978) 20-27.
  48. G. Stein, J. Menzel, and H. Dörr, "Industrial Manufacture of Massively Nitrogen-Alloyed Steels," accepted for publication in Proc. "HNS-88" (Lille, France) ed. J. Foot and A. Hendry (London: Institute of Metals, 1989).
  49. W. Holzgruber, "Process Technology for High Nitrogen Steels," accepted for publication in Proc. "HNS-88" (Lille, France) ed. J. Foot and A. Hendry (London: Institute of Metals, 1989).
  50. P.J. Uggowitzer, M.O. Speidel, and E. Werner, "Fracture Toughness of Cold Worked Austenitic Steels," *Mechanical Behaviour of Materials - V* (New York: Pergamon, 1987), 401-410.
  51. E.B. Kula, Army Materials Technology Laboratory, Watertown, Massachusetts; private communication with author, 1988.
  52. M.O. Speidel, "Properties and Applications of High-Nitrogen Steels," accepted for publication in Proc. "HNS-88" (Lille, France) ed. J. Foot and A. Hendry (London: Institute of Metals, 1989).
  53. J. Menzel, G. Stein, and P. Dahlmann, "Massively Nitrogen-Alloyed Bolt Materials for High-Strength and High-Temperature Applications," accepted for publication in Proc. "HNS-88" (Lille, France) ed. J. Foot and A. Hendry (London: Institute of Metals, 1989).

# EFFECT OF NITROGEN AND CARBON ON FCC-HCP STABILITY IN AUSTENITIC STEELS\*

R.P. Reed and M.W. Austin  
National Institute of Standards and Technology  
Boulder, Colorado

## INTRODUCTION

High-nitrogen austenitic steels have recently been developed for low-temperature use.<sup>1</sup> For a long time it has been recognized that both nitrogen and carbon increase austenite stability with respect to formation of delta ferrite at high temperatures and body-centered cubic (bcc) martensite at low temperatures.<sup>1,2</sup> Yet, the effects of nitrogen and carbon on austenite (fcc) stability relative to hexagonal close-packed (hcp) martensite and the stacking-fault energy have not been adequately clarified.

## MATERIALS AND PROCEDURES

The austenitic alloys used for this program are listed in Table 1. The solid-solution solutes Cr, Ni, and Mn were held constant; the interstitial solutes C and N were varied. Grain sizes ranged from 80 to 100  $\mu\text{m}$ . These alloys are a subset of a series of laboratory heats of nine alloys that were previously used to measure strength, toughness, lattice parameters, and elastic moduli from 4 to 295 K.<sup>1</sup>

TABLE 1. Chemical Composition (wt. %)

Alloy*	C	N	Cr	Ni	Mn
1	0.038	0.042	18.3	10.1	1.57
3	0.112	0.044	18.3	10.1	1.51
5	0.076	0.135	18.0	9.9	1.50
9	0.095	0.264	20.3	10.0	1.42

\*The alloys also contained 0.02 P, 0.02 S, 0.5 Si, 0.2 Mo, and 0.2 Cu.

The tensile specimens were flat with a 38-mm gage length that was 6.4 mm wide and 3.2 mm thick. —These specimens were incrementally deformed in tension at 76 K to plastic strains of 0.05 and 0.10. Following the first

\*Submitted to Scripta Metallurgica.



strain increment, the specimens were warmed to room temperature, and x-ray diffraction peaks were measured. Then the specimens were returned to 76 K for the second strain increment.

A horizontal Bragg-Brentano type of x-ray diffractometer was used with Cu radiation, a 0.3-mm receiving slit, and a Ge solid-state detector set for K-alpha radiation. Specimens were scanned for 12 s per  $0.02^\circ$  step at room temperature. Data files were constructed by subtracting the background, correcting for the Lorentz polarization, and deleting the Cu K-alpha-2 contribution with a Rachinger algorithm.

To analyze the fcc structure, diffraction peaks  $(111)_f$  and  $(200)_f$  were used; to analyze the hcp strain-induced structure, diffraction peaks  $(10.0)_h$  and  $(10.1)_h$  were used.

## RESULTS

Analysis of the austenite peaks,  $(111)_f$  and  $(200)_f$ , showed a consistency in the relative intensities of each specimen; this implies little variability of preferred orientation among the specimens.

The intensity traces of alloys 5 and 9, strained at 76 K to 0.05 and 0.10, are shown in Figure 1. The hcp diffraction peaks used for this analysis were the  $(10.0)_h$  and  $(10.1)_h$ . These hcp peaks and most of the fcc and bcc peaks do not overlap; this enables accurate estimates of integrated intensity. In alloys 1, 3, and 5, the  $(110)_b$  peak, representative of strain-induced bcc martensite, overlaps the  $(111)_f$  peak.

The relative intensities of the hcp peaks were estimated by using both computer-assisted curve fitting and graphical analyses. The curve fitting to Lorentzian profiles used least-squares analyses and then integrated the area within the final curve. From graphs such as that in Figure 1, peak heights and half-widths were measured; their product was used as a relative measure of integrated peak intensity. Both techniques produced very similar data, which agreed within 10%.

The hcp-martensite peak intensities were averaged. The average values of these peak intensities are plotted versus atomic percentage of C and N content ( $[C] + [N]$ ) in Figure 2. In this plot, the fit of alloy-3 data is not good. The relative peak intensities of all four alloys can be fitted very well if the interstitial content is portrayed as  $3[C] + [N]$ , which is shown in the insert of Figure 2.

## DISCUSSION

Figure 2 shows that the addition of both C and N to an Fe-20Cr-10Ni austenitic alloy increases the fcc stability with respect to formation of strain-induced, hcp martensite. If we consider the data of alloy 3, we must conclude that C is more effective than N in austenite stabilization. When the factor  $3[C] + [N]$  is used, the volume percent hcp versus interstitial content is clearly linear. Thus, C-and-N stabilization of austenite against hcp martensite is similar to their stabilization of austenite against bcc

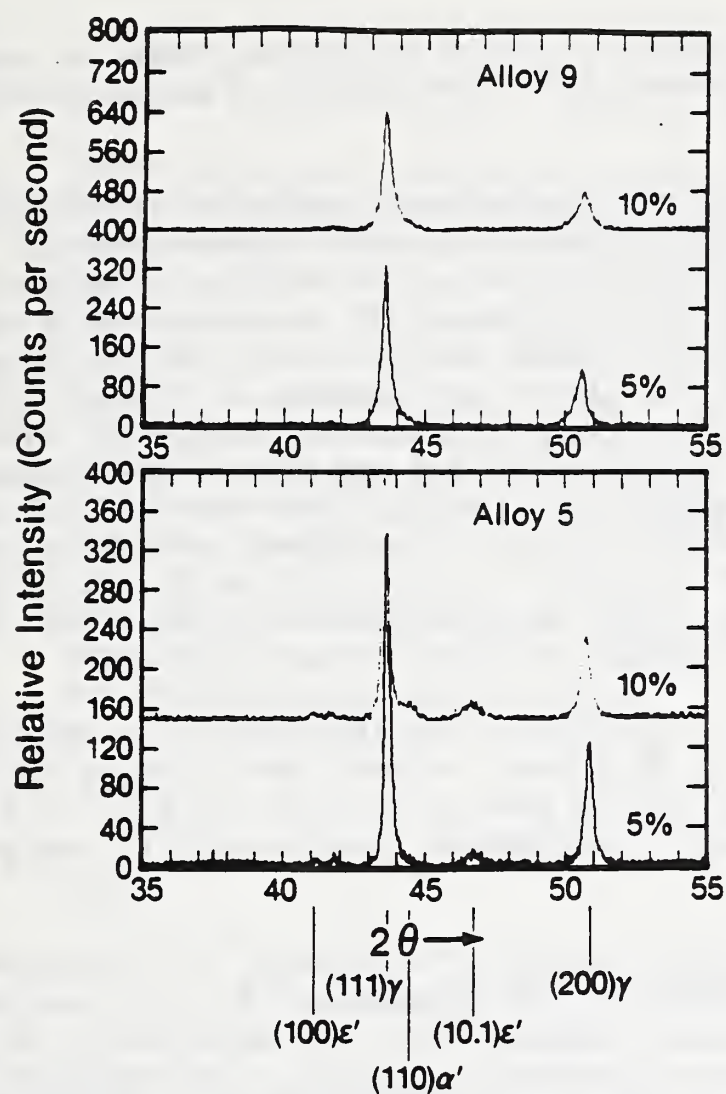


Figure 1. Sample x-ray diffraction peaks of fcc ( $\gamma$ ), hcp ( $\epsilon$ ), and bcc ( $\alpha'$ ) structures following 5 and 10% plastic deformation at 76 K.

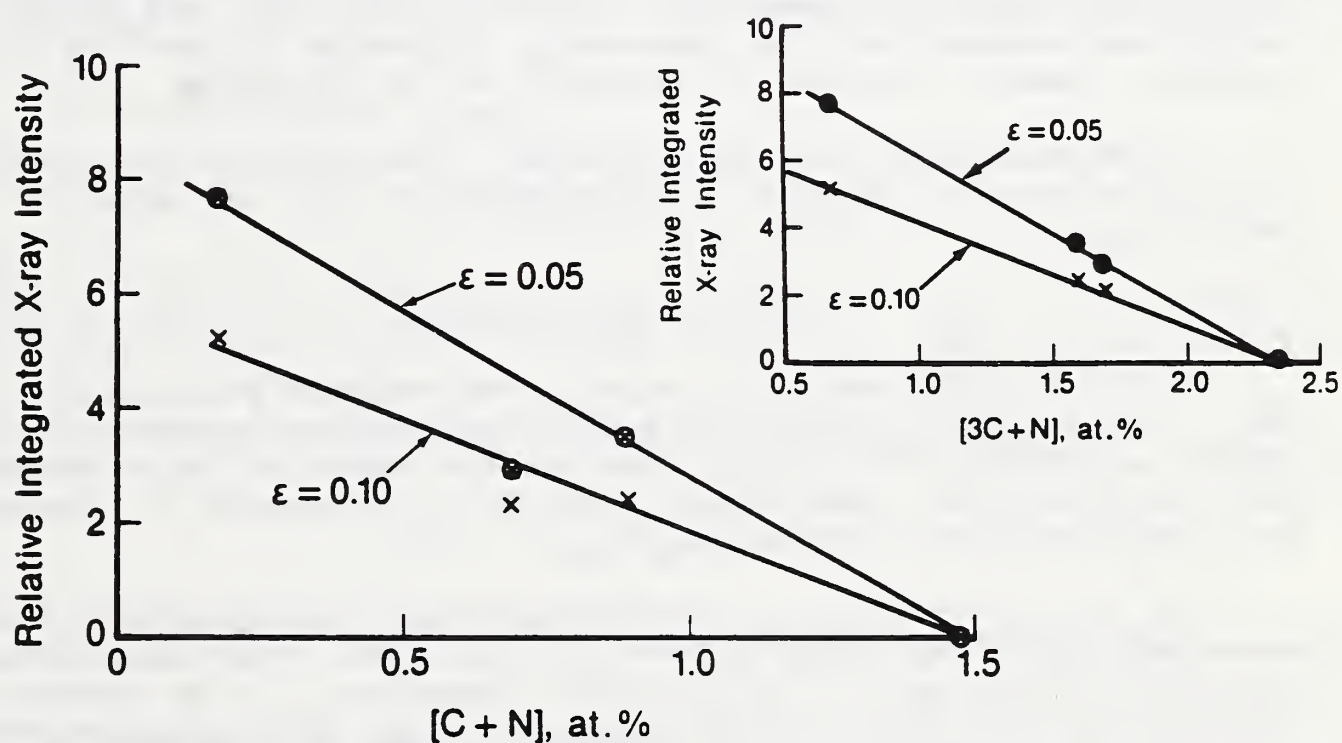


Figure 2. Relative integrated x-ray peak intensities of selected hcp diffraction lines following 76-K plastic deformation (at strains indicated) versus [C + N].



martensite formation. Usually, however, C and N have been judged to contribute about equally in empirically developed calculations of martensite-start temperatures on cooling and straining.<sup>1,2</sup>

The effect of C on the stacking-fault energy of austenitic stainless steels has been studied.<sup>3</sup> The contribution of C to the stacking-fault energy was 26 mJ/m<sup>2</sup> per wt.%, a modest increase. The effects of additions of C and N ([C] + [N] < 0.364 wt.%, [N] < 0.264 wt.%) on the stacking-fault energy of an Fe-18Cr-10Ni alloy were examined with x-rays.<sup>4</sup> Within data scatter, the stacking-fault energy was almost independent of [C] and [N], perhaps increasing slightly with increasing interstitial contents. With transmission electron microscopy, values of 24 ± 3 and 23 ± 4 mJ/m<sup>2</sup> were measured for the stacking-fault energy of an Fe-17Cr-12Ni-2Mo-0.02C alloy with [N] of 0.08 and 0.25 wt.%, respectively.<sup>5</sup> Weak-beam microscopy measurements showed that [N] in excess of 0.24 wt.% (to 0.52 wt.%) had little effect on the stacking-fault energy of an Fe-19Cr-7Ni-8Mn-0.03C alloy, but at 0.21 wt.% N, the stacking-fault energy was considerably higher.<sup>6</sup>

Thus, in austenitic steels, [C] increased the stacking-fault energy slightly. The role of [N] is not quite clear: either the stacking-fault energy is independent of [N]<sup>5</sup> or, if the one datum point at 0.21 wt.% N of Stoltz and VanderSande<sup>6</sup> is strongly considered, stacking-fault energy decreases with increased [N].

The increase of stacking-fault energy as [C] increases is consistent with the suppression of hcp martensite as [C] increases. But the constancy or reduction of stacking-fault energy, compared with the suppression of hcp martensite as [N] increases, deserves further discussion. The suppression of hcp as [N] increases suggests that the free-energy difference between fcc and hcp structures increases with increasing [N]. Yet, the stacking-fault-energy data suggest that the free-energy difference between the fcc and hcp structures remains constant or decreases as [N] increases.

Following Ishida<sup>7</sup> and earlier works<sup>8,9</sup> the stacking-fault energy ( $\gamma$ ) of an alloy consists of bulk ( $\gamma_B$ ), segregation ( $\gamma_S$ ), and magnetic ( $\gamma_M$ ) contributions:

$$\gamma = \gamma_B + \gamma_S + \gamma_M \quad (1)$$

In Fe-18Cr-10Ni austenitic alloys, the magnetic state at room temperature is paramagnetic for the fcc and hcp structures and ferromagnetic for the bcc structure. On cooling, these alloys remain in the paramagnetic state until the Néel temperature, about 40 K, is reached.<sup>10</sup> Therefore, for this discussion we neglect  $\gamma_M$ .

The bulk contribution to the stacking-fault energy of alloys is represented as the sum of the difference of the bulk free-energy ( $G$ ) and interaction parameters ( $W$ ) of the alloy components. If we assume that interstitial N and the Fe-Cr-Ni austenite matrix form a two-component (A,N) system that can be described by Ishida's regular-solution model, then

$$\gamma_B = \frac{1}{2V^{2/3}} \left[ \Delta G_A^{f-h}(1-X_N) + \Delta G_N^{f-h}X_N + \Delta W_A^{f-h}X_N(1-X_N) \right], \quad (2)$$

where  $X_N$  is the concentration of N, and  $V$  is the molar volume. The suppression of hcp with increasing  $[N]$  (Fig. 2) implies an increase in the free-energy difference between the two structures. Thus, with N addition, the sum of the first two terms of Equation 2 is expected to increase. If the change of the interaction parameter is positive (implying increased order of N in the fcc phase), the third term of Equation 2 also increases  $\gamma_B$  with increasing  $[N]$ . When  $W$  is zero (in the ideal-solution model), this third term is inconsequential, but, when  $W_{AN}^{f-h}$  is negative, the third term of Equation 2 may balance the positive contribution of the first two terms. A negative  $W_{AN}^{f-h}$  implies that N in the hcp structure is more ordered than in the fcc structure.<sup>9</sup>

The fault-segregation contribution,  $\gamma_S$ , to the stacking-fault energy depends on changes in the chemical-free energy ( $\Delta G_c$ ), elastic energy ( $\Delta G_e$ ), and surface-free energy ( $\Delta G_s$ ):

$$\gamma_S = \frac{1}{2V^{2/3}} [\Delta G_c + \Delta G_e + \Delta G_s], \quad (3)$$

where

$$\Delta G_c = W_{AN}^h \left( X_N - X_N^h \right)^2 + RT \left[ X_N \ln \left( \frac{X_N^h}{X_N} \right) + (1-X_N) \ln \left( \frac{1-X_N^h}{1-X_N} \right) \right], \quad (4)$$

and  $X_N^h$  is the concentration of N in the fault. If  $X_N^h \neq X_N$ ,  $\Delta G_c$  decreases only when  $W_{AN}^h$  is negative, that is, an increased concentration of N species is ordered in the fault.

The elastic-energy term is

$$\Delta G_e = \frac{2}{9} \mu \frac{1+\nu}{1-\nu} \left( \frac{dV}{dX} \right)^2 \frac{1}{V} \left( X_N^h - X_N \right)^2, \quad (5)$$

where  $\mu$  is the shear modulus, and  $\nu$  is Poisson's ratio.<sup>7</sup> With nitrogen addition there is an attendant volume increase.<sup>1</sup> Thus,  $\Delta G_e$  is expected to increase if  $X_N^h \neq X_N$ .

To a first approximation, the surface free-energy term<sup>7,9</sup> is given by

$$\Delta G_s = \frac{1}{4} W_{AN} \left( X_N^h - X_N \right)^2, \quad (6)$$

and  $\Delta G_s$  is directly proportional to the interaction parameter if segregation is present.

In summary, Equations 1 through 6 are used to describe interstitial alloying effects on stacking-fault energy. It follows that the apparent divergence of the phase transformation and stacking-fault-energy data with



increasing [N] may be explained qualitatively if N segregation with increased ordering at stacking faults occurs. Increased N ordering at stacking faults decreases the hcp interaction parameter, providing negative terms to a regular solution model of stacking-fault-energy dependence on structure free energy, composition, and interaction parameters. Nitrogen ordering could be achieved when N occupies either split-interstitial sites or preferentially couples with another alloying element, such as Cr.<sup>11</sup>

#### REFERENCES

1. R.P. Reed, Alloying, p. 225, American Society for Metals, Metals Park, Ohio (1988).
2. Handbook of Stainless Steels, ed. D. Peckner and I.M. Bernstein, McGraw-Hill, New York (1978).
3. P.J. Brofman and G.S. Ansell, Metall. Trans. 9,879 (1978).
4. H.M. Ledbetter and M.W. Austin, Materials Studies for Magnetic Fusion Energy Applications at Low Temperatures - VIII, p. 271, ed. R.P. Reed, NBSIR 85-3025, National Institute of Standards and Technology, Boulder, Colorado (1985).
5. R. Taillard and J. Foct, Proc. "HNS-88" (Lille, France), ed. J. Foct and A. Hendry, Institute of Metals, London (1989).
6. R.E. Stoltz and J.B. VanderSande, Metall. Trans. 11,1033 (1980).
7. K. Ishida, Phys. Status Solidi 36a,717 (1976).
8. J.P. Hirth, Metall. Trans. 1,2367 (1970).
9. T. Ericsson, Acta Metall. 14,1073 (1966).
10. E.R. Jones, T. Datta, C. Almasan, D. Edwards, and H.M. Ledbetter, Mater. Sci. Eng. 91,181 (1987).
11. R.P. Reed, J. Met. 41,16 (1989).

# LOW-TEMPERATURE PROPERTIES OF HIGH-MANGANESE AUSTENITIC STEELS\*

R. P. Reed, P. T. Purtscher, and L. A. Delgado

National Institute of Standards and Technology  
Boulder, Colorado

## ABSTRACT

The low-temperature properties of high-Mn austenitic steels are reviewed. Emphasis is placed on strength, toughness, elastic properties, thermal expansion, and magnetic properties, those properties most critical for materials used in cryogenic structures. Strength and toughness parameters and mechanisms are discussed, including alloying, martensitic transformations, twinning, and grain size. Information is included from many recent studies, particularly Japanese studies, of alloy development for superconducting magnet applications at 4 K.

STRONG STRUCTURAL ALLOYS are required to withstand the large magnetic forces of superconducting magnets. Since structural failure in these applications would result in unacceptable loss, these structural alloys must also have excellent fracture toughness. Many of the low-temperature applications, such as those in magnetic-fusion-energy reactors and high-energy-physics magnets, require materials with high elastic properties and low thermal and electrical conductivities. Austenitic steels have been almost exclusively selected for these uses. Recently, the Japan Atomic Energy Research Institute<sup>(1)</sup> has stimulated the Japanese steel companies to develop even stronger (1200-MPa yield strength at 4 K) and tougher (200-MPa/m fracture toughness at 4 K) austenitic steels for future use for structural constraint of the large magnetic fields. The impetus to achieve these goals in Japan, coupled with research at the National Bureau of Standards and other laboratories in the United States, has led to development of even better Fe-Cr-Ni and Fe-Mn-Cr austenitic steels. The compositions of the high-Mn steels that have been recently developed are summarized in Fig. 1. Those with high Cr contents meet the Japanese corrosion-resistance requirements; those with low Cr contents were developed prior to the corrosion-resistance requirement or were developed for other applications. All contain sufficient Mn to stabilize the austenitic structure against martensitic transformation on cooling.

This paper summarizes our understanding of the behavior of these high-Mn austenitic steels at cryogenic temperatures. The most significant design parameters—strength, toughness, and physical properties—are emphasized.

---

\* All compositions in this paper are in wt.%, unless otherwise specified.



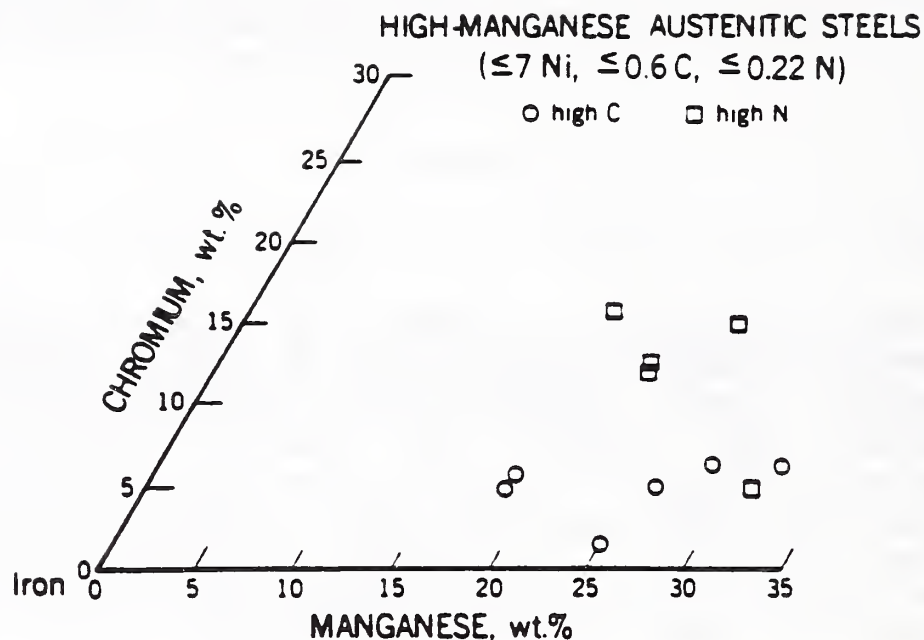


Figure 1. Portion of the Fe-Mn-Cr ternary diagram with compositions of recently developed high-Mn austenitic steels.

## STRUCTURE

Additions of Cr to Fe-Mn alloys serve two purposes: (1) improvement of corrosion resistance and (2) retardation of the intergranular failure mechanism of the Fe-Mn binary alloys (discussed later). Additions of Cr have little effect on the austenite stability of the Fe-Mn alloys, as illustrated in Fig. 2<sup>(2)</sup>. Neither the thermally induced  $\alpha$  (bcc) and  $\epsilon$  (hcp) transformations nor the strain-induced  $\alpha'$  and  $\epsilon'$  transformations are significantly affected. Additions of Cr greater than approximately 15% result in high-temperature  $\delta$  ferrite or  $\sigma$  phase (at high Mn contents). Alloying with relatively small amounts of Ni, C, or N is needed to suppress these high-temperature phases that are deleterious to fracture. Also, from Fig. 2, notice that at Mn contents greater than about 22%, no strain-induced  $\alpha'$  is detected, even at 4 K. The strain-induced  $\epsilon'$ -martensitic structure is suppressed above about 32% Mn, and the thermal  $\epsilon$ -martensitic phase is suppressed above about 28% Mn<sup>(4)</sup>.

Although Fig. 2 is taken primarily from Horiuchi et al.<sup>(2)</sup>, similar studies were conducted earlier by Namekata and Higashi<sup>(3)</sup> at temperatures ranging from 4 to 273 K. They also studied the effect of 6% Ni addition to Fe-Mn-Cr alloys and found that neither  $\epsilon$  nor  $\epsilon'$  was detected at Mn contents higher than 25%.

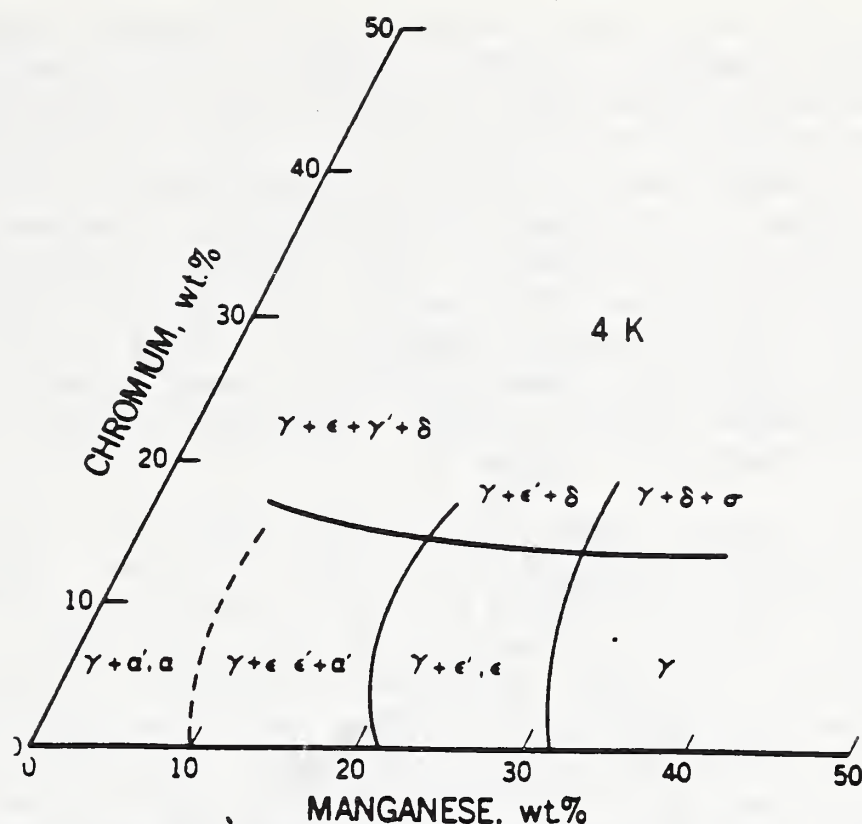


Figure 2. Portion of the Fe-Mn-Cr ternary diagram illustrating alloy dependence of phases formed during deformation or cooling to 4 K<sup>(2)</sup>.

Additions of Ni and C to Fe-Mn alloys enhance austenite ( $\gamma$ ) stability. The Fe-rich portion of the Fe-Mn-Ni ternary diagram<sup>(6)</sup> containing both thermally and strain-induced phases at 76 K is shown in Fig. 3. From this figure, it is apparent that the addition of about 10% Ni to alloys having greater than about 15% Mn is sufficient to prevent the formation of both  $\alpha'$  and  $\epsilon'$  formation at low temperatures. Even less Ni is required for austenitic thermal stability if C, N, or even Cr is present. Similarly, C additions increase  $\gamma$  stability<sup>(6)</sup>, as illustrated in Fig. 4. Although a ternary Fe-Mn-N phase diagram was not discovered in review for this paper, N additions are also expected to increase austenite stability.

Thus, to achieve austenite that is stable with respect to martensite, Mn, Ni, C, or N is added. To prevent high-temperature phases, Ni, C, or N is added and Cr is kept to about 15% or lower. If corrosion resistance is desirable, 10 to 15% Cr must be added.

## STRENGTH

### Mechanisms

There are four distinct deformation mechanisms in high-Mn austenitic steels at low temperatures: slip, deformation twinning, transformation to  $\epsilon$  martensite, and transformation to  $\alpha'$  martensite.



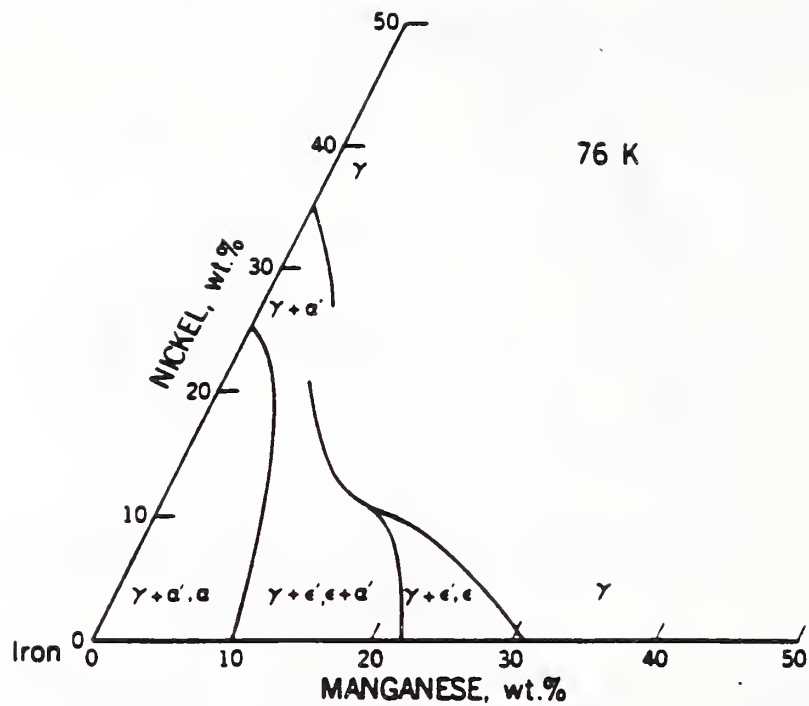


Figure 3. Portion of the Fe-Mn-Ni ternary diagram illustrating alloy dependence of phases formed during deformation or cooling to 76 K<sup>(5)</sup>.

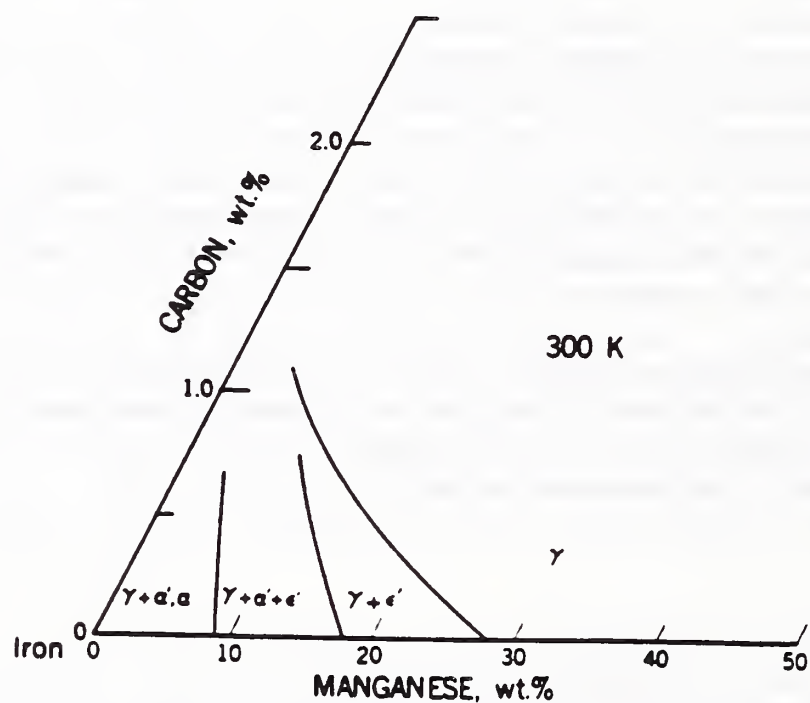


Figure 4. Portion of the Fe-Mn-C ternary diagram illustrating alloy dependence of phases formed during deformation or cooling to 300 K<sup>(6)</sup>.

Slip - In very stable austenite or at higher temperatures, the only deformation mechanism is slip. Figure 5, which is based on data from Remy and Pineau<sup>(7)</sup>, shows that slip is found at high temperatures and high Mn contents. Additions of Cr, Ni, C, and N reduce the temperature and the Mn content at which slip is the dominant deformation mechanism. These alloying elements increase austenite stability with respect to  $\alpha'$  martensite formation and are expected to increase (or, at least, not to decrease) the stacking-fault energy. Since slip occurs by dislocation nucleation and motion, the factors that affect dislocation dynamics control the flow strength in this regime. These factors include long-range interactions with dislocation cells or grain boundaries; shorter range, temperature-dependent interactions with interstitials such as C and N; and dynamic recovery.

Deformation Twinning - At lower temperatures or Mn contents, deformation twinning is observed. Twins have been associated with bundles of stacking faults aligned on  $(111)_\gamma$  planes. Figure 6 shows the etched surface of an Fe-22Mn-13Cr-5Ni-0.22N alloy with 10% elongation at 76 K. The broad bands are thought to represent deformation twinning, since no  $\epsilon'$  was detected using x-ray diffraction, no  $\alpha'$  was detected using magnetic measurements, and simple slip bands would not be expected to etch. As shown in Fig. 5, the addition of C to Fe-Mn alloys tends to increase the temperature range of deformation twinning, but the addition of Cr decreases the range of twinning while increasing the occurrence of  $\epsilon'$  martensite. Little is known of the quantitative effect of deformation twinning on stress-strain characteristics, although the results of a study by Tomota et al.<sup>(8)</sup> of Fe-31Mn and Fe-36Mn-alloy flow strengths imply that twinning does not substantially alter the tensile behavior, as slip does.

Transformation to  $\epsilon'$  Martensite - Transformation to  $\epsilon'$  martensite, rather than slip or twinning, occurs at lower temperatures and Mn contents (Fig. 5). Formation of  $\epsilon'$  martensite during deformation increases the rate of work hardening<sup>(8)</sup>. The platelets of  $\epsilon'$  on  $(111)_\gamma$  are thought to segment the austenite grains, considerably obstructing the dislocation motion through effective reduction in grain size. This effect of  $\epsilon'$  formation on stress-strain behavior is illustrated in Fig. 7. In the absence of  $\alpha'$  formation, strain-induced  $\epsilon'$  continuously increases with a linear dependence on strain (Fig. 7)<sup>(2)</sup>.

Transformation to  $\alpha'$  Martensite - At even lower temperatures or Mn contents (see Figs. 2 through 4),  $\alpha'$  martensitic transformation is strain induced. In a manner similar to Fe-Cr-Ni alloy deformation behavior<sup>(9)</sup>,  $\alpha'$  formation has two effects<sup>(8)</sup>, which are illustrated in Fig. 7. At strains usually less than 0.10,  $\alpha'$  forms at slip-band intersections as laths with a  $\langle 110 \rangle_\gamma$  axial direction corresponding to the common direction of  $(111)_\gamma$  intersection. These laths effectively reduce the flow stress by relieving stress, transmitting dislocation pile-ups, or both. Subsequent  $\alpha'$  formation acts in the opposite direction, increasing the rate of work hardening. At larger strains, presumably the slip-band intersection sites for  $\alpha'$  formation have been exhausted and  $\alpha'$  forms from  $\epsilon'$ . This produces a maximum in the dependence curve of  $\epsilon'$  on strain. Thus at low temperatures, metastable polycrystalline austenitic steels can have characteristic stress-strain curves, very similar in shape to single-crystal curves, with three stages<sup>(10)</sup>.



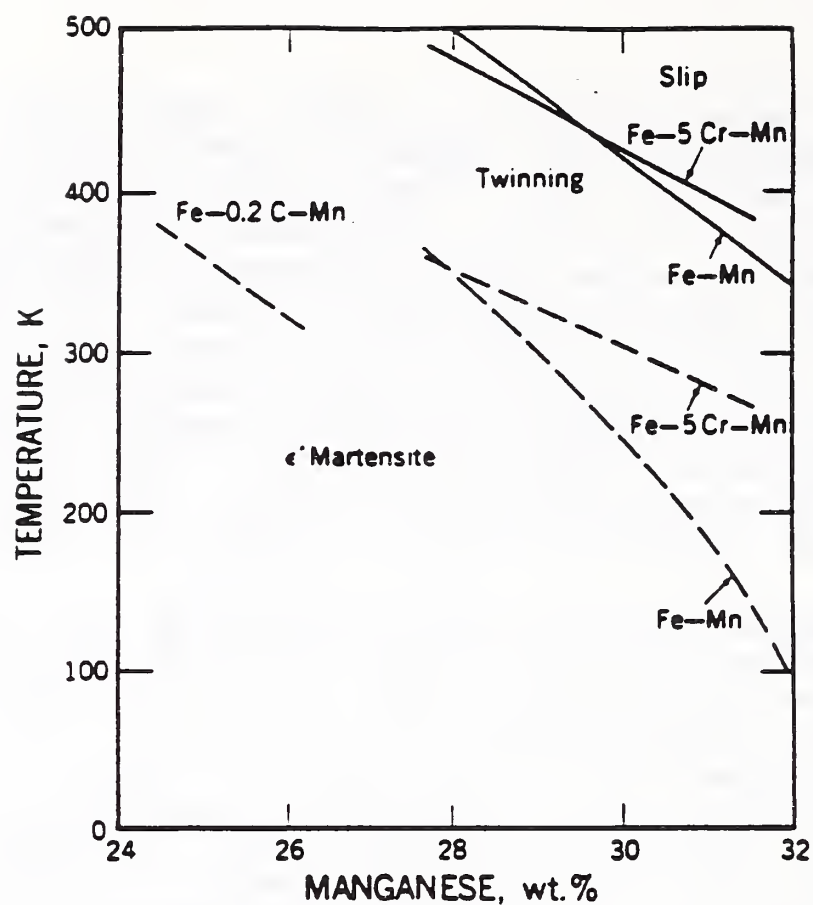


Figure 5. Deformation mechanisms in Fe-Mn-(Cr or C) alloys as a function of temperature and Mn content(<sup>7</sup>).



Figure 6. Photomicrograph of Fe-22Mn-13Cr-5Ni-0.22N austenitic steel deformed in tension to 10% elongation at 76 K.

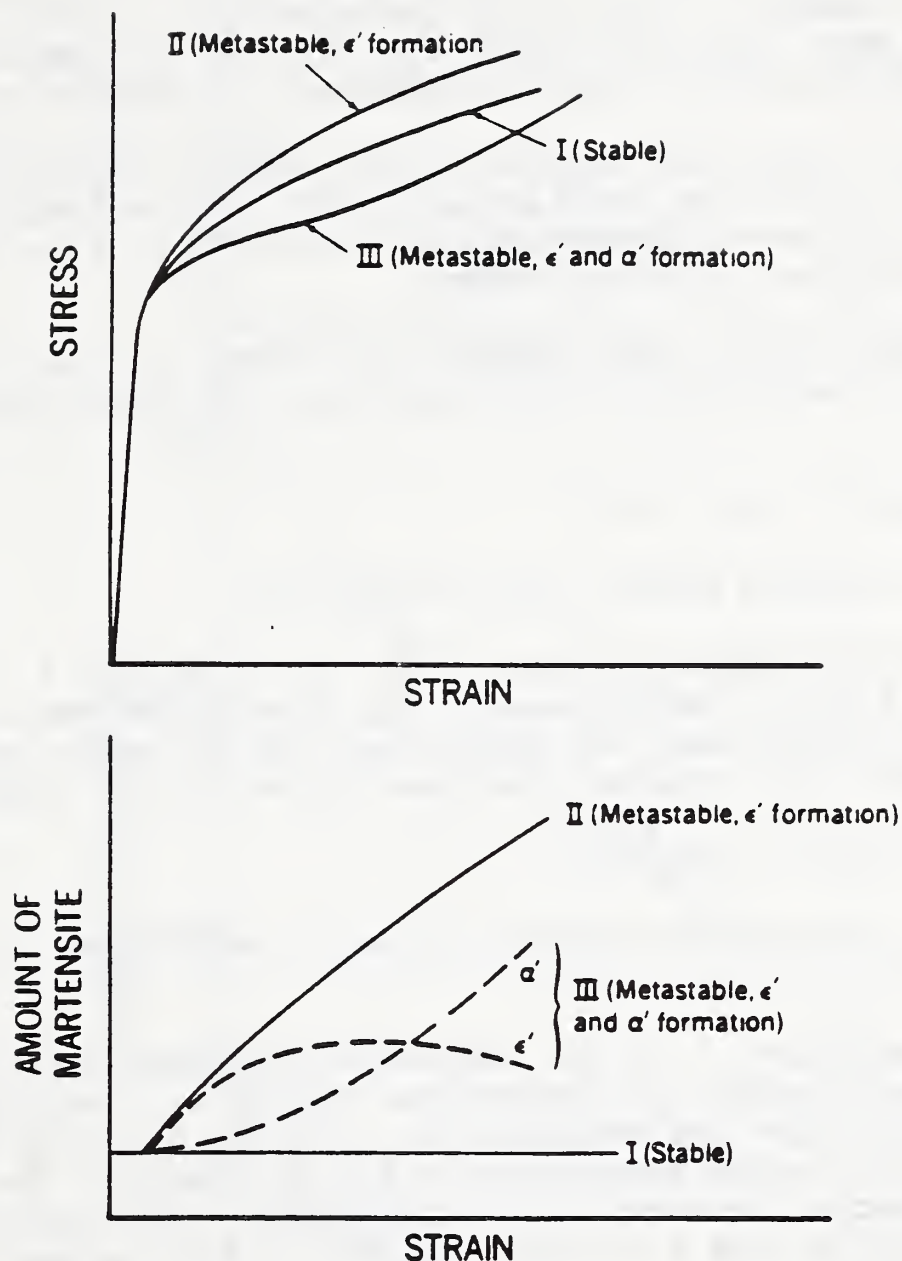


Figure 7. Stress-strain and associated martensite transformation characteristics for austenitic steels at low temperatures.

**Alloying Effects** - Although solid-solution alloying elements, such as Cr and Ni, may affect the flow or fracture properties by influencing the relative stability of the austenite (thus affecting  $\alpha'$ ,  $\epsilon'$ , or twinning deformation mechanisms), they contribute virtually nothing to the flow strength of stable high-Mn austenitic steels (whose deformation mechanism is slip). This lack of influence is understandable, because these elements have effective volumes close to Fe ( $V_{Ni}/V_{Fe} = 0.93$ ,  $V_{Cr}/V_{Fe} = 1.02$ )<sup>(11)</sup>. This similarity results in similar lattice parameter changes with alloying additions. However, additions of the much smaller elements C and N, which presumably occupy interstitial lattice sites, increase strength



considerably at low temperatures. The effective volume of C relative to Fe is 0.34; that of N, 0.30<sup>(11)</sup>. In Fe-Cr-Ni alloys, the smaller N atom produces larger changes in the lattice parameter (a): at 295 K, (1/a) (da/dc) = 0.218 for C and 0.240 for N!<sup>(11)</sup>, where c is composition in at.%. We expect a similar lattice-parameter dependence in high-Mn austenites.

We conducted regression analyses on all high-Mn austenitic steel data at 295, 76, and 4 K that we could gather<sup>(12-26)</sup>. We defined high-Mn steel as any steel having an austenitic structure on cooling to low temperature and Mn as the principal alloying element.

The dependencies of yield strength ( $\sigma_y$ , in MPa) on C and N content ([C] and [N], in wt.%) and grain size (d, in  $\mu\text{m}$ ) were analyzed using the expression

$$\sigma_y = \sigma_0 + a[C] + b[N] + kd^{-1/2}, \quad (1)$$

where  $\sigma_0$  is the strength before C and N additions.

The results are listed in Table 1 and plotted in Fig. 8. Brackets drawn about the N and C coefficients in Fig. 8 represent one standard deviation; the brackets about the data points for the ratios of N/C coefficients represent the estimated fractional error (F.E.), using

$$\text{F.E.} = \pm (b^2 P_C^2 + a^2 P_N^2)^{1/2} / ab, \quad (2)$$

where  $P_C$  and  $P_N$ , the probable errors in a and b, were taken as one standard deviation (Table 1).

Notable results are: (1) The temperature dependencies of the C and N strengthening contributions are larger than that of  $\sigma_0$ , implying shorter range stress fields from the interstitials. (2) The ratio of these contributions are plotted versus temperature in Fig. 8 along with the ratios for identically determined Fe-Cr-Ni alloy data<sup>(27,28)</sup>. It is apparent that the relative contribution from N is higher in the Fe-Mn-Cr alloys than in the Fe-Cr-Ni austenites.

Table 1. Regression Analysis of C, N, and Grain-Size Contributions to Tensile Yield Strength in Eq. 1.

Temperature (K)	Number of Data Points	Coefficients (MPa/wt.%)				Standard Deviation (MPa/wt.%)				
		$\sigma_0$	a	b	k	$\sigma_y$	$\sigma_c$	a	b	k
4	58	551	773	2140	1140	77	52	142	178	161
77	25	264	315	1580	1060	76	64	44	145	454
295	66	118	132	683	462	53	23	24	46	89

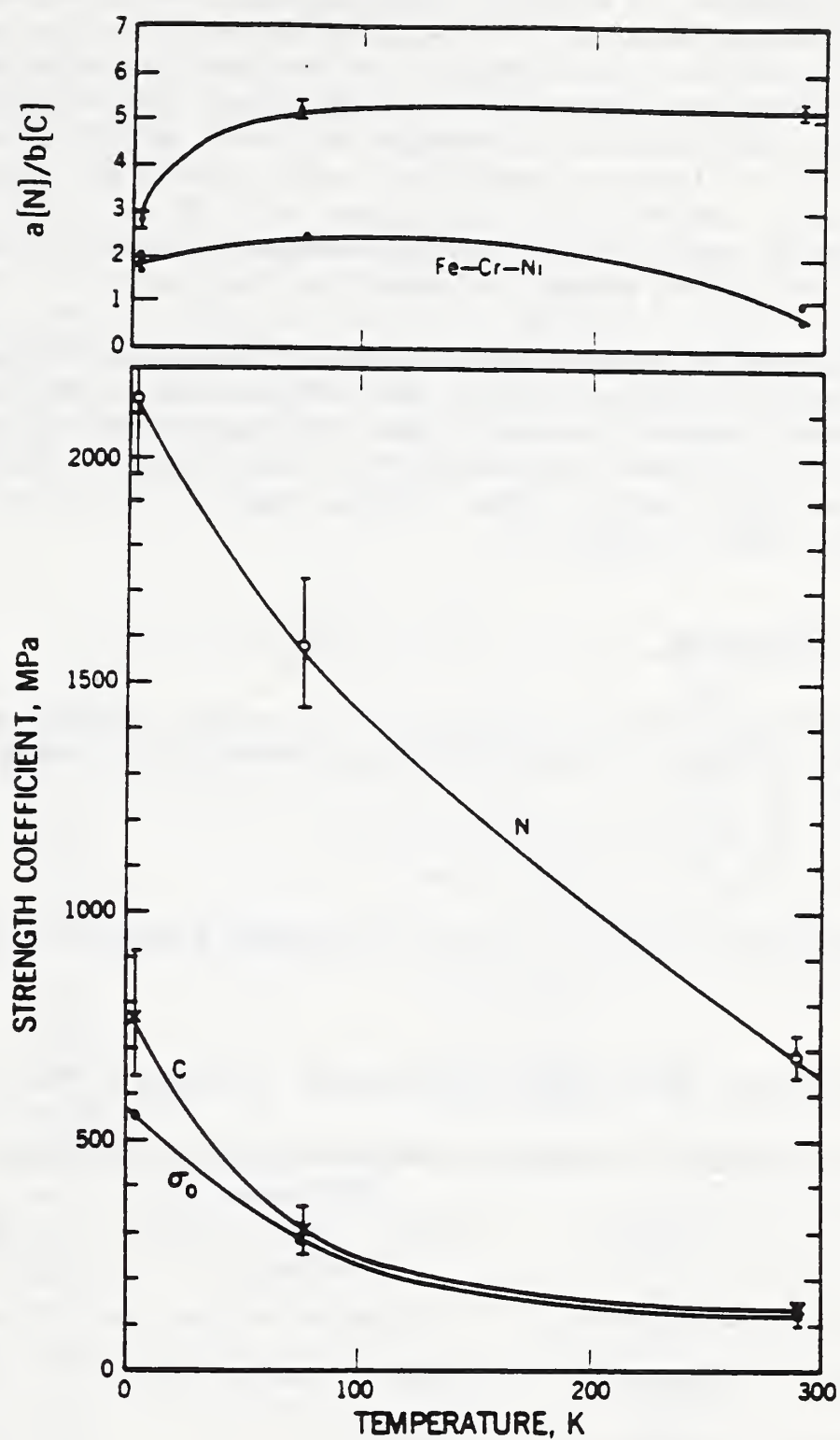


Figure 8. Regression analyses results for the dependence of yield strength on C and N content and grain size at low temperatures.

Furthermore, in the Fe-Cr-Ni alloys, N strengthens more than C at low temperatures; in the Fe-Mn-Cr alloys the reverse is true. (3) Comparison of the coefficients with results of previous Fe-Cr-Ni regression anal-



yses<sup>(27,28)</sup> indicates that the magnitude of the strengthening contribution from C and N is less in Fe-Mn-Cr alloys than in Fe-Cr-Ni and Fe-Cr-Ni-Mo (316-type) alloys. However, the smaller contribution to interstitial strengthening in the Fe-Mn-Cr alloys is offset by two factors: the strength,  $\sigma_0$ , is almost twice that of Fe-Cr-Ni alloys (see Table 2) at 4 K, and the solubility of C and N in Fe-Mn-Cr alloys is about twice that in Fe-Cr-Ni alloys. Lula<sup>(29)</sup> lists the predicted and measured N solubilities at 1873 K for Fe-15Mn-15Cr and Fe-15Ni-15Cr alloys as 0.29 and 0.13 wt.%, respectively. Both Mn and Cr additions increase the solubility of N in austenite; Ni addition results in slightly lower N solubility.

The addition of N to Fe-Mn-Cr austenites increases their strength by about a factor of three more than the addition of C (Fig. 8). This very significant distinction between C and N strengthening is not predictable on the basis of size or modulus misfit<sup>(9)</sup>, which leads to the suspicion that N is positioned differently in the lattice than C, possibly in pairs<sup>(9)</sup> or ordered within short range<sup>(30)</sup>.

### GRAIN SIZE DEPENDENCE

The published data<sup>(15-17,20,25,31-33)</sup> on the effects of grain size on tensile yield strength, using the Hall-Petch relationship, are included in Fig. 9. Here,

$$\sigma_y = \sigma_0' + kd^{-1/2}, \quad (3)$$

where  $\sigma_0'$  includes all grain-size-independent contributions.

Table 2. Nitrogen and Carbon Contributes to Tensile Yield Strength.

Source	Alloy	Nitrogen			Carbon		
		4 K	76 K	295 K	4 K	76 K	295 K
		(MPa/wt.%)			(MPa/wt.%)		
This paper	Fe-Mn-Cr	2140	1580	680	770	320	130
Simon, Reed, 1986 <sup>(28)</sup>	Fe-Ni-Cr	3190			1660		
Reed, Simon, 1984 <sup>(27)*</sup>	Fe-Ni-Cr	3400	2080	420	1700	840	830
Simon, Reed, 1986 <sup>(28)</sup>	Fe-Ni-Cr-Mo	2780			1690		

\* Did not include a grain-size term in the analysis.

The results of our regression analyses (using Eq. 1) in calculating the grain-size dependence,  $k$ , are also included in Fig. 9. A typical 4-K value of  $k$  for Fe-Cr-Ni alloys<sup>(28)</sup> is 1090 MPa/ $\mu\text{m}^{-1/2}$ ; for Fe-Cr-Ni-Mo alloys, 810 MPa/ $\mu\text{m}^{-1/2}$ <sup>(34)</sup>. The lower average values for these alloys are outside the data spread of individual Fe-Mn-Cr-alloy studies. The increased grain-boundary contribution of the Fe-Mn-Cr alloys implies increased alloy segregation at their grain boundaries, presumably by C and N.

The dependence of flow strength on grain size is quite strongly dependent on temperature, increasing by a factor of 2 from 295 to 4 K. Purer face-centered cubic metals, such as 99.95% Cu, exhibit about a 30% increase in  $k$  from 295 to 4 K<sup>(35)</sup>. Thus, the stronger temperature dependence of the grain size influence on flow strength also probably reflects more impurity segregation at grain boundaries of the austenite structure. However, as illustrated in Fig. 9, there is no clear trend of  $k$  as a function of C and N content.

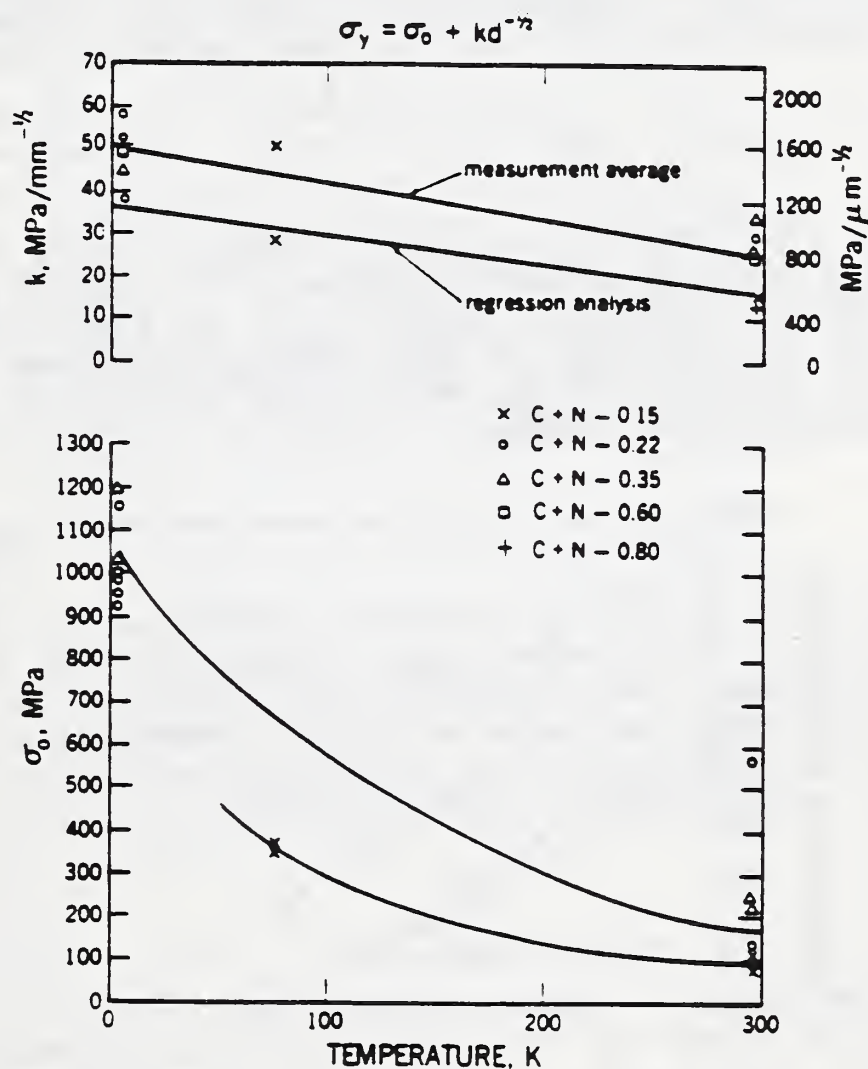


Figure 9. Summary of literature data on the Hall-Petch constants of high-Mn austenitic steels at low temperatures. Also included are the  $k$  results of the regression analyses of this study.



## TEMPERATURE DEPENDENCE

From analyses of the temperature dependence of many austenitic steels, we found that for most alloys at low temperatures, the log of the yield strength is linearly and inversely related to the temperature. This is illustrated in Fig. 10 for several high-Mn alloys<sup>(22)</sup>, and can be expressed as

$$\sigma_y = \sigma_0 \exp(-AT), \quad (4)$$

where  $\sigma_0$  is the yield strength at absolute zero and A is a constant, the slope of  $\ln \sigma_y$  versus temperature, T. This slope is proportional to the estimated stacking-fault energy of the austenitic alloys<sup>(22)</sup>.

Near room temperature, most alloys deviate from logarithmic dependence (Fig. 10), but there is no other evidence that this deviation signifies a change of the deformation mechanism. Many of these alloys are completely stable: there is no strain-induced martensite. The macroscopic contours of the stress-strain curves remain the same. Obviously, fundamental studies are needed to assess the significance of the temperature-dependence trends.

## TOUGHNESS

**MECHANISMS** - The toughness of binary Fe-Mn alloys is degraded by intergranular fracture, even in stable austenite<sup>(4,15)</sup>. Recent studies<sup>(4,15)</sup> have not succeeded in detecting segregation at the grain boundaries; thus, at present, there is no remedy for this fracture mechanism in the binary alloys. However, additions of the order of 5% Cr or Ni or small amounts of C do inhibit intergranular fracture.

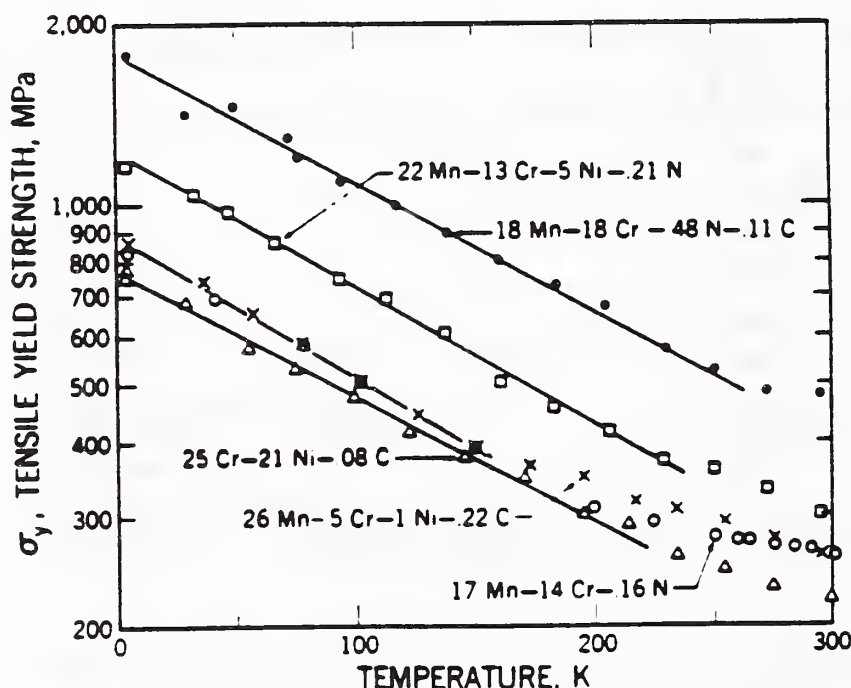


Figure 10. Temperature dependence of austenitic alloy yield strengths at low temperatures.

At low temperatures, Fe-Mn-Cr and Fe-Mn-Cr-Ni alloys with high N contents or low austenite stabilities exhibit faceting of the stacking-fault clusters on  $(111)_\gamma$  in impact or fracture toughness tests<sup>(4,36-38)</sup>. This brittle-looking faceting is similar to that reported by Tobler and Meyn<sup>(39)</sup> as slip-band cracking on compact-tension specimen fracture surfaces in high-N alloys. These facets usually have other  $(111)_\gamma$  traces on their surfaces (Fig. 11a). The fracture surfaces following fracture toughness tests at low temperatures are seldom dominated by these  $(111)_\gamma$  facets; elongated, shallow dimples are the prevalent morphological structure (Fig. 11a). At higher temperatures or in more stable structures, the faceting is reduced and the elongated dimples are dominant on the fracture surfaces (Fig. 11b). This change is usually associated with increased toughness. Perhaps the reduction of fracture-surface faceting is assisted by Ni addition. This is the case for Fe-Cr-Ni alloys<sup>(40)</sup>. Yamamoto et al.<sup>(20)</sup> and Suemune et al.<sup>(41)</sup> have also found that Ni increases the toughness of the Fe-Mn-Cr alloys, but the fracture mechanisms in their studies were not identified. It is still uncertain whether the role of Ni in Fe-Mn-Cr austenite fracture is to increase toughness by increasing the stacking-fault energy (suppressing  $\epsilon'$  formation, deformation twinning, and stacking-fault clusters) or to affect the toughness of alloys that fail by void growth and coalescence.

At higher temperatures, decreased strengths, higher Ni contents, or lower stress concentrations, typical ductile dimple fracture is prevalent (Fig. 11c). Nonmetallic inclusions are associated with most ductile dimples. Yamamoto et al.<sup>(20)</sup> and Suemune et al.<sup>(41)</sup> have both obtained excellent correlations between reduced S content (to reduce MnS inclusions) and toughness at low temperatures for Fe-22Mn-(13-15)Cr-(1-7)Ni austenitic steels. Apparently, the conditions, such as those illustrated in Fig. 11b, reflect the fracture morphology transition between faceting and dimpling. In this transition, many of the shallow, elongated dimples do not appear to be nucleated at inclusions.

### Strength Dependence

The dependence of toughness on strength in high-Mn austenitic alloys is similar to that in Fe-Cr-Ni alloys. The inverse dependence of yield strength of a series of Fe-20Cr-10Ni-C+N alloys (the shaded band) is shown in Fig. 12; the lines on each side of the band indicate the data spread of all Fe-Cr-Ni base metals that we have measured at 4 K. The  $K_{IC}(J)$  fracture toughness values plotted in this figure were converted from J-integral measurements using

$$[K_{IC}(J)]^2 = EJ_{IC}, \quad (5)$$

where E is Young's modulus. The compact tensile specimens measured were oriented in the TL direction ( $J_{IC}$  measurements are about 10 to 20% lower in this orientation than in the LT orientation). The tensile yield-strength data in Fig. 12 were measured in the transverse direction. The individual data points portray our measurements of high-Mn austenites. The several data points of the solution-treated alloys 18Mn-16Cr-5Ni-0.2N and 22Mn-13Cr-5Ni-0.2N reflect test and material variability. The location of these high-Mn-alloy data points on the high side of the trend lines probably reflects increased steel cleanliness. The fracture appearance of these high-Mn alloys varies: high-yield-strength alloys have more  $(111)_\gamma$  facets; low-yield-strength alloys have larger dimples.



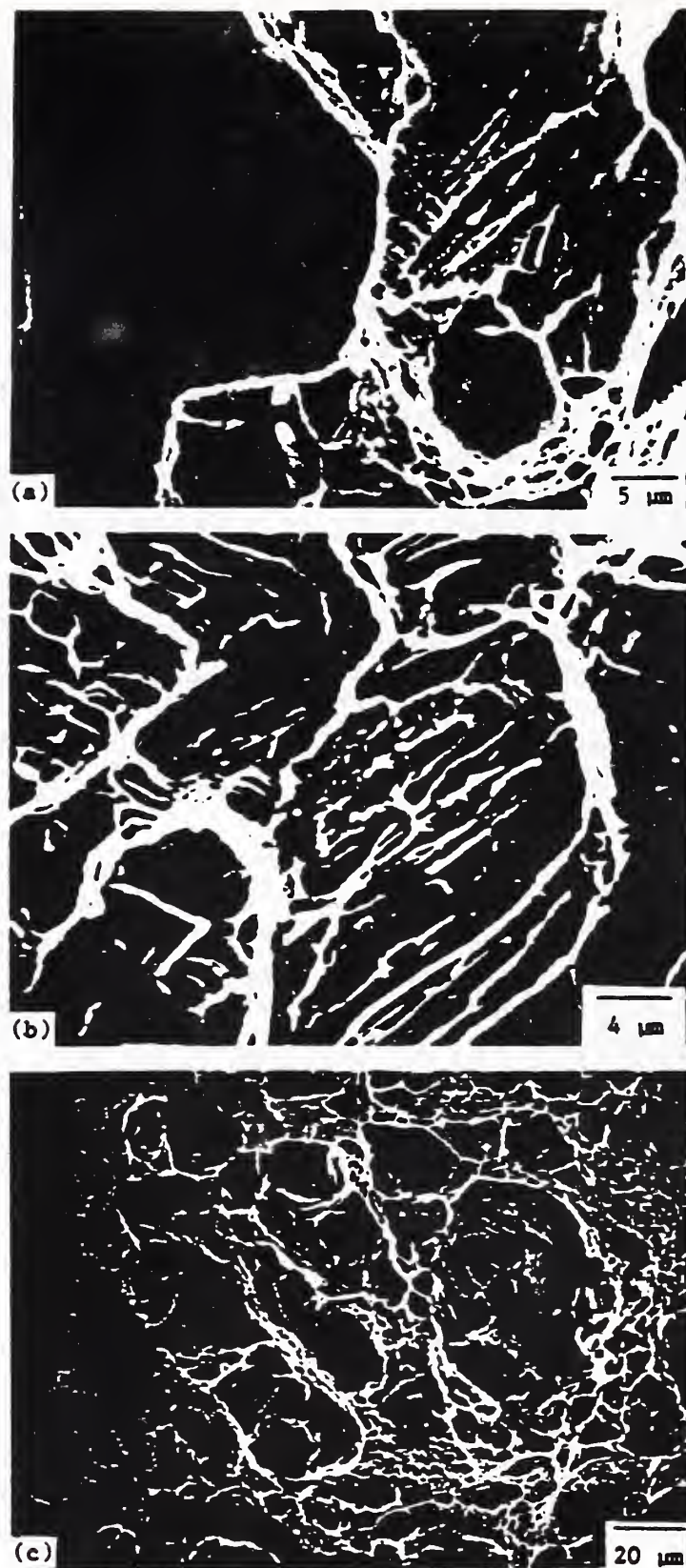


Figure 11. (a) Fracture surface of a compact-tension specimen of Fe-8Mn-20Cr-7Ni-0.37N alloy, tested at 4 K, displaying  $(111)_\gamma$  brittle facet and elongated, shallow microvoid dimples.

(b) Fracture surface of a compact-tension specimen of Fe-22Mn-13Cr-5Ni alloy tested at 4 K.

(c) Fracture surface of tensile specimen of Fe-22Mn-13Cr-5Ni alloy tested at 4 K.

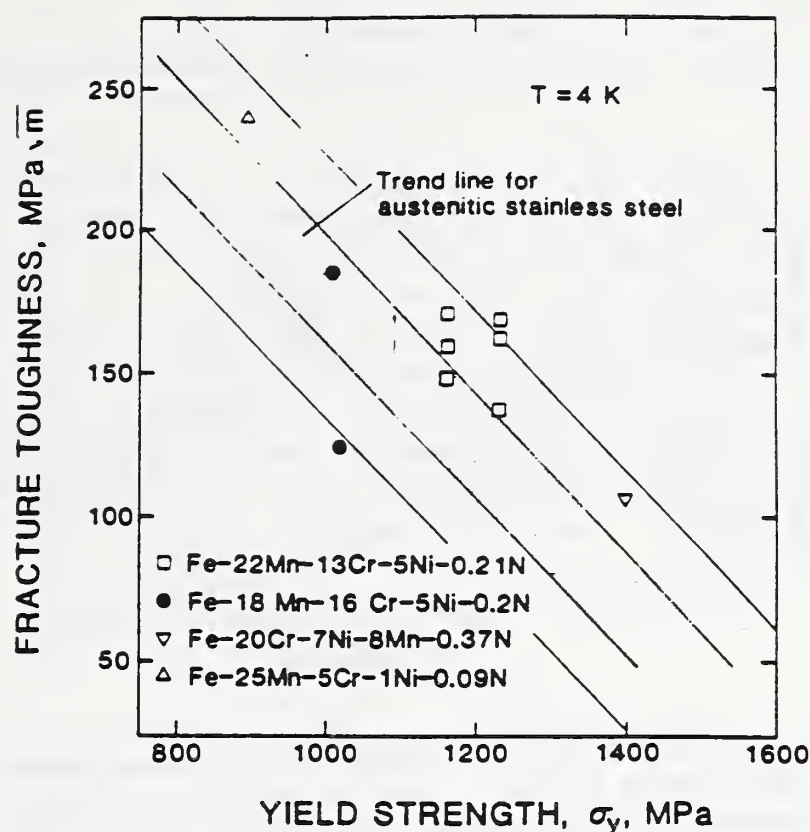


Figure 12. Dependence of fracture toughness on tensile yield strength at 4 K for (1) a series of Fe-Cr-Ni alloys with controlled amounts of C and N (shaded band), (2) all Fe-Cr-Ni austenitic steels measured at NBS (wide band), and (3) high-Mn austenitic steels measured at NBS.

## PHYSICAL PROPERTIES

At low temperatures, high-Mn austenites are antiferromagnetic; at high temperatures, they are usually paramagnetic. The magnetic transformation at their Néel temperature significantly influences their elastic properties, thermal expansion, and magnetic susceptibility.

Magnetic susceptibility is probably the best indicator of the Néel temperature. At the transition temperature, magnetic susceptibility peaks sharply (Fig. 13). The data of Collings<sup>(42)</sup> show dependence of the Néel temperature on composition: The Néel temperature of 13Mn-18Cr-3Ni is 160 K higher than that of 5Mn-22Cr-13Ni.

The transition to an antiferromagnetic state produces a softening of the elastic properties. This softening is relatively large, as illustrated by Ledbetter's data<sup>(43)</sup> in Fig. 14 for a Fe-26Mn-5Cr alloy. Both Young's modulus ( $E$ ) and the shear modulus ( $G$ ) decrease about 8% through the Néel temperature. The bulk modulus ( $B$ ) is less affected; Poisson's ratio ( $\nu$ ) increases about 8%.



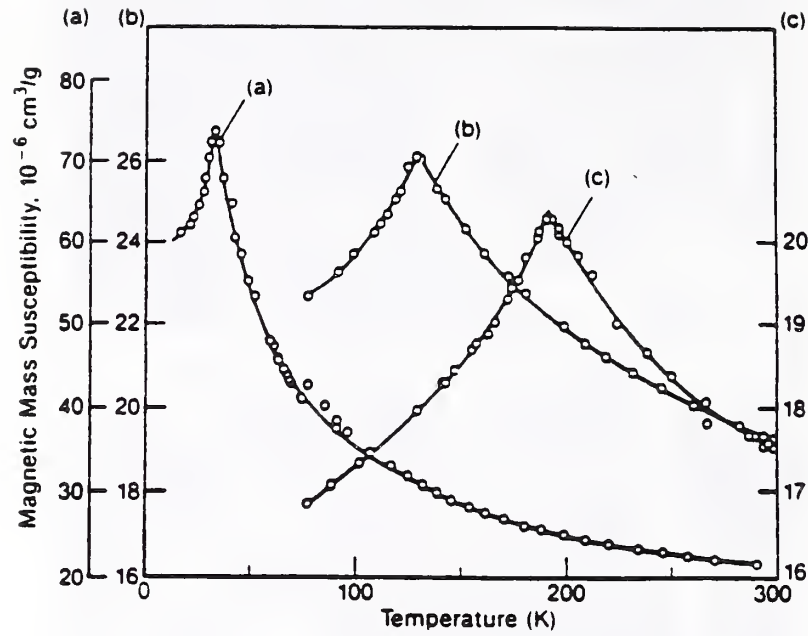


Figure 13. Magnetic susceptibility dependence on temperature and alloy content for three Fe-Mn-Cr-Ni alloys [Collings<sup>(38)</sup>]. The three susceptibility scales refer to alloy designations (a) Fe-22Cr-13Ni-5Mn, (b) Fe-21Cr-6Ni-9Mn, and (c) Fe-18Cr-3Ni-13Mn.

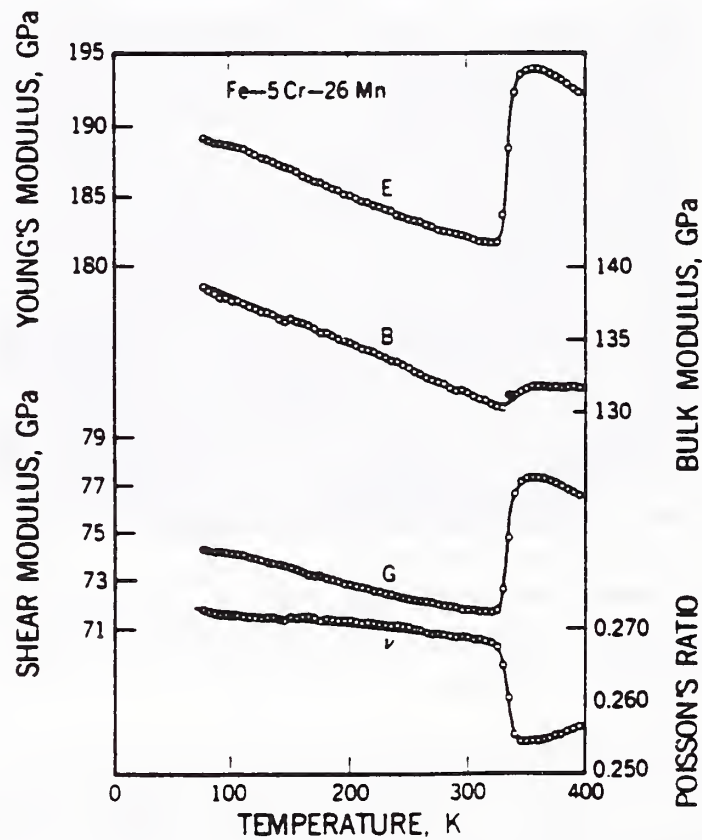


Figure 14. Elastic properties for an Fe-26Mn-5Cr alloy at low temperatures [Ledbetter<sup>(39)</sup>].

The magnetic transition also strongly affects thermal expansion. Below the Néel temperature ( $T_N$ ), there is positive magnetostriction in the antiferromagnetic state, which reduces the thermal expansion coefficient. Even at temperatures up to 100 K above the transition temperature, there is limited magnetic ordering that lowers the coefficient.

Richter and Pepperhoff<sup>(44)</sup> have measured the thermal expansion characteristics of a number of Fe-Mn base alloys at low temperatures. They observed that C and Cr additions tend to lower  $T_N$  and reduce the volume magnetostriction (Fig. 15). In the Fe-Mn binary system, Mn additions of 32 to 50% increase  $T_N$ , and Mn additions of 32 to 40% increase the volume magnetostriction; further additions of Mn decrease both terms. Thus, the amount of thermal expansion depends critically on the location of the Néel temperature. In general, the lower the Néel temperature, the higher the expansion coefficient. Sasaki et al.<sup>(45)</sup> have developed an empirical relation suggesting a nearly linear, inverse dependence of the thermal expansion coefficient on  $T_N$ .

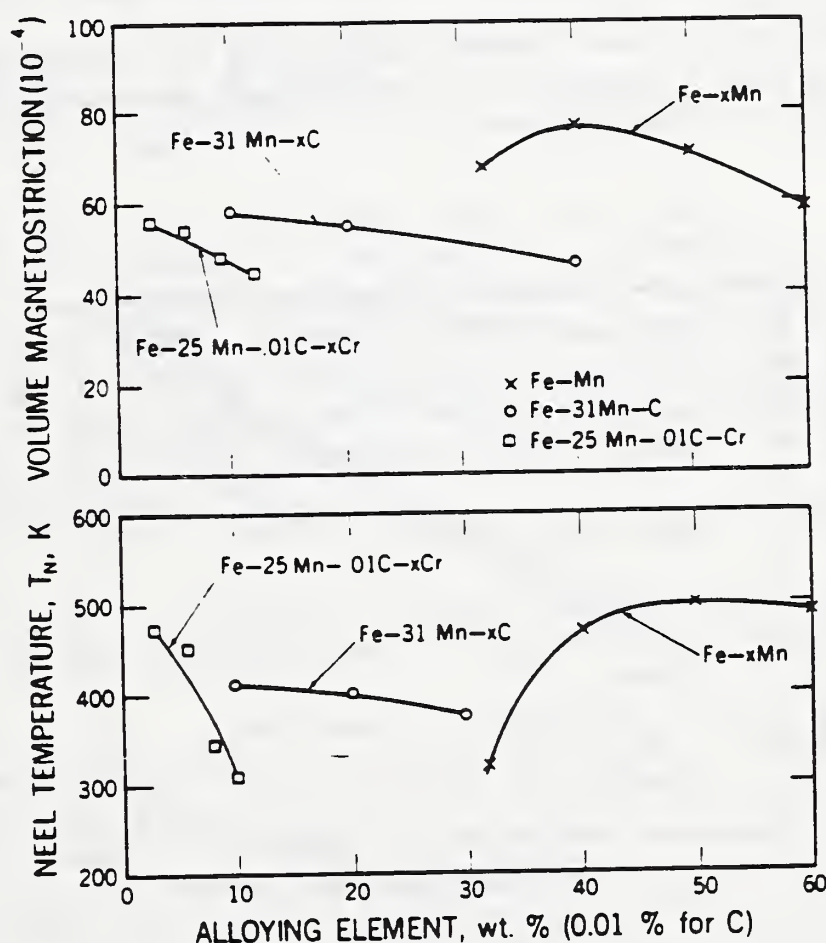


Figure 15. Effects of alloying on Néel temperature and volume magnetostriction of Fe-Mn-base alloys<sup>(40)</sup>.



In principle, high-Mn austenitic alloys may be designed to produce varying contraction characteristics at low temperatures. If an alloy is desired with a lower thermal contraction matching that of a low-alloy ferritic steel, the Mn content should be high enough to ensure that  $T_N$  is above room temperature (Fig. 16). If a high-Mn steel is to approximate the contraction characteristics of Cu, Al, or Fe-Cr-Ni alloys, the Mn content should be lower.

#### SUMMARY

The strength, toughness, and selected physical properties of high-Mn austenitic steels at low temperatures have been reviewed. Compared with Fe-Cr-Ni austenitic steels, the high-Mn steels have several distinct characteristics.

The solubility of N and C is higher, which enables the attainment of higher strengths. More hcp martensite is induced by deformation. The hcp phase increases the rate of work hardening during deformation. In toughness tests, increased fracture faceting on  $\{111\}_\gamma$  is observed in lower stacking-fault-energy alloys. Binary Fe-Mn alloys are more susceptible to intergranular fracture. Therefore, high-Mn austenites are easier to strengthen than Fe-Cr-Ni austenites, but more troublesome to toughen.

The elastic properties and thermal expansion are strongly influenced by the magnetic transition from the high-temperature paramagnetic state to antiferromagnetism at low temperatures.

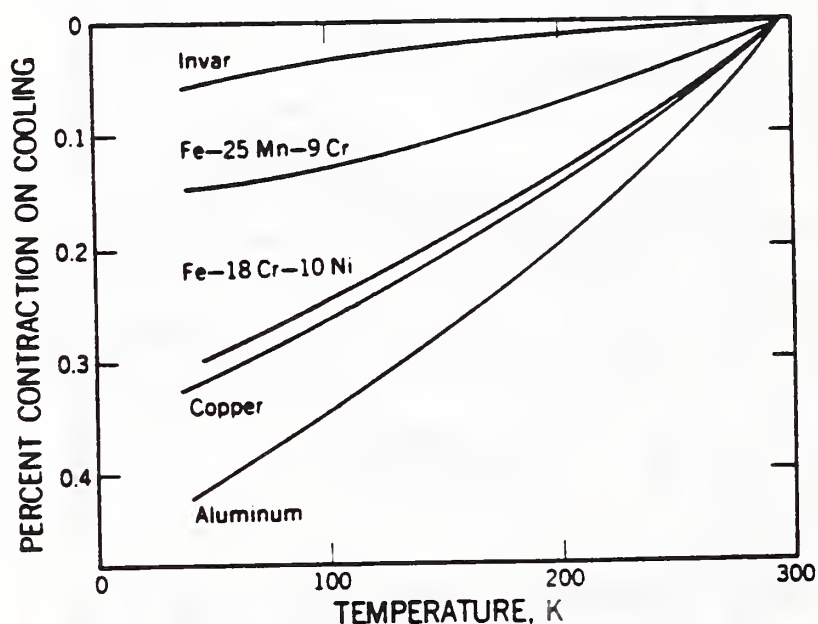


Figure 16. Percent contraction of various face-centered cubic structural alloys on cooling.

## REFERENCES

1. Shimamoto, S., H. Nakajima, K. Yoshida, and E. Tada, in "Advances in Cryogenic Engineering - Materials," vol. 32, pp. 23-32, Plenum Press, New York (1986).
2. Horiuchi, T., R. Ogawa, and M. Shimada, in "Advances in Cryogenic Engineering - Materials," vol. 32, pp. 33-42, Plenum Press, New York (1986).
3. Namekata, J. and K. Higashi, J. Iron Steel Inst. Jap. 66, 355 (1980)
4. Tomota, Y., M. Strum, and J.W. Morris, Metall. Trans. A 18A, 1073-81 (1987).
5. Schaller, A., M.A. Shtremel, and A.A. Petrunenkov, Neue Hütte 7, 253-57 (1979).
6. "Recent Developments of High Manganese Structural Steels," Daido Steel Co., Ltd., Nagoya, Japan (1984).
7. Remy, L. and A. Pineau, Mater. Sci. Eng. 28, 99-107 (1977).
8. Tomota, Y., M. Strum, and J.W. Morris, Metall. Trans. A 17A, 537-47 (1986).
9. Reed, R.P., in "Materials at Low Temperatures," pp. 295-341, American Society for Metals, Metals Park, Ohio (1983).
10. Reed, R.P. and R.L. Tobler, in "Advances in Cryogenic Engineering - Materials," vol. 28, pp. 49-56, Plenum Press, New York (1982).
11. Reed, R.P., in Alloying, American Society for Metals, Metals Park, Ohio (1988); to be published.
12. Sakamoto, T., Y. Nakagawa and I. Yamauchi, in "Advances in Cryogenic Engineering - Materials," vol. 32, pp. 65-71, Plenum Press, New York (1986).
13. Guntner, C.J. and R.P. Reed, ASM Trans. Quart. 55, 399-419 (1962).
14. Tone, S., M. Shimada, T. Horiuchi, Y. Kasamatsu, H. Nakajima, and S. Shimamoto, in "Advances in Cryogenic Engineering - Materials," vol. 32, pp. 89-96, Plenum Press, New York (1986).
15. Strum, M.J., "Control of Cryogenic Intergranular Fracture in High-Manganese Austenitic Steels" Ph.D. Thesis, University of California, Berkeley, LBL-22650, Lawrence Berkeley Laboratories, Berkeley, California (Dec. 1986).
16. Rao, V.K., D.M.R. Taplin, and P.R. Rao, Metall. Trans. 6A, 77-86 (1975).
17. Ishikawa, K., K. Hiraga, T. Ogata, and K. Nagai, in "Austenitic Steels at Low Temperatures," pp. 295-309, Plenum Press, New York, (1983).
18. Yoshimura, H., H. Sumitomo, H. Masumoto, and K. Suemune, in "Cryogenic Properties of Metals and Welds," pp. 247-255, International Cryogenic Materials Conference, Boulder, Colorado (1987)
19. Yamagami, N., Y. Kohsaka, and C. Ouchi, presentation at United States-Japan Workshop on Low Temperature Structural Materials and Measurements for Magnetic Fusion Applications, Technical Research Center, Nippon-Kokan K.K., Kawasaki, Japan (1985)
20. Yamamoto, S., N. Yamagami, and C. Ouchi, in "Advances in Cryogenic Engineering - Materials," vol. 32, pp. 57-64, Plenum Press, New York (1986)



21. Tone, S., M. Hiromatsu, J. Numata, T. Horiuchi, H. Nakajima, and S. Shimamoto, in "Advances in Cryogenic Engineering - Materials," vol. 32, pp. 89-96, Plenum Press, New York (1986).
22. Reed, R.P. and J.M. Arvidson, in "Advances in Cryogenic Engineering - Materials," vol. 30, pp. 263-70, Plenum Press, New York (1984).
23. Kaji, H., M. Hiromatsu, S. Tone, M. Shimada, and S. Shimamoto, "The Development of a 22Mn-13Cr-5Ni Nonmagnetic Steel Plate for Cryogenic Applications," Kobelco Technical Bulletin 1093, Kobe Steel Co., Kobe, Japan (Nov. 1985).
24. Suemune, K., T. Sakamoto, T. Ogawa, T. Okazaki, S. Maehara, H. Nakajima, and S. Shimamoto, in "Advances in Cryogenic Engineering - Materials," vol. 34, pp. 123-29, Plenum Press, New York (1988).
25. Ouchi, I., Nippon Kokan K.K., Kawasaki, Japan; unpublished data (1988).
26. Muira, R., K. Ohnishi, H. Nakajima, Y. Takahashi, and K. Yoshida, in "Austenitic Steels at Low Temperatures," pp. 287-93, Plenum Press, New York (1983).
27. Reed, R.P. and N.J. Simon, in "Advances in Cryogenic Engineering - Materials," vol. 30, pp. 127-36, Plenum Press, New York (1984).
28. Simon, N.J., and R.P. Reed, J. Nucl. Mater. 141-143, 44-8 (1986).
29. Lula, R.A., in "Manganese Stainless Steels," pp. 30-1, The Manganese Centre, Paris, France (1986).
30. Byenes, M.L.G., M. Grujicic, and W.S. Owen, Acta Metall. 35, 1853-62 (1987).
31. Kato, T., M. Fujikura, S. Yahagi, and K. Ishida, Tetsu-to-Hagane 67, 587-95 (1981).
32. Yoshimura, H., H. Masumoto, and T. Inoue, in "Advances in Cryogenic Engineering - Materials," vol. 28, pp. 115-25, Plenum Press, New York (1982).
33. Ogawa, R. and J.W. Morris, in "Advances in Cryogenic Engineering - Materials," vol. 30, pp. 177-84, Plenum Press, New York (1984).
34. Reed, R.P., N.J. Simon, P.T. Purtscher, and R.L. Tobler, in "Proceedings, International Cryogenic Engineering Conference," pp. 786-90, Berlin, Butterworths, London, England (1986).
35. Reed, R.P., R.P. Walsh, and F.R. Fickett, in "Advances in Cryogenic Engineering - Materials," vol. 34, pp. 299-308, Plenum Press, New York (1988).
36. Thompson, L.D., in "Mechanical Properties and Phase Transformations in Engineering Materials," pp. 391-408, AIME Metallurgical Society, Warrendale, Pennsylvania (1986).
37. Kato, T., S. Fukai, M. Fujikura, and K. Ishida, Trans. ISIJ 16, 673-79 (1976).
38. Defilippi, D.P., K.G. Brickner, and E.M. Gilbert, Trans. AIME 245, 2141-48 (1969).
39. Tobler, R.L. and D. Meyn, Cleavage-like fracture along slip planes in Fe-18Cr-3Ni-13Mn austenitic stainless steel at liquid helium temperature, Metall. Trans.; accepted for publication.
40. Purtscher, P.T., R.P. Walsh, and R.P. Reed, in "Advances in Cryogenic Engineering - Materials," vol. 34, pp. 379-386, Plenum Press, New York (1988).

41. Suemune, K., K. Sugino, H. Masumoto, H. Nakajima, and S. Shimamoto, in "Advances in Cryogenic Engineering - Materials," vol. 32, pp. 51-6, Plenum Press, New York (1986).
42. Collings, E.W., in "Advances in Cryogenic Engineering - Materials," vol. 26, pp. 37-47, Plenum Press, New York (1979).
43. Ledbetter, H.M., Physica 119B, 115-8 (1983).
44. Richter, F. and W. Pepperhoff, Arch. Eisenhüttenw. 47, 45-50 (1976)
45. Sasaki, T., K. Watanabe, K. Nohara, Y. Ono, N. Kondo, and S. Sato, Trans. Iron Steel Inst. Jap. 22, 1010-20 (1982).





# DISCONTINUOUS YIELDING IN AUSTENITIC STEELS AT LOW TEMPERATURES

R.P. Reed and N.J. Simon

National Institute of Standards and Technology  
Boulder, Colorado,

The effects of strain rate and coolant state on the discontinuous yielding characteristics of a number of austenitic steels at 4 K were studied. In liquid helium at 4 K, a transition in initiation stress and strain as a function of strain rate was identified. In gaseous helium at 4 K, discontinuous yielding began at significantly lower stresses and strains than in liquid helium. Results are interpreted in terms of macroscopic heat balances and localized generation of heat from moving dislocations.

## INTRODUCTION

At very low temperatures, the specific heat and the thermal conductivity of stainless steels and many other alloys are very low. Thus, it is difficult to maintain the low temperature of the alloy when a source of heat is applied. During plastic deformation in liquid helium (4 K), only a small amount of the applied energy is stored in the alloy as defect formation energy; most is converted to heat, which must be removed. Reed and Walsh<sup>1</sup> described two distinct modes of transient heating that occurred as a function of strain rate during straining of austenitic steels at 4 K: thermal waves and thermal spikes. Thermal waves were associated with macroscopic (overall) warming of the specimen; thermal spikes were associated with discontinuous yielding and microscopic (local) specimen heating. They concluded that (1) relatively little (~10%) energy is stored; (2) much more heat is transferred from the deforming tensile specimen to the liquid than is conducted through the specimen ends; and (3) at high strain rates, the transition from nucleate to film-boiling heat transfer at the liquid interface causes thermal waves, an indication of overall specimen heating.

Thermal spikes as high as 60 K have been reported.<sup>1-5</sup> Associated with discontinuous (serrated) yielding, they occur at low strain rates. In tests in which thermal spikes are prevalent, the temperature of the deforming specimen remains at 4 K prior to the strain instability; no precursor temperature increases have been detected. We think discontinuous yielding may be a two-step process: (1) the triggering event that probably occurs at the microscopic level and (2) the subsequent dislocation avalanche at very high



strain rates at the macroscopic level. This subsequent plastic deformation occurs in bands across the specimen, similar to Lüders bands. The bands are about  $10^{-2}$  m wide with a typical extension of  $1.3 \times 10^{-4}$  m. The local temperature rise, confined to the strained region, is adequately described by assuming adiabatic conditions.

Previous studies<sup>1-5</sup> of discontinuous yielding in austenitic stainless steels described temperature rises of about 50 K in the deformation region with very high local strain rates. Attempts have been made to analyze and characterize discontinuous yielding at very low temperatures. Originally, Basinski<sup>6</sup> reported low-temperature discontinuous yielding in aluminum alloys and suggested that localized temperature rises, due to adiabatic conditions, caused unstable plastic deformation. Later, on the basis of more macroscopic temperature measurements (maximum of 55 K during serration), he argued that thermal instability, rather than mechanical instability, was the basis for the nucleation event.<sup>7</sup> This fundamental question has not yet been resolved, because nucleation events probably have microscopic origins. Like Basinski, Medvedev<sup>8</sup> suggested a thermal heat balance between work of deformation and conduction from the specimen to account for the discontinuous yielding process. Using computer simulation, Kubin et al.<sup>9</sup> described the low-temperature mechanical instabilities in terms of heat transfer to the thermal bath and an Arrhenius rate equation. Shibata et al.<sup>10</sup> also used computer simulation of unstable low-temperature deformation and found a balance between heat and mechanical instabilities similar to that described by Kubin et al., although a more realistic model for the stress dependence of the exponential term was assumed. Like Reed and Walsh,<sup>1</sup> they considered three elements in the heat balance: stored energy, heat conduction along the specimen, and heat conduction to the coolant. Their results indicate that a triggering event is unnecessary—the dynamics between mechanical work and the thermal balance account for mechanical-thermal instabilities.

Moving dislocations cause local heating of alloys. Eshelby and Pratt<sup>11</sup> derived an expression (based on an internal source of dislocations) for the local temperature rise at a distance,  $r_d$ , from the dislocation in a metal:

$$\Delta T = \frac{b\sigma\bar{v}}{2\pi\kappa} \ln \left( \frac{2\kappa}{\bar{v}r_d} \right), \quad (1)$$

where  $b$  is the Burgers vector;  $\sigma$ , the applied stress;  $\bar{v}$ , the average dislocation velocity;  $\kappa$ , the thermal diffusivity [thermal conductivity ( $\lambda$ ) divided by the specific heat per unit volume of the metal]. For a number of dislocations,  $n$ , spaced over a distance,  $\ell$ , on a glide plane at low temperatures,  $\Delta T$  is estimated to be

$$\Delta T = n \frac{b\sigma\bar{v}}{2\pi\lambda} \ln \left( \frac{2n\kappa}{\bar{v}\ell} \right). \quad (2)$$

Armstrong et al.<sup>12</sup> pointed out that more localized slip-band formation, promoting fewer slip bands per active dislocation, results in larger temperature rises in Eq. 2. Nonuniform slip, confined to slip bands, is a trait of face-centered cubic metals at low temperatures. The degree of slip localization is thought to be affected by the stacking-fault energy.

The local heating of dislocation ensembles was studied by Malygin.<sup>13</sup> For absorption of heat along the moving dislocations, he considered only the local heat capacity, not the local thermal conductivity. Using a Green's function, he calculated individual temperature rises of  $10^{-2}$  K for moving dislocations, a value less than Eshelby and Pratt's estimate from Eq. 2. For an active Frank-Read source, Malygin calculates that the amount of heat generated is  $Q = Q_i n/3$ , where  $Q_i$  is the heat generated by the leading loop and  $n$  is the number of loops. For a slip band with active sources on close, parallel slip planes, local temperature rises were estimated:

$$\Delta T = Wt'/C_V, \quad (3)$$

where  $t'$  is the time,  $C_V$  is specific heat per unit volume, and  $W = \sigma_k \dot{\epsilon}$ ;  $\sigma_k = B\bar{v}/b$  and  $\dot{\epsilon} = b\rho_m\bar{v}$ ;  $\rho_m$  represents the mobile dislocation density, and  $B$ , a viscous drag stress. Temperature rises of 5 to 50 K can be calculated for low specific heat and high dislocation velocities.

In this paper, we use the results of more than one hundred tensile tests of austenitic stainless steels at 4 K to characterize stress and strain for the initiation of discontinuous yields. For AISI alloy types 304L, 304HN, 310, and 316LN in liquid helium and types 310 and 304HN in a gaseous helium environment, initiation stress and strain for discontinuous yielding were measured at various strain rates. Alloy 304L has low strength and low austenite stability; under plastic deformation, it transforms easily to martensite. Alloys 304HN and 316LN are nitrogen-strengthened high-strength alloys; under large plastic deformations, they transform slightly to martensite. Alloy 310 is completely stable. We report our measurements in the form of heat-balance calculations.

## EXPERIMENTAL PROCEDURES

Specimens of alloys 304L and 310 were machined from 1.9-cm-diameter bar stock; specimens of alloy 304HN, from a 16-cm-diameter billet; specimens of alloy 316LN, from 5.0-cm-thick plate. Alloys 304L, 304HN, and 316LN were annealed; alloy 310 was tested in the partially sensitized condition. Actual chemical compositions for these alloys were given previously;<sup>1</sup> nominally, in wt.% they are: alloy 304L, 18Cr-10Ni-1Mn-0.02C-0.03N; alloy 304HN, 20Cr-8Ni-2Mn-0.06C-0.28N; alloy 310, 25Cr-21Ni-2Mn-0.09C-0.03N; alloy 316LN, 18Cr-10Ni-1Mn-0.02C-0.16N. The heat-treatment schedules, hardness, grain size,<sup>1</sup> and microstructures<sup>14</sup> of the alloys were also discussed previously. Round, tensile specimens<sup>14</sup> were machined to a 6.35-mm diameter along a gage length of 41.9 mm, increasing with a radius of 9.52 mm to 12.7-mm-diameter threaded ends. The entire specimen length was 71.4 mm.

The cryostat, strain-gage extensometers, and temperature-sensing equipment have been described elsewhere.<sup>14,15</sup> Most tests were conducted in boiling liquid helium; a few tests were conducted in gaseous helium (at 4 K) with liquid-helium reservoirs above and below the specimen to regulate the temperature. Elongation was measured over a specimen gage length of 3.8 cm. Crosshead rates were varied from 0.001 to 2 cm/min. Reported strain rates (from  $4 \times 10^{-6}$  to  $4 \times 10^{-3} \text{ s}^{-1}$ ) refer to the nominal rate of plastic deformation within the reduced section of the specimens.



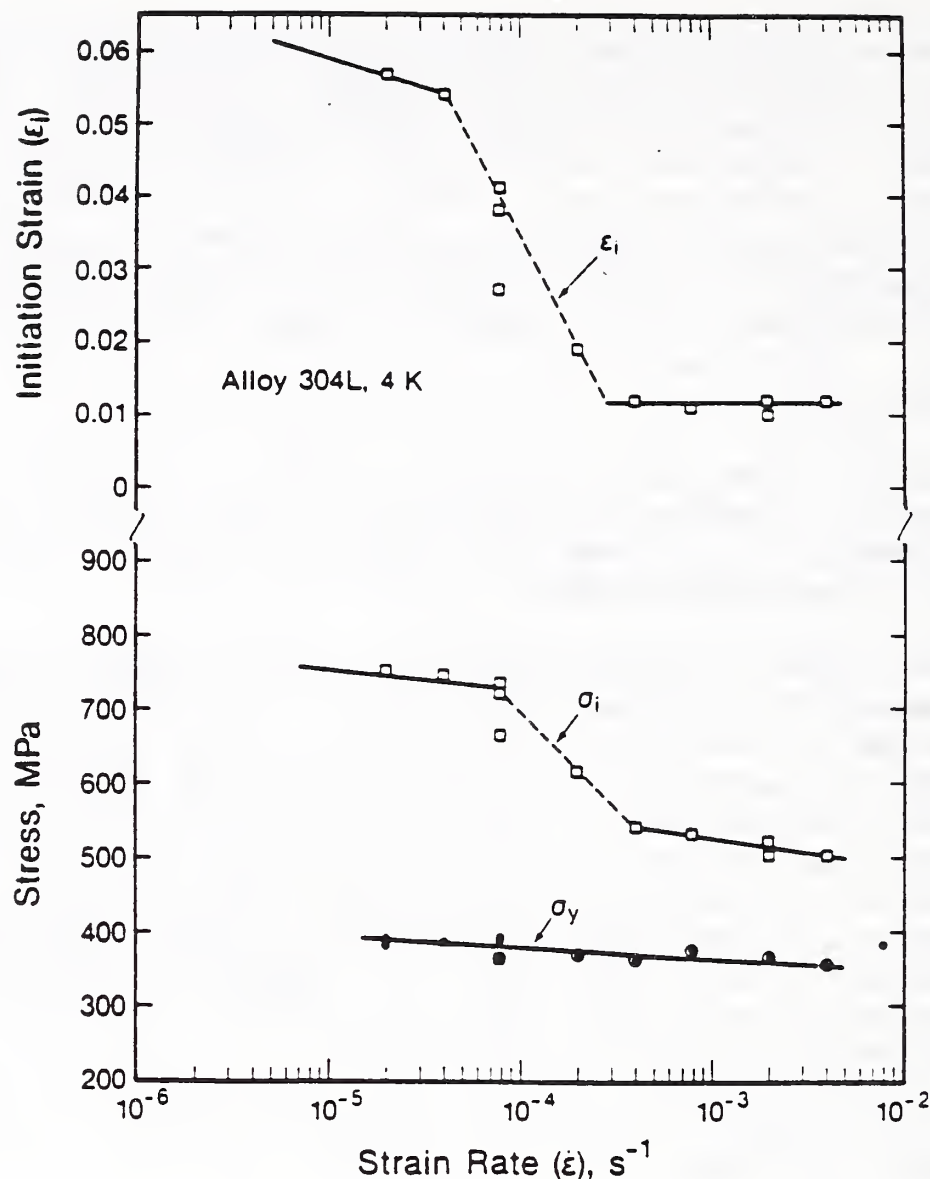


Figure 1. The stress and strain at initiation of discontinuous yielding and the tensile yield strength versus strain rate at 4 K for alloy 304L.

## EXPERIMENTAL RESULTS

For all alloys tested, the stress-strain curves at 4 K were initially smooth and, subsequently, discontinuous yielding initiated. The effects of strain rate on the stress,  $\sigma_i$ , and strain,  $\epsilon_i$ , to initiate the first observable discontinuous yield in boiling liquid helium are shown in Figs. 1 through 3 for alloys 304L, 310, and 316LN, respectively. Clearly, at low and high strain rates,  $\sigma_i$  is essentially independent of strain rate; at intermediate strain rates, a transition occurs. All three alloys behave similarly. Alloy 310 was tested in gaseous helium, as well as liquid helium, at 4 K. Both  $\sigma_i$  and  $\epsilon_i$  were considerably less in the gaseous environment (Fig. 2); in fact, the values are comparable to the high strain-rate values that would be obtained in liquid helium. Another alloy, 304HN, was also tested at 4 K in both liquid and gaseous helium at a low strain rate ( $8 \times 10^{-5} s^{-1}$ ). The results are similar: in liquid,  $\sigma_i = 1730$  MPa; in gas,  $\sigma_i = 1440$  MPa. The yield strength values,  $\sigma_y$  (0.2% offset), were not affected by the state of the cryogen.

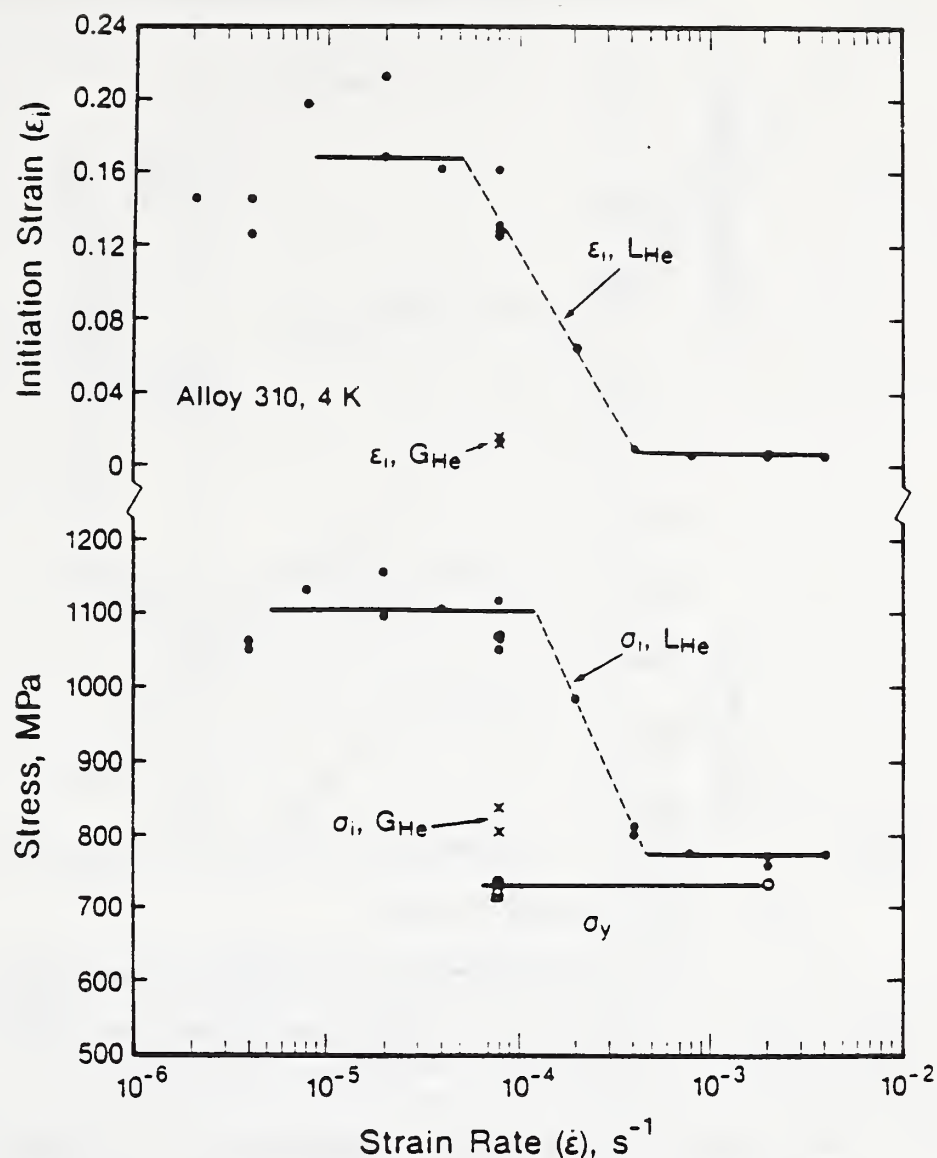


Figure 2. The stress and strain at initiation of discontinuous yielding and the tensile yield strength versus strain rate at 4 K in liquid helium ( $L_{He}$ ) for alloy 310. Also included are measurements from testing in gaseous helium ( $G_{He}$ ) at 4 K.

The absolute values of  $\sigma_i$  for the same  $\dot{\epsilon}$  range vary appreciably among alloys. However,  $\sigma_i$  does correlate with  $\sigma_y$ . Figure 4 shows  $\sigma_i$  versus  $\sigma_y$  for more than eighty measurements of austenitic steels in liquid helium. Some steels are Fe-Cr-Ni-base alloys with varying carbon and nitrogen content; some are high-manganese austenitic steels, usually with chromium and nickel added; and many are experimental alloys from previous studies at the National Bureau of Standards. The  $\sigma_i$ - $\sigma_y$  correlation is quite good; the solid line depicts the relation (in MPa)

$$\sigma_i = 320 + \sigma_y. \quad (4)$$

All values were measured at low  $\dot{\epsilon}$  within the high- $\sigma_i$ , low- $\dot{\epsilon}$  plateaus illustrated in Figs. 1 through 3. The dashed lines were constructed from the high- $\dot{\epsilon}$ -plateau measurements shown in these figures. In essence, increased strain rates reduce the constant (to 110 from 320 MPa) in Fig. 4 and Eq. 4 but do not significantly change the linear dependence of  $\sigma_i$  on  $\sigma_y$ .

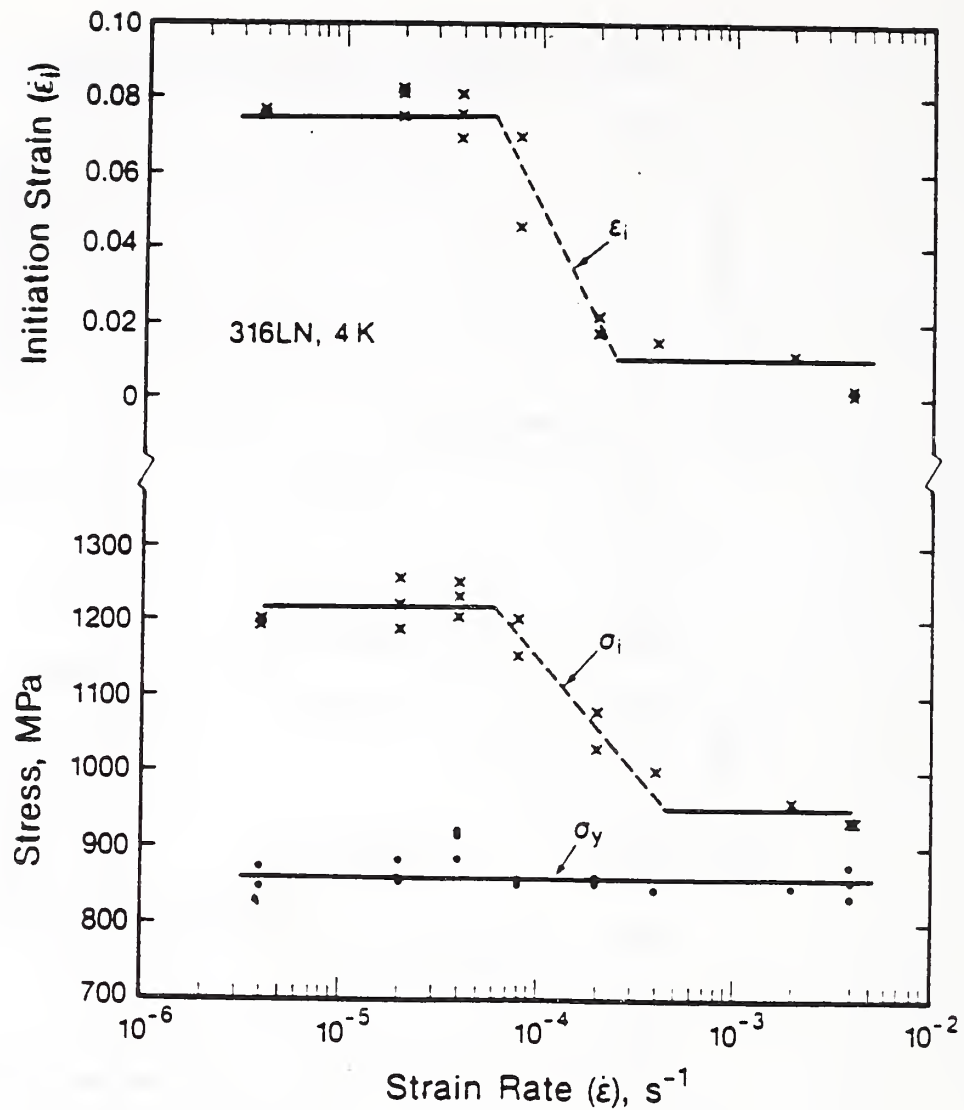


Figure 3. The stress and strain at initiation of discontinuous yielding and the tensile yield strength versus strain rate at 4 K for alloy 316LN.

## DISCUSSION

### Implications of the Experimental Results

From the experimental results, we consider the following points to be characteristic of discontinuous yielding:

1. Both  $\sigma_i$  and  $\epsilon_i$  differ radically in alloys 310 (Fig. 2) and 304HN when measured in gaseous and liquid environments, even though the strain rate and nominal test temperature were equivalent. This strongly implies that surface heat transfer plays a major role in the initiation of discontinuous yielding.
2. The transition from high  $\sigma_i$  (and  $\epsilon_i$ ) at low  $\dot{\epsilon}$  to low  $\sigma_i$  (and  $\epsilon_i$ ) at high  $\dot{\epsilon}$  may be interpreted in two ways: (1) The high  $\dot{\epsilon}$  effectively increases the dislocation velocity:

$$\dot{\epsilon} = b\bar{v}\rho_m, \quad (5)$$



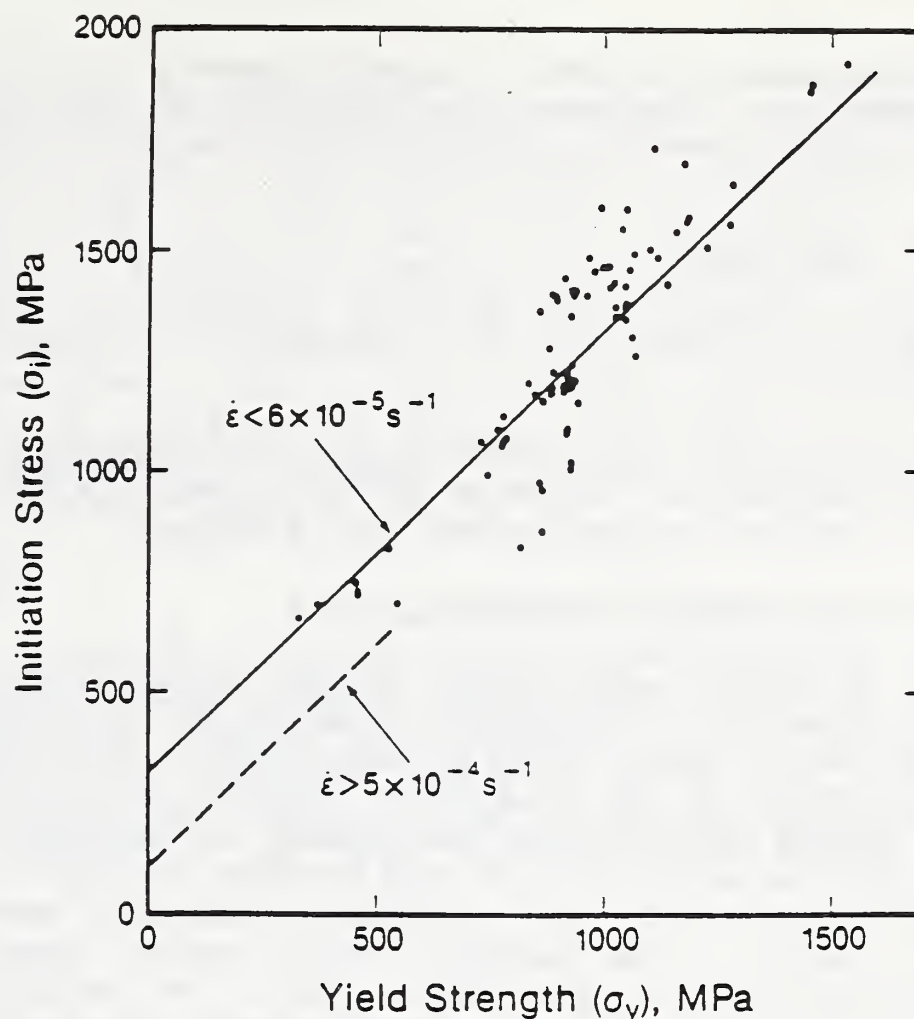


Figure 4. The stress at initiation of discontinuous yielding versus yield strength for many austenitic steels at 4 K in liquid helium at  $\dot{\epsilon} < 6 \times 10^{-5} \text{ s}^{-1}$ . Dashed line is an estimate of dependency of  $\sigma_i$  on  $\sigma_y$  for  $\dot{\epsilon} > 5 \times 10^{-4}$  from the data for alloys 304L, 310, and 316LN shown in Figs. 1 through 3.

and thus increases the internal dislocation heating. (2) The high  $\dot{\epsilon}$  increases the rate of heat generated from the energy of deformation:

$$E_{\text{def}} = \dot{\epsilon} \sigma V, \quad (6)$$

where  $V$  is the volume of the deformed region and  $E_{\text{def}} = \dot{\epsilon} E_{\text{def}}$ , following the nomenclature used by Reed and Walsh.<sup>1</sup> This increased heating rate may result in a different mode of boiling heat transfer (film rather than nucleate) to the liquid helium in a manner like that suggested for the occurrence of thermal waves at high  $\dot{\epsilon}$ .<sup>1</sup>

3. The dependence of  $\sigma_i$  on  $\sigma_y$  (Fig. 4, Eq. 4) is very interesting. Consider that the flow strength,  $\sigma$ , is the sum of contributions from strain hardening,  $\sigma_d$ , and solution hardening,  $\sigma_f$ :

$$\sigma = \sigma_d + \sigma_f. \quad (7)$$

The solution hardening contribution,  $\sigma_f$ , may be equated to the yield strength,  $\sigma_y$ . At the initiation of the first discontinuous yield,  $\sigma$  equals  $\sigma_i$ . Thus,  $\sigma_d$  has a constant value of 320 MPa (from Eqs. 4 and 7). This constancy of  $\sigma_d$ , which represents dislocation-dislocation interactions, suggests that, for initiation of

discontinuous yielding, a constant number of dislocations must be accumulated. The usual representation of the effect of the total dislocation density,  $\rho_t$  (created by plastic deformation), on stress is

$$\sigma_d = \alpha G b \rho_t^{1/2}, \quad (8)$$

where  $\alpha$  is a constant,  $G$  is the shear modulus, and  $b$  is the Burgers vector.

These implications require more careful consideration, but first, to assist in understanding the discussion following, we briefly discuss heat transfer from the specimen to gaseous and liquid helium.

#### Surface Heat-Transfer Mechanisms at 4 K

Two different heat-transfer regimes encountered in steady-state pool boiling of helium at atmospheric pressure are indicated in Figure 5. This figure presents typical boiling heat-transfer data abstracted from two review papers.<sup>16,17</sup> It also shows a typical curve for heat transfer to gaseous helium at 4 K, using the Raithby and Hollands's correlation for laminar and turbulent flow at high Rayleigh numbers.<sup>18</sup> Heat-flux rate,  $Q/A$ , is plotted against  $\Delta T$ , the temperature difference between the solid surface and the liquid. In the nucleate-boiling region, vapor bubbles are created at nucleation sites on the solid surface. In the film-boiling region, bubbles form so rapidly that a vapor blanket is established that prevents liquid from contacting the surface. The heat-transfer coefficient,  $h$  ( $= Q/A \cdot \Delta T$ ), is therefore lower than in the nucleate region. When the peak nucleate-boiling heat-flux rate,  $(Q/A)_{\max}$ , is reached, the difference in temperature,  $\Delta T$ , between the specimen and the liquid may suddenly increase by an order of magnitude.

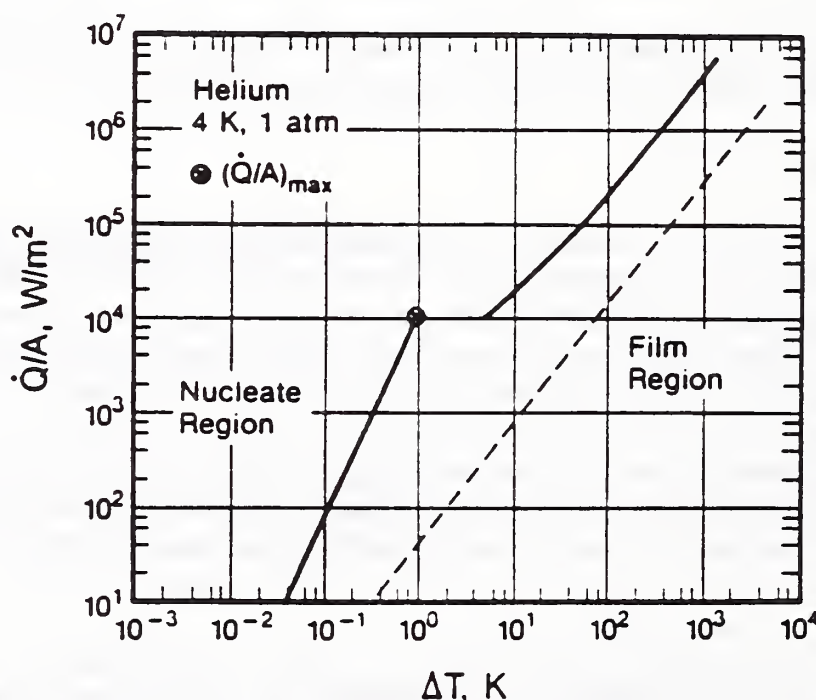


Figure 5. Typical nucleate-boiling and film-boiling heat transfer in liquid helium at 4 K (solid line). Predicted heat transfer in gaseous helium at 4 K (dashed line).



The value of  $(Q/A)_{\max}$  is typically about  $10^4$  W/m<sup>2</sup>; it is nearly independent of  $\Delta T$  and various geometrical and surface factors, which do change the shape and position of the nucleate-boiling curve. For example, smoother surfaces with smaller asperities shift the nucleate boiling curve in Fig. 5 to the right, raising  $\Delta T$  by an order of magnitude without changing  $(Q/A)_{\max}$ .<sup>17</sup> The slope,  $d \log(Q/A)/d \log \Delta T$  can also increase.<sup>19</sup> However, a change from a horizontal to vertical heat-transfer surface may increase  $(Q/A)_{\max}$  only about 20%.<sup>16,19</sup> By reducing the size of miniature heaters in liquid nitrogen, a decrease in  $(Q/A)_{\max}$  was attained; for normal heaters, size was not a factor.<sup>19</sup> Increases in  $(Q/A)_{\max}$  to  $10^5$  W/m<sup>2</sup> or more have been observed only with pulsed heat inputs,<sup>20</sup> that is, transient rather than steady-state heat-transfer conditions.

### Surface Heat Transfer

The influence of the test environment on the low-temperature discontinuous-yielding process implies that the energy-heat balance is not simply confined to heat generation from moving dislocations in localized bands. The deformation energy,  $E_{\text{def}}$ , is either stored as energy,  $E_{\text{SE}}$ , or dissipated as heat, and the dominant heat-conduction path is through the specimen surface to the test environment.<sup>1,9,10</sup> Thus, since energy is conserved at any instant of time,<sup>1</sup>

$$E_{\text{def}} = E_{\text{SE}} + Q_s, \quad (9)$$

where  $Q_s$  is the heat-dissipation and  $E_{\text{SE}} = E_{\text{SE}}/\dot{\epsilon}$ .

Using a macroscopic approach, we can calculate  $E_{\text{def}}$  as  $\sigma_i \dot{\epsilon}_i V$ , where  $V$  is the deformed specimen volume to be considered.<sup>1</sup> From the values for alloy 310 (Fig. 2), for example when  $\dot{\epsilon}_i$  is  $8 \times 10^{-5}$  s<sup>-1</sup>,  $\sigma_i$  equals 1100 MPa and a possible deformed volume is  $\pi r^2 t$ , where  $r$  is the specimen radius and  $t$  is the "activated" thickness of the specimen cross section to be considered. For comparison with Fig. 5,  $E_{\text{def}}/A_s$  needs to be calculated ( $A_s = 2\pi r t$  is the surface area of heat transfer). For these data,  $E_{\text{def}}/A_s = 221$  W/m<sup>2</sup>, a rate well below the critical value,  $(Q/A)_{\max}$ , of about  $10^4$  W/m<sup>2</sup> for the transition from nucleate-boiling to film-boiling heat transfer (Fig. 5). A local warming of about 0.2 K is predicted by Fig. 5 for these conditions when the specimen is tested in liquid helium. A heat transfer rate of 167 W/m<sup>2</sup> is calculated for the gaseous-helium condition (from Fig. 2,  $\dot{\epsilon}_i = 8 \times 10^{-5}$  s<sup>-1</sup>,  $\sigma_i = 830$  MPa); Fig. 5 shows that this corresponds to a local temperature rise of about 4 K. These diverse results suggest that a different approach is needed to rationalize the measurements in liquid and gas.

Consider the heat-transfer process across a portion of one grain (e.g., a slip band) at the specimen surface. Microscopically, the heat per unit time and length from a moving dislocation is  $b\sigma\bar{v}$ .<sup>11</sup> We consider an ensemble of  $n$  moving dislocations (within a slip band); then the heat dissipation,  $Q$ , from this ensemble is simply  $nb\sigma\bar{v}l_d$  ( $l_d$  = average dislocation length). The number of moving dislocations within the local area ( $A_l$ ) of concern may be conservatively estimated from the average mobile dislocation density,  $\rho_m$ , as  $n = \rho_m \cdot A_l$ . Here,



$$\rho_m = \rho_t - \rho_n, \quad (10)$$

with  $\rho_n$  the number of dislocations that have been generated but probably have become immobilized in networks. The applied stress minus the stress at which dislocations begin to generate (taken here as the yield stress) is, from Eqs. 7 and 8,

$$\sigma - \sigma_y = \alpha G b \rho_t^{1/2}. \quad (11)$$

When Eqs. 10 and 11 are combined and  $\alpha$  ( $\sim 1$ ) is dropped,

$$\rho_m = \sigma_d^2 / (G b)^2 - \rho_n. \quad (12)$$

Our transmission-electron-microscopy studies of austenitic stainless steels with plastic-deformation strains less than about 0.10 found little dislocation-network formation. Therefore, we assume that  $\rho_m \gg \rho_n$  and  $\rho_n$  can be eliminated from Eq. 12. Then,

$$Q = \frac{\sigma_d^2 \sigma_i \bar{v} \ell_d A_\ell}{G^2 b} \quad (13)$$

With the local microscopic heat-flux rate represented by  $Q/A_s$ , the heat-transfer area from the specimen is represented by  $dt$  ( $d$  = average grain size;  $t$  = width of the dislocation slip band), and  $A_\ell = \pi d^2/4$  and  $\ell_d \sim t$  ( $\sim 10 \mu\text{m}$ ). Using these relations with Eq. 13, we obtain

$$\frac{Q}{A_s} = \frac{\pi}{4} \frac{\sigma_d^2 \sigma_i \bar{v} d}{G^2 b} \quad (14)$$

The average dislocation velocity  $\bar{v}$  was estimated by Alden<sup>21</sup> to be about  $10^{-6}$  m/s after the yield strength is reached at 295 K. Suzuki<sup>22</sup> related dislocation velocity to  $\exp B(\sigma - \sigma_0)$  with  $B$  a constant and  $\sigma_0$  related to the athermal stress contribution. More commonly, Vreeland<sup>23</sup> and many others considered that  $\bar{v} \sim \sigma^m$ , with the exponent,  $m$ , having values up to 40 for face-centered cubic metals. Alden used  $\bar{v} = \sigma_c / \tau_0$  with  $\sigma_c$  an effective stress containing a network-hardening term subtracted from the applied stress and  $\tau_0$  a viscous drag constant. From Eq. 14 and  $\bar{v} = 10^{-6}$  m/s,  $G = 80$  GPa at 4 K, and  $b = 3 \times 10^{-10}$  m;  $Q/A_s$  equals  $4.6 \times 10^3$  W/m<sup>2</sup>. This heat-flux rate is very close to the critical value for triggering the transition from nucleate-boiling to film-boiling heat transfer (Fig. 5).

The local internal specimen heating from moving dislocations may also be estimated using the model of Eshelby and Pratt.<sup>11</sup> To use Eq. 2 to calculate the local temperature increase, we consider that  $\sigma = \sigma_i$ ,  $\bar{v} = 10^{-6}$  m/s,  $b = 3 \times 10^{-10}$  m, and that at 4 K,  $\kappa = 1.7 \times 10^{-5}$  m<sup>2</sup>/s and  $\lambda = 0.5$

W/(m·K). The number of moving dislocations,  $n$ , is again related to the strain-hardening component of the flow stress as  $n = \rho_m \cdot A_\ell$  and  $\rho_m = \sigma_d^2 / (Gb)^2$  following arguments previously presented. Here,  $A_\ell$  represents the area encompassing the moving dislocations and is taken as  $\pi d^2/4$  ( $d = 10^{-4}$ ), the equivalent of a slip band extending through a large grain. With these assumptions and data,  $\Delta T$  equals 47 K, a high value. Ideally, as the temperature rises,  $\lambda$  increases, and  $\kappa$  remains approximately constant, resulting in a reduced  $\Delta T$ .

These models and calculations suggest that (1) at the microscopic level, significant local temperature increases are achievable from moving dislocations in low-conductivity materials (at low temperatures) and (2) at low temperatures in helium gas or liquid, solid or surface heat-transfer rates are not sufficient to keep up with the heat generated by the moving dislocations.

## SUMMARY

At the strain rates at which we observed initiation of discontinuous yielding, the calculated macroscopic specimen heating was not large enough to trigger the transition from nucleate to film boiling and thus induce a sudden, large temperature increase in the specimen. However, on a microscopic scale, we have shown that significant local temperature rises ( $\sim 47$  K) may be induced by motion of multiple dislocations at 4 K in austenitic steels. The heat flux from moving dislocations in surface grains is of the same magnitude as the critical heat-transfer flux for the transition from nucleate to film boiling. This suggests that the transition in initiation stress ( $\sigma_i$ ) and strain ( $\epsilon_i$ ) for discontinuous yielding is caused by local changes in the liquid heat-transfer mechanism. It also suggests that the lower  $\sigma_i$  and  $\epsilon_i$  values associated with tests in gaseous helium at 4 K are directly attributable to the difference in heat-transfer coefficients in helium liquid (nucleate boiling) and helium gas.

These conclusions imply that, after sufficient flow stress is attained, the deforming specimen contains a multitude of local hot spots (slip bands). As the specimen continues to deform,  $Q/A$  eventually increases beyond  $(Q/A)_{\max}$  and triggers the transition to film heat transfer, abruptly changing the local temperature in the disturbed region.

The constancy of dislocation-interaction stress,  $\sigma_d$ , for the initiation of discontinuous yields for a large number of austenitic steels suggests that a minimum number of dislocations are required to initiate the local rise in temperature. This minimal dislocation density is independent of stacking-fault energy, type and number of solutes, and yield-strength level since a wide variety of austenitic steels are represented in the data. This condition implies a local heating process that depends on dislocation generation, rather than on pile-up stresses that are more dependent on the above material parameters.



## ACKNOWLEDGMENTS

This work was partially supported by the Office of Fusion Energy, U.S. Department of Energy. We thank V. D. Arp for essential consultations. L. A. Delgado and R. P. Walsh carefully conducted most of the tensile measurements.

## REFERENCES

1. R. P. Reed and R. P. Walsh, Tensile strain-rate effects in liquid helium, in: "Advances in Cryogenic Engineering - Materials," vol. 34, Plenum, New York (1988), pp. 199-208.
2. D. T. Read and R. P. Reed, Heating effects during tensile tests of AISI 304L stainless steel at 4 K, in "Advances in Cryogenic Engineering - Materials," vol. 26, Plenum, New York (1980), pp. 91-101.
3. T. Ogata and K. Ishikawa, "Workshop on Standardization of Fracture Toughness Testing of Low Temperature Structural Materials," National Research Institute for Metals, Tsukuba Labs., Ibaraki, Japan (March 1986).
4. W. G. Dobson and D. L. Johnson, Effect of strain rate on measured mechanical properties of stainless steel at 4 K, in: "Advances in Cryogenic Engineering - Materials," vol. 30, Plenum, New York (1984), pp. 185-192.
5. N. Yamagami, Y. Kohsaka, and C. Ouchi, "Report to Joint U.S./Japan Working Group on Structural Materials at Low Temperatures," Technical Research Center, Nippon Kokan K.K., Kawasaki, Japan (October 1986).
6. Z. S. Basinski, The instability of plastic flow of metals at very low temperatures, Proc. Roy. Soc. A240:229-242 (1957).
7. Z. S. Basinski, The instability of plastic flow of metals at very low temperatures. II, Aust. J. Phys. 13:354-350 (1960).
8. E. M. Medvedev, On the character of low temperature discontinuous plastic deformation of metals, Cryogenics 16: 533-536 (1976).
9. L. P. Kubin, Ph. Spiess, and Y. Estrin, Computer simulation of the low temperature instability of plastic flow, Acta Metall. 30:385-394 (1982).
10. K. Shibata, H. Sakamoto, K. Fujita, and T. Fujita, Computer simulation of serration near liquid helium temperatures in: "Advances in Cryogenic Engineering - Materials," vol. 34, Plenum, New York (1988), pp. 217-223.
11. J. D. Eshelby and P. L. Pratt, Note on the heating effect of moving dislocations, Acta Metall. 4:560-562 (1956).
12. R. W. Armstrong, C. S. Coffey, and W. L. Elban, Adiabatic heating at a dislocation pile-up avalanche, Acta Metall. 30:2111-2116 (1982).
13. G. A. Malygin, Local heating in dislocation ensembles at low temperatures, Sov. J. Low Temp. Phys. 5(11):633-637 (1979).
14. R. P. Reed and R. P. Walsh, Tensile strain-rate effects in liquid helium, in: "Materials Studies for Magnetic Fusion Energy Applications at Low Temperatures - X," NBSIR 87-3067, National Bureau of Standards, Boulder, Colorado (1987), pp. 9-30.
15. R. P. Reed and R. P. Walsh, Low temperature tensile characteristics of copper and aluminum, in: "Materials Studies for Magnetic Fusion



- Energy Applications at Low Temperatures - IX," NBSIR 87-3050, National Bureau of Standards, Boulder, Colorado (1986), pp. 107-140.
16. E. G. Brentari, P. S. Giarratano, and R. V. Smith, "Boiling Heat Transfer for Oxygen, Nitrogen, Hydrogen, and Helium," NBS Technical Note 317, National Bureau of Standards, Boulder, Colorado (1965).
  17. W. B. Bald and T-Y. Wang, The nucleate pool boiling dilemma, Cryogenics 16:314-315 (1976).
  18. R. M. Fand and J. Brucker, A correlation for heat transfer by natural convection from horizontal cylinders that accounts for viscous dissipation, Int. J. Heat Mass Trans. 26:709-726 (1983).
  19. T. H. K. Frederking, Cryogenic heat transfer: He<sup>4</sup> Kapitza conductances including phase change effects, in: "Heat Transfer 1982," vol. 1, Hemisphere Publishing Corp., Washington (1983), pp 323-342.
  20. L.-H. Lin and T. H. K. Frederking, Influence of the Kapitza resistance on nucleate boiling of liquid helium, Lett. Heat Mass Trans. 9:473-478 (1982).
  21. T. H. Alden, Theory of mobile dislocation density: application to the deformation of 304 stainless steel, Metall. Trans. A 18A:51-62 (1987).
  22. T. Suzuki, Dislocation motion and yield stress in pure copper and its dilute alloys, in: "Dislocation Dynamics," McGraw-Hill, New York (1968), pp. 551-572.
  23. T. Vreeland, Dislocation velocity in copper and zinc, in: "Dislocation Dynamics," McGraw-Hill, New York (1968), pp. 529-549.





## INFLUENCE OF INTERSTITIAL CONTENT ON FRACTURE TOUGHNESS

P.T. Purtscher and R.P. Reed  
Fracture and Deformation Division  
National Institute of Standards and Technology  
Boulder, Colorado

The effects of interstitial content on tensile properties, martensitic transformation, and inclusion content are examined in relationship to the measured fracture toughness of austenitic stainless steels at cryogenic temperatures. Metallographic sections show that void nucleation occurs ahead of a crack only after the applied  $J$  exceeds a large fraction of the measured toughness,  $J_{Ic}$ . A stress intensity factor is calculated for void nucleation from a simple model that considers the yield strength and inclusion spacing.

### INTRODUCTION

Increasing the interstitial carbon and nitrogen content increases the yield strength of austenitic steels at low temperatures. The high strength combined with high elastic modulus and good thermal properties make these steels attractive for use in cryogenic structures. However, to build an efficient, yet safe structure, high fracture toughness is required.

Experience<sup>1</sup> has shown that there is an empirical relationship between yield strength ( $\sigma_y$ ) and fracture toughness ( $K_{Ic}$ ) for austenitic steels at 4 K:

$$K_{Ic} = 500 - 0.3\sigma_y \pm 20 \text{ MPa}/\text{m} \quad [1]$$

A similar relationship is found for martensitic steels, aluminum, and titanium alloys at ambient temperatures.<sup>2</sup>

In practice, we know that other factors such as the inclusion content<sup>3,4</sup> and strain-induced martensitic transformation (TRIP effect)<sup>5-7</sup> influence ductile fracture. Research has focused on ductile fracture characteristics: void nucleation, growth, and coalescence in the complex stress state ahead of a crack. Most fundamental work has followed the Rice and Johnson approach<sup>8-10</sup> of relating the toughness to growth of voids ahead of the crack, assuming that void nucleation is relatively easy and contributed little to

---

\* Contributed to the proceedings of international conference on High Nitrogen Steels.

the magnitude of fracture toughness. Recently, we presented a model for estimating the stress intensity factor required to nucleate microvoids ahead of a crack and argued that void nucleation is significant in ductile fracture of austenitic steels at low temperatures.<sup>11</sup>

In this paper, we present new mechanical test data at 76 and 4 K for a series of seven austenitic stainless steels with varying carbon and nitrogen contents. We examine the crack path, microstructure, and void growth at loads near  $J_{Ic}$ , using the light microscope and scanning electron microscopy (SEM). The purpose of this work is to show how the interstitial content of austenitic steels influences fracture toughness.

## MATERIALS AND PROCEDURES

The base composition of the seven steels is Fe-18Cr-10Ni-1.5Mn-0.022P-0.017S-0.54Si-0.2Mo-0.2Cu. The interstitial content for each alloy is different and is shown in Table 1. All specimens were annealed at 1423 K for 2 h and water quenched.

The inclusion content of each steel was determined by examining a mechanically polished section transverse to the rolling direction in the SEM. Inclusions were counted at two different magnifications by a computer-aided technique that measured the average diameter, area, and shape factor for each inclusion.

The tensile tests of all the steels were performed according to a newly proposed standard for testing in liquid helium and are described in detail by Reed and Simon.<sup>12</sup> The strain-induced transformation was monitored during tensile testing at 76 K of steels 2, 5, and 8. The martensite content was measured magnetically. Again, the details are described by Reed and Simon.<sup>12</sup>

Fracture toughness tests were performed on all steels at 76 K and on steels 2, 3, and 8 at 4 K. Compact specimens, 25 mm thick, were machined from the annealed plates in the T-L orientation. The test procedures followed the ASTM E 813-87 standard. Additional tests on #2 and 8 at 76 K were interrupted at an applied J level  $< J_{Ic}$ .

Table 1. Interstitial Content

Table 1. Interstitial Content

Alloy	C(wt%)	N(wt%)	C+N(at%)
2	0.058	0.039	0.45
3	0.089	0.039	0.69
5	0.067	0.120	0.88
6	0.094	0.120	0.95
7	0.030	0.240	1.29
8	0.057	0.240	1.38
9	0.085	0.240	1.47

Base composition is Fe-18Cr-10Ni.



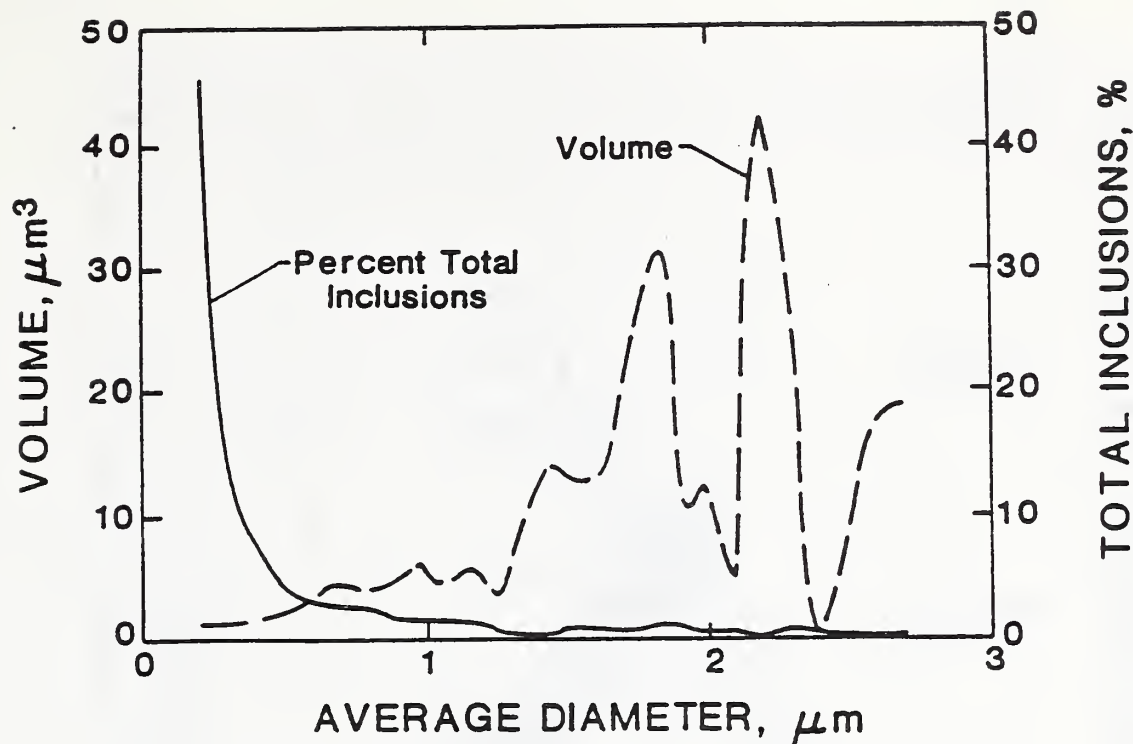


Figure 1. Histogram of the number and volume of inclusions for different average diameter inclusions.

Following the toughness testing, all specimens were sectioned in half; one half was fatigue post-cracked to reveal the fracture surface and the other half was polished so that the cross section from the center of the specimen could be examined in the SEM.

## RESULTS

The majority of inclusions have an average diameter of  $< 1 \mu\text{m}$  and are roughly spherical. The average spacing between inclusions at 400X was 46 to 53  $\mu\text{m}$  and a total area fraction was about 0.0015. The spacing at 2000X dropped to about 25  $\mu\text{m}$  because numerous small inclusions were detected. Figure 1 shows a histogram of the number and volume associated with inclusions of different average diameters. The volume was estimated by assuming an average diameter for each bracket, calculating the volume of one inclusion, and multiplying by the number of inclusions in the given bracket.

A complete summary of the tensile results are found in a separate paper.<sup>12</sup> The fracture toughness results are plotted as a function of tensile yield strength in Figure 2. The results are similar to the previous trend.<sup>1</sup>

Figure 3 shows normalized values of the percent martensite content plotted as a function of interstitial content for various amounts of applied strain in the tensile test. For steel 2, most of the transformation occurs between 10 and 30% elongation. The maximum martensite content was about 85%. For alloy 5, a similar trend is observed, but the maximum value is reduced to 60%. In alloy 8, the martensite content increases with strain, but the amount of transformation is smaller and more uniform. The trends at 4 K are similar to 76 K, but that the maximum amount of martensite which forms at 4 K is slightly lower.<sup>13</sup>



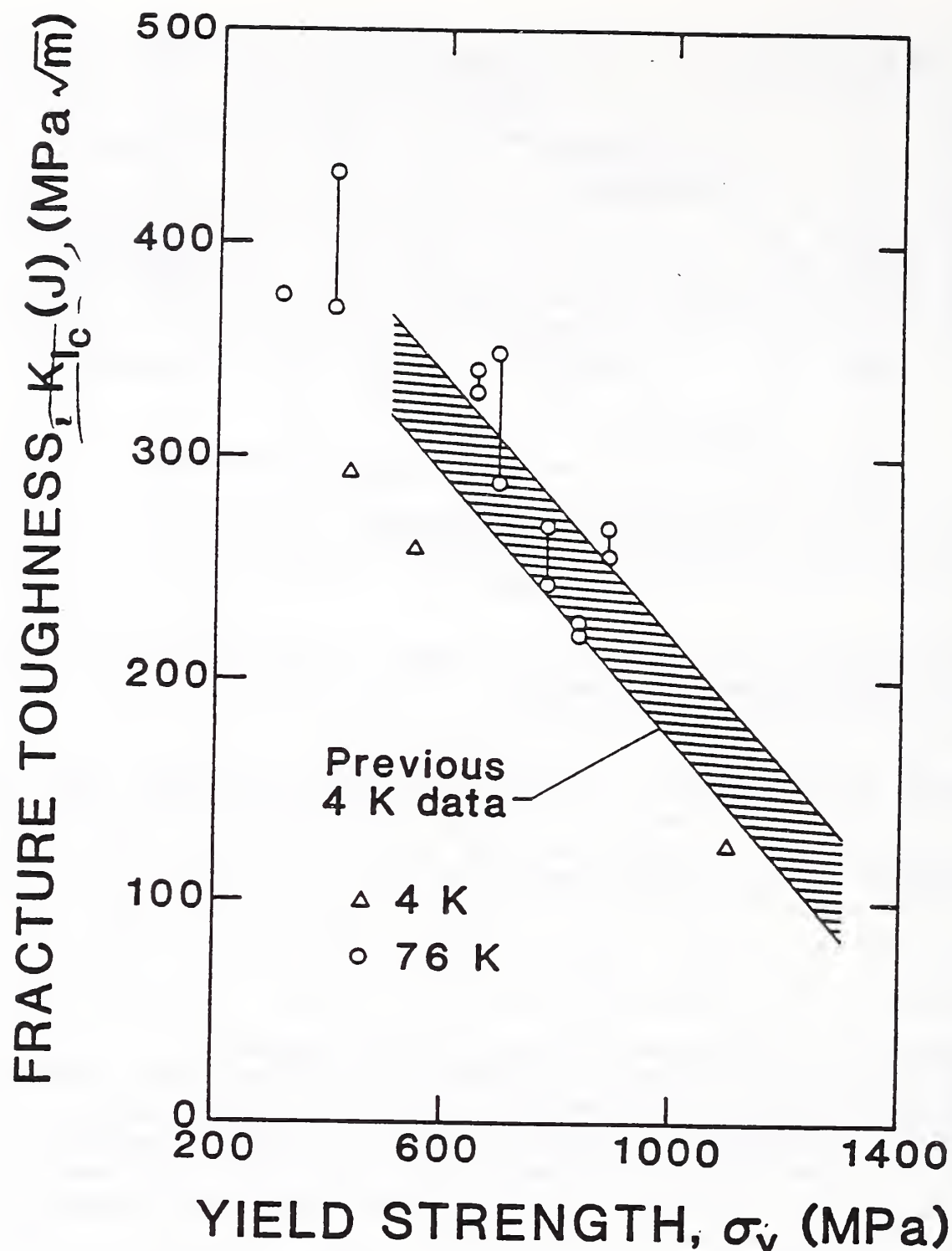


Figure 2. Fracture toughness vs. yield strength data at 76 and 4 K compared to previous 4 K data.<sup>1</sup>

Figure 4 shows the microstructure ahead of the crack in alloy 2 tested at 76 K to an applied  $J = 0.35 J_{IC}$ . The heavily deformed areas are at angles to the plane of maximum stress that lies directly ahead of the crack. The dark etching areas contain strain-induced martensite. Little martensite is present directly ahead of the crack; this implies that the plastic strain in this region was relatively low. Finite element calculations from different sources<sup>14,15</sup> indicate that the stresses directly ahead of the crack should have a maximum value of 3 to 4 times the tensile yield stress. For alloy 8 tested at 76 K (applied  $J_e = 0.8 J_{IC}$ ), the load-displacement curve was nearly linear-elastic and there was little plasticity evident at the crack tip.

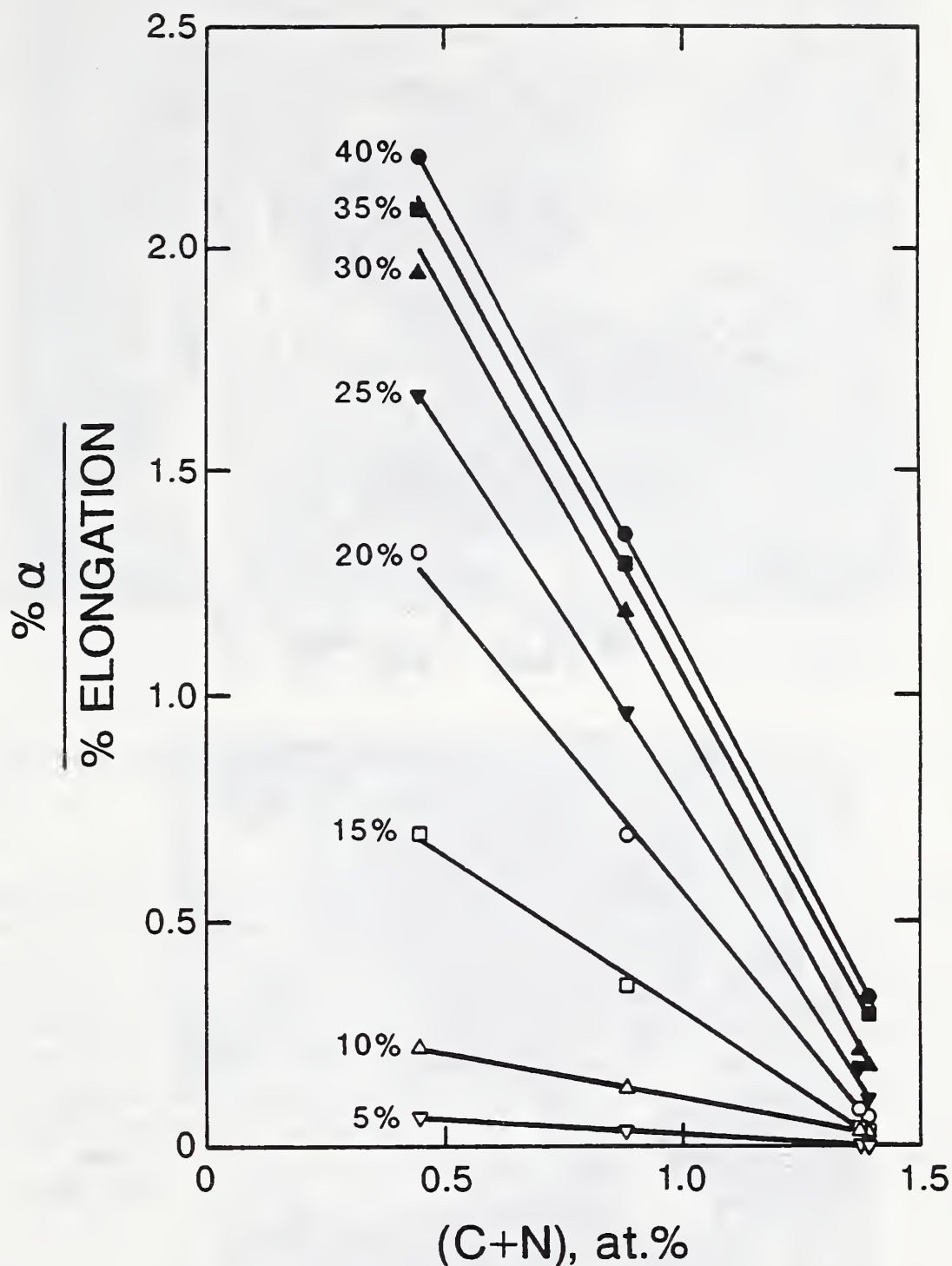


Figure 3. Martensite transformation vs. interstitial content as a function of strain at 76 K for alloys 2, 5, and 8.

The fracture surfaces from the toughness specimens tested at 76 K consisted mainly of equiaxed dimples, about 50  $\mu\text{m}$  in diameter, that nucleated from the larger inclusions in the matrix. Smaller dimples arranged in planar arrays to connect the large dimples in three dimensions in a manner that may be described as void sheet coalescence. Higher percentages of the small dimples were found on specimens from alloys 2 and 3. Figure 5 shows a representative fractograph from alloy 8 at 76 K. At 4 K, the fracture surfaces were similar, but there is a larger percentage of smaller dimples between the 50  $\mu\text{m}$  diameter dimples. No stretched zone was observed between the fatigue precracked surface and the dimpled rupture features that could be related to the measured toughness.<sup>16</sup>



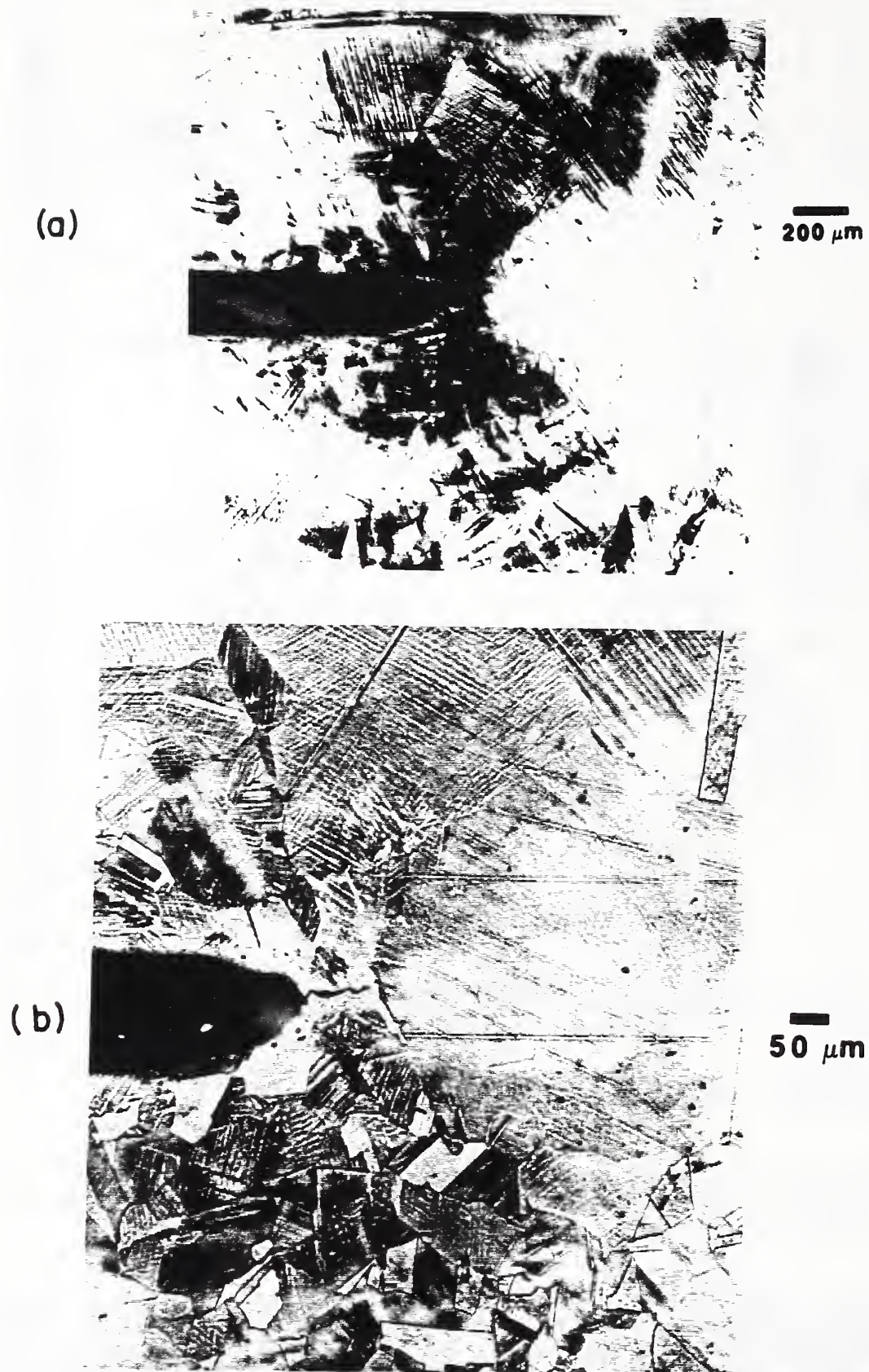


Figure 4 Etched microstructure of the area around the blunted crack tip in alloy 2. The test was interrupted at an applied energy =  $0.35 J_{Ic}$ .



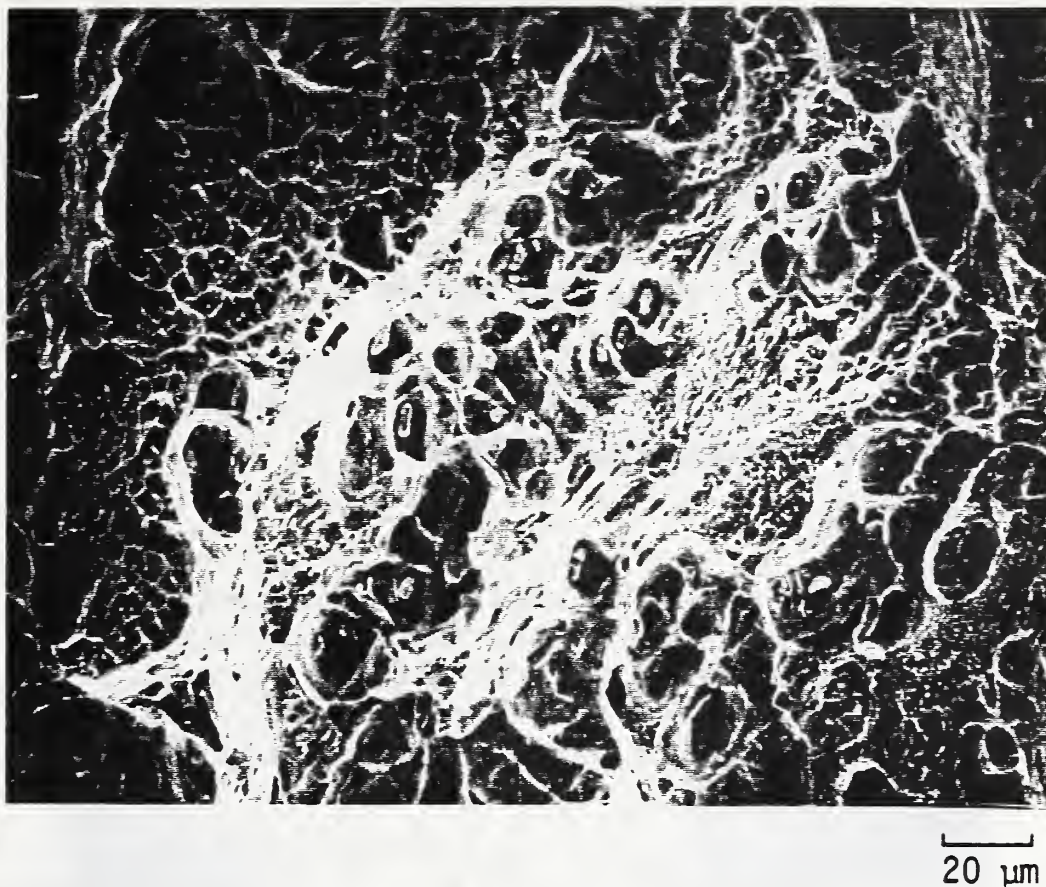


Figure 5. Fracture surface from toughness specimen of alloy 8 tested at 4 K.

Examination of sectioned specimens that had been loaded to applied energies less than  $J_{IC}$  showed that no voids could be found ahead of the crack. For alloy 2, the test was stopped at an applied  $J$  equal to approximately 35% of  $J_{IC}$ ; for alloy 8, the applied  $J$  was 80% of the critical value. The direction of crack growth in the specimens tested in the normal fashion was confined to the region of high stress, low strain ahead of the crack. Figure 6 shows a sequence of blunting and crack growth that illustrates these observations in alloy 8 tested at 76 K.

## DISCUSSION

The interstitial content influenced the tensile yield strength and the strain-induced martensitic transformation as expected,<sup>17</sup> but the inclusion content was found to be similar in all seven steels. These results are typical of all the reported cryogenic mechanical properties of austenitic steels.<sup>18</sup>

Extensive strain-induced transformation occurs during testing depending upon the test temperature and interstitial content. However, the geometries of the uniaxial tension and fracture mechanics specimens produce different stress and strain patterns. Transformation does not occur prior to void nucleation at the inclusions that will eventually form the fracture surface in the toughness test. Apparently, the local stress and strain that produce void nucleation are not influenced directly by strain-induced martensite formation.

(a)



200  $\mu\text{m}$

(b)



Figure 6 SEM micrographs of the polished cross section from crack-tip regions in alloy 8, a) test stopped at applied  $J = 0.8 J_{Ic}$  and b) test stopped at applied  $J > J_{Ic}$ .



Observations of the sectioned toughness specimens suggest that the applied energy associated with nucleation of voids accounts for a large fraction of the measured fracture toughness. The growth of voids from these larger inclusions and coalescence by nucleation and growth of smaller voids apparently requires little additional applied energy. Therefore, growth-controlled models for ductile fracture will not be very precise.

LeRoy et al.<sup>19</sup> have described void nucleation in terms of the critical interfacial strength between the matrix and inclusions ( $s_c$ ) and assuming

$$s_c = s_H \sqrt{\epsilon} + \sigma \quad [2]$$

where  $\sigma$  = the applied (macroscopic) stress,  $\epsilon$  = plastic strain and  $s_H$  = a material constant so that the product ( $s_H/\epsilon$ ) portrays the microscopic stress from dislocation pileups. A critical strain can be calculated in terms of the constants,  $s_c$  and  $s_H$ , and the applied stress. The critical strain can then be used for the fracture strain ( $\epsilon_f$ ) in an expression like eq. 3 from Ashby<sup>20</sup> to form eq. 4

$$K_{Ic} \sim (2\pi\sigma_y r^* E \epsilon_f)^{1/2} \quad [3]$$

$$K_{nuc} = \left( \frac{s_c - 3.5\sigma_y}{s_H} \right) \left( 4.5\sigma_y E L \right)^{1/2} \quad [4]$$

where  $E$  = Young's modulus,  $r^*$  = a characteristic distance like the inclusion spacing,  $K_{nuc}$  = stress intensity factor for nucleation,  $L = r^*$ , and representing the stress in front of the crack tip,  $\sigma = 3.5\sigma_y$ .

Values for  $s_H$  and  $s_c$  were estimated in previous work<sup>11</sup> to be about 2400 and 5000 MPa. Using a value of  $E = 200$  GPa and  $L = 50 \mu\text{m}$ , we can calculate a value of  $K_{nuc}$  for each test temperature and composition. The calculated values are compared to the measured values and plotted in Figure 7 as a function of interstitial content. The best agreement occurs for the 4 K data and higher interstitial contents, indicating that nucleation accounts for a larger share of the measured fracture toughness at lower temperature and higher strengths.

## CONCLUSIONS

1. Increasing the interstitial content raises the yield strength, makes void nucleation ahead of the crack easier, and reduces fracture toughness of austenitic stainless steels at low temperatures.
2. Increasing the interstitial content reduces the extent of the strain-induced transformation. The transformation does not appear to affect the local stress and strain at the inclusions which form the fracture surface.
3. Increasing the interstitial content does not affect the inclusion size and distribution.



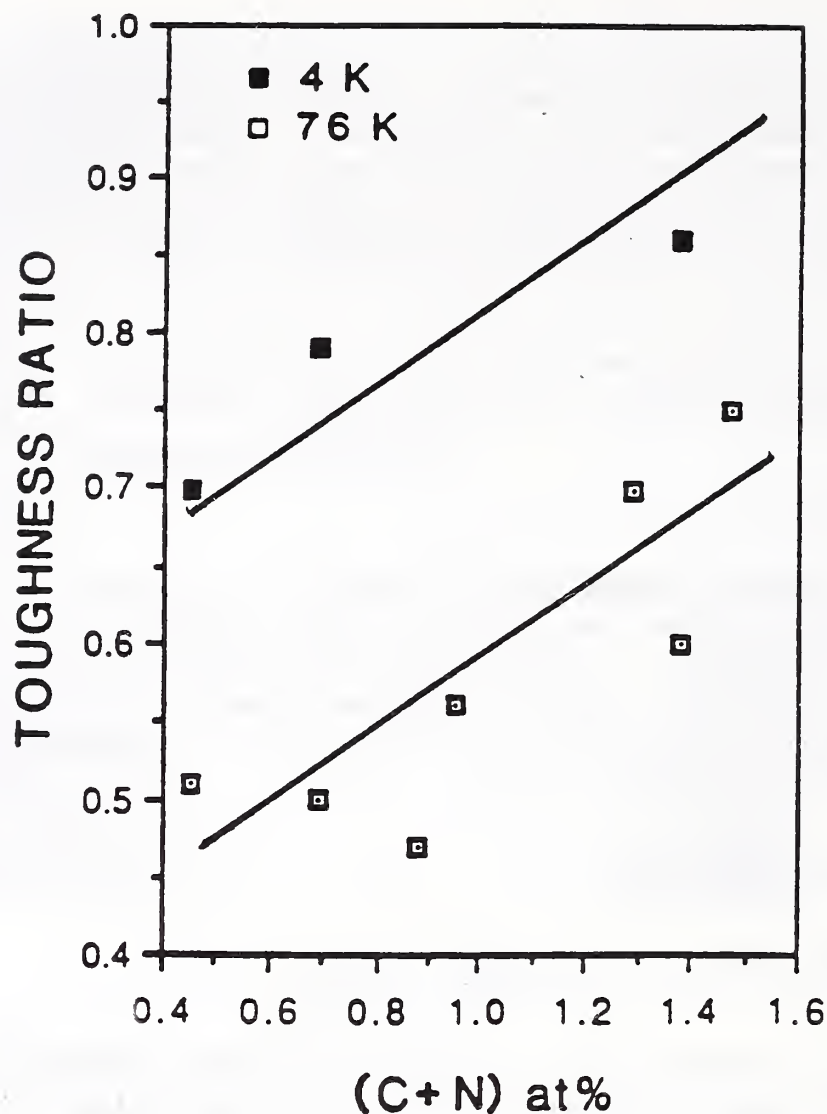


Figure 7. Toughness ratio (predicted nucleation stress intensity factor divided by the measured toughness) plotted vs. the interstitial content.

#### ACKNOWLEDGMENTS

This work was partially sponsored by DOE, Office of Fusion Energy. The authors thank R.P. Walsh, D.A. Shepherd, and L. Delgado for their help in obtaining the experimental data.

#### REFERENCES

1. R.L. Tobler, D.T. Read, and R.P. Reed: in Fracture Mechanics Thirteenth Conference, ASTM STP 743, R. Roberts, ed., American Society for Testing and Materials, Philadelphia, 1981, p. 350.
2. R.J.H. Wanhill: Eng. Fract. Mech., vol. 10, 1978, p. 337.
3. J.C. Lautridou and A. Pineau: Eng. Fract. Mech., vol. 15, 1981, p. 1259.
4. A.D. Wilson: J. Eng. Matl. Tech., vol. 101, 1979, p. 265.

5. E.R. Parker and V.F. Zackay: Eng. Fract. Mech., vol. 5, 1973, p. 147.
6. D. Fahr: Met. Trans., vol. 2A, 1971, p. 1883.
7. S. D. Antolovich and B. Singh: Met. Trans., vol. 2A, 1971, p. 2135.
8. J.R. Rice and M. A. Johnson: in Inelastic Behavior of Solids, M.F. Kanninen, et al., eds., McGraw-Hill, New York, 1970, p. 641.
9. R.O. Ritchie and A.W. Thompson: Met. Trans., vol. 16A, 1985, p. 233.
10. W.M. Garrison, Jr.: Met. Trans., vol. 17A, 1986, p. 669.
11. P.T. Purtscher, D.T. Read, and R.P. Reed: Fracture Mechanics: Perspectives and Directions (Twentieth Symposium), ASTM STP 1020, R.P. Wei and R.P. Gangloff, Eds., American Society for Testing and Materials, Philadelphia, 1989, pp. 443-446.
12. R.P. Reed and N.J. Simon: in these proceedings.
13. R.P. Reed and C.J. Guntner: Trans. AIME, vol. 230, 1964, p. 1713.
14. R.M. McMeeking: J. Mech. Phys. Solids, vol. 25, 1977, p. 357.
15. C.F. Shih: J. Mech. Phys. Solids, vol. 29, 1981, p. 305.
16. P.T. Purtscher: J. Test. Eval., vol. 15, 1987, p. 296.
17. R.P. Reed: in Materials at Low Temperature, R.P. Reed and A.F. Clark, eds., American Society for Metals, Metals Park, Ohio, 1983, p. 295.
18. J.W. Morris, Jr. and E.N.C. Dalder: J. Metals, vol. 37, 1985, p. 24.
19. G. LeRoy, J.D. Embury, G. Edwards, and M.F. Ashby: Acta Met., vol. 29, 1981, p. 1509.
20. M.F. Ashby: Prog. Mat. Sci.; Bruce Chalmers Anniversary Volume, p. 1.





METALLOGRAPHIC STUDY OF THE CRACK-TIP REGION FROM FRACTURE  
MECHANICS SPECIMENS OF AUSTENITIC AND FERRITIC STEELS<sup>+</sup>

P.T. Purtscher\*, R.P. Reed\*, and D.K. Matlock\*\*

Fracture and Deformation Division

\*National Institute of Standards and Technology Division  
Boulder, Colorado

\*\*Advanced Steel Processing and Products Research Center, Colorado  
School of Mines  
Golden, Colorado

Metallographic sections of blunted and growing cracks in steels with different strain-hardening capacities are observed in the light and scanning electron microscopes. The strain distribution around the crack-tip region is inferred from the etching behavior and microhardness readings. The direction of initial growth is approximately straight ahead of the fatigue precrack in the high strain-hardening austenitic steels and at an angle of about 45° in the low strain-hardening ferritic steel. These observations are discussed in terms of different criteria for ductile fracture in fracture mechanics specimens.

## INTRODUCTION

The absence of stretch zones on the fracture surface of austenitic steels tested at cryogenic temperatures<sup>1</sup> indicates that the strain distribution at the crack tip must be significantly different from the strain around cracks in ferritic steels. The stress and strain distributions around a crack in fracture mechanics specimens affect the fracture criteria used in modeling fracture toughness. McMeeking<sup>2</sup> suggested, based on his finite element calculations, that if the crack grows straight ahead of the tip, a critical-stress fracture criterion is appropriate (example in ref. 3); on the other hand, angled crack-growth indicates a critical plastic strain criterion (examples in ref. 4 and 5).

Many criteria have been proposed to describe ductile fracture in fracture mechanics specimens. One approach<sup>6</sup> relates fracture toughness to the growth of voids ahead of the crack tip, assuming that void nucleation contributes little to the measured toughness. Others<sup>7,8</sup> have followed this approach, but incorporated microstructural features to describe the local strain and the characteristic distance for fracture. In contrast, an expression for the stress intensity factor for void nucleation has been developed and shown to compare favorably to fracture toughness in high-strength austenitic steels.<sup>9</sup>

---

\*Contributed to proceedings of MRS Advanced Materials meeting in Tokyo, June, 1988.

In this paper, the crack-tip regions in fracture mechanics specimens of austenitic and ferritic steels are examined and the initial crack growth directions are determined. The observations are discussed with respect to the strain-hardening capacities of the steels, finite element results, and different fracture criteria.

## MATERIALS AND PROCEDURES

Two austenitic steels tested at 76 K and a ferritic steel tested at 233 K, are used in this study. Alloy #1 is a low strength, high strain-hardening austenitic stainless steel (similar to AISI 304); alloy #2 is a higher strength, austenitic stainless steel (high nitrogen version of AISI 304); alloy #3 is a ferritic steel (similar to ASTM A533B) with a yield strength in between that for alloys #1 and 2. The chemical compositions and fracture toughnesses of the steels are listed in Table 1 and the true stress-true strain curves are shown in Figure 1. A complete analysis of the mechanical properties of these steels and test procedures can be found elsewhere.<sup>10-11</sup>

Table I. Steel compositions (wt. %) and fracture toughness.

Alloy	Cr	Ni	Mn	P	S	Si	Mo	C	N	$K_{Ic}$ (MPa/m)	T(K)
1	18.3	10.1	1.6	0.021	0.019	0.5	0.2	0.06	0.04	375	76
2	20.3	10.0	1.4	0.024	0.016	0.5	0.2	0.06	0.24	270	76
3	0.1	0.8	1.3	0.007	0.008	0.2	0.5	0.19	---	256	233

Standard and interrupted fracture toughness tests (i.e. applied J,  $J_a$ , less than the fracture toughness,  $J_{Ic}$ ) were performed on side-grooved, compact specimens of alloys #1 and 2 in liquid nitrogen (76 K). A similar specimen from alloy #3 was tested in cooled alcohol (233 K) where a ductile crack initiated at the fatigue crack tip, but the specimen ultimately failed by cleavage. The austenitic specimens were loaded to a crack extension of about 1.5 mm, then unloaded, warmed to room temperature and sectioned along the centerline perpendicular to the crack plane. One half was fatigue post-cracked to reveal the extent of crack growth during the test while the other half was polished to observe the crack-tip geometry. The fracture surface from the broken specimen of alloy #3 was observed in the scanning electron microscope before the two halves were glued together with epoxy for sectioning. Diamond pyramid hardness readings (DPH) and etching solutions<sup>12</sup> were used to delineate the strain-hardened regions around the crack tips.

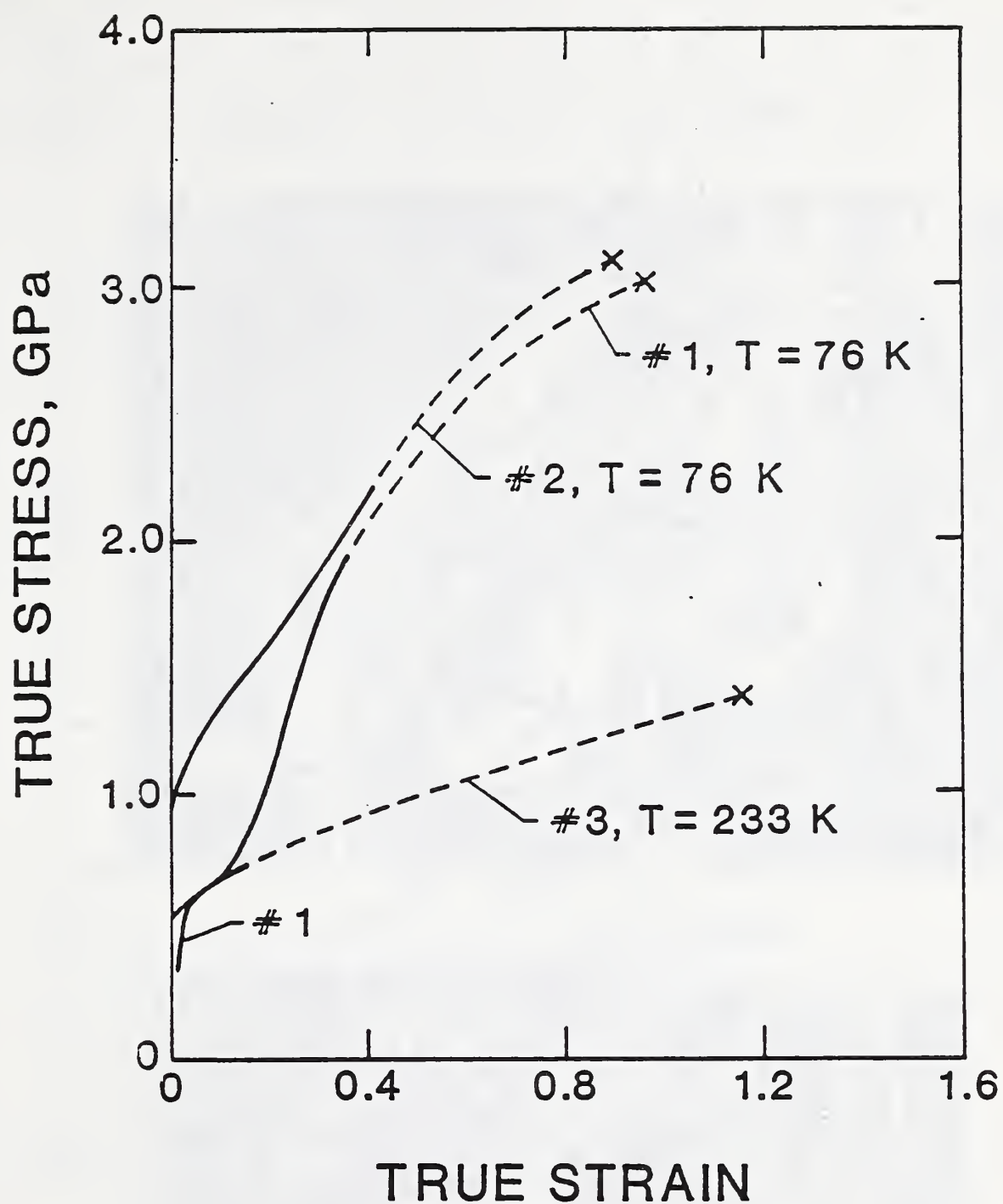


Figure 1. True-stress-strain curves for the three alloys. Dotted lines represent post necking extrapolation to measured (indicated by X) stress-strain point at fracture.

#### OBSERVATIONS

No stretch zones formed on the fracture surface of the compact specimens from alloys #1 and 2. In contrast, a small, well-defined stretch zone is found on the fracture surface of alloy #3 between the fatigue precrack features and the dimpled rupture features of the overload region. These observations are similar to that shown in ref. 1.



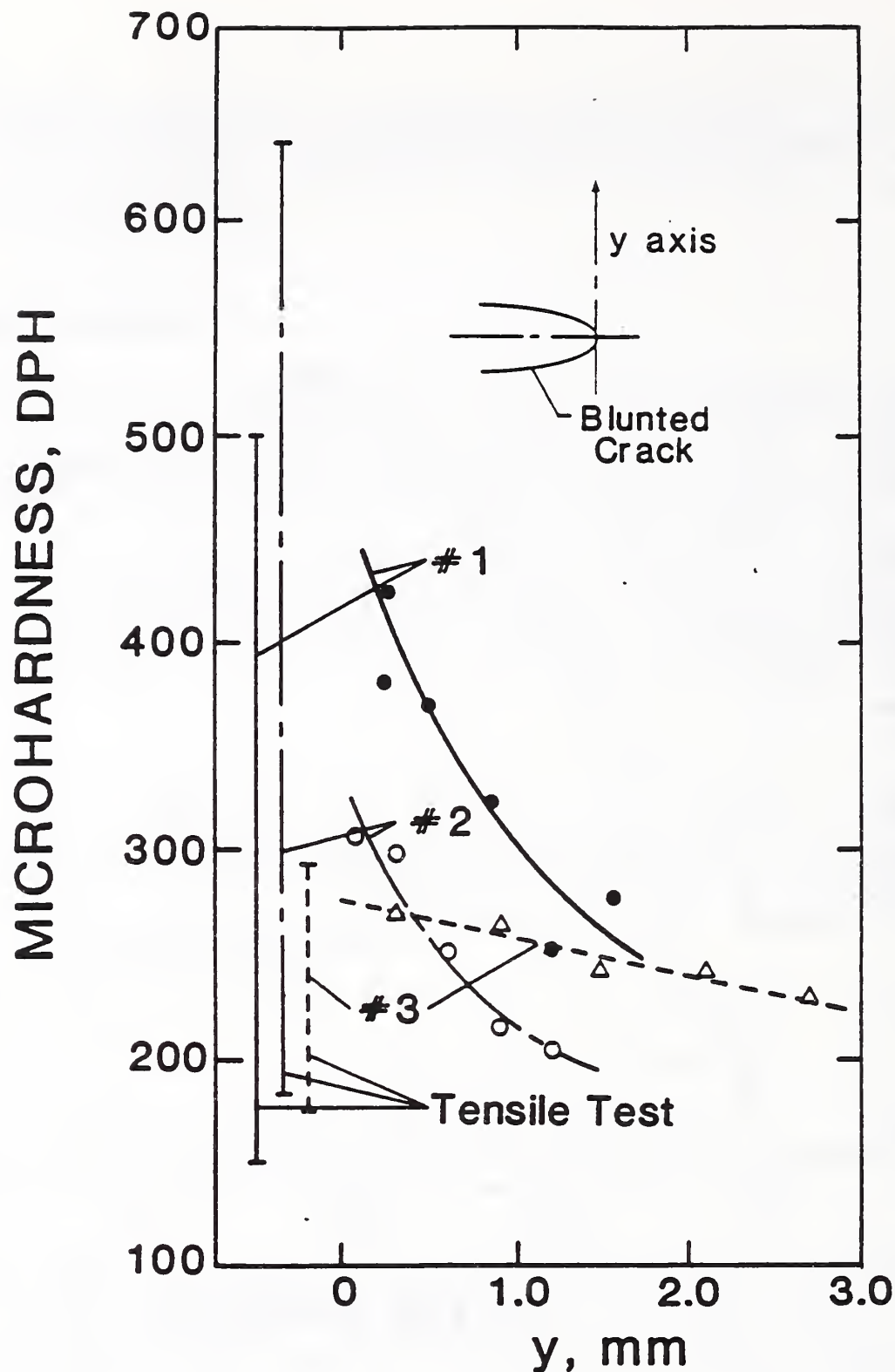


Figure 2. Hardness gradients from grip to necked region in tensile tests and around the crack tip for the three alloys.

Figure 2 shows the gradients of microhardness readings from tensile and fracture toughness test specimens. The range of DPH measured in the tensile test defines the strain-hardening capacity (SHC) of each steel. Alloys #1 and 2 have a high SHC while alloy #3 has a lower SHC. A large gradient in the DPH values was observed around the crack tip for alloy #1 with a DPH close to the crack tip that approaches the maximum DPH measured in the necked region of the tensile specimen. For alloy #3 which had the lowest SHC in the tensile test, the DPH values around the crack tip are more uniform and spread over a larger area. The maximum DPH near the tip is similar to the maximum measured in the tensile test.

Figure 3 shows representative dimpled rupture features from both the austenitic and ferritic steel samples. Alloys #1 and 2 (Fig. 3a) exhibited a range of dimple morphologies where the dimples formed primarily at MnS inclusions. Alloy #3 (Fig. 3b) displayed smaller and more uniform dimples which nucleated at the carbides that form on tempering the steel.

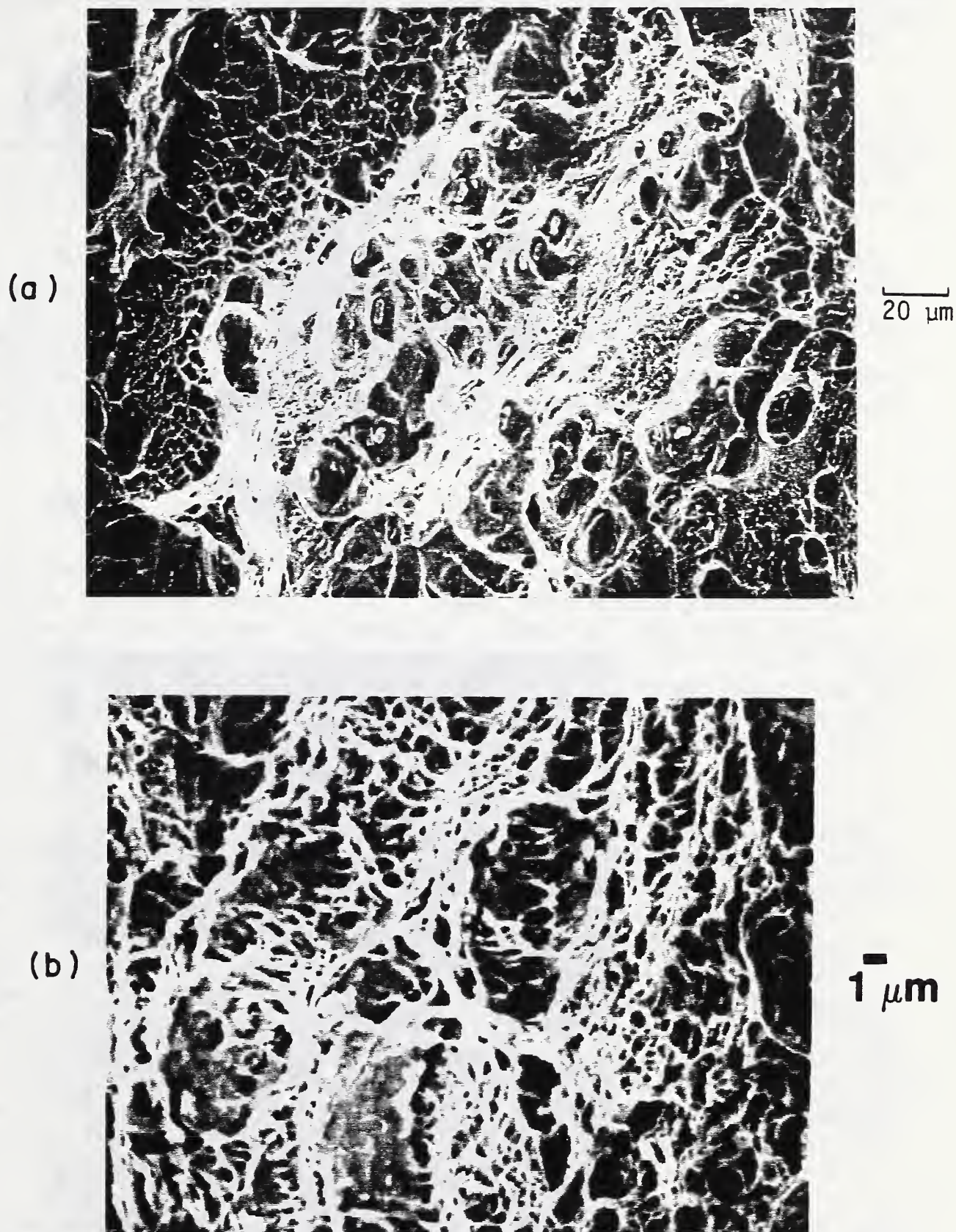


Figure 3. Fracture surfaces from compact specimens (a) alloy #2 tested at 76 K and (b) alloy #3 tested at 233 K.



The sectioned crack from alloy #1 interrupted at  $J_a = 0.35 J_{Ic}$  is shown in Fig. 4. The stain etch (Fig. 4a) shows that there is a sharp gradient in the strain-induced martensite concentrated at  $45^\circ$  to the crack plane. In addition, selected microhardness readings indicate that the strain hardening is concentrated in the dark-etching bands. With a different etch and higher magnification (Fig. 4b), a small crack can be seen directly ahead of the blunted tip.



Figure 4. Section of crack tip from alloy #1 at  $J_a = 0.35 J_{Ic}$  (a) stain etch<sup>12</sup> and (b) oxalyic acid etch.



A specimen of alloy #2 stopped at  $J_a = 0.8 J_{IC}$ , Fig. 5a, exhibited a smaller crack opening displacement (COD or  $\delta$ )(in comparison to alloy #1). DPH readings and the stain etch indicated that the region of strain hardening were proportionately smaller, but retained a shape similar to that shown in Fig. 4. No crack was present at the tip, but the blunted shape extended directly ahead and does not show shear crack formation along the strain hardened regions at  $45^\circ$  to the crack plane.

A section through the growing crack in alloy #2,  $J_a > J_{IC}$ , is shown in Fig. 5b. Few voids have opened around the growing crack and the DPH profile (Fig. 2) indicates that the strain hardening is concentrated in a zone that is smaller than the plastic zone.

In Fig. 6 from alloy #3 ( $J_a > J_{IC}$ ), the initial growth has a zig-zag appearance similar to crack growth associated with slip-line fields.<sup>6</sup> The geometry of the plastic zone in A533B steel has been shown<sup>13</sup> to match theoretical predictions<sup>2</sup> with dimensions in the plane of the crack equal to the COD, and equal to twice the COD at  $45^\circ$ . Again, void nucleation and growth are confined to a zone smaller than the plastic zone determined by the DPH profile (Fig. 2).

## DISCUSSION

The straight-ahead growth in the austenitic steels is interpreted to be controlled by the peak stress (3 to 4 times the tensile yield stress according to the finite element predictions<sup>2</sup>) ahead of the crack while the angled crack growth in the ferritic steel is interpreted to be controlled by strain. In both cases, few voids are observed to have formed away from the growing crack in the plastic zone. The crack-growth behavior and the appearance of the crack-tip region (stretch zone formation) in the two types of steel can be explained by the strain hardening.

When the crack opens in alloys #1 and 2 (higher SHC), the crack-tip strength increases from localized strain hardening, and a relatively small plastic zone develops directly ahead of the blunted tip (shown by the microhardness gradients and the etching behavior). The matrix which will eventually fail and form the fracture surface does not flow significantly until voids nucleate at the larger MnS inclusions. The increased flow stress due to constraint and the low test temperature produce void nucleation on the crack plane where stress is highest, directly ahead of the tip. After nucleation, the matrix can flow around the particles leading to void growth and coalescence. Again because of the low test temperature, the flow stresses are high and void growth is minimal. No stretch zone is observed because the material on the fracture surface was not strained appreciably prior to void nucleation.

In contrast, when the crack opens in alloy #3 with the lower SHC, the crack tip has a lower strength and the strain hardening is distributed over a larger plastic zone (evidenced by the microhardness data). The plastic zone extends ahead of the crack, but the highest strains are concentrated in bands at  $45^\circ$  to the tip where voids nucleate at small tempered carbides.

(a)



200  $\mu\text{m}$

(b)



Figure 5. Crack-tip sections from specimens of alloy #2: (a)  $J_a = 0.8 J_{Ic}$  shows no void nucleation ahead of the blunted tip and (b)  $J_a > J_{Ic}$  showing the straight-ahead growth.



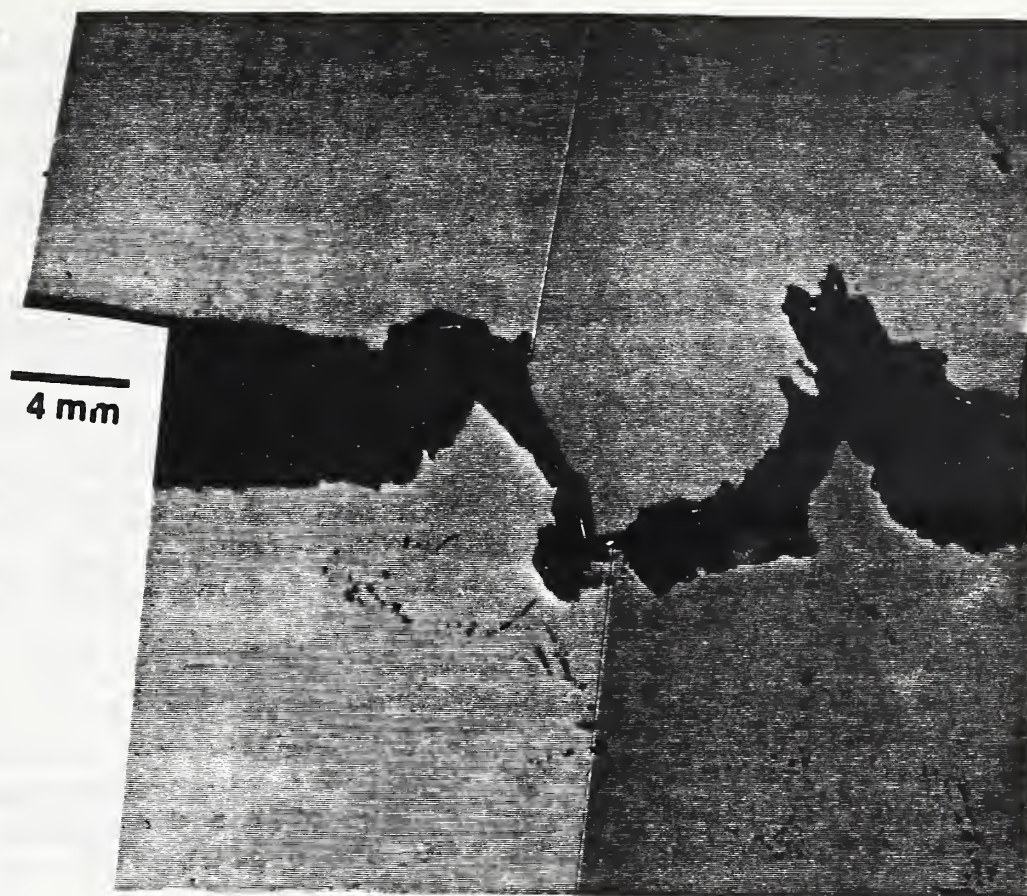


Figure 6. Section of crack tip in alloy #3 with  $J_a > J_{Ic}$  showing the angled path of initial crack growth.

The extent of growth is limited by the spacing of the particles; that is, little additional COD is required for the voids to grow and coalesce to produce the angled crack growth. The stretch zone forms because the material on the fracture surface was strained appreciably prior to void nucleation.

In both types of steels, void nucleation was limited to a process zone which can be defined by the observations to have a diameter approximately equal to the plastic COD. Conditions for void nucleation are only met in this zone where the stress and strain gradients are large. The measured fracture toughnesses (Table 1) and a general failure criterion must be related to the effect of stress and strain on both void nucleation and growth within the process zone. The contribution of void growth is small here because of the short spacing between carbides in alloy #3 and the low test temperature for alloys #1 and 2. The size of the process zone should be related to the COD, which determines the scale over which the enhanced forces act, and the size and spacing of the microstructural features (second phase particles), which determine the resistance of the steel to fracture.

## SUMMARY and CONCLUSIONS

All of the steels tested for this investigation fail in a ductile manner, and the measured fracture toughness values are relatively high. A stretch zone is observed on the fracture surface of a ferritic steel tested at 233 K where the initial crack growth is at  $45^\circ$  to the blunted tip. No



stretch zone is observed on the fracture surface of the austenitic steels tested at 76 K where the initial crack growth is straight-ahead. These observations have led to the following conclusions:

1. Stretch zones form on the fracture surface when the material is strained significantly prior to void nucleation.
2. In the austenitic steels (high SHC) where no stretch zone forms and the crack grows directly ahead of the blunted tip, fracture toughness is controlled by the peak stress ahead of the crack tip.
3. In the ferritic steel (low SHC) where a stretch zone forms on the fracture surface and an angled crack-growth path is observed, fracture toughness is controlled by the maximum strain which occurs at  $45^\circ$  to the crack tip.
4. In both cases, void nucleation was observed in only a limited region around the crack. The conditions for nucleation, and similarly for fracture toughness, are best described by a function of both stress and strain over a distance that is related to the COD and the size and spacing of void-nucleating particles.

#### ACKNOWLEDGEMENTS

The DOE Office of Fusion Energy provided partial support of this work. The authors wish to thank Jurgen Heerens from the GKSS-Research Center, Geesthacht, West Germany for providing machined specimens of the ferritic steel.

#### REFERENCES

1. P.T. Purtscher, J. Test. Eval., vol. 15, 1987, p.296.
2. R.M. McMeeking, J. Mech. Phys. Solids, vol. 25, 1977, p. 357.
3. S.P. Rawal and J. Gurland, in Proceedings of Second International Conference on Mechanical Behavior of Materials, Federation of Materials Societies, Dearborn, MI, 1976, p. 1154.
4. C.D. Beachem and G.R. Yoder, Metall. Trans., vol. 4A, 1973, p. 1145.
5. F. Zia-Ebrahimi, D.K. Matlock, and G. Krauss, Scripta Metall., vol. 16, 1982, p. 987.
6. J.R. Rice and M.A. Johnson, in Inelastic Behaviour of Solids, edited by M.F. Kanninen, W.F. Adler, A.R. Rosenfield, and R.I. Jaffee, McGraw-Hill, New York, 1968, p. 641.
7. R.O. Ritchie and A.W. Thompson, Metall. Trans., vol. 16A, 1985, p. 233.

8. W.M. Garrison, Jr., Metall. Trans., vol. 17A, 1986, p. 669.
9. P.T. Purtscher, D.T. Read, and R.P. Reed, Fracture Mechanics: Prospectives and Directions (Twentieth Symposium), edited by R. Wei and R.P. Gangloff, American Society for Testing and Materials, Philadelphia, 1989, pp. 433-446.
10. P.T. Purtscher and R.P. Reed, to be published in Proceedings of High Nitrogen Steels '88.
11. J. Heerens, K. Schwable, and A. Cornec, in Fracture Mechanics: Eighteenth Symposium, ASTM STP 945, edited by D.T. Read, and R.P. Reed American Society for Testing and Materials, Philadelphia, 1988, p.374.
12. R.P. Reed, Acta Metall., vol. 10, 1962, p. 865.
13. R.H. Van Stone, T.B. Cox, J.R. Low, Jr., and P.A. Psioda, Int. Met. Rev., vol. 30, 1985, p. 157.





TENSILE, FRACTURE, AND FATIGUE PROPERTIES OF NOTCHED ALUMINUM  
ALLOY SHEETS AT LIQUID NITROGEN TEMPERATURE†

R.L. Tobler, R.P. Walsh and R.P. Reed  
Fracture and Deformation Division  
National Institute of Standards and Technology  
Boulder, Colorado

J.K. Han  
Korea Advanced Institute of Science and Technology  
Seoul, Korea

L. Ma  
Institute of Metal Research Acedemia Sinica  
Shenyang, People's Republic of China

Notched sheet specimens of four high strength aluminum alloys were tested to evaluate their potential for a Superconducting Super Collider application. Alloys 7075-T6, 7475-T761, 2219-T87, and 2090-T8E41 were tested in liquid nitrogen at 76 K, in tension-tension fatigue, at a stress ratio of 0.1. The alloys are compared in terms of their static tensile and fracture properties, and fatigue resistance for a life of  $4 \times 10^4$  cycles.

## INTRODUCTION

Notched key collars are to be used in the Superconducting Super Collider (SSC) dipole magnets (1). The key collars are locked in position on cryogenic magnetic coils so the magnetic coils can be prestressed when the keys are pressed in. Safe structural design is critical because the key collars are highly stressed repeatedly at 4 K. A fatigue life of  $4 \times 10^4$  cycles is anticipated. So far, alloy 7075-T6 has been selected as the construction material. Preliminary analysis and experiments support the adequacy of 7075-T6: model coils were energized 3500 times to the full operating field strength of 6.6 T; they were also energized several times to 9 T, at 1.8 K, and no cracking was observed in the collars (1). In this study, we report various mechanical property measurements enabling a preliminary comparison of the relative merits of 7075-T6 and three competing alloys at 76 K.

## MATERIALS

Four commercial aluminum alloys were tested in their as-received tempers: 7075-T6, 7475-T761, 2219-T87, and 2090-T8E41. Alloy 7475-T761 was obtained in the form of a 2.10 mm thick clad sheet because unclad sheet was not available from several suppliers. The other three alloys were obtained in the desired form, 1.60 mm thick sheets, unclad. Nominal compositions in weight percent are:

7075	-	5.6%Zn-2.5%Mg-1.6%Cu-0.23%Cr, balance Al
7475	-	5.7%Zn-2.3%Mg-1.5%Cu-0.22%Cr, balance Al
2219	-	6.3%Cu-0.3%Mn-0.18%Zr-0.10%V-0.06%Ti, balance Al
2090	-	2.86%Cu-2.05%Li-0.12%Zr, balance Al

Figure 1 shows the specimen geometries. Unnotched specimens for routine tensile tests were fabricated with the loading axis transverse to the principal rolling direction of the sheet. The notched specimens for tensile and axial fatigue tests were also fabricated in the transverse orientation. The square notch shown in Fig. 1 essentially duplicates the notched condition of the actual SSC key collar: the radius, ligament size, thickness, and notch depth of our specimens are nearly the same as for the part used in service. The actual key collar notch has tapered sides with an angle of  $3^\circ$  (1), but this taper has a negligible effect on the notch stress concentration factor  $K_t$ , which is approximately 3.9 for both the key collar and our specimens.

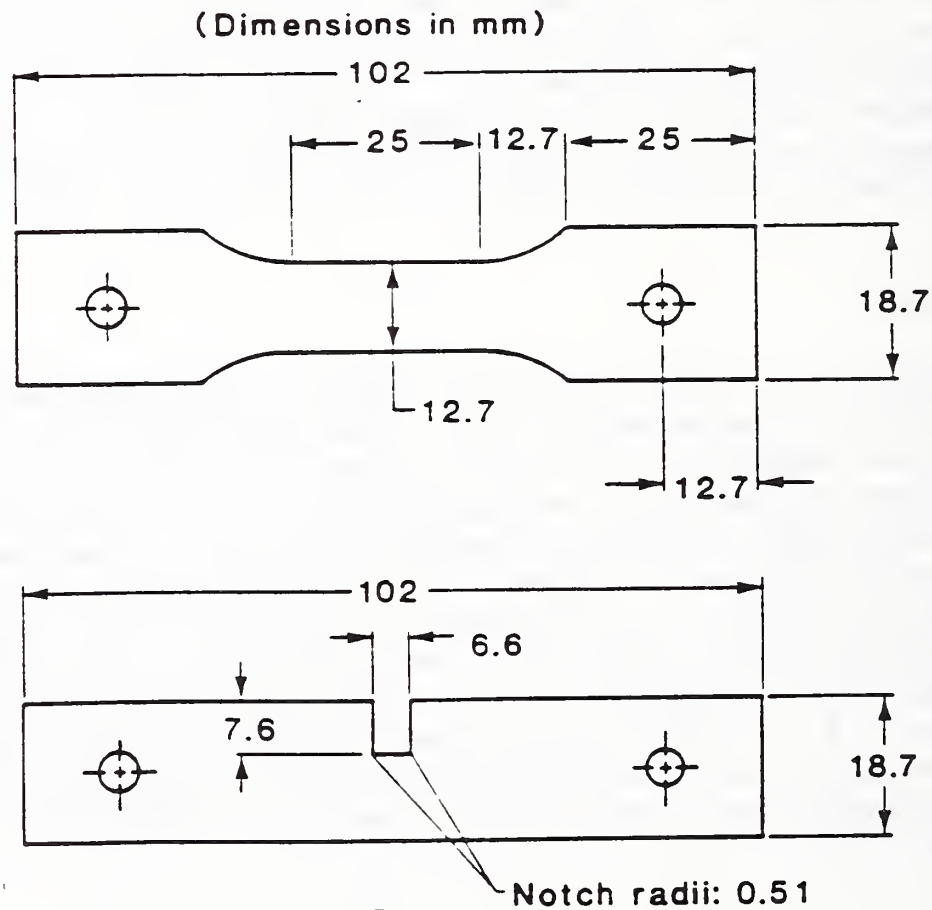


Figure 1. Specimen geometries.

## PROCEDURES

All specimens were ground and polished to remove surface markings from the as-received sheets. The 7475-T761 material, originally 2.10 mm thick, included superficial layers of alcladding 0.08 mm thick. These specimens were ground equally on each side, not only to remove the cladding (typically, alloy 7072) but to reduce the thickness to more closely match the thicknesses of the other three alloys. Specimens of the three other (unclad) alloys were ground slightly on each side. Finally, all specimens were electro-polished in a solution of 30% nitric acid and 70% methanol.

After polishing the specimens, we measured their dimensions and notch root radii using a micrometer or a shadowgraph. The nominal dimensions are given in Fig. 1. The notch radii were measured at both corners and on both sides of each specimen, and the four readings were averaged. The minimum values of the four readings for each specimen were  $0.555 \text{ mm} \pm 7\%$ . The mean values of the four readings for each specimen were  $0.600 \text{ mm} \pm 10\%$ . The specimen thicknesses varied with the extent of grinding and polishing; typical values were: 7075-T6, 1.53 mm; 7475-T761, 1.81 mm; 2219-T87, 1.61 mm; 2090-T8E41, 1.45 mm.

Conventional tensile tests were performed at a crosshead rate of 0.5 mm/min and a corresponding strain rate of  $3.3 \times 10^{-4} \text{ s}^{-1}$ . The gage length for elongation measurements was 29 mm. The unnotched tensile specimen performed well for alloys 2090, 2219, and 7475, but during tests of 7075-T6 several specimens failed at the pin holes in the grips. To complete the characterization of 7075-T6, we machined some modified specimens that had a reduced gage-section width of 6.35 mm; this ensured failures in the gage length.

Tensile tests of notched specimens were performed to measure the notch tensile strength (NTS) at 76 K. The first series of 2090-T8E41 specimens used for this purpose had irregular notch tip radii, which caused low NTS values and low fatigue resistance; the data for these specimens were discarded and new specimens were machined.

The specimens were gripped and mounted in a cryostat for testing. Liquid nitrogen surrounds the specimen for tests at 76 K. Fatigue tests were conducted using servohydraulic machines in the load control mode with 10 or 25 kN load ranges. The minimum-to-maximum fatigue stress ratio  $R$  was 0.1. To begin a test, the mean load was applied at once, and the load amplitude was adjusted while the frequency  $f$  was only 1 Hz. The frequency was then gradually stepped up to 9, 10, or 15 Hz in increments of 1 Hz while the load amplitude was re-adjusted.



## RESULTS

### Tensile Properties

Table 1 lists the tensile test data for unnotched specimens of all alloys tested in this study. With decreasing temperature between 295 and 76 K, the yield strengths YS and ultimate tensile strengths UTS increase significantly while the values of tensile elongation EL and Young's modulus E vary slightly. Such trends are typical for aluminum alloys and present no surprises.

Table 1. Tensile Test Results for Unnotched Specimens.

Alloy	Temp. K	YS MPa	UTS MPa	El %	E GPa
7075 -T6	295	504	589	16.5	61.2
	295	499 avg = 502	589 avg = 589	17.3 avg = 16.9	65.1 avg = 63.2
	76	589	716	15.5	76.4
	76	589 avg = 589	711 avg = 714	16.0 avg = 15.8	70.4 avg = 73.2
7475 -T761	295	462	514	17.3	65.9
	295	458 avg = 460	515 avg = 515	16.8 avg = 17.1	66.6 avg = 66.3
	76	548	635	17.5	78.2
	76	549 avg = 549	637 avg = 636	17.0 avg = 17.3	72.3 avg = 75.3
2219 -T87	295	398	475	12.8	69.9
	295	396 avg = 397	475 avg = 475	12.4 avg = 12.6	65.7 avg = 67.8
	76	484	596	14.0	80.9
	76	484 avg = 484	598 avg = 597	12.9 avg = 13.5	72.0 avg = 76.5
2090 -T8E41	295	488	528	12.0	77.2
	295	487 avg = 488	527 avg = 528	12.1 avg = 12.1	70.8 avg = 74.0
	76	552	637	10.5	--
	76	550 avg = 551	643 avg = 640	11.1 avg = 10.8	76.9

Note: The unnotched specimen diagrammed in Fig. 1 was used in most tensile tests, but 7075 at 76 K required a modified specimen (see text).

## Fracture Resistance

Table 2 lists the tensile test data for notched specimens at 76 K. Also shown are the notch-strength ratios (NSR = NTS/UTS) and notch-yield ratios (NYR = NTS/YS). These ratios are widely used as qualitative indicators of notch sensitivity and fracture toughness. In particular, it has been shown that the NYR for round bar specimens generally correlates with the plane-strain fracture toughness parameter,  $K_{Ic}$  (2). The NYR's for our alloys range from 0.76 to 0.90, and are always less than 1, indicating that the alloys are notch sensitive. Figure 2, a plot of YS versus NYR for the four alloys, demonstrates there is an inverse relationship such as would be expected for parameters associated with strength and toughness.

As indicated by Fig. 2, the fracture resistance of alloy 2090-T8E41 is not outstanding compared to the other alloys of this study at 76 K. This came as a surprise since superior toughness at cryogenic temperatures has been reported elsewhere for alloy 2090 (4-6). This may imply that rankings based on qualitative NYR data for thin specimens (our study) yield different conclusions from quantitative rankings based on  $K_{Ic}$  values for thick specimens (other studies). Or perhaps the disparate findings reflect the fact that the fracture toughness of alloy 2090-T8E41 at cryogenic temperatures depends on metallurgical factors (such as extent of recrystallization, degree of texturing, and distribution of precipitates) which can vary from heat to heat.

Table 2. Notched Tensile Strengths (NTS), Notch-Strength Ratios (NSR), Notch-Yield Ratios (NYR), and Notched Fatigue Strength Ratios (NSFR) at 76 K.

Alloy	Specimen	NTS MPa	NSR <sup>a</sup>	NYR <sup>b</sup>	NFSR <sup>c</sup> at 10 <sup>5</sup> cycles
7475-T761	1	483	0.74	0.86	0.21
	2	461			
		avg = 472			
7075-T6	1	478	0.63	0.76	0.21
	2	423			
		avg = 450			
2219-T87	1	450	0.73	0.90	0.21
	2	420			
		avg = 435			
2090-T8E41	1	425	0.69	0.80	0.23
	2	464			
	3	441			
		avg = 443			

<sup>a</sup> Obtained by dividing NTS by UTS.

<sup>b</sup> Obtained by dividing NTS by YS.

<sup>c</sup> Obtained by dividing NFS at 10<sup>5</sup> cycles by NTS.

As indicated by Fig. 2, the fracture resistance of alloy 2090-T8E41 is not outstanding compared to the other alloys of this study at 76 K. This came as a surprise since superior toughness at cryogenic temperatures has been reported elsewhere for alloy 2090 (4-6). This may imply that rankings based on qualitative NYR data for thin specimens (our study) yield different conclusions from quantitative rankings based on  $K_{IC}$  values for thick specimens (other studies). Or perhaps the disparate findings reflect the fact that the fracture toughness of alloy 2090-T8E41 at cryogenic temperatures depends on metallurgical factors (such as extent of recrystallization, degree of texturing, and distribution of precipitates) which can vary from heat to heat.

### Fatigue Life

Our fatigue data for notched specimens at 76 K are presented in Fig. 3. Typically, the measurements consist of two tests at each of three stress levels bracketing a life of  $4 \times 10^4$  cycles. The average life at a given stress is plotted in Fig. 3.

As a measure of fatigue resistance, we report the notched fatigue strength, NFS; this is the maximum stress corresponding to fatigue failure at a specified number of cycles. The NFS values were estimated from the trend lines in Fig. 3. For  $4 \times 10^4$  cycles at 76 K, the alloy ranking in descending order is:

2090-T8E41:	NFS = 129 MPa,
7475-T761:	NFS = 109 MPa,
7075-T6:	NFS = 103 MPa, and
2219-T87:	NFS = 102 MPa.

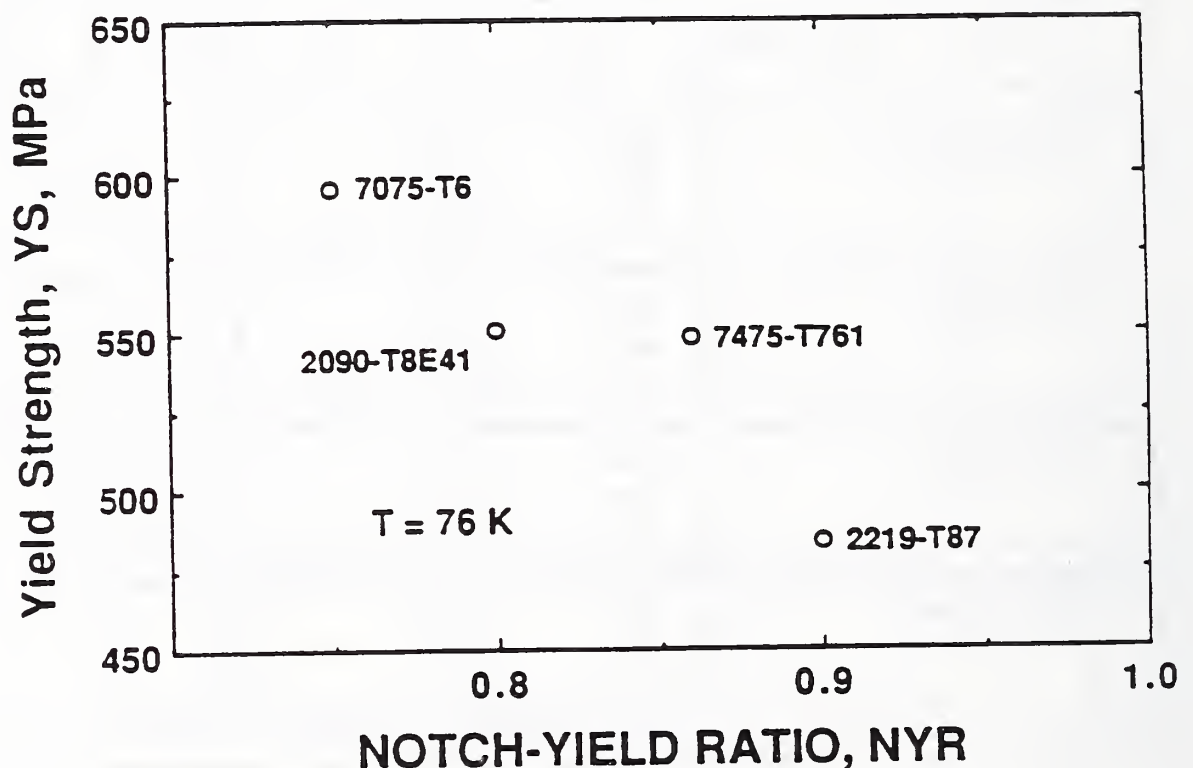


Figure 2. Yield strength versus notch-yield ratio for the four alloys tested at 76 K.



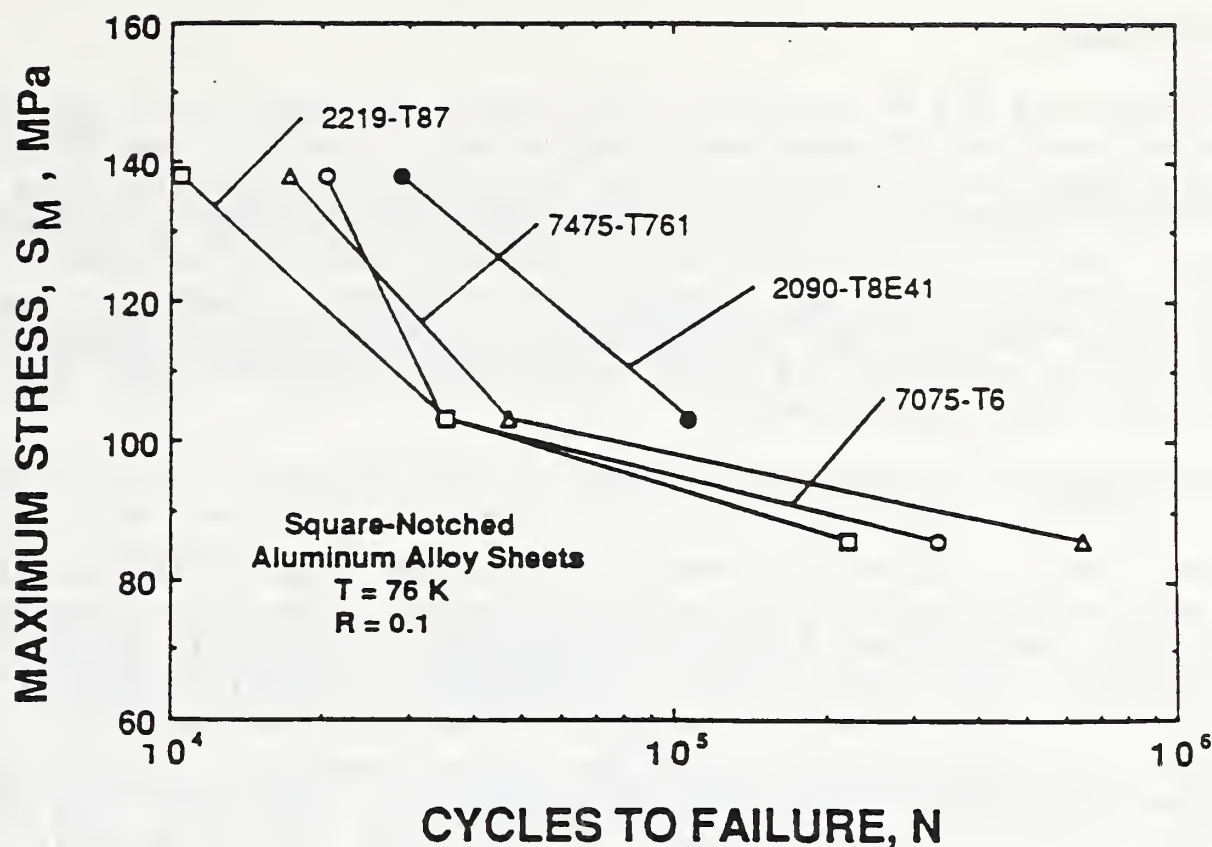


Figure 3. Notched specimen fatigue test results for the four alloys tested at 76 K.

To compare the NFS values with NTS values for these alloys we define a parameter called the notched fatigue strength ratio  $NFSR = NFS/NTS$ . We made this comparison at  $10^5$  cycles where the NFS estimates from Fig. 4 are most reliable. As shown in Table 2, for a life of  $10^5$  cycles, the NFSR's for all four alloys are in close agreement at 0.21-0.23. We conclude that 2090-T8E41 offers a higher fatigue resistance in the notched condition at 76 K, but the differences among these high strength aluminum alloys can be normalized to NTS values.

## DISCUSSION

### General Observations

Fatigue data at cryogenic temperatures are not abundant in the open literature but some data that are available indicate that the face centered cubic metals including aluminum alloys show some regular property trends. McCammon and Rosenberg (3) observed that the conventional fatigue strengths of unnotched specimens at cryogenic temperatures tend to increase with increasing ultimate tensile strength. Similarly, our data suggest that the fatigue strength of notched specimens scales approximately with the notched tensile strength, under certain conditions (that is, a life of about  $10^5$  cycles). Therefore the conventional tensile properties of smooth and notched specimens bear some relationship to their fatigue resistances, and the tensile properties are potentially useful for screening.

## Alloy Screening

Although the NTS is related to  $1/Y_S$  (Fig. 2), there is not an exact correlation, and the NFS apparently scales better with NTS than with  $1/Y_S$ . For four alloys, we found that the NFS is nearly a constant fraction (0.21-0.23) of the NTS (Table 2); this implies that tensile tests of notched specimens, which are relatively easy to perform, can help to predict the fatigue resistance of notched specimens at  $10^5$  cycles. More data are needed to confirm the value of the NFS/NTS ratio as a screening parameter for fatigue, and to ascertain the range of applicability for various alloys, temperatures, and stress levels.

## Alloy Selection

Many aluminum alloys that remain ductile and tough at low temperatures can be used in cryogenic structures but different alloys have advantages and disadvantages that influence material selection for specific applications. In this study at 76 K, no one alloy is universally superior: 7075-T6 offers the highest yield and tensile strengths in the unnotched condition, 7475-T761 offers the highest strength in the notched condition, 2219-T87 offers the highest notch-yield ratio (fracture toughness), and 2090-T8E41 offers the highest notched fatigue strength for the cycle life of interest. The material availability and cost must be considered as well as the mechanical properties.

Among the 7000 series alloys, 7075-T6 is readily available and widely used at room temperature. Our study indicates that 7075-T6 has higher strength than 7475-T761, but its fatigue strength in the notched condition is slightly lower due to its higher notch sensitivity. Alloys from the 2000 series, however, are usually preferred for cryogenic applications. Alloy 2219-T87 is especially attractive for cryogenic aerospace applications because it is readily weldable. This advantage is lost, however, for SSC key collars which do not require welding.

Alloy 2090 is a relatively new material that offers a 7% lower density and a 10% higher modulus than other aluminum alloys. Again, the advantages are significant in aerospace applications, and not in SSC applications. At the present time, alloy 2090 is disadvantageous in terms of availability and cost.

## Service Applications

Relating laboratory data to service behavior is a practical problem that was minimized in this study by testing a notch configuration equivalent to that of the specific application. The square notch geometry used in this study nearly matches the notch configuration of the service component, but other differences must be considered. The SSC key collars are stamped, not milled and electro-polished as our laboratory specimens were. For test specimens, electro-polishing provides a smooth, uniform surface which improves fatigue resistance and aids material comparisons by reducing data scatter. Stamping may affect the performance of the manufactured parts if, for example, residual stresses are created without subsequent stress relief treatment. Another consideration is the manner of loading in service, especially any difference in the fatigue (minimum-to-maximum) stress ratio; higher stress ratio usually decrease the cycles to failure for a given range (maximum minus minimum) stress.



## CONCLUSIONS

The following conclusions emerge from this study of the fatigue behavior of notched high strength aluminum alloys at 76 K:

1. In terms of yield strength, the rank in descending order is: 7075-T6 (589 MPa), 2090-T8E41 (551 MPa), 7475-T761 (549 MPa), and 2219-T87 (484 MPa).
2. In terms of notched tensile strength, the rank in descending order is: 7475-T761 (472 MPa), 7075-T6 (450 MPa), 2090-T8E41 (443 MPa), and 2219-T87 (435 MPa).
3. In terms of notched fatigue strength for  $4 \times 10^4$  cycles, the rank in descending order is: 2090-T8E41 (129 MPa), 7475-T761 (109 MPa), 7075-T6 (103 MPa), and 2219-T87 (102 MPa).
4. In terms of notch-yield ratio, the rank in descending order is 2219-T87 (0.90), 7475-T761 (0.86), 2090-T8E41 (0.80), and 7075-T6 (0.76).
5. The ratio of the notched fatigue strength at  $10^5$  cycles to the notched-tensile strength is nearly constant (0.21-0.23).

## ACKNOWLEDGEMENTS

The sheets of 2090 and 7475 were provided through the courtesy of Dr. R. Shepard of the Alcoa Technical Center, Alcoa Center, PA. This work was sponsored by the Superconducting Super Collider Central Design Group, Universities Research Association, with Dr. T. Scalise as the project monitor. We are grateful to Dr. Scalise for discussion and review the manuscript.

## SYMBOLS USED

E	- Young's modulus
EL	- tensile elongation
NFS	- notched fatigue strength
NFSR	- notched fatigue strength ratio (NFS/NTS)
NSR	- notch-strength ratio (NTS/UTS)
NTS	- notched tensile strength
NYR	- notch-yield ratio (NTS/YS)
UTS	- ultimate tensile strength
YS	- yield strength



## REFERENCES

- (1) Peters, C., Mirk, K., Wandestforde, A., and Taylor, C., presented at the Tenth International Conference on Magnet Technology, Boston, September 21-25, 1987.
- (2) Kaufman, J.W., Sha, G.T., Kohn, R.F., and Bucci, R.J., in: Cracks and Fracture, ASTM STP 601, Amer. Soc. Test. Maters., Philadelphia, 1976, pp. 169-190.
- (3) McCammon R.D., and Rosenberg, H.M., Proc. Roy. Soc. Lond., A, Vol. 242, 1957, pp. 203-211.
- (4) Dorward, R.C., Scripta Metall., Vol.20, 1986, pp. 1379-1383.
- (5) Glazer, J., Verzasconi, S.L., Sawtell, R.R., and Morris, J.W., Jr., Metall. Trans., Vol.18A, 1987, pp.1695-1701.
- (6) Venkateswara Rao, K.T., Hayashigatani, H.F., Yu, W., and Ritchie, R.O., Scripta Metall., Vol. 22, 1988, pp. 93-98.

## ELASTIC CONSTANTS OF FOUR Fe-Cr-Ni-Mn ALLOYS

S.A. Kim<sup>a</sup>, H.M. Ledbetter<sup>a</sup>, and Y. Li<sup>b</sup>

<sup>a</sup>Institute for Materials Science and Engineering  
National Bureau of Standards  
Boulder, Colorado 80303 (U.S.A.)

<sup>b</sup>Institute of Metal Research  
Academia Sinica  
Shenyang (P.R. China)

### ABSTRACT

Using ultrasonic methods, we measured the complete polycrystalline elastic constants of four Fe-Cr-Ni-Mn alloys. Combining these results with those reported previously for five similar alloys, we focused on the alloying effects of chromium, nickel, and manganese. The alloys contain 16 to 23 atomic percent chromium, 7 to 28 atomic percent nickel, and 0 to 13 atomic percent manganese. Only Mn produced regular effects, consistent with volume changes. Both Cr and Ni produced surprising increases in the bulk modulus and equally surprising decreases in the shear modulus. We hypothesize that changing the bonding electrons from d-character to s-character explains such irregularities. We fitted the measurements to Ducastelle's model, which contains two terms: bandstructure and repulsive energies.

### 1. INTRODUCTION

In cryogenic applications, austenitic stainless steels are used extensively for storage and handling because they resist corrosion and show relatively high strength, stability, and toughness.

Austenitic stainless steels are formed by adding f.c.c.-stabilizing elements such as nickel or manganese to the Fe-Cr system. Nickel in Fe-Cr not only acts as a strong austenite stabilizer, it also improves material properties [1]. Nickel shortage during World War II forced manufacturers to reduce or replace nickel with other elements such as manganese and nitrogen. Many questions arose. How do these replacements affect mechanical properties such as tensile strength, yield strength, elongation, weldability, formability, machinability, and corrosion resistance? Many researchers [2-4] considered these effects.

Intended for Materials Science and Engineering.

Elastic constant changes caused by reducing or replacing nickel with manganese in Fe-Cr-Ni were studied recently [5,6]. Elastic constants interrelate fundamental physical properties. Also, they are key design parameters. For cryogenic-equipment design, for example, thermal expansivity ( $\beta$ ) and thermal conductivity ( $\kappa$ ) are important variables to consider. Both  $\beta = \beta(\gamma, \rho, C_v, B)$  and  $\kappa = \kappa(\theta, \gamma, T)$  relate to elastic constants. We denote  $\gamma$  = Grüneisen parameter,  $\rho$  = mass density,  $C_v$  = specific heat,  $\theta$  = pervasive parameter,  $T$  = temperature, and  $B$  = bulk modulus. Elastic constants also relate closely to plastic-deformation properties.

In this study, we determined the elastic constants of four Fe-Cr-Ni-Mn alloys. We combined these results with our previous results for five similar alloys. From the set of nine, we deduced alloying effects of Cr, Ni, and Mn.

## 2. MEASUREMENTS

### 2.1 Materials

Alloys were prepared at the Institute of Metal Research (Shenyang). Table 1 shows the chemical compositions. The alloys received the following heat treatments. Alloy Fe-16Cr-28Ni: annealed 1 h at 1253 K, quenched in water to 993 K, and cooled in air for 16 h. Alloy Fe-23Cr-12Ni-5Mn: annealed 1 h at 1338 K and quenched in water. Alloys Fe-21Cr-9Ni-9Mn and Fe-21Cr-7Ni-9Mn: annealed 1 h at 1323 K and quenched in water.

### 2.2 Sound-velocity measurements

Room-temperature ultrasonic-sound velocities were determined by a pulse-echo-superposition technique. Quartz piezoelectric crystals with fundamental resonances between 3 and 9 MHz were used as transducers. X-cut and a.c.-cut transducers were used to produce longitudinal and shear waves, respectively. A transducer was rigidly cemented to a specimen's flat and parallel surface using phenyl salicylate as the bonding agent. Experimental details and the methods of obtaining the correct transit time were reported elsewhere [7]. The ultrasonic sound velocity,  $v$ , was computed from

$$v = \frac{2\ell}{t} . \quad (1)$$

Here,  $\ell$  denotes specimen length and  $t$  round-trip transit time.



Table 1. Chemical compositions, atomic percent.

Alloy	Cr	Ni	Mn	N	C	Si	P	S	Mo	V	Cu	Al	Ti	Fe
Fe-16Cr-28Ni-0Mn <sup>a</sup>	16.36	28.08	0.19	<0.02	0.11	0.34	0.02	0.01	0.89	0.29	-	0.41	2.16	Balance
Fe-23Cr-12Ni-5Mn <sup>b</sup>	23.48	12.04	4.97	1.22	0.21	0.57	0.04	0.01	1.49	0.24	-	-	-	Balance
Fe-21Cr-9Ni-9Mn	20.62	8.86	8.94	0.97	0.14	0.64	0.03	0.01	-	-	0.05	0.14	0.06	Balance
Fe-21Cr-7Ni-9Mn	21.36	7.05	9.07	1.01	0.17	0.99	0.04	<0.01	-	-	0.07	<0.06	0.06	Balance

<sup>a</sup> Also contains 0.01B

<sup>b</sup> Also contains 0.17Nb

### 2.3 Density measurement

Using distilled water as a standard, and Archimedes's method, we determined the specimen's density:

$$\rho = \frac{\rho_w}{1 - (m_w/m_a)} \quad (2)$$

Here,  $\rho_w$  = density of water,  $m_w$  = specimen mass in water, and  $m_a$  = specimen mass in air.

### 3. RESULTS

The elastic moduli are related to longitudinal,  $v_l$ , and transverse,  $v_t$ , ultrasonic sound velocities by

$$\text{longitudinal modulus: } C_l = \rho v_l^2 \quad (3)$$

$$\text{shear modulus: } G = \rho v_t^2 \quad (4)$$

$$\text{Young modulus: } E = \frac{3\rho v_t^2(v_l^2 - \frac{4}{3}v_t^2)}{v_l^2 - v_t^2} \quad (5)$$

$$\text{bulk modulus: } B = \rho(v_l^2 - \frac{4}{3}v_t^2) \quad (6)$$

$$\text{Poisson ratio: } \nu = \frac{1}{2} \frac{(v_l^2 - 2v_t^2)}{(v_l^2 - v_t^2)} \quad (7)$$

Table 2 shows room-temperature elastic constants and mass density.

Table 2. Elastic constants of Fe-Cr-Ni-Mn alloys corrected for C+N and Mo.

Alloy	Density (g/cm <sup>3</sup> )	C <sub>ℓ</sub> (GPa)	G (GPa)	B (GPa)	E (GPa)	ν
Fe-16Cr-28Ni-0Mn	8.029	269.1	72.77	172.2	191.5	0.3149
Fe-23Cr-12Ni-5Mn	7.879	259.8	72.96	162.6	190.3	0.3048
Fe-20Cr-9Ni-9Mn	7.825	253.8	76.94	151.2	197.3	0.2826
Fe-21Cr-7Ni-9Mn	7.802	254.9	76.51	153.0	196.7	0.2858
Fe-19Cr-1Ni-12Mn	7.734	253.3	74.7	153.7	192.8	0.291
Fe-19Cr-3Ni-13Mn	7.817	247.2	75.1	147.1	192.6	0.282
Fe-22Cr-6Ni-9Mn	7.838	252.8	75.4	152.3	194.1	0.288
Fe-22Cr-12Ni-5Mn	7.884	257.9	73.9	159.4	192.1	0.299
Fe-20Cr-9Ni-2Mn	7.860	260.5	77.7	156.9	200.1	0.287

Estimated error in the velocity measurements is  $d(\ln v) = [(d(\ln l))^2 + (d(\ln t))^2]^{1/2}$ . Both  $v_\ell$  and  $v_t$  of  $|d(\ln v)| < 0.08\%$  are expected. On density measurements, we estimate  $|d(\ln \rho)| < 0.01\%$ . Uncertainties in the elastic moduli are therefore  $3/2 |d(\ln C_\ell)| = |d(\ln G)| = |d(\ln B)| = |d(\ln E)| = 1/2 |d(\ln \nu)| < 0.3\%$ .

By linear-least-squares analysis,  $C = C_0 + ax_{Cr} + bx_{Ni} + cx_{Mn} + e$ , where  $e$  is the residual error associated with the response  $C$ , we determined the separate effects of chromium, nickel, and manganese. Table 3 shows the results, which reflect measured values corrected for both C+N and Mo content, using results reported previously [8,9]. The mean square error,  $s^2$ , is calculated from the error sum of squares with five degrees of freedom;  $s^2$  for  $C_\ell$ ,  $G$ ,  $B$ ,  $E$ , and  $\nu$  is  $3.89$ ,  $2.70$ ,  $11.9$ ,  $10.1$ , and  $5.6 \times 10^{-5}$ , respectively. We neglected variations in other alloying elements.

TABLE 3. Compositional variation of elastic constants based on nine Fe-Cr-Ni-Mn alloys:  $C = C_0 + ax_{Cr} + bx_{Ni} + cx_{Mn}$ ;  $x$  is in atomic percent.  $C_0$  and  $a$ ,  $b$ ,  $c$ , units are GPa, except dimensionless  $\nu$ .

C	C <sub>0</sub>	$\frac{a}{C_0} \times 10^3$	$\frac{b}{C_0} \times 10^3$	$\frac{c}{C_0} \times 10^3$
C <sub>ℓ</sub>	264.7	-0.7682	1.025	-3.526
G	84.11	-2.556	-3.190	-3.412
B	152.3	0.5837	4.180	-3.569
E	213.9	-2.203	-2.354	-3.495
ν	0.2651	2.675	4.946	0.2591

#### 4. DISCUSSION

A simple sphere-in-hole model (Bitter [10], Eshelby [11]) leads to expected elastic-stiffness changes related to volume changes,  $dV$ . If we focus on the bulk and shear moduli, then it follows that, for these materials, [8]

$$\frac{\Delta B}{B} = -1.69 \frac{dV}{V} \quad (8)$$

and

$$\frac{\Delta G}{G} = -2.06 \frac{dV}{V} . \quad (9)$$

Here, we took  $\nu = 0.290$  and other parameters reported previously [8]. From the numbers in Table 4, we expect that Mn will decrease B and G, that Cr will decrease both by a smaller amount, and that Ni will increase both. Among these six expectations, four are met. Contrary to expectation, Cr increases B, and Ni decreases G. Thus, a simple sphere-in-hole model, based on volume, fails to explain the alloy behavior. This suggests strong electronic changes.

Considering Mn, for B and G, we find its effect similar to that found previously for Fe-Cr-Ni alloys [13] where Mn varied up to 6 at. pct. Those alloys contained lower N content, averaging 0.6 at. pct. Despite Mn's many peculiar elemental properties, including a large change of this system's Néel temperature [14], it affects elastic properties in a regular, expected way. It is interesting that Mn contains 7 bonding electrons, close to the alloy's number: 7.8. Thus, among all possible d-electron alloying elements, Mn may least disrupt the alloy's electronic structure. As discussed by Pettifor [15], Mn prefers a c.p.h. or an f.c.c. crystal structure to a b.c.c. crystal structure.

TABLE 4. Properties of constituent atoms and one reference alloy.

	V (Å <sup>3</sup> )	B (GPa)	E (GPa)	G (GPa)	$\nu$
Fe	11.70	166.9	212.4	82.4	0.288
Cr	11.94	161.9	279.5	115.3	0.212
Ni	10.87	186.0	220.6	84.7	0.302
Mn	12.22	124.4	197.7	76.5	0.292
Fe-18Cr-8Ni <sup>a</sup>	11.59	158.2	199.6	77.4	0.290

<sup>a</sup> Refs. 7, 12.



Considering Cr, we find the unexpected result that B increases and that B and G change oppositely. Almost all elastic-constant models predict the same sign for  $(1/x)(dB/B)$  and  $(1/x)(dG/G)$ . A sign difference signals an interatomic-bonding change that affects (in this case) dilatational modes more than shear modes. Ledbetter and Kim [9] reported similar behavior for Mo alloyed into Fe-Cr-Ni. Cr and Mo are isoelectronic; both represent b.c.c. paradigms. We expect both to disrupt strongly the f.c.c. electronic structure (interatomic bonds), and produce unusual changes in f.c.c.-alloy physical properties. Also, we note that Cr, despite possessing a shear modulus 50 pct. larger than the Fe-Cr-Ni alloy, decreases the alloy's shear modulus. Mo, with a 60 pct. larger shear modulus, also decreases the alloy's shear modulus. Thus, rule-of-mixture models fail drastically for these d-electron alloys. Alloying alters sharply the electronic state.

Considering Ni, except for its magnetism, a typical f.c.c. element, we find its alloying effects surprisingly large and hard to understand, especially the sign difference in  $(1/x)(dB/B)$  and  $(1/x)(dG/G)$ . Again, this suggests an interatomic-bonding change, in this case affecting shear modes more than dilatational modes. Thus, electronically, Ni behaves differently from Cr. Even though both are 3d-electron transition metals, Cr possesses only six bonding electrons while Ni possesses ten.

The present results for Ni differ from those found in another study [16] in Fe-21Cr-xNi-9Mn (at. pct.) where Ni varied from 4 to 11 at. pct. and the alloys contained lower N content, averaging 0.8 at. pct. For the shear modulus, that study found  $(1/x)(dG/G) = 0.861 \times 10^{-3}$ , much smaller than the present result. The reason for this difference remains under study.

Above, we described irregular responses of B and G (which reflect dilatational and shear stiffness, respectively) to alloying. By irregular, we mean inconsistent with responses expected from volume effects, Eqs. (8) and (9). We can achieve some understanding of these irregular responses by realizing that B and G reflect mainly changes in the s-electrons and d-electrons, respectively. The s-electrons represent a wide, spherically symmetrical distribution. In contrast, d-electrons represent a narrow, localized, highly directional distribution. The shear modulus G represents resistance to changes in interatomic-bond angles (the d-electrons). The bulk modulus B represents resistance to changes in interatomic-bond lengths (both s-electrons and d-electrons). For transition metals, Pettifor [17] showed that the bulk modulus arises largely from the s-electron contribution, a contribution enhanced strongly by the ion-core orthogonality constraint. Pettifor emphasized also that the s-electrons figure prominently in transition-metal cohesion; they provide a repulsive pressure that counters the strong d-electron attraction. Thus, the d-electrons often contribute negatively to the bulk modulus. The negative contribution of d-electrons to the bulk modulus arises also in the renormalized-atom transition-metal cohesive-energy model of Gelatt et al. [18]. For the cohesive energy,  $E(r)$ , they find four components: (1) renormalization energy, (2) s-band formation energy, (3) d-band broadening energy, and (4) s-d hybridization energy. Combined and expressed as  $E(r)$ , the last two terms show a negative curvature versus  $r$ . The bulk modulus relates to  $E(r)$  by [19]

$$B = \frac{1}{12\pi r_0} \left( \frac{\partial^2 E(r)}{\partial r^2} - \frac{2}{r} \frac{\partial E(r)}{\partial r} \right)_{r=r_0} \quad (10)$$

The renormalization and s-band terms show a positive curvature; thus they contribute positively to B. As electrons change from d-character to s-character, we expect bulk modulus to increase and shear modulus to decrease. The present study shows that both Cr and Ni cause such changes. A previous study [9] showed the same for Mo. It remains undetermined whether changing the d-electron character from  $e_g$  to  $t_{2g}$  [20] affects the elastic constants. These two subbands possess a different wave-function symmetry. The  $e_g$  subband shows six lobes along  $\langle 111 \rangle$  directions. For these f.c.c. alloys, the Young-modulus maxima occur along  $\langle 111 \rangle$  directions.

The opposite changes in the bulk and shear moduli cause us to focus on the Poisson ratio

$$\nu = \frac{1}{2} \cdot \frac{3B - 2G}{3B + G} \quad (11)$$

In differential form, we obtain

$$\begin{aligned} \frac{d\nu}{\nu} &= \frac{9BG}{(3B+G)(3B-2G)} \left( \frac{dB}{B} - \frac{dG}{G} \right) \\ &= 0.624 \left( \frac{dB}{B} - \frac{dG}{G} \right) \end{aligned} \quad (12)$$

The factor 0.624 applies to the Fe-18Cr-8Ni reference alloy. From Eq. (12), we see that the opposite changes in B and G combine to produce a large  $d\nu/\nu$ . This reminds us of the Köster-Franz [21] view that "Poisson's ratio depends to a much greater extent on the conditions of bonding than do the other elastic constants." Considering the Voigt bound, Ducastelle [22] derived the following simple relationship:

$$\nu_V = \frac{1}{2} \cdot \frac{3 - \bar{x}}{6 - 7\bar{x}} \quad (13)$$

Here,  $\bar{x} = q/p$ , the ratio of the bandstructure-energy and repulsive-energy exponential coefficients, with  $p > q$ . We can extend this model to the Reuss bound:

$$\nu_R = \frac{9 - 4\bar{x}}{33 - 38\bar{x}} \quad (14)$$

Finally, we can obtain the physically more realistic Hill-model result:

$$\nu_H = \frac{87 - 34\bar{x}}{333 - 386\bar{x}} \quad (15)$$



Solving for  $\bar{x}$ , we obtain

$$\bar{x} = \frac{333\nu - 87}{386\nu - 34} . \quad (16)$$

Thus, the Poisson ratio leads directly to the Ducastelle-model q/p ratio, which gives the relative contribution of bandstructure energy,  $U_b$ , and repulsive energy,  $U_r$ , to cohesion [9]:

$$\left| \frac{U_b}{U_r} \right| = \frac{p}{q} . \quad (17)$$

Ducastelle's model represents almost the simplest possible equilibrium model of a transition metal, two terms: a repulsive term and an attractive bandstructure term. Better models contain more terms. For example, the renormalized-atom model of Gelatt et al. contains four principal energy terms. Positive contributions to the bulk modulus arise from two terms: renormalization and s-band. The renormalization energy relates to the free-atom wave functions. The s-band energy is given by

$$\Delta E_s = E_0 + 3/5 E_f - E_s^r . \quad (18)$$

Here,  $E_0$  denotes the bottom of the s-band,  $E_f$  denotes Fermi energy, and  $E_s^r$  denotes the renormalized-atom one-electron energy. Negative contributions to the bulk modulus arise from the combined d-band broadening and s-d hybridization. Neither the renormalization energy nor the d-band terms show large curvature near the equilibrium volume. Thus, the s-band term dominates the bulk modulus. However, for copper, for example, considering only eq. (18) predicts a bulk modulus approximately 50% too high. Thus, we cannot neglect the the d-band terms, which contribute negatively. The large positive curvatures of  $E_0$  and  $E_f$  near the equilibrium volume result from an effective compression caused by s-d hybridization. (In the 3d-row, K and Cu possess atomic volumes of 71.4 and 11.7 Å<sup>3</sup>, respectively!)

Table 5 shows the results of fitting Ducastelle's model to our nine alloys, to an 18Cr-8Ni alloy [7], and to seven f.c.c. elements. Columns 2-4 show the input:  $\nu$  = Poisson ratio, B = bulk modulus, U = cohesive energy. Columns 5 and 6 show the percentage bandstructure contributions to U and to B. Columns 7-9 show various forms of the p and q coefficients. As described by Fürth [23],  $pqr^2$  correlates with harmonic properties such as the bulk modulus; and  $(p+q)r$  correlates with anharmonic properties such as thermal expansivity, thermal-expansivity temperature derivative, bulk-modulus temperature derivative, and bulk-modulus pressure derivative.

Although the bandstructure energy dominates the cohesive energy, it contributes only 16 to 34 percent to the bulk modulus. For our nine alloys, we note a larger variation in  $(p+q)r$  than in  $pqr^2$ . Thus, these alloys would show larger variations in thermal expansivity than in elastic stiffness, and the usual elastic-stiffness/thermal-expansivity empirical interrelationships should be less reliable.



TABLE 5. Ducastelle-model parameters.

Material	$\nu$	B (GPa)	U (GJ/m <sup>3</sup> )	$U_b/U$	$B_b/B$	q/p	(p+q)r	pqr <sup>2</sup>
Ag	0.364	101.2	27.8	0.76	0.30	0.32	13.3	32.7
Au	0.424	173.5	35.9	0.71	0.34	0.42	14.5	43.5
Co	0.310	188.9	63.8	0.84	0.23	0.19	14.1	26.6
Cu	0.341	135.3	47.5	0.79	0.28	0.27	12.3	25.6
Fe	0.314	188.3	58.7	0.83	0.24	0.20	14.4	28.9
Ni	0.302	186.0	65.0	0.86	0.22	0.17	14.6	25.8
Pt	0.395	282.7	62.2	0.73	0.32	0.38	14.4	40.9
Fe-18Cr- 8Ni	0.290	158.2	58.6	0.89	0.19	0.12	15.8	24.3
Alloy 1	0.315	172.2	59.5	0.83	0.24	0.20	13.6	26.1
2	0.305	162.6	58.1	0.85	0.23	0.17	14.2	25.2
3	0.283	151.2	58.4	0.91	0.16	0.09	17.2	23.3
4	0.286	153.0	58.2	0.90	0.18	0.11	16.5	23.7
5	0.291	153.7	57.8	0.89	0.19	0.13	15.5	23.9
6	0.282	147.1	57.9	0.92	0.16	0.09	17.2	22.9
7	0.288	152.3	58.2	0.90	0.18	0.12	15.9	23.6
8	0.299	159.4	58.1	0.87	0.21	0.15	14.6	24.7
9	0.287	156.9	58.7	0.90	0.18	0.11	16.3	24.1

## 5. CONCLUSIONS

Concerning the elastic constants of these quaternary Fe-Cr-Ni-Mn alloys, we reached four conclusions:

1. Manganese lowers all the elastic stiffnesses and the Poisson ratio. This agrees with expectations based on volume change.
2. Both Cr and Ni increase bulk modulus and decrease shear modulus. This agrees with results reported previously for Mo. Such opposite alloying effects for B and G disagree with most theoretical models. A qualitative explanation arises by invoking a change in bonding electrons from d-character to s-character.

3. The strong Ni alloying effects differ from those found previously for lower Ni concentrations.
4. Except for Mn, which behaved regularly, the other alloying elements, Cr and Ni, caused unusually large changes in the Poisson ratio, an elastic constant that responds strongly to changes in the type of interatomic bonding.

#### REFERENCES

1. J.H.G. Monypenny, *Stainless Iron and Steel*, Wiley, New York, 1931, p. 157.
2. R.B. Gunia and G.R. Woodrow, *J. Metals*, 5 (1970) 413-430.
3. B.N. Ferry and J.F. Eckel, *J. Metals*, 5 (1970) 99-107.
4. H.I. McHenry, in *Austenitic Steels at Low Temperatures*, Plenum, New York, 1983, pp. 1-28.
5. H.M. Ledbetter, *Metall. Trans. A*, 11 (1980) 1067-1069.
6. H.M. Ledbetter, *Mater. Sci. Eng.*, 29 (1977) 255-260.
7. H.M. Ledbetter, N.V. Frederick, and M.W. Austin, *J. Appl. Phys.*, 51 (1980) 305-309.
8. H.M. Ledbetter and M.W. Austin, *Mat. Sci. Eng.*, 70 (1985) 143-149.
9. H.M. Ledbetter and S.A. Kim, *J. Mater. Res.*, 3 (1988) 40-44.
10. F. Bitter, *Phys. Rev.*, 37 (1931) 1527-1547.
11. J.D. Eshelby, *J. Appl. Phys.*, 25 (1954) 255-261.
12. H.M. Ledbetter and M.W. Austin, *Metal Sci.*, 3 (1987) 101-104.
13. H.M. Ledbetter, *J. Mater. Sci.*, 20 (1985) 2923-2929.
14. E.R. Jones, T. Datta, C. Almasan, D. Edwards, and H.M. Ledbetter, *Mater. Sci. Eng.*, 91 (1987) 181-188.
15. D.G. Pettifor, *J. Phys. C*, 3 (1970) 367-377.
16. H.M. Ledbetter, Ming Lei, and Yiyi Li, to be published.
17. D.G. Pettifor, *J. Phys. F*, 8 (1978) 219-230.
18. C.D. Gelatt, H. Ehrenreich, and R.E. Watson, *Phys. Rev. B*, 15 (1977) 1613-1627.
19. S. Raimes, *The Wave Mechanics of Electrons in Metals*, North-Holland, Amsterdam, 1961, p. 275, eqn. 9.90.

20. J.B. Goodenough, Phys. Rev., 120 (1960) 67-83.
21. W. Köster and H. Franz, Metall. Rev., 6 (1961) 1-55.
22. F. Ducastelle, J. Physique, 31 (1970) 1055-1062.
23. R. Fürth, Proc. Roy. Soc., A183 (1944) 87-110.





## NICKEL EFFECT ON ELASTIC CONSTANTS OF Fe-Cr-Ni ALLOYS

M. Lei and H. Ledbetter

Institute for Materials Science and Engineering  
National Institute of Standards and Technology  
Boulder, Colorado 80303, USA

Y. Li

Institute of Metal Research  
Shenyang, People's Republic of China

Using a kilohertz-frequency standing-wave method, we determined the effect of Ni content on the elastic constants of Fe-Cr-Ni alloys containing nominally 20.3 mass percent Cr. Nickel varied from 6.1 to 11.8 mass percent. As expected, we found little change. For example, for five alloys, the Young modulus averaged  $196.1 \pm 1.7$  GPa. Similarly, the shear modulus averaged  $77.3 \pm 0.4$  GPa. Internal friction measured both in extension and torsion showed no systematic composition dependence. The small elastic-constant changes agree with deductions based on atomic size. However, the small decrease in bulk modulus and accompanying increase in shear modulus deserve focus, which we provide by using a Ducastelle model for transition-metal alloys. The model contains two terms: bandstructure and ion-core-repulsion.

Effects of carbon and nitrogen [1] and manganese [2] on elastic properties of Fe-Cr-Ni alloys were reported. Also, one of the authors [3] reported measurements and modeling of molybdenum-alloying effect on Fe-Cr-Ni-alloy elastic constants. Here we report new measurements and modeling on the effect of nickel.

Materials were produced at the Institute of Metal Research, Shenyang, China. Table 1 shows their chemical compositions.

Intended for publication in Materials Science and Engineering.

Table 1. Chemical composition (mass %), balance Fe.

Alloy	Cr	Ni	Mn	C	Si	S	P	N
21	20.02	6.13	9.29	0.020	0.51	0.011	0.011	0.15
22	20.15	6.20	9.35	0.035	0.58	0.010	0.013	0.22
24	20.25	8.02	9.25	0.017	0.51	0.013	0.009	0.20
25	20.43	10.17	9.00	0.014	0.48	0.013	0.009	0.20
29	20.37	11.77	9.22	0.018	0.40	0.015	0.010	0.28

We determined the Young and shear moduli and the associated internal friction by using a Marx kilohertz-frequency resonance method [4, 5]. Measurement details were described elsewhere [6]. Here we give expressions for Young modulus,  $E$ , and torsional modulus (shear modulus),  $G$ :

$$E = 4\rho f_s^2 l_s^2 = 4\rho l_s^2 \left[ f_o^2 + (f_o^2 - f_q^2) \frac{m_q}{m_s} \right], \quad (1)$$

and

$$G = 4\rho f_s^2 l_s^2 = 4\rho l_s^2 \left[ f_o^2 + (f_o^2 - f_q^2) \frac{m_q}{m_s} \left( \frac{d_q}{d_s} \right)^2 \right]. \quad (2)$$

Here,  $\rho$  and  $l$  denote mass density and specimen length;  $f$  denotes frequency;  $m$  and  $d$  indicate mass and diameter. The subscripts  $s$ ,  $o$ , and  $q$  denote specimen, complete oscillator, and quartz crystal. The specimen's internal friction,  $Q_s^{-1}$ , is determined by

$$Q_s^{-1} = Q_o^{-1} + (Q_o^{-1} - Q_q^{-1}) m_q/m_s. \quad (3)$$

Table 2 shows the principal measurement results. Since the materials are quasi-isotropic, we invoke the well-known relationships for bulk modulus,  $B$ , and Poisson ratio,  $\nu$ :

$$B = \frac{GE}{3(3G - E)}, \quad (4)$$

and

$$\nu = \frac{E}{2G} - 1. \quad (5)$$

Figure 1 shows elastic moduli and Poisson's ratio versus nickel content. We see that nickel increases slightly the Young and shear moduli and decreases both bulk modulus and Poisson ratio. To verify that the changes are real, not measurement error, we focused on measurement inaccuracy. For the longitudinal mode, we repeated one measurement ten times and found that the standard deviation is 0.08 GPa. For the shear mode, we repeated one measurement six times and found a standard deviation of 0.05 GPa.



Table 2. Effect of nickel on Fe-Cr-Ni-alloy elastic constants and internal friction.

Alloy	Ni (mass pct.)	$\rho$ (g/cm <sup>3</sup> )	E (GPa)	G (GPa)	$Q_E^{-1}$ (10 <sup>-5</sup> )	$Q_G^{-1}$ (10 <sup>-5</sup> )
21	6.13	7.786	195.0	76.9	2.9	5.7
22	6.20	7.681	195.0		10.5	
24	8.02	7.764	195.6	77.4	5.5	5.4
25	10.17	7.772	195.8		5.9	
29	11.77	7.759	195.6	77.6	6.9	2.6

Studies by Ledbetter and Austin [7] showed that nickel slightly decreases the effective atomic volume. Volume changes usually cause physical-property changes. For example, consider the bulk modulus of Fe. From 0 to 300 K, it decreases 2.95%, while the volume increases 0.59%. Ignoring the thermal contribution to elastic softening, we obtain

$$\frac{\Delta B/B}{\Delta V/V} = - \frac{0.0295}{0.0059} = -4.96. \quad (6)$$

Thus, we expect the bulk modulus to increase approximately 5% per percent volume decrease.

A quantum-mechanical theory by Ducastelle [8] leads to simple relationships among volume, bulk modulus, and cohesive energy. In the theory, the total energy,  $U$ , arises from two sources: d-band energy,  $U_b$ , calculated by a tight-binding approximation and Born-Mayer ion-core repulsive energy,  $U_r$ . Thus,

$$U = U_b + U_r = -W_0 e^{-qr} + C e^{-pr}. \quad (7)$$

Here,  $W_0$ ,  $C$ ,  $p$ , and  $q$  are constants; and  $r$  denotes the atomic radius. A simple expression arises for the equilibrium radius:

$$r_0 = \frac{1}{p-q} \ln \frac{pC}{qW_0}. \quad (8)$$

For the bulk modulus, Ducastelle obtained

$$B = V_0 \left( \frac{\partial^2 U}{\partial V^2} \right)_{V_0} = \frac{r_0^2}{9V_0} \left( \frac{\partial^2 U}{\partial r^2} \right)_{r_0} = B_r + B_b = \frac{pq r_0 U_c}{9V_0(p-q)} (2 + pr_0 - 2 - qr_0). \quad (9)$$

Here,  $U_c$  denotes cohesive energy, and  $V_0 = 4\pi r_0^3/3$  denotes atomic volume. Thus, Ducastelle's model predicts that decreased atomic volume leads to increased bulk modulus. If volume changes little, then we must consider changes in other parameters.

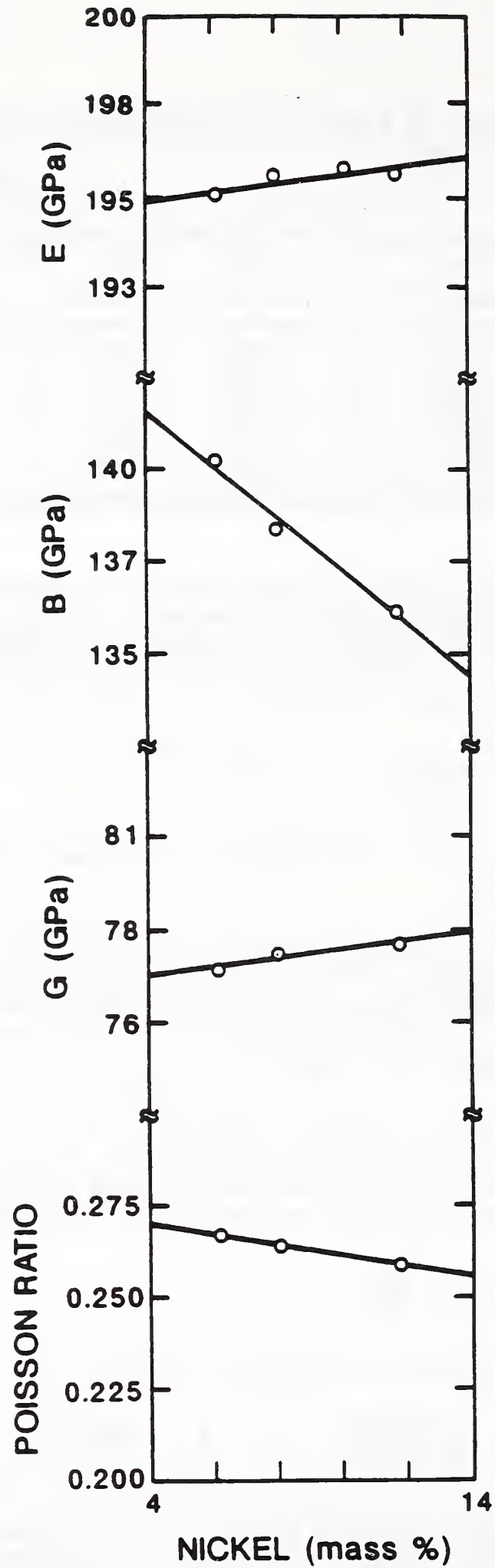


Fig. 1. Compositional variation of E - Young modulus, B - bulk modulus, G - shear modulus, and  $\nu$  - Poisson ratio.

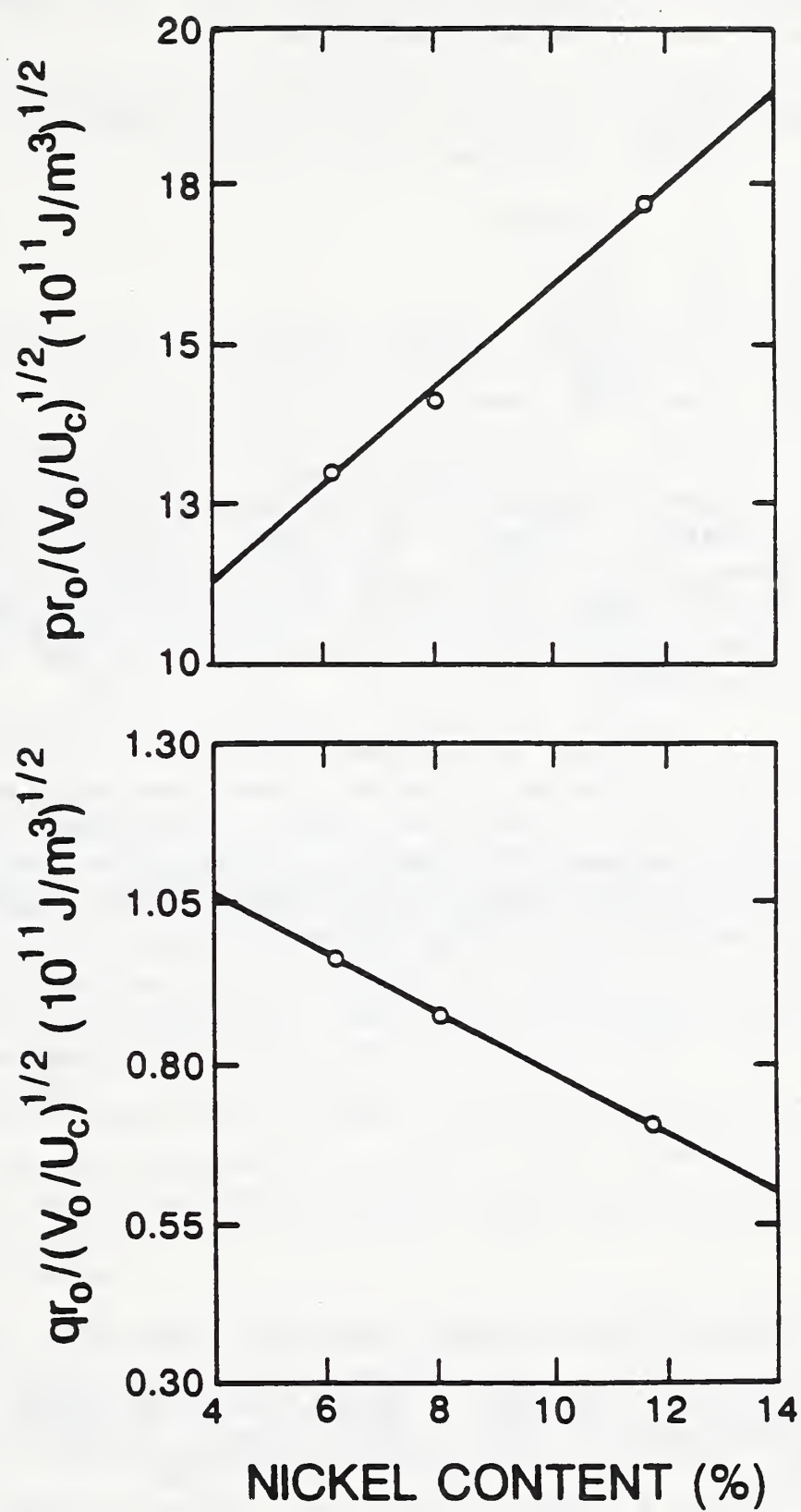


Fig. 2. Compositional variation of  $pr_0/\sqrt{V_0/U_c}$  and  $qr_0/\sqrt{V_0/U_c}$ .



Despite some limitations of Ducastelle's model, we can use it to estimate  $pr_0$  and  $qr_0$ , parameters characterizing the repulsive and band-structure energies. For this estimate, besides Eq. (9), we need another relationship among  $p$ ,  $q$ , and physical properties. We choose the Poisson ratio  $\nu$ . Using Ducastelle's expression for  $\nu$ :

$$\nu = \frac{1}{2} \cdot \frac{3 - (q/p)}{6 - 7(q/p)}, \quad (10)$$

together with Eq. (9), we obtain

$$pr_0 = 3 \left[ \frac{14\nu - 1}{12\nu - 3} \cdot \frac{BV_0}{U_c} \right]^{\frac{1}{2}}, \quad (11)$$

and

$$qr_0 = 3 \left[ \frac{12\nu - 3}{14\nu - 1} \cdot \frac{BV_0}{U_c} \right]^{\frac{1}{2}}. \quad (12)$$

In this study, we ignore the volume change caused by nickel alloying and take  $V_0/U_c$  as a constant. Figure 2 shows that  $p$  increases and  $q$  decreases as nickel increases. Since  $p$  and  $q$  characterize repulsive and bandstructure energy, respectively, added nickel to Fe-Cr-Ni alloy will decrease the contribution of repulsive energy and increase that of the bandstructure energy to the total energy.

In summary, we find that Ni alloyed into f.c.c. Fe-Cr-Ni alloys produces small elastic-constants changes, consistent with small atomic-volume change. However, the small bulk-modulus decrease coupled with a small shear-modulus increase provides a surprise and a challenge to theory. Applying Ducastelle's model suggests that adding nickel increases the bandstructure: core-repulsion energy balance.

#### ACKNOWLEDGMENT

M. Lei is a visiting scientist from the Institute of Metal Research (Shenyang).

#### REFERENCES

1. H.M. Ledbetter and M.W. Austin, Mater. Sci. and Eng., 70 (1985) 143-149.
2. H.M. Ledbetter and S.A. Kim, J. Mater. Sci., 23 (1988) 2129-2132.
3. H.M. Ledbetter and S.A. Kim, J. Mater. Res., 3 (1988) 40-44.
4. J. Marx, Rev. Sci. Instrum., 22 (1951) 503-509.
5. W.H. Robinson and A. Edgar, IEEE Trans. Sonics Ultrason., SU-21 (1974) 98-105.
6. H.M. Ledbetter, Ming Lei, and M.W. Austin, J. Appl. Phys., 59 (1986) 1972-1976.
7. H.M. Ledbetter and M.W. Austin, National Institute of Standards and Technology, Boulder, Colorado (1986), unpublished.
8. F. Ducastelle, J. Phys., 31 (1970) 1055-1062.

# NITROGEN EFFECT ON ELASTIC CONSTANTS OF F.C.C. Fe-18Cr-19Mn ALLOYS

S. Lin and H. Ledbetter

Institute for Materials Science and Engineering  
National Institute of Standards and Technology  
Boulder, Colorado 80303, U.S.A.

## ABSTRACT

Previously, we studied effects of interstitial carbon-plus-nitrogen on the elastic constants of f.c.c. Fe-18Cr-10Ni-1Mn alloys. Consistent with a volume increase, all the elastic stiffnesses decrease with increasing C+N. The present alloys show different behavior: even though volume increases, interstitial nitrogen atoms increase the bulk modulus. We describe that 3d-electron elements show a peculiar bulk-modulus-electron-concentration behavior ( $B$  versus  $n_e$ ). At first  $B$  increases with increasing  $n_e$ ; beyond a critical concentration,  $B$  decreases rapidly. Applying Ducastelle's model (bandstructure and repulsion energies) shows that interstitial nitrogen increases the bandstructure contribution to the bulk modulus.

## 1. INTRODUCTION

Adding f.c.c. stabilizing elements such as nickel or manganese to Fe-Cr alloys produces various types of austenitic stainless steels, which show different physical properties. The interstitial atoms—nitrogen and carbon—stabilize the f.c.c. lattice and improve the strength, toughness, and corrosion resistance [1]. Nitrogen-strengthened austenitic stainless steels find extensive low-temperature applications, and they interest many researchers [1-5].

Ledbetter and coworkers [5] reported the effects of carbon and nitrogen interstitials on the elastic constants of AISI-304 stainless steels (Fe-18Cr-10Ni-1Mn). They found that carbon and nitrogen decrease all the elastic stiffnesses.

In this study, we considered higher-Mn alloys and found big differences between Fe-18Cr-19Mn and Fe-18Cr-10Ni-1Mn. Especially, nitrogen interstitial atoms affect the elastic constants differently. We think that the lower Ni content produces a negligible elastic-constant change.

Intended for Materials Science and Engineering.

TABLE 1

Chemical composition of high-Mn stainless steels (at.%), balance Fe

Alloy	N	C	Si	Mn	Cr	Ni	Mo	V
1	1.51	0.06	0.638	19.97	14.62	0.296	0.079	0.117
2	2.22	0.62	0.668	18.24	18.96	0.210	0.045	0.053
3	3.05	0.18	0.495	19.85	19.22	0.528	0.006	0.126
4	3.70	0.27	0.991	18.89	18.01	0.118	1.160	0.147

## 2. MEASUREMENTS

### 2.1 Materials

We obtained four stainless steels from a commercial source. They had a similar base composition, but different interstitial-atom content. Table 1 shows the detailed chemical compositions.

### 2.2 Sound-velocity methods

We used a pulse-echo-overlap technique [6] to measure the longitudinal and transverse sound velocities at ambient temperature. The specimens were cut into 1.5-cm cubes and were ground so that opposite faces were flat and parallel within 5  $\mu\text{m}$ . Quartz piezoelectric crystals with fundamental resonances between 2 and 7 MHz were glued to the specimens with phenyl salicylate. An x-cut transducer was used for longitudinal waves and an ac-cut transducer for transverse waves. Further experimental details were given elsewhere [6]. The sound velocity  $v$  was obtained from

$$v = 2l/t. \quad (1)$$

Here,  $l$  denotes the specimen length and  $t$  the round-trip transit time.

### 2.3 Mass-density measurement

We used Archimedes's method to determine the specimen's mass density. Details are described elsewhere [7].

## 3. RESULTS

Elastic-stiffness constants were derived from the general relationship

$$C_i = \rho v_i^2. \quad (2)$$



Here,  $\rho$  denotes mass density and subscript  $i$  denotes the mode of the sound wave. For the usual quasiisotropic elastic constants we have the following relationships:

$$\text{longitudinal modulus} = C_{\ell} = \rho v_{\ell}^2, \quad (3)$$

$$\text{shear modulus} = G = \rho v_t^2, \quad (4)$$

$$\text{bulk modulus} = B = C_{\ell} - (4/3)G, \quad (5)$$

$$\text{Young's modulus} = E = 3GB/(C_{\ell}-G), \quad (6)$$

$$\begin{aligned} \text{Poisson's ratio} = \nu &= (E/2G)-1 \\ &= \frac{1}{2}(C_{\ell}-2G)/(C_{\ell}-G). \end{aligned} \quad (7)$$

Here,  $v_{\ell}$  and  $v_t$  denote the longitudinal and transverse sound velocities.

Table 2 shows the results for  $\rho$ ,  $C_{\ell}$ ,  $G$ ,  $B$ ,  $E$ , and  $\nu$ . Figure 1 shows the relative elastic-constant changes with carbon-plus-nitrogen content. Table 3 gives the least-squares results obtained by a linear fit:

Table 2. Mass density and elastic constants at  $T = 295$  K

Alloy	N+C (at.%)	Density (g/cm <sup>3</sup> )	$v_{\ell}$ (km/s)	$v_t$ (km/s)	$C_{\ell}$ (GPa)	$G$ (GPa)	$B$ (GPa)	$E$ (GPa)	$\nu$
1	1.575	7.765	5.607	3.188	244.1	78.92	138.9	199.1	0.261
2	2.843	7.716	5.655	3.172	246.8	77.64	143.2	197.3	0.270
3	3.230	7.690	5.671	3.163	247.3	76.94	144.7	196.1	0.274
4	3.972	7.671	5.697	3.146	249.0	75.92	147.7	194.5	0.281

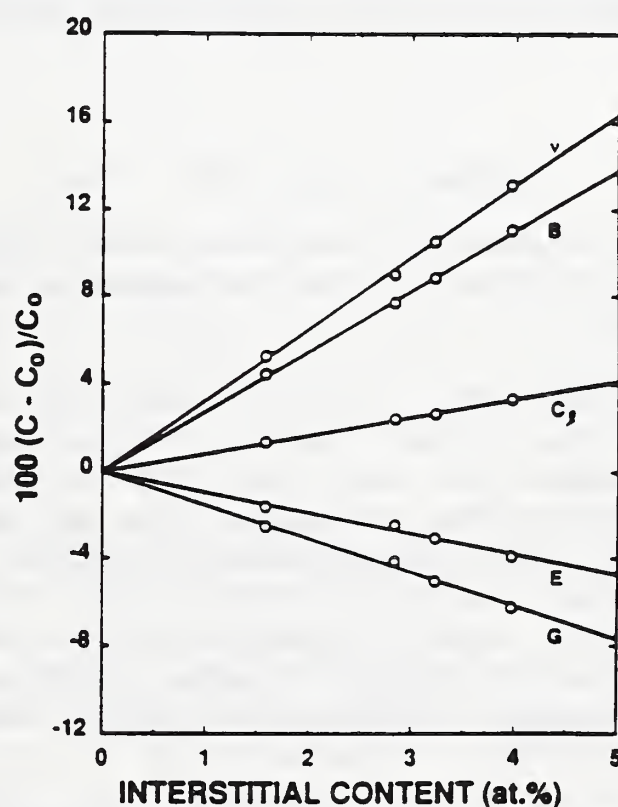


Fig. 1. Variation of elastic constants with interstitial carbon-plus-nitrogen content for high-manganese austenitic stainless steels at 295 K.

TABLE 3. Least-squares parameters for various elastic constants at 295 K

	$C_p$ (GPa)	G (GPa)	B (GPa)	E (GPa)	$\nu$
C(0)	241.0	80.98	133.0	202.3	0.248
a	2.005	-1.247	3.667	-1.912	0.00811
100·a/C(0)	0.832	-1.540	2.758	-0.945	3.269

$$C = C_0 + ax_{C+N}. \quad (8)$$

Here,  $x_{C+N}$  denotes atomic percentage of interstitial atoms: carbon plus nitrogen. Table 3 also shows  $100 \cdot a/C_0$ , the percentage change in elastic-constant per percentage change in alloying element.

To calculate the unit-cell size we used the following formula:

$$a^3 = V = \frac{M \cdot N}{\rho}. \quad (9)$$

Here,  $a$  denotes the unit-cell dimension,  $V$  the related volume,  $\rho$  the mass density,  $M$  the effective atomic mass,  $N$  the effective number of atoms in each unit cell.

Figure 2 shows the unit-cell size versus combined interstitial-atom content.

#### 4. DISCUSSION

High-manganese austenitic stainless steels (Fe-18Cr-19Mn) show different interstitial-alloying effects from low-manganese austenitic stainless steels (Fe-18Cr-10Ni-1Mn).

As in Fe-18Cr-10Ni-1Mn, in Fe-18Cr-19Mn the interstitial carbon-plus-nitrogen increases the volume. In Fig. 2, two lines show the linear-least-squares analysis results for these two types of alloys; the solid line corresponds to Fe-18Cr-19Mn; the dashed line corresponds to Fe-18Cr-10Ni-1Mn [8]. For these two cases, these results indicate the same interstitial-induced volume change. In Fe-18Cr-19Mn alloys, the interstitial carbon-plus-nitrogen decreases the shear modulus and Young's modulus but increases the bulk modulus. In Fe-18Cr-10Ni-1Mn alloys, interstitial carbon plus nitrogen decreases all the elastic stiffnesses. Eshelby's model based on volume change explains these decreases.

Small volume changes usually cause large physical-property changes. In unalloyed iron, pressure studies [9] show that

$$\frac{\Delta B/B}{\Delta V/V} = - \frac{\Delta B}{\Delta P} = -5.29. \quad (10)$$

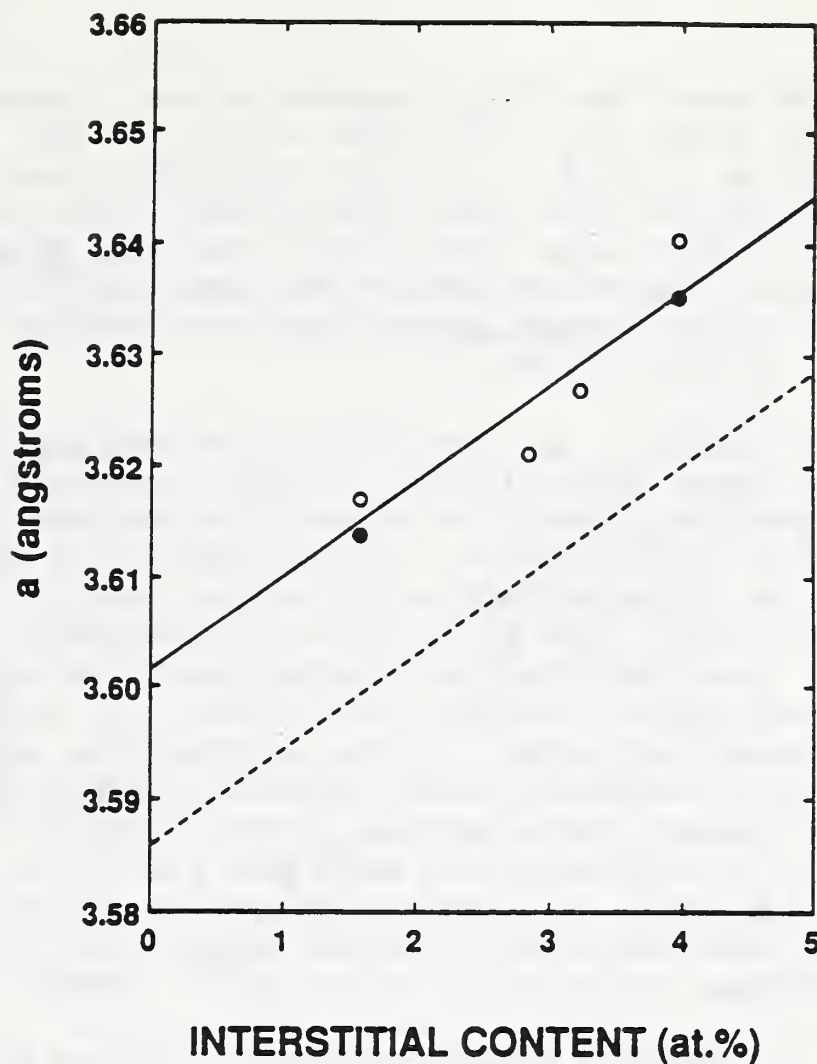


Fig. 2. Unit-cell size versus combined interstitial-atom content. Dashed line indicates low-manganese austenitic stainless steels. Filled symbols from x-ray diffraction. Open symbols from macroscopic mass density.

Going from alloy 1 to alloy 4, the volume change is

$$\Delta V/V = 3\Delta a/a = 2.2\%. \quad (11)$$

If we use Eq. (10) to estimate the interstitial-atom-induced volume effect, we get

$$\Delta B/B = -5.29 \Delta V/V = -12\%. \quad (12)$$

This contrasts with the measured value: 6.3%, with opposite sign! The simple volume effect fails to explain this unusual bulk-modulus behavior.

By measurement, we obtained  $(1/x_{N+C})(\Delta B/B) = 0.028$ , where  $x_{N+C}$  denotes interstitial concentration. Compared with the low-manganese case where  $(1/x_{N+C})(\Delta B/B) = -0.0085$  or an Eshelby-model prediction  $(1/x_{N+C})(\Delta B/B) = -0.0104$ , this is too high in absolute value by a factor of approximately 3, and is opposite in sign. For the shear modulus, we have  $(1/x_{N+C})(\Delta G/G) = -0.015$ , which is almost two times larger than  $-0.0052$  found in low-manganese stainless steels. But it comes close to an Eshelby-model prediction:  $(1/x_{N+C})(\Delta G/G) = -0.012$ .



For the zero-interstitial-content elastic constants, we get  $B_0 = 133.0$  GPa,  $G_0 = 81.0$  GPa,  $E_0 = 202.3$  GPa, and  $\nu_0 = 0.248$ . For the low-manganese case, we get  $B_0 = 159.6$ ,  $G_0 = 78.8$ ,  $E_0 = 203.2$ , and  $\nu_0 = 0.280$ . Thus, Mn does not change much the shear and Young's moduli, but it decreases the bulk modulus 17%. This large change correlates with manganese's large atomic volume, which expands the lattice and makes the lattice more compressible. A low Poisson ratio suggests weak interatomic bonding caused by increased atomic separation, as shown in Fig. 2.

In these alloys, the interstitials strongly affect the Poisson ratio. Measurement shows  $(1/x_{N+C})(\Delta\nu/\nu) = 0.0327$ , compared to  $-0.0015$  for low-manganese stainless steels, a factor of approximately  $-22$ ! In Fe-18Cr-10Ni-1Mn alloys [10], when an interstitial C or N atom is added to the f.c.c. unit cell, the compound  $Fe_4X$  or  $FeX$  exists locally (where X denotes C or N interstitial atom). The existence of intermetallic compounds means localized electrons. Localized-electron bonding lowers Poisson's ratio and increases the shear modulus but not the bulk modulus. In high-manganese alloys, this kind of compound may exist, but the bulk-modulus increase and the shear-modulus decrease indicate weaker covalent bonding or less-localized electrons. The large Poisson's-ratio increase shows a change in atomic bonding [11]. We suppose that in high-manganese stainless steels M-X electrons behave more itinerant than local. In coherent-potential-approximation calculations, Ohta [12] thinks that carbon and nitrogen simply provide extra valence electrons. These additional itinerant electrons would increase the bulk modulus.

Cho [13] showed a linear correlation between bulk modulus  $B$  and net-bonding-valence-electron concentration  $n_e$ . For nonmagnetic 3d-electron elements, a linear correlation exists; but for magnetic 3d-electron elements,  $B$  first increases linearly with increasing  $n_e$ . Beyond a critical concentration near  $5.3 \times 10^{29} \text{m}^{-3}$ ,  $B$  decreases rapidly. We calculated the net-bonding-electron concentration of the present four alloys, and we found that, going from alloy 1 to alloy 4,  $n_e$  changes from  $5.46 \times 10^{29} \text{m}^{-3}$  to  $5.39 \times 10^{29} \text{m}^{-3}$ , while the bulk modulus changes from 138.9 to 147.4 GPa. These alloys behave similar to 3d-electron elements. Figure 3 shows the correlation between  $B$  and  $n_e$  for 3d-electron elements, Fe-18Cr-19Mn alloys, and Fe-18Cr-10Ni-1Mn alloys. To make these calculations, we adopted Cho's suggested valences. The free-electron model fails to explain the irregular behavior of 3d-electron elements or alloys. Such a simple model usually applies only to sp-electron metals. We note that  $n_e$  decreases with increasing nitrogen. The extra electrons are more than offset by the increasing volume. Also, a small electron-concentration change causes a large bulk-modulus change.

Now, we consider another viewpoint: electrons in a simple band model. Ducastelle's [15] model of cohesion uses a simple interatomic potential:

$$U = U_b + U_r = -W_0 e^{-qr} + C e^{-pr}. \quad (13)$$

Here,  $U$  denotes total energy,  $U_b$  d-band energy,  $U_r$  repulsive energy,  $r$  interatomic spacing, and  $W_0$ ,  $C$ ,  $p$ ,  $q$  constants.

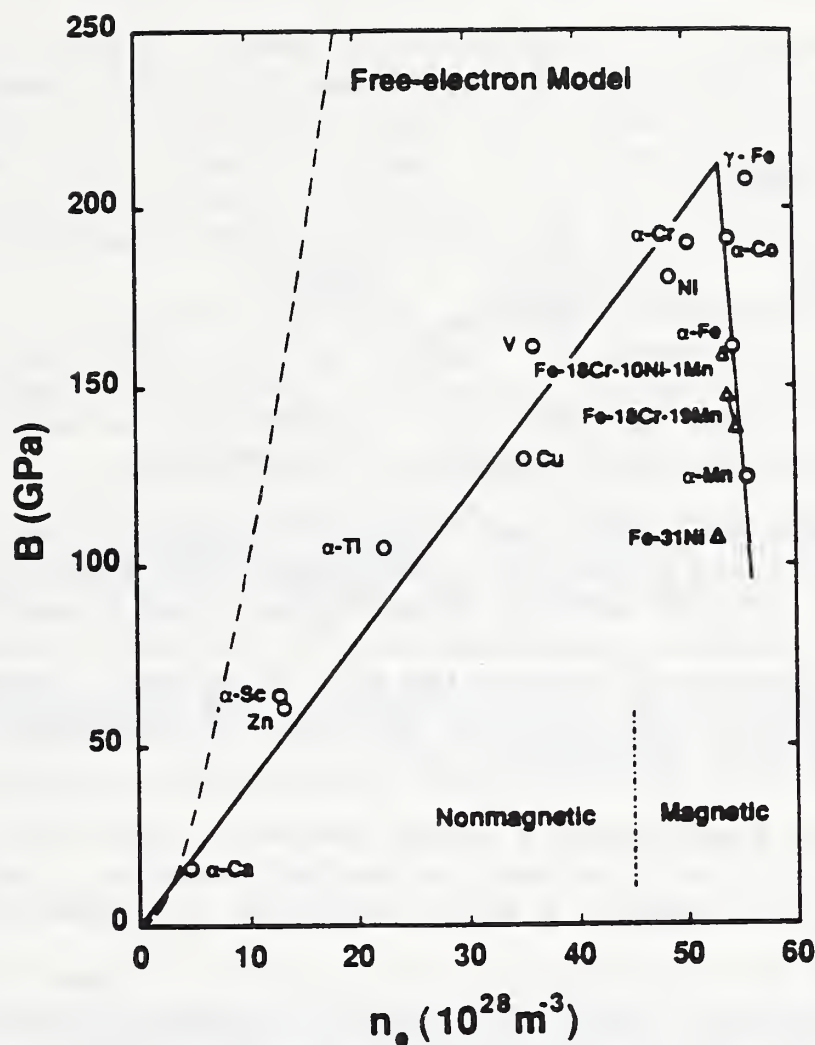


Fig. 3. Correlation between bulk modulus  $B$  and net-bonding-valence-electron concentration  $n_e$  for 3d-electron metals and alloys. The  $\gamma$ -Fe point came from reference [14]. By magnetic we mean that the material shows either ferromagnetism or antiferromagnetism at ambient, or lower, temperatures. The nonmagnetic-magnetic boundary represents a rough approximation.

Considering the Voigt bound, Ducastelle obtained for the Poisson ratio

$$\nu = \frac{1}{2} \cdot \frac{3-x}{6-7x} \quad (14)$$

where  $x = q/p$ . Solving for  $x$ , we get

$$x = \frac{12\nu-3}{14\nu-1} \quad (15)$$

Then the Poisson ratio leads directly to the Ducastelle-model ratio  $q/p$ , which shows the relative contribution of bandstructure energy  $U_b$  and repulsive energy  $U_r$  to cohesive energy [16]:

$$\left| \frac{U_b}{U_r} \right| = \frac{p}{q} . \quad (16)$$

In Ducastelle's model

$$B = V_0 \left[ \frac{\partial^2 U}{\partial V^2} \right]_{V=V_0} = \frac{r_0^2}{9V_0} \left[ \frac{\partial^2 U}{\partial r^2} \right]_{r=r_0} = \frac{pqr_0^2 U_0}{9V_0} . \quad (17)$$

Here,  $V$  denotes volume and subscript  $o$  represents the equilibrium state. And we can separate  $p$  and  $q$  by using Eqs. (15) and (17).

Table 4 shows the results of fitting Ducastelle's model to our four alloys. Columns 5 and 6 show the percentage bandstructure contributions to  $U$  and  $B$ . Columns 7-9 show several forms of the  $p$  and  $q$  coefficients, where  $pqr^2$  correlates with harmonic properties such as the bulk modulus,  $(p+q)r$  correlates with anharmonic properties such as thermal expansivity, thermal-expansivity temperature derivative, bulk-modulus temperature derivative, and bulk-modulus pressure derivative [17].

Although the bandstructure energy dominates the cohesive energy, it contributes only 12 to 19 percent to the bulk modulus. Larger variation in  $(p+q)r$  than in  $pqr^2$  suggests a larger variation in thermal expansivity than in elastic stiffness.

With increasing interstitial content, bandstructure energy contributes less to cohesion, but contributes more to the bulk modulus, contrary to many simple models where bulk modulus is proportional to cohesive energy.

TABLE 4. Ducastelle-model parameters

Alloy	$\nu$	$B$ (GPa)	$U_0/V_0$ (GJ/m <sup>3</sup> )	$U_b/U$	$B_b/B$	$q/p$	$(p+q)r$	$pqr^2$
1	0.261	138.9	57.9	0.95	0.12	0.05	21.9	21.6
2	0.270	143.2	57.4	0.92	0.16	0.09	17.5	22.5
3	0.274	144.7	57.3	0.91	0.17	0.10	16.5	22.7
4	0.281	147.4	57.0	0.89	0.19	0.13	15.3	23.3



## 5. CONCLUSIONS

From this study, we reached four principal conclusions:

1. Alloying interstitial carbon-plus-nitrogen into high-manganese Fe-18Cr-19Mn alloys decreases the shear modulus and Young's modulus, but increases bulk modulus, which is inconsistent with the volume increase. The shear-modulus change agrees with Eshelby's model. In a previous study on the effects of interstitial carbon-plus-nitrogen in Fe-18Cr-10Ni-1Mn alloys, all the elastic stiffnesses decreased with increasing C+N, consistent with volume effects.
2. Interstitial carbon-plus-nitrogen increases Poisson's ratio remarkably; this indicates interatomic-bonding change. The interstitial-contributed bonding electrons behave itinerantly, increasing the bulk modulus.
3. The 3d-electron elements show a peculiar bulk-modulus-electron-concentration behavior. At first  $B$  increases with increasing  $n_e$ ; beyond a critical concentration,  $B$  decreases rapidly. The present alloys contain higher electron concentration than the critical, and they behave like the magnetic 3d-electron elements.
4. Applying Ducastelle's model (repulsion and bandstructure energies) suggests that interstitial carbon-plus-nitrogen decreases the contribution of bandstructure energy to cohesion and increases the contribution to the bulk modulus.

## ACKNOWLEDGMENTS

Our thanks to M.W. Austin and S.A. Kim, who assisted with measurements. Sihan Lin is a visiting scientist from Tsinghua University, Beijing, P.R. China. Alloys for the study came from M. Harzenmoser and P. Uggowitzer (Zürich). Partial support for this study came from the DoE Office of Fusion Energy.

## REFERENCES

- [1] P.J. Uggowitzer and M. Harzenmoser, in High Nitrogen Steels, The Institute of Metals London, 1989, p. 174.
- [2] R.P. Reed and N.J. Simon, in High Nitrogen Steels, The Institute of Metals, London, 1989, p. 180.
- [3] K. Fritscher, in High Nitrogen Steels, The Institute of Metals, London, 1989. p. 208
- [4] H.M. Ledbetter, Mater. Sci. Eng., 29 (1977) 255-260.
- [5] H.M. Ledbetter and M.W. Austin, Mater. Sci. Eng., 70 (1985) 143-149.
- [6] H.M. Ledbetter, N.V. Frederick, and M.W. Austin, J. Appl. Phys., 51 (1980) 305-309.
- [7] S.A. Kim, H.M. Ledbetter, and Yiyi Li, unpublished research (1989).
- [8] H.M. Ledbetter and M.W. Austin, Mater. Sci. Tech., 3 (1987) 101-104.

- [9] M.W. Guinan and D.N. Beshers, J. Phys. Chem. Solids, 29 (1968) 541-549.
- [10] H.M. Ledbetter, M.W. Austin, and S.A. Kim, Mater. Sci. Eng., 85 (1987) 85-89.
- [11] W. Köster and H. Franz, Metall. Rev., 6 (1961) 1-55.
- [12] Y. Ohta (Nagoya University), personal communication (1989).
- [13] S.-A. Cho, Trans. Jap. Inst. Met., 22 (1981) 643-652.
- [14] H.M. Ledbetter, Phys. Stat. Solidi (a), 85 (1984) 89-96.
- [15] F. Ducastelle, J. Physique, 31 (1970) 1055-1062.
- [16] H.M. Ledbetter and S.A. Kim, J. Mater. Res., 3 (1988) 40-44.
- [17] R. Fürth, Proc. Roy. Soc., A183 (1944) 87-110.

LOW-TEMPERATURE MAGNETIC-ELASTIC ANOMALIES  
IN F.C.C. Fe-Cr-Ni ALLOYS

H. LEDBETTER

Institute for Materials Science and Engineering  
National Institute of Standards and Technology  
Boulder, Colorado, 80303, USA

Using ultrasonic methods, we measured the complete elastic constants of several polycrystalline face-centered-cubic Fe-Cr-Ni alloys at low temperatures: 4-295 K. The alloys represent nine interstitial (carbon-plus-nitrogen) compositions. We also measured d.c. magnetic susceptibility. Upon cooling, a paramagnetic-antiferromagnetic (Néel) phase transition occurs. The Néel transition temperature depends strongly on interstitial content. We fit both composition and temperature effects to Ducastelle's 3d-electron model, which contains two terms: bandstructure and repulsive energies.

## 1. Introduction

The study reported here represents part of a larger study to determine and understand the low-temperature elastic-magnetic properties of f.c.c. Fe-Cr-Ni alloys, which provide the basis for commercial austenitic steels. For the same nine alloys, which contain 0.08 to 0.36 mass percent (0.34 to 1.47 atomic percent) of interstitial carbon-plus-nitrogen, there exist several previous reports: ambient-temperature elastic constants [1], liquid-helium-temperature elastic constants [2], low-temperature magnetic susceptibility [3], and low-temperature neutron diffraction [4].

Here, we analyze the elastic constants by Ducastelle's model [5]. Considering the substitutional element, the studied alloys [1] consisted on average of Fe-19.4Cr-9.5Ni-1.6Mn (atomic percent). These were nine carbon-plus-nitrogen contents: 0.34, 0.45, 0.69, 0.79, 0.88, 0.95, 1.29, 1.38, 1.47 (atomic percent). For this Fe-Cr-Ni composition, the alloys are unstable at low temperatures. The interstitial C+N stabilizes the f.c.c. crystal structure. We found no evidence of crystal-structure transitions.

Intended for publication in Physica B; proceedings of ISOMES '89.



## 2. Elastic and magnetic results

Figure 1 shows, for alloy 1, the temperature variation of four polycrystalline quasiisotropic elastic constants. Upon cooling the alloy, at the Néel temperature (47.9 K), all the elastic stiffnesses (dilatational and shear) soften. Below  $T_N$ , the stiffnesses, especially the bulk modulus, tend to resume a normal temperature dependence. Above  $T_N$ , the Poisson ratio behaves normally; but, below  $T_N$  it shows an abnormal slope indicating continued magnetic changes. Also, the bulk modulus, representing dilatational stiffness, begins to soften well above  $T_N$ , at approximately 125 K. The heating and cooling curves overlap, indicating zero hysteresis. Near  $T_N$ , using x-ray diffraction, we detected neither a volume change nor a change from cubic symmetry [6].

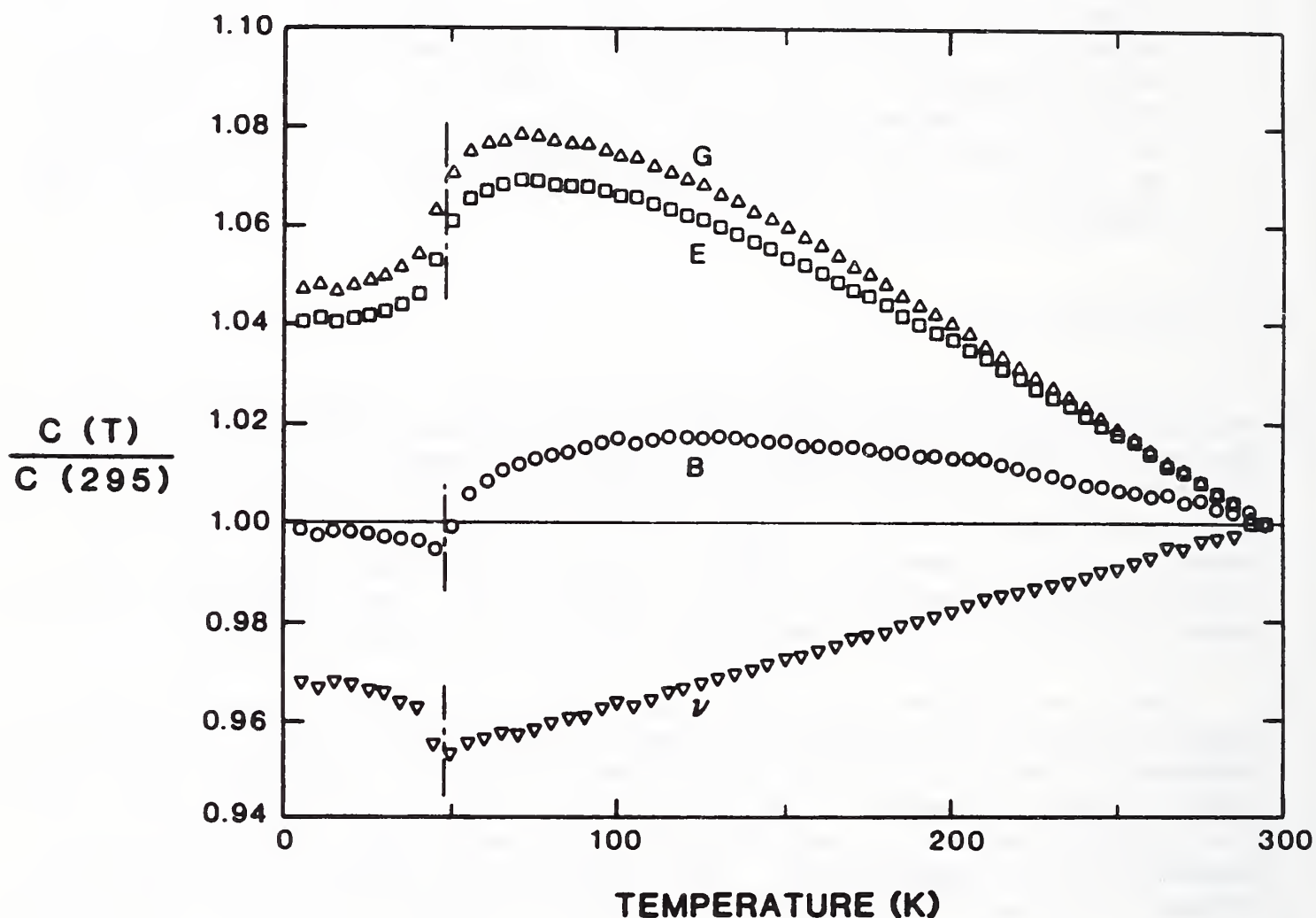


Fig. 1. For alloy 1, temperature variation of four polycrystalline elastic constants:  $G$  = shear modulus,  $E$  = Young modulus,  $B$  = bulk modulus,  $\nu$  = Poisson ratio. Values normalized to ambient temperature. Broken vertical lines indicate Néel temperature.

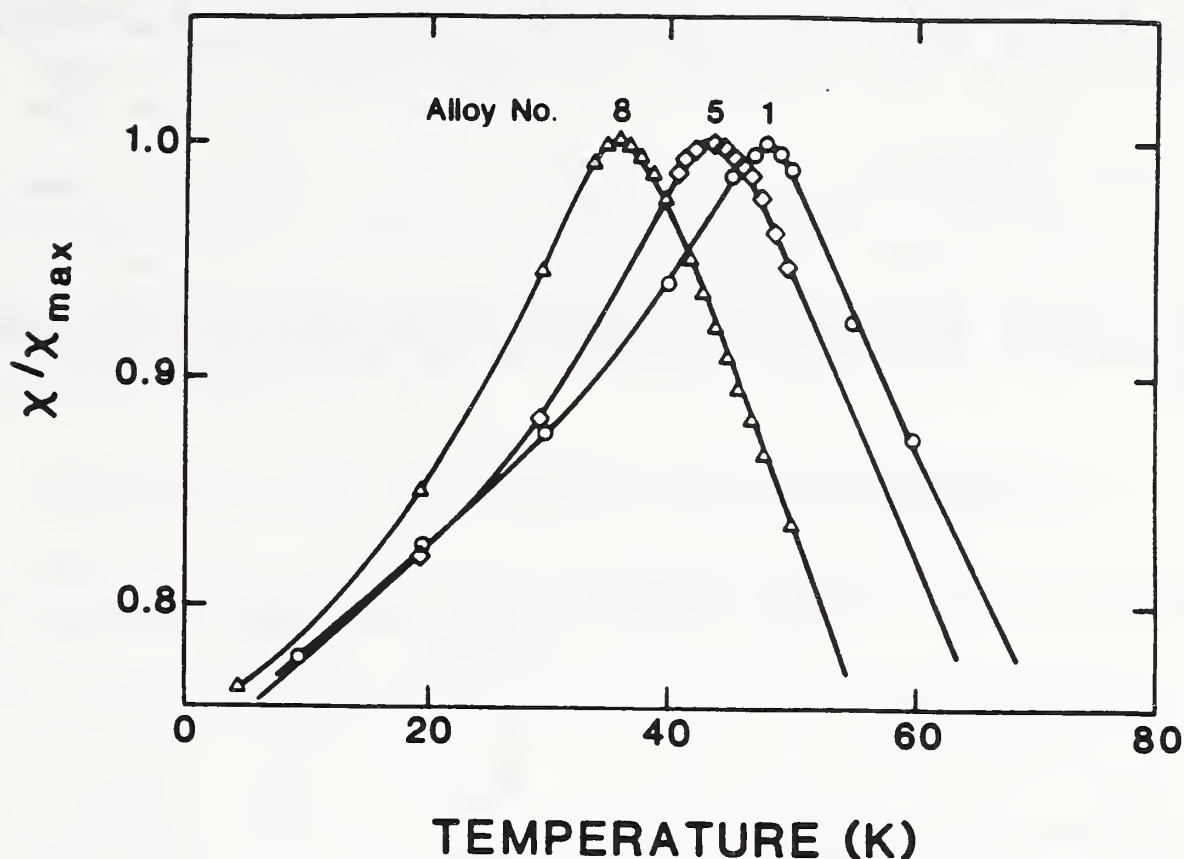


Fig. 2. For alloys 1, 5, and 8, temperature variation of d.c. magnetic susceptibility. Magnetic transition temperature shifts systematically with increasing interstitial-atom content. Specimens were cooled to 5 K in zero field and measured during warming in 1.0 mT.

Figure 2 shows typical magnetic-susceptibility-temperature curves. All these alloys show a distinct peak as a function of temperature. The behavior characterizes a paramagnetic-to-antiferromagnetic phase transition [7]. Above the transition temperature, the susceptibility is well described by a Curie-Weiss law:

$$\chi(T) = \chi_0 + \frac{C}{T + \theta} . \quad (1)$$

Here,  $\chi_0$ ,  $C$ , and  $\theta$  denote constants, which we reported previously [3].

The temperature-independent  $\chi_0$  results from underlying diamagnetism and Pauli spin paramagnetism caused by the lattice dilation and the lower Fermi energy. The average effective moment per atom obtained from the average value of  $C$  was  $1.14 \pm 0.07 \mu_B$ . Neutron diffraction [4] gave a lower moment:  $\approx 0.5 \mu_B$ . This indicates weak external-electron s-d hybridization.

### 3. Ducastelle model

Ducastelle [5] considered a simple interatomic potential:

$$U = U_b + U_r = -Ae^{-qr} + De^{-Pr} . \quad (2)$$

Here,  $U$  denotes energy, subscript  $b$  bandstructure, subscript  $r$  repulsive, and  $r$  interatomic spacing. Considering the Voigt bound, Ducastelle derived the following simple relationship for the Poisson ratio:

$$\nu_V = \frac{13 - x}{26 - 7x} \quad (3)$$

Here,  $x = q/p$ , the ratio of the bandstructure-energy and repulsive-energy exponential coefficients, with  $p > q$ . We can extend this model to the Reuss bound:

$$\nu_R = \frac{9 - 4x}{33 - 38x} \quad (4)$$

Finally, we can obtain the physically more realistic Hill-model result:

$$\nu_H = \frac{87 - 34x}{333 - 386x} \quad (5)$$

Solving for  $x$ , we obtain

$$x = \frac{333\nu - 87}{386\nu - 34} \quad (6)$$

Thus, the Poisson ratio leads directly to the Ducastelle-model  $q/p$  ratio, which gives the relative contribution of bandstructure energy  $U_b$ , and repulsive energy,  $U_r$ , to cohesion:

$$\left| \frac{U_b}{U_r} \right| = \frac{p}{q} \quad (7)$$

We can separate  $p$  and  $q$  by considering the bulk modulus. In Ducastelle's model

$$B = V_0 \left( \frac{\partial^2 U}{\partial V^2} \right)_{V=V_0} = \frac{r_0^2}{9V_0} \left( \frac{\partial^2 U}{\partial r^2} \right)_{r=r_0} = \frac{pq r_0^2 U_0}{9V_0} \quad (8)$$

Here,  $V$  denotes volume and subscript  $o$  the equilibrium state.

#### 4. Model-fitting results and discussion

Table I shows the results of fitting Ducastelle's model to our nine alloys, to an 18Cr-8Ni alloy [8], and to seven f.c.c. elements. Columns 2-4 show the input:  $\nu$  = Poisson ratio,  $B$  = bulk modulus,  $U$  = cohesive energy. Columns 5 and 6 show the percentage bandstructure contributions to  $U$  and to  $B$ . Columns 7-9 show various forms of the  $p$  and  $q$  coefficients. As des-



cribed by Fürth [9],  $pqr^2$  correlates with harmonic properties such as the bulk modulus; and  $(p+q)r$  correlates with anharmonic properties such as thermal expansivity, thermal-expansivity temperature derivative, bulk-modulus temperature derivative, and bulk-modulus pressure derivative.

Although the bandstructure energy dominates the cohesive energy, it contributes only 16 to 34 percent to the bulk modulus. For our nine alloys, we note a larger variation in  $(p+q)r$  than in  $pqr^2$ . Thus, these alloys would show larger variations in thermal expansivity than in elastic stiffness, and the usual elastic-stiffness-thermal-expansivity empirical interrelationships should be less reliable.

TABLE I. Ducastelle-model input and derived parameters.

Material	$\nu$	B (GPa)	U (GJ/m <sup>3</sup> )	$U_b/U$	$B_b/B$	$q/p$	$(p+q)r$	$pqr^2$
Ag	0.364	101.2	27.8	0.76	0.30	0.32	13.3	32.7
Au	0.424	173.5	35.9	0.71	0.34	0.42	14.5	43.5
Co	0.310	188.9	63.8	0.84	0.23	0.19	14.1	26.6
Cu	0.341	135.3	47.5	0.79	0.28	0.27	12.3	25.6
Fe	0.314	188.3	58.7	0.83	0.24	0.20	14.4	28.9
Ni	0.302	186.0	65.0	0.86	0.22	0.17	14.6	25.8
Pt	0.395	282.7	62.2	0.73	0.32	0.38	14.4	40.9
Fe-18Cr- 8Ni	0.290	158.2	58.6	0.89	0.19	0.12	15.8	24.3
Alloy 1	0.315	172.2	59.5	0.83	0.24	0.20	13.6	26.1
2	0.305	162.6	58.1	0.85	0.23	0.17	14.2	25.2
3	0.283	151.2	58.4	0.91	0.16	0.09	17.2	23.3
4	0.286	153.0	58.2	0.90	0.18	0.11	16.5	23.7
5	0.291	153.7	57.8	0.89	0.19	0.13	15.5	23.9
6	0.282	147.1	57.9	0.92	0.16	0.09	17.2	22.9
7	0.288	152.3	58.2	0.90	0.18	0.12	15.9	23.6
8	0.299	159.4	58.1	0.87	0.21	0.15	14.6	24.7
9	0.287	156.9	58.7	0.90	0.18	0.11	16.3	24.1

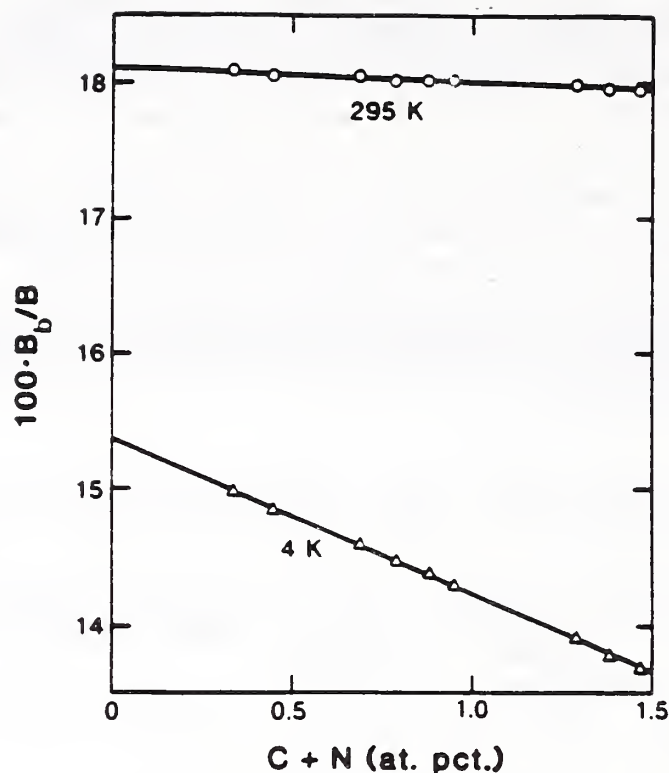


Fig. 3. Compositional variation of bandstructure contribution to bulk modulus. The low-temperature (antiferromagnetic) variation differs sharply from the ambient-temperature (paramagnetic) variation.

Ducastelle's model represents almost the simplest possible equilibrium model of a transition metal, two terms: a repulsive term and an attractive bandstructure term. Better models contain more terms. For example, the renormalized-atom model of Gelatt and coworkers [10] contains four principal energy terms. Positive contributions to the bulk modulus arise from two terms: renormalization and s-band. The renormalization energy relates to the free-atom wave functions. The s-band energy is given by

$$\Delta E_s = E_0 + (3/5) E_f - E_s^r . \quad (9)$$

Here,  $E_0$  denotes the bottom of the s-band,  $E_f$  denotes Fermi Energy, and  $E_s^r$  denotes the renormalized-atom one-electron energy. Negative contributions to the bulk modulus arise from the combined d-band broadening and s-d hybridization. Neither the renormalization energy nor the d-band terms show large curvature near the equilibrium volume. Thus, the s-band term dominates the bulk modulus. However, for copper, for example, considering only eq. (9) predicts a bulk modulus approximately 50% too high. Thus, we cannot neglect the d-band terms, which contribute negatively. The large positive curvatures of  $E_0$  and  $E_f$  near the equilibrium volume result from an effective compression caused by s-d hybridization. (In the 3d-row, K and Cu possess atomic volumes of 71.4 and 11.7 Å<sup>3</sup>, respectively!)

Figure 3 shows the composition variation of the bandstructure component of the bulk modulus. At low temperatures,  $U_b$  contributes less to  $B$ . Surprisingly, the 295-K and 4-K variations differ strongly, indicating different alloying (perhaps volume) effects at the two temperatures.

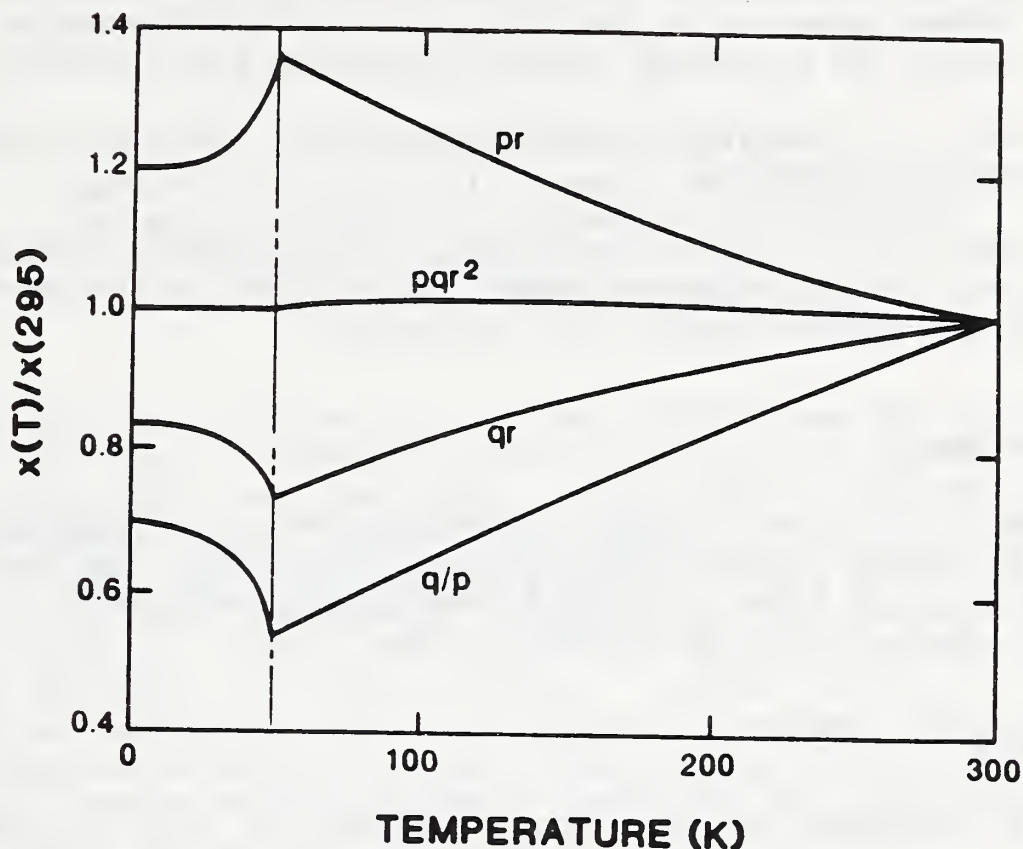


Fig. 4. For alloy 1, temperature variation of Ducastelle-model parameters. Néel temperature equals 47.9 K.

Figure 4 shows the temperature variations of the Ducastelle-model parameters. As temperature decreases,  $p$  increases while  $q$  decreases. Both  $p$  and  $q$  change abruptly at  $T_N$ . The product  $pq$  shows relative temperature independence, reflecting the relatively small bulk-modulus change. The large temperature-induced changes in  $p$  and  $q$  present a surprise. It remains to see whether similar changes occur in nonmagnetic materials.

## 5. Conclusions

From this study, we reached six conclusions:

1. At low temperatures, in f.c.c. Fe-19Cr-10Ni alloys, elastic-constant anomalies arise principally from a paramagnetic-antiferromagnetic (Néel) phase transition.
2. Adding interstitial carbon-plus-nitrogen to these alloys expands the unit cell and decreases the Néel temperature.
3. Ducastelle's model, containing only two energy terms with four parameters, provides a simple, useful approach to describe physical-property changes at magnetic phase transitions.



4. Focusing on the repulsive exponential parameter,  $p$ , and the bandstructure exponential parameter,  $q$ , we find that (i) during cooling to  $T_N$ ,  $p$  increases approximately 40% and then abruptly decreases; (ii) similarly,  $q$  decreases approximately 30% and then abruptly increases; (iii) the  $pq$  product remains relatively unchanged versus temperature, reflecting the small bulk-modulus change; (iv) except for a scaling factor, the  $q/p(T)$  ratio looks like  $\nu(T)$ .
5. Above  $T_N$ , both  $p$  and  $q$  behave smoothly, failing to reflect the bulk-modulus softening.
6. This simple approach provides a link with more sophisticated (and complicated) cohesive-energy models where the energy-elastic-constant relationships remain less transparent.

### Acknowledgments

The studies described here represent part of a large group effort. At the University of South Carolina: C. Almasan, T. Datta, R.D. Edge, D. Edwards, E.R. Jones. At Oak Ridge National Laboratory: J.W. Cable. At NIST: M.W. Austin, S.A. Kim, M. Lei.

### References

- [1] H.M. Ledbetter and M.W. Austin, Mater. Sci. Eng. 70 (1985) 143.
- [2] H.M. Ledbetter, M.W. Austin, and S.A. Kim, Mater. Sci. Eng. 85 (1987) 85.
- [3] E.R. Jones, T. Datta, C. Almasan, D. Edwards, and H.M. Ledbetter, Mater. Sci. Eng. 91 (1987) 181.
- [4] C. Almasan, T. Datta, R.D. Edge, E.R. Jones, J.W. Cable, and H. Ledbetter, J. Mag. Mag. Mater., forthcoming.
- [5] F. Ducastelle, J. Physique, 31 (1970) 1055.
- [6] M.W. Austin and H.M. Ledbetter, unpublished research, NIST, Boulder, 1989.
- [7] S. Chickazumi, Physics of Magnetism (Wiley, New York, 1964) p. 82.
- [8] H.M. Ledbetter, N.V. Frederick, and M.W. Austin, J. Appl. Phys., 51 (1980) 305.
- [9] R. Fürth, Proc. Roy. Soc., A183 (1944) 87.
- [10] C.D. Gelatt, H. Ehrenreich, and R.E. Watson, Phys. Rev. B, 15 (1977) 1613.

LOW-TEMPERATURE THERMAL EXPANSION OF Fe-Cr-Ni  
ALLOYS WITH VARIOUS C+N CONTENTS

M.W. Austin and H.M. Ledbetter

Fracture and Deformation Division  
Institute for Materials Science and Engineering  
National Institute of Standards and Technology  
Boulder, Colorado 80303 (U.S.A.)

Using x-ray diffraction, we measured between 295 and 5 K the unit-cell size of several Fe-Cr-Ni alloys containing nominally 19Cr and 10Ni (mass percent). The alloys contained various carbon-plus-nitrogen interstitial levels: 0.69 to 1.47 atomic percent. Two facts motivated our study. First, below 100 K these alloys undergo paramagnetic—antiferromagnetic transitions that affect physical properties, especially elastic constants, which relate strongly to atomic volume. Second, studies on  $\gamma$ -iron particles (which share the same crystal structure, atomic volume, and approximate Néel temperature ( $T_N$ ) as our alloys) show a 0.3% volume increase during cooling through the Néel transition. For the alloys, within our measurement error (0.05%), we failed to find a volume change at  $T_N$ . Nor did we detect a departure from cubic symmetry arising from antiferromagnetic spin alignment. All the alloys fit a simple two-parameter expression for the dilatation  $\Delta l/l$ .

Solids possess three fundamental cohesive properties: cohesive energy, bulk modulus (reciprocal compressibility), and volume. Small volume changes produce large physical-property changes. And a small volume change, say only 0.1%, induces enormous stress:

$$\sigma = B(\Delta V/V) = 200 \text{ GPa} \cdot 0.001 = 200 \text{ MPa}. \quad (1)$$

This approximates the typical austenitic-steel yield strength (207 MPa). Such a steel shows an approximate bulk modulus of  $B = 200 \text{ GPa}$ . Volume changes at structural (first-order) phase transformations: in the f.c.c. - b.c.c. martensitic transformation in Fe-31Ni, volume increases 2.6% [1]. Although thermodynamics prohibits volume changes at second-order phase transitions [2], the  $V(T)$  curve may show a discontinuity, thus a change in thermal expansivity:  $\beta = (1/V)(dV/dT)$ .

In studying  $\gamma$ -iron particles, Ehrhart and coworkers [3] used x-ray diffraction to measure volume between 300 and 6 K, through the paramagnetic-antiferromagnetic ordering temperature near 70 K ( $T_N$ ). Cooling showed a cubic-tetragonal crystal-symmetry change and a 0.3% volume increase.

Intended for publication in Materials Science & Engineering.



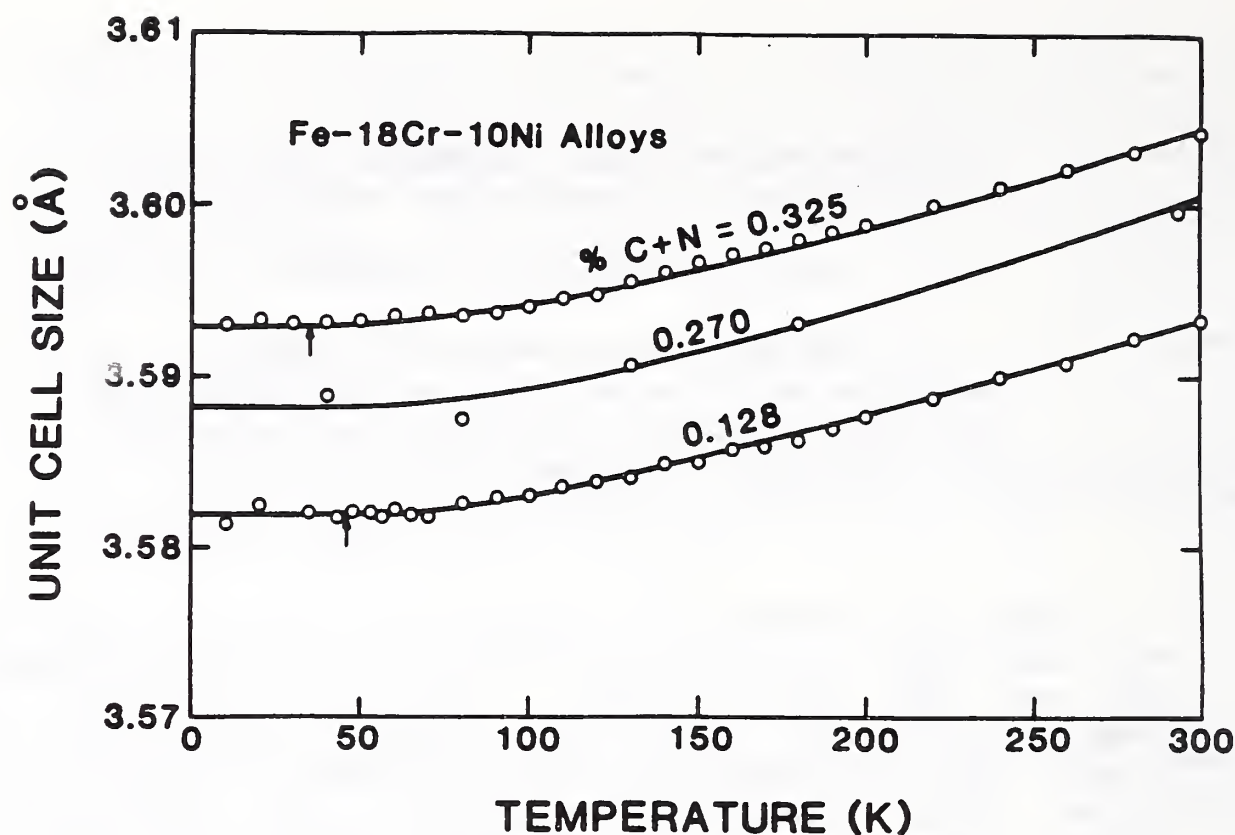


Fig. 1. Unit-cell size for Fe-20Cr-10Ni alloys with three carbon contents, shown as mass percent. Arrows indicate Néel transition temperature determined by d.c. magnetic susceptometry.

The present report represents a similar study on bulk Fe-Cr-Ni alloys. In many ways, these alloys resemble  $\gamma$ -iron: (1) same crystal structure; (2) similar atomic volumes (unit-cell size 3.59 versus 3.58 Å [3]); (3) similar Néel temperatures (46–87 versus 67 K [3]); (4) similar low-temperature electron-spin structures [3, 4]; (5) similar neutron-diffraction atomic moments, 0.55 versus 0.63  $\mu_B$  [9]; (6) similar elastic constants [5]. Fe-Cr-Ni alloys occur in many low-temperature engineering applications requiring dimensional stability. Thus, the question — does their volume increase measurably during cooling through  $T_N$ ? — contains both practical and scientific importance.

The studied alloys were already described in detail: their chemical compositions, elastic properties, and magnetic properties [6–9].

We determined volume-versus-temperature by x-ray diffraction from bulk specimens. Specimens consisted of 1-mm by 10-mm discs cut from stock with a diamond saw, annealed at 1100°C for 30 min, and electropolished. Each specimen was mounted inside an evacuated cryostat attached to a horizontal 20-cm-radius Bragg-Brentano x-ray diffractometer. At each temperature, we scanned specimens continuously at 0.5° (2 $\theta$ ) min<sup>-1</sup>. We used 0.5-mm receiving slits and 0.1-mm scatter slits. After subtracting background, we least-squares fitted both  $K\alpha_1$  and  $K\alpha_2$  peaks to Lorentzian profiles. To correct for displacement error, we extrapolated  $a_0(hkl)$  versus  $\cos\theta \cot\theta$  to  $\theta = 90^\circ$ . At 300 K, this correction was 0.002 Å; at 4 K it was 0.005 Å.



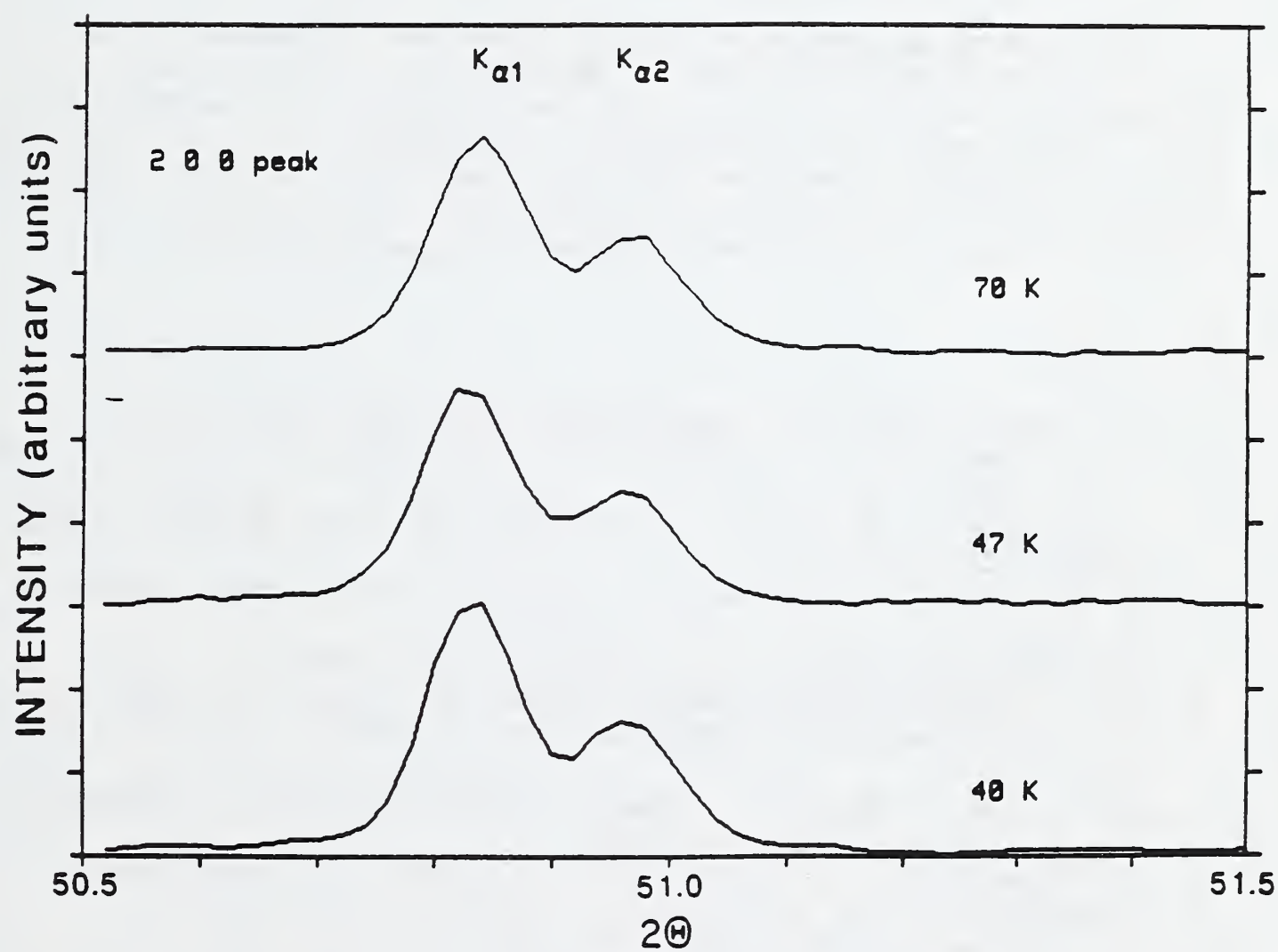


Fig. 2. Profile of (200) diffraction peak at three temperatures: above, near, near  $T_N$ . No peak splitting appears.

Figure 1 shows results for alloys with three C+N contents. Curves in the figure represent least-squares fits to the function

$$\Delta a/a_0 = a_0 + b/[\exp(c/T) - 1]. \quad (2)$$

Here  $a$  denotes unit-cell size;  $T$  absolute temperature;  $d_0$ ,  $b$ , and  $c$  adjustable parameters. This function relates to one used by Swenson [10] to describe the temperature dependence of silicon's thermal expansivity.

Figure 2 shows intensity profiles of the (200) diffraction peak at temperatures above and below  $T_N$ . These fail to show evidence of departure from cubic symmetry.

We need to recognize the obvious question — why, upon cooling through  $T_N$ , do the Fe-Cr-Ni alloys fail to show a symmetry loss, a volume increase, and a detectable change in thermal expansivity? Why do the alloys behave differently from  $\gamma$ -iron, which they resemble strongly?

The remarkable complexity [11] of magnetism in 3d-electron metals provides several possible answers. Examples include (1) strong sensitivity of magnetic-exchange energy to interatomic spacing; (2) competing Fe-Fe, Fe-Ni, Fe-Cr (and so on) interactions; (3) changes in s-d hybridization; (4) shifts in itinerant-bound electrons; (5) competition among various possible magnetic states: antiferromagnetic, ferromagnetic, spinglass. After considering many possibilities, we plan to suggest an answer.

## REFERENCES

1. J.F. Breedis and C.M. Wayman, Trans AIME, 224 (1962) 1128.
2. L.D. Landau and E.M. Lifshitz, Statistical Physics, Pergamon, London, 1959, chap. 14.
3. P. Ehrhart, B. Schönfeld, H.H. Ettwig, and W. Pepperhoff, J. Mag. Mag. Mater., 22 (1980) 79.
4. Y. Ishikawa, Y. Endoh, and T. Takimoto, J. Phys. Chem. Solids, 31 (1970) 1225.
5. H.M. Ledbetter, Phys. Stat. Solidi (a), 85 (1984) 89.
6. H.M. Ledbetter and M.W. Austin, Mater. Sci. Eng., 70 (1985) 143.
7. H.M. Ledbetter, M.W. Austin, and S.A. Kim, Mater. Sci. Eng., 85 (1987) 85.
8. E.R. Jones, T. Datta, C. Almasan, D. Edwards, and H.M. Ledbetter, Mater. Sci. Eng., 91 (1987) 181.
9. C. Almasan, T. Datta, R.D. Edge, E.R. Jones, J.W. Cable, and H. Ledbetter, J. Mag. Mag. Mater., forthcoming.
10. C.A. Swenson, J. Phys. Chem. Ref. Data, 12 (1983) 179.
11. W. Marshall (ed.), Theory of Magnetism in Transition Metals, Academic, New York, 1967.

# WELDING





## WELDING PROGRAM

LEADER: T.A. Siewert  
CONTRIBUTORS: C.N. McCowan, D.P. Vigliotti

### OBJECTIVES

- Investigation of the metallurgical factors that affect the mechanical properties of stainless-steel weldments at cryogenic temperatures.
- Contribution to the development of improved filler metals for welding stainless steels for use at 4 K.
- Evaluation of the mechanical properties of weldments at 4 K.
- Development of methods for detecting defects and evaluation of their significance in stainless steel weldments.

### RESEARCH HIGHLIGHTS

- In a study relating inclusions and fracture toughness, type 316L GMA welds were produced with shielding gases containing a range of oxygen contents. The strength at 4 K remained constant while the 35% variation in the fracture toughness was explained by the variation in the inclusion density. Sections through samples loaded to 85% of  $K_{IC}(J)$  revealed substantial crack growth (0.1 to 0.25 mm).
- A fracture toughness of a type 310 stainless steel weld (25Cr-20Ni) was evaluated at 4 K. The type 310 weld had substantially poorer toughness than the other high Ni welds but was similar to that for type 310 base metal. The toughness was not affected by the inclusion content. Microstructural evaluation revealed the lower than expected toughness was due to fracture propagation through an interdendritic phase.
- Substantial effort is being applied to understanding the micromechanisms of fracture initiation and propagation in stainless steel welds at 4 K. Specimens are loaded to various levels above and below  $K_{IC}(J)$  and then sectioned for microstructural analysis. Various stainless steel alloys behave similarly with void growth being the minor component of the fracture process and microcrack linkage being the major component. This is in opposition to most textbooks on fracture which indicate void growth is the dominant fracture mechanism (from room temperature studies).

## SUMMARY OF MECHANICAL PROPERTY MEASUREMENTS OF WELDS

Weld Alloy [designation]	Welding Process	Tensile	Charpy Impact	Fracture Toughness	Fatigue Crack Growth Rate	Report Volume* (page)
<u>AUSTENITIC STAINLESS STEELS</u>						
Fe-13Cr-13Ni-20Mn-0.2C	SMAW	XI		XI		XI (171)
Fe-13Cr-20Ni-9Mn-2Nb	SMAW	I, II	I, II, VIII			I (159, 169) II (299) VIII (29)
Fe-15Cr-12Ni-10Mn	SMAW	IV	IV, VIII			IV (453) VIII (29)
Fe-16Cr-15Ni-4Mo	SMAW	IV		IV		IV (275)
Fe-16Cr-16Ni-2Mo	FCAW	II		III	III, VI	III (155) VI (199)
Fe-16Cr-16Ni-4Mo	FCAW	IV	IV, VIII	IV		IV (275) VIII (29)
Fe-16Cr-35Ni-4Mn [330 modified]	SMAW	I	I, VIII	II		I (159) II (299) VIII (29)
Fe-17Cr-9Ni-Mn-N	SMAW	IX	IX			IX (217)
Fe-17Cr-16Ni-4Mo	SMAW	IV		IV		IV (275)
Fe-18Cr-11Ni-2Mo-N	EBW LBW	X X	X X	X X		X (299)
Fe-18Cr-16Ni-6.5Mn-2Mo	SMAW	IX	IX			IX (257)
Fe-18Cr-16Ni-9Mn-N	GMAW	III, IV	IV	III, IV	III, VI	III (155) IV (275, 453) V (199)
Fe-18Cr-18Ni-2Mo-5Mn-N	SMAW	IV	IV			IV (453)
Fe-18Cr-20Ni-5Mn-N	GMAW	IX, XI		IX, XI		IX (247) XI (247)
Fe-18Cr-20Ni-6Mn-0.3Nb	GMAW	IV	IV	IV		IV (275)
Fe-18Cr-20Ni-6Mn-0.2Ti	GMAW	IV	IV	IV		IV (275)
Fe-19Cr-12Ni-2Mo [316]	SMAW	II	II, VIII	II		II (315) VIII (29)
Fe-19Cr-12Ni-2Mo [316L]	EBW	IV		IV	IV, VI	IV (275, 415) VI (199)
	GMAW	III, IV	III, IV, VIII	IV		III (155, 195) IV (303) VIII (29)

\* MATERIALS STUDIES FOR MAGNETIC FUSION ENERGY APPLICATIONS AT LOW TEMPERATURES: NBSIR 78-884 (I); NBSIR 79-1609 (II); NBSIR 80-1627 (III); NBSIR 81-1645 (IV); NBSIR 82-1667 (V); NBSIR 83-1690 (VI); NBSIR 84-3000 (VII); NBSIR 85-3025 (VIII); NBSIR 86-3050 (IX); NBSIR 87-3067 (X); NBSIR 88-3082 (XI)



SUMMARY OF MECHANICAL PROPERTY MEASUREMENTS OF WELDS, continued

Weld Alloy Designation]	Welding Process	Tensile	Charpy Impact	Fracture Toughness	Fatigue Crack Growth Rate	Report Volume* (page)
-19Cr-12Ni-2Mo [16L], continued	GTAW	III,IV, XI	III,IV, VIII	IV	XI	III (155,195) IV (303) VIII (29) XI (215)
	SAW	III,IV, V	III,IV, V	III,IV	III,VI	III (155,195) IV (275,415) V (233) VI (199)
	SMAW	II,III, IV	II,VIII	II,III, IV	III,IV,VI	II (299,315) III (155,167) VI (199) VIII (29)
-19Cr-12Ni-2Mo-N [16LN]	SMAW	II	II,VIII	II		II (299) VIII (29)
-19Cr-16Ni-7Mn	GMAW	IV	IV			IV (453)
-20Cr-10Ni [308]	SMAW	I	I,VIII			I (169) VIII (29)
-20Cr-10Ni [308L]	FCAW	III		III	III,VI	III (155) VI (199)
	GMAW	III		III	III,VI	III (155) VI (199)
	GTAW	XI			XI	XI (215)
	SMAW	II,III	II,VIII	II,III	III,VI	II (299) III (155) VI (199) VIII (29)
-20Cr-10Ni-N [308LN]	FCAW	IV		IV	IV,VI	IV (275,415) V (199)
-20Cr-10Ni-9Mn-N	SMAW	I	I			I (159,169)
-20Cr-16Ni-7Mo-2W	SAW	IV		IV		IV (275)
-20Cr-34Ni-2Mo-Nb	SMAW	VII		VII		VII (253)
-21Cr-6Ni-9Mn-N	GTAW	XI			XI	XI (215)
	SMAW	I,II	I,II			I (159,169) II (299)

MATERIALS STUDIES FOR MAGNETIC FUSION ENERGY APPLICATIONS AT LOW TEMPERATURES: NBSIR 78-884 (I); NBSIR 79-1609 (II); NBSIR 80-1627 (III); NBSIR 81-1645 (IV); NBSIR 82-1667 (V); NBSIR 83-1690 (VI); NBSIR 84-3000 (VII); NBSIR 85-3025 (VIII); NBSIR 86-3050 (IX); NBSIR 87-3067 (X); NBSIR 88-3082 (XI)

SUMMARY OF MECHANICAL PROPERTY MEASUREMENTS OF WELDS, continued

Weld Alloy [designation]	Welding Process	Tensile	Charpy Impact	Fracture Toughness	Fatigue Crack Growth Rate	Report Volume* (page)
<u>AUSTENITIC STEELS</u>						
Fe-15Mn-8Ni-1Mo-0.7C	SAW	VIII		VIII		VIII (15)
Fe-5Cr-25Mn-1Ni		V		V,VII	V,VI	V (233) VI (199) VII (245)
Fe-6.5Cr-25Mn-3Ni-1Mo	SMAW	V		V	V,VI	V (233,245) VI (199)
<u>ALUMINUM ALLOYS</u>						
Al-5Mg [5183]	GMAW	III		IV	IV	III (155,217) IV (323)
Al-5Mg-0.12Ti [5556]	GMAW	III		IV	IV	III (155, 217) IV (323)
<u>Copper Alloys</u>						
Cu-0.08Ag [C10700]		XI				XI (201)
Cu-0.4Be-1.8Ni [C17510]		XI				XI (201)

\* MATERIALS STUDIES FOR MAGNETIC FUSION ENERGY APPLICATIONS AT LOW TEMPERATURES: NBSIR 78-884 (I); NBSIR 79-1609 (II); NBSIR 80-1627 (III); NBSIR 81-1645 (IV); NBSIR 82-1667 (V); NBSIR 83-1690 (VI); NBSIR 84-3000 (VII); NBSIR 85-3025 (VIII); NBSIR 86-3050 (IX); NBSIR 87-3067 (X); NBSIR 88-3082 (XI)

THE FRACTURE TOUGHNESS OF  
25Cr-22Ni-4Mn-2Mo STAINLESS STEEL  
WELDS AT 4 K\*

C.N. McCowan and T.A. Siewert  
Fracture and Deformation Division  
National Institute of Standards and Technology  
Boulder, Colorado

A 25Cr-22Ni-4Mn-2Mo stainless steel gas metal arc welding electrode composition was used to make welds having several different inclusion contents for fracture toughness ( $K_{IC}(J)$ ) testing at 4 K. The inclusion contents of the welds were changed by increasing the oxygen content of the argon-oxygen shielding gas mixture. The yield and ultimate strengths of the welds at 4 K were nearly constant, with values near 875 and 1100 MPa respectively. The fracture toughness of the welds varied from 130 to 165 MPa·m<sup>1/2</sup>, but this variation in toughness could not be related to the inclusion content. The metallography and fractography results show that, although the welds fractured in a ductile mode, failure occurred predominately at intercellular regions of the austenitic solidification structure. This intercellular, rather than a transdendritic, fracture mode is thought to explain the absence of a strong correlation with inclusion content seen with other stainless steel welds.

## INTRODUCTION

The cryogenic strength and toughness of stainless steel weld compositions that have a primary ferritic (FA) mode of solidification, such as AWS type 308 and 316 stainless steels, and experimental compositions that have a fully austenitic (A) mode of solidification, have been evaluated more extensively than the stainless steel welds which have a primary austenitic (AF) mode of solidification.<sup>1-5</sup> For welds solidifying in the AF mode, ferrite forms during the final stages of solidification when the liquid remaining between the growing austenitic cells becomes enriched to a eutectic composition.<sup>6-11</sup> This solidification sequence results in a different composition and ferrite morphology than that occurring in the FA solidification mode, and the nature of the ferrite-austenite boundary is changed. These changes could have a substantial effect on the performance of a weld. This study evaluates the toughness of a modified type 310 stainless steel weld metal that solidifies in an AF mode to determine if this composition is suitable for cryogenic use. In addition, the effect of inclusions on the cryogenic toughness of this weld composition are evaluated.

\*Contribution of the National Institute of Standards and Technology.



## MATERIALS AND PROCEDURES

The composition of the 1.2 mm diameter stainless steel gas metal arc (GMA) electrode used to make the four welds in this study is given in Table 1. The welding was performed at approximately 250A and 22V. The travel speed was  $2.8 \text{ mm} \cdot \text{s}^{-1}$  with a contact tip-to-work distance of 19 mm. An average of 12 weld beads were required to complete the single-vee groove weldment shown in Figure 1. The base material used was 25-mm-thick type 304L plate. Interpass temperatures were held at about 150 C.

To attain a variation in the inclusion content of the welds, the oxygen content of the argon-oxygen shielding gas mixture used to make the welds was changed. To provide baseline data, two welds (1D and 1S), were produced with 100% argon shielding. Weld 1S was produced with a standard 19-mm-diameter gas cup but additional shielding was provided for the 1D weld by using a second, larger diameter gas cup which also had a flow of argon.<sup>12</sup> This double shield was used to further reduce the oxygen content in the atmosphere surrounding the arc. The 1R0 and 1H0 welds were made using shielding gases having 2 and 10 vol% oxygen respectively and a conventional 19 mm diameter gas cup.

Table 1. The Chemical Composition of the Welding Electrode.

C	Si	Mn	P	S	Cr	Ni	Mo	Ti	Cu	Nb	Ta
0.02	0.18	4.4	0.010	0.009	24.9	22.3	2.1	0.04	0.02	0.01	0.01

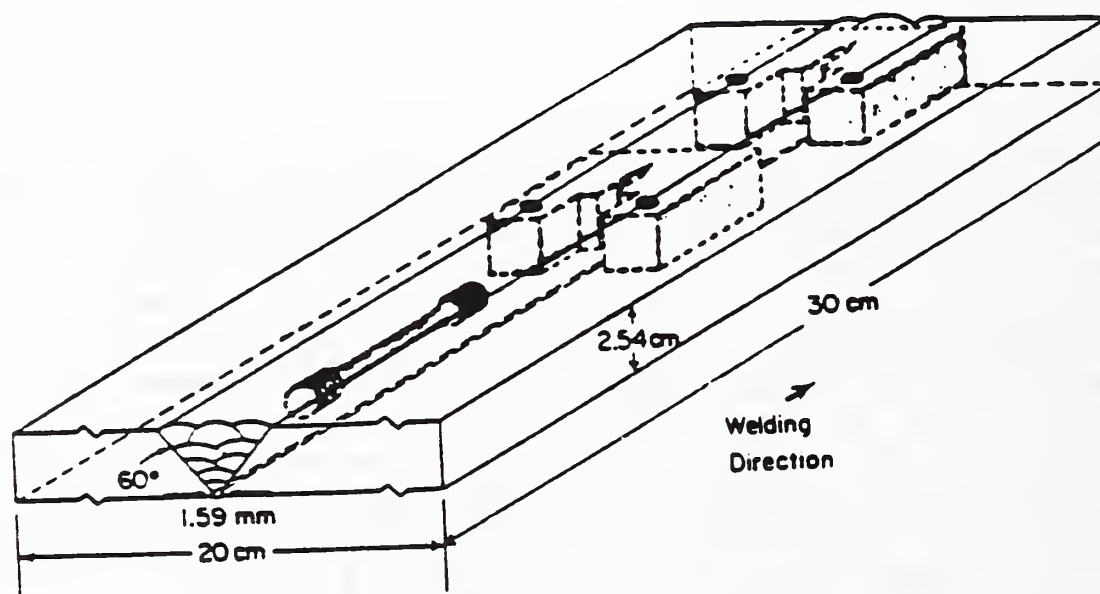


Figure 1. The welding configuration used for the study.

A compact tension and a tensile specimen were machined from each of the welds for testing at 4 K. The locations from which these specimens were removed from the welds are also shown in Figure 1. The compact tension specimens were fatigue precracked in liquid N (76 K) and then side grooved to a depth of 10% of the thickness per side. The fracture toughness testing was conducted at 4 K (specimens immersed in liquid He) using the single specimen compliance test method.<sup>8</sup> For the 4 K tensile testing, the specimens were strained at a rate of  $2 \times 10^{-4}$ . Details of the testing apparatus are available elsewhere.<sup>13-14</sup>

## RESULTS

### A. Microscopy

The location of the ferrite at intercellular regions of the austenite matrix (Figure 2) identifies the solidification mode of all four welds as AF. In Figure 3, the intercellular ferrite is shown at a higher magnification: Commonly the ferrite is located at triple points in the cell structure and appears to have nucleated at  $\text{MnSiO}_3$ -type inclusions. It is evident that both the ferrite and the inclusions in these welds interact with the migrating grain boundaries during cooling.

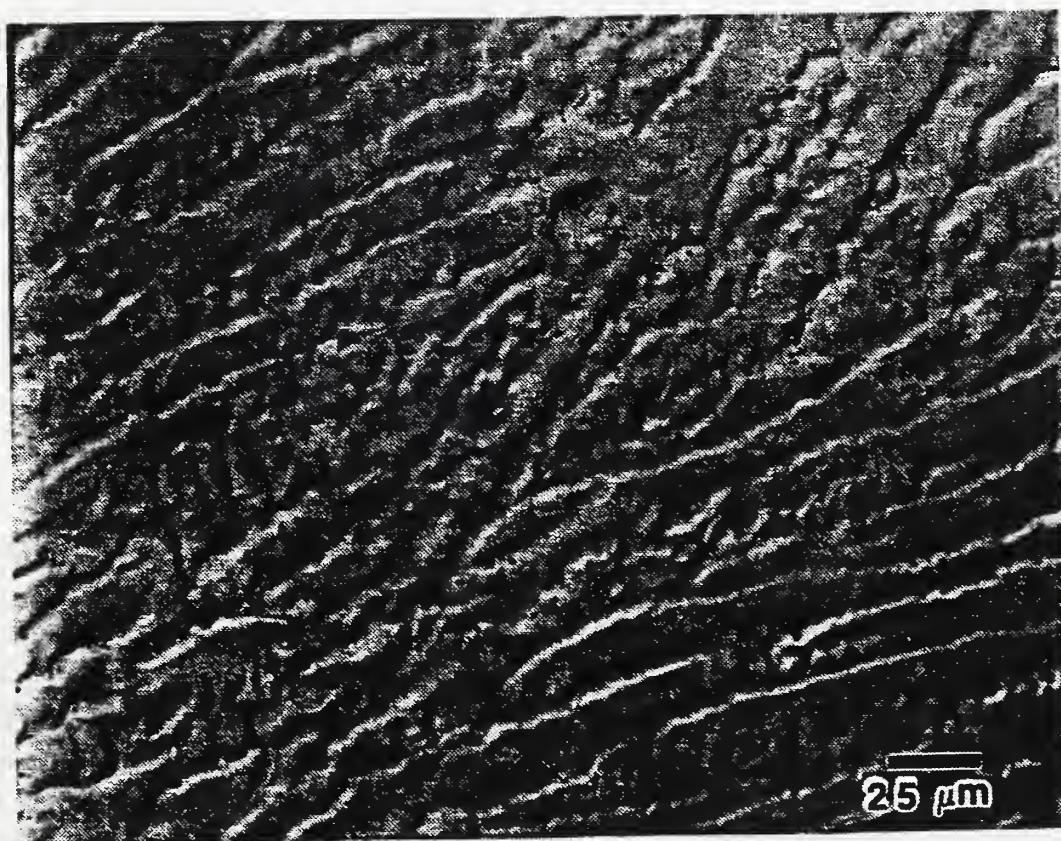


Figure 2. The welds had a cellular austenitic matrix with ferrite present at the intercellular regions.





Figure 3. The ferrite often appeared to have nucleated at  $\text{MnSiO}_3$  type inclusions.

The types of inclusions observed in the microstructure and the inclusion density (inclusions per unit area) varied with the oxygen content of the welds. At low oxygen contents, spherical,  $\text{MnSiO}_3$  type inclusions and Ti-rich inclusions were most common (Figure 4). As the oxygen content of the welds increased (1R0 and 1H0), the number of  $\text{MnSiO}_3$  and Ti-rich inclusions per unit area increased, and large, Cr-rich inclusions were also frequently observed. The large number of Cr- and Ti-rich inclusions observed was unexpected and precluded the collection of inclusion density counts for comparison to previously collected inclusion data. It is clear in Figure 5, however, that the welds had very different inclusion contents and so any effect of inclusion content on the toughness should be apparent.

#### B. Mechanical Properties

The 4-K tensile and fracture toughness results for the welds are given in Table 2. The average yield strength, ultimate strength, and fracture toughness ( $K_{IC}(\text{J})$ ) values of the welds were 878 MPa, 1104 MPa, and  $143 \text{ MPa}\cdot\text{m}^{1/2}$  respectively. The yield and tensile strength are probably underestimated by these averages, however, because the low values reported for the 1S weld are attributed to a solidification crack in the specimen. Several other notes concerning the missing data in Table 2 are: (1) the 1R0 tensile specimen was accidentally tested at a very high strain rate ( $7.5 \times 10^{-1}$ ) and failed prior to reaching a 0.2% offset yield strength, and (2) no fracture toughness value is reported for the 1S weld because the test was stopped at the first sign of crack growth so that the specimen could be sectioned for metallographic examination of the crack front region.





Figure 4. The spherical inclusions are  $\text{MnSiO}_3$  type inclusions typically found in stainless steel welds. The more angular, dark inclusions were rich in Cr and/or Ti.

The strength and toughness values determined for the welds in this study are representative of the type 300 series stainless steel welds. In Figure 6, for example, the strength and toughness of the 25Cr-22Ni welds were similar to those found for a previously tested AISI 310 weld (25Cr-21Ni-2Mn-0.10C) and are near the middle of the strength-toughness zone determined for type 308 and 316 stainless steel welds.<sup>1,15,16</sup> Unexpectedly, no trend of increasing toughness with decreasing inclusion contents in the welds was found. The weld having the highest inclusion content (1H0) had a toughness similar to the weld with the lowest inclusion content (1D).

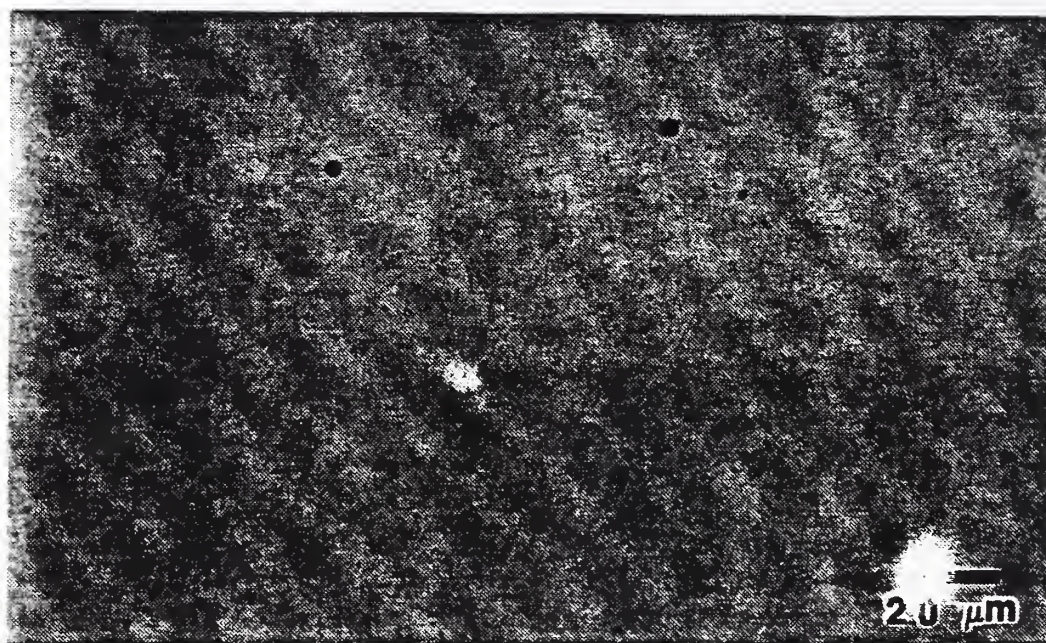
Table 2. The 4 K tensile and fracture toughness results.

Weld	Yield Strength (MPa)	Ultimate Strength (MPa)	Elongation (%)	Reduction in Area (%)	$K_{IC}$ (J) (MPa $\sqrt{m}$ )
1D	907	1178	15.6	9.6	128.6
1S	836	907	2.8	8.0	---
1R0	---	---	---	---	164.8
1H0	890	1227	24.1	14.5	135.2

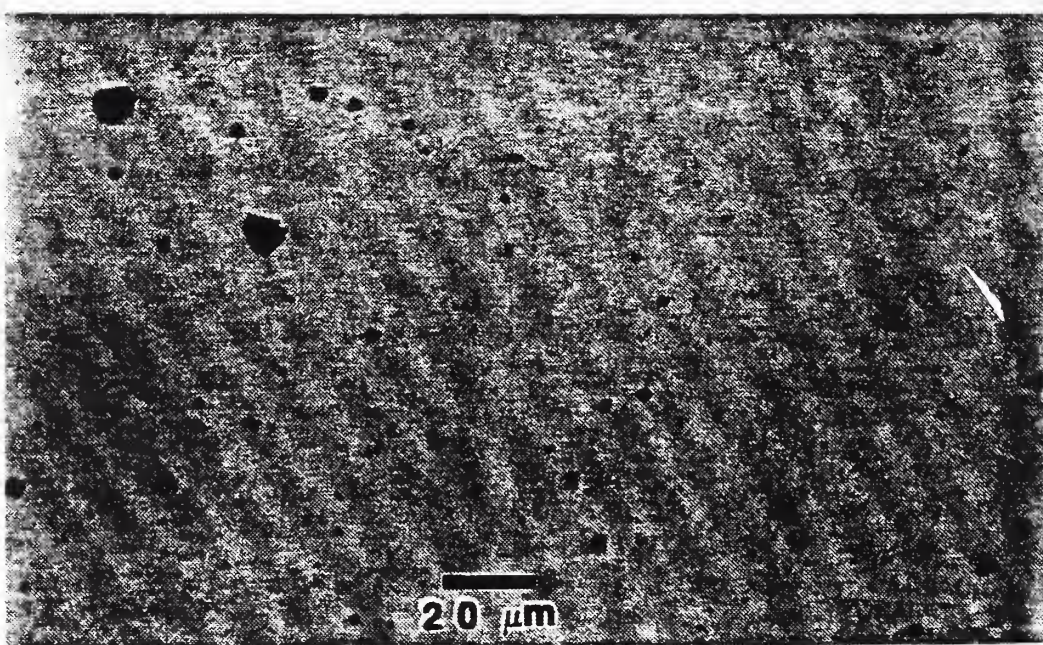




(a)



(b)



(c)

Figure 5. The inclusion distributions for the (a) 1D weld, (b) the 1R0 weld, and (c) the 1H0 weld are shown.



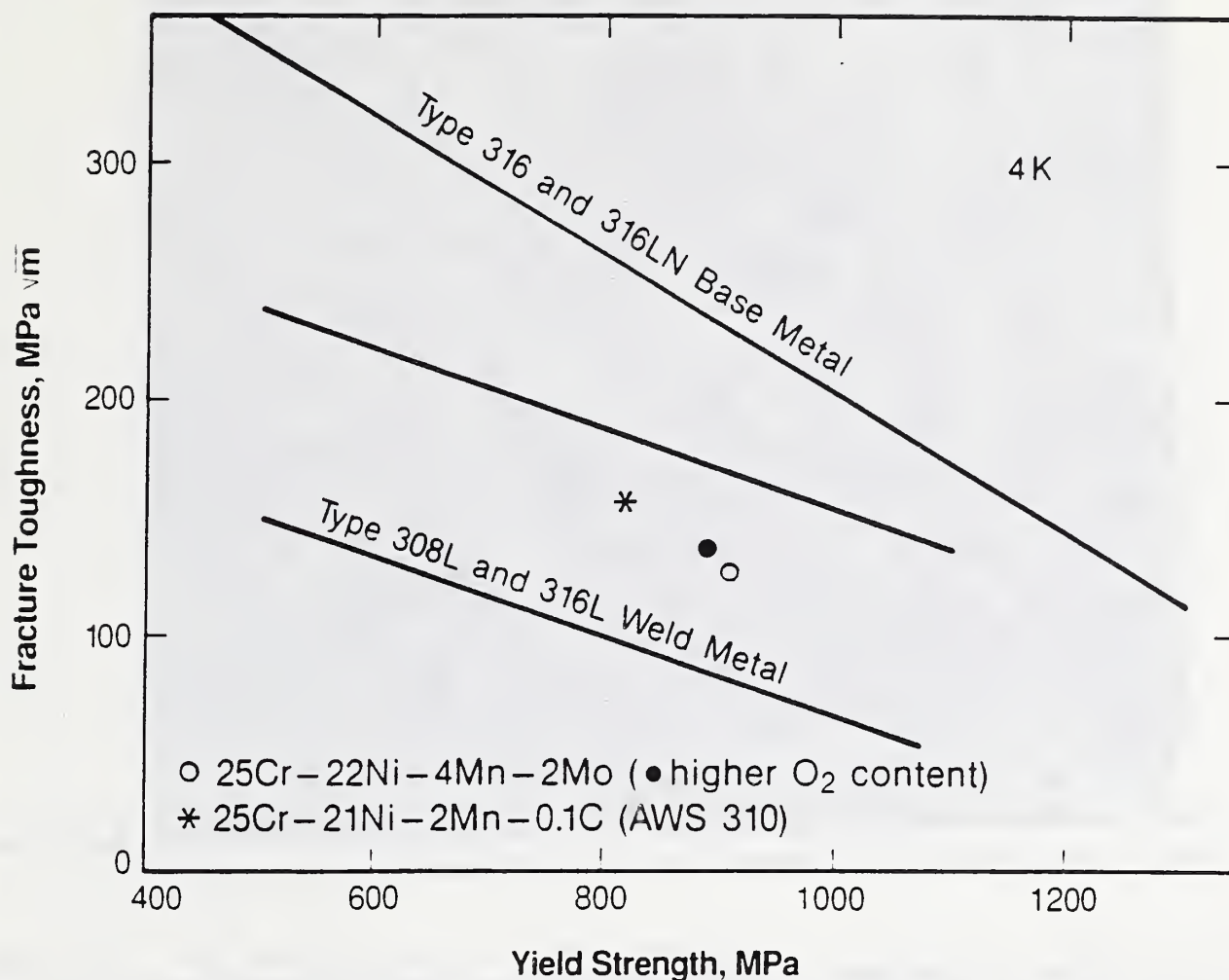


Figure 6. The strength and toughness of the 1D and 1Ho welds are compared here with previous data collected for type 300 series stainless steel welds and base materials.

Based on the difference in the inclusion contents of the 1D and 1HO welds (Figure 5), but similar toughness, inclusion content does not appear to control the crack initiation in these weld specimens. Since previous studies have shown a similar change in inclusion content to cause a 35% change in toughness at 4 K,<sup>12</sup> we evaluated fracture surfaces and metallographic sections from the weld specimens to determine the cause for this anomalous behavior.

### C. Failure Analysis

The fracture surfaces of both tensile and compact tension specimens indicated that failures occurred in a ductile manner, but the fracture path was determined by the microstructure. The fracture surface of the 1D tensile specimen, for example, is shown in Figure 7 to be dominated by ductile dimples that form a pattern of peaks and valleys. Areas having these ribbed patterns were observed to some extent on each of the tensile fracture surfaces and were recognized as being similar to the solidification cell dimensions shown in Figure 3. This peak-valley pattern could be generated if fracture occurred preferentially through the intercellular regions of the solidification structure.



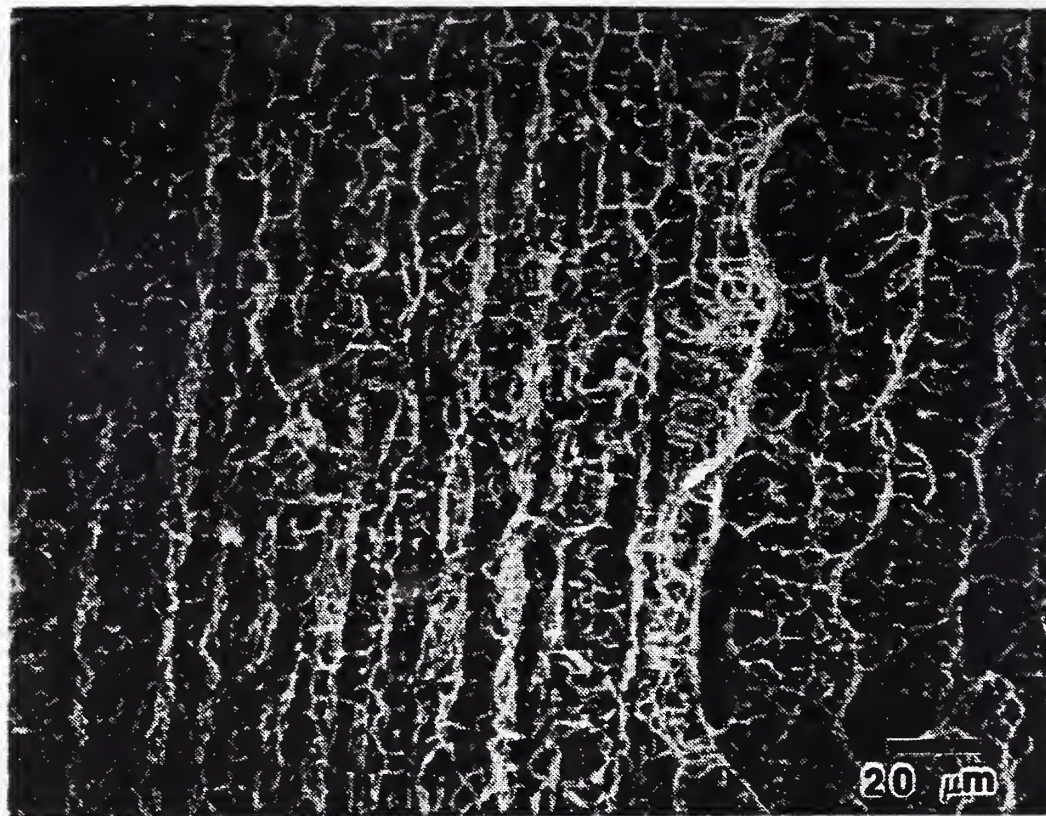


Figure 7. The fracture surface of the 1D tensile specimen showed a ductile dimple network that formed a series of peaks and valley.

Further evidence of intercellular fracture was found during examination of the compact tensile specimens. A transverse section through the initial crack growth region in the 1S compact tension specimen, Figure 8, produced fracture surface profiles that closely resemble the austenitic cell structure. When examining the crack path, numerous peaks and valleys can be found that terminate at intercellular positions in the matrix and the end of the crack tip is located at a cell boundary. In addition, voids observed in the matrix are located exclusively at intercellular regions, most are at triple points of the austenitic cell matrix. Because the fracture toughness test was stopped at crack initiation for the examination of this specimen, a  $K_{IC}(J)$  value could not be determined. The applied load at crack initiation, however, was within 10% of those estimated for crack growth in the 1D and 1H0 test specimens, so the fracture toughness would be expected to be comparable.

The observations of void formation at triple points in the austenitic cell structure suggested that the ferritic phase, often present at these sites, was playing a key role in fracture initiation. Further examination of the fracture surfaces of the compact tension specimens revealed that ferrite was present at many of the void sites, but whether the voids initiated at ferrite-austenite interfaces, in the ferrite, or in the austenite was not clear. Metallographic cross sections of deformed tensile specimens (Figure 9), however, did indicate that: (1) the ferrite was fracturing in a brittle manner as plastic flow occurred in the austenitic matrix, (2) the ferrite-austenitic interface was generally intact, (3) cracks sometimes linked neighboring ferrite particles, and (4) several cracks, apparently nucleated at inclusions in the cell cores, were observed to change growth directions and follow along the cell boundary upon reaching the intercellular regions. These observations suggest that the probable cause of void initiation at ferrite particles is a result of the brittle fracture of the ferrite.



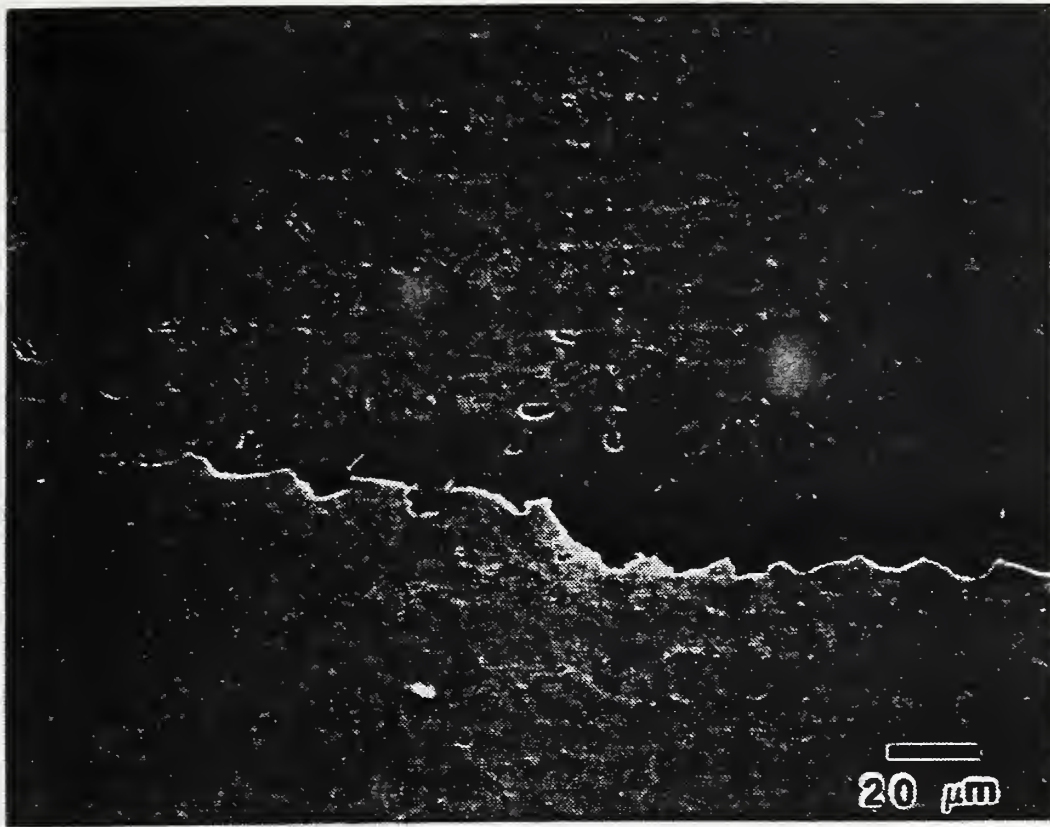


Figure 8. The crack path for the 1S compact tension specimen is shown to follow the intercellular regions of the microstructure.



Figure 9. In the 1S tensile specimen, deformation of the austenitic matrix often resulted in the fracture of ferrite particles and sometimes cracks at inclusion sites were observed. The textured appearance of the matrix is due to plastic flow.

These observations, except that of the apparently strong ferrite-austenite interface, are different from those made in deformed ferrite plus austenite stainless steel welds that have solidified in an FA solidification mode. In a previous study of type 316L weld tensile specimens that solidified in an FA mode, ferrite was not found to fracture nor were cracks at inclusions or between ferrite particles observed after 50% elongation at 4 K.<sup>12</sup>

For the welds in this study, the AF solidification mode seems to have produced ferrite and intercellular compositions that limited the toughness. In a 22Cr-14Ni weld, for example, Brooks estimated the intercellular compositions to be enriched in Ni and Cr by approximately 2 wt.%. The ferrite composition was approximately 34Cr-8Ni.<sup>9</sup> At nominal alloy contents farther from the liquidus trough of the Fe-Cr-Ni ternary diagram than Brook's alloys, such as the 25Cr-22Ni welds in this study, even more extensive differences between the core and intercellular compositions could occur. In addition, the welds evaluated in this study would be expected to have a Mo-enriched ferrite phase and intercellular regions that are enriched in Mo and Mn. Unfortunately, the detailed microanalysis required to quantitatively determine the level of microsegregation in these welds was beyond the scope of this study. The microsegregation, however, did not produce cell core chemistries that transformed to martensite during deformation at 4 K, so the corduroy type fracture mechanism reported by Lippold is not applicable to these welds.<sup>17</sup>

## CONCLUSIONS

1. The fracture toughness values of the 25Cr-22Ni-4Mn-2Mo at 4 K were typical of those that have been determined for type 308, 316, and 310 stainless steel welds of similar strength and average inclusion contents.
2. The failure of the tensile and compact tension specimens occurred predominately at intercellular regions in the weld microstructure.
3. The failures are suspected to initiate at local brittle fractures in the ferrite, which then link along intercellular paths to form a crack.

## ACKNOWLEDGMENTS

The electrode was furnished by Sandvik Steel Company.

## REFERENCES

1. Tobler, R.L., Siewert, T.A., and McHenry, H.I., 1986, Strength-Toughness Relationship for Austenitic Stainless Steel Welds at 4 K, Cryogenics, July, pp. 3922-395.
2. McCowan, C.N., Siewert, T.A., and Tobler, R.L. 1986, Tensile and Fracture Properties of an Fe-18Cr-20Ni-5Mn-0.16N Fully Austenitic Weld Metal at 4 K, Journal of Engineering Materials and Technology, October, pp. 340-343.



3. Elmer, J.W., McHenry, H.I., and Whipple, T.A., 1981, Strength and Toughness of Fully Austenitic Stainless Steel Filler Metals at 4 K, in: Materials Studies for Magnetic Fusion Energy Applications at Low Temperature - IV, NBSIR 81-1645, National Bureau of Standards, Boulder, Colorado, pp. 289-302.
4. Tobler, R.L., Trevisan, R.E. and Reed, R.P., 1985, Tensile and Fracture Properties of an Fe-14Mn-8Ni-1Mo-0.7 Fully Austenitic Weld Metal at 4 K, Cryogenics, Volume 25, pp. 447-451.
5. Yamagami, N., Kahsaka, Y., and Ouchi, L., 1987, Mechanical Properties of Welded Joints In Mn-Cr and Ni-Cr Stainless Steels at 4 K, in: Advances in Cryogenic Engineering - Materials, Clark, A.F. and Reed, R.P., Ed., Plenum Press, Volume 34, pp. 359-366.
6. David, S.A., Goodwin, G.M., and Braski, D.N., 1979, Solidification Behavior of Austenitic Stainless Steel Filler Metals, Welding Journal, Nov., pp. 330s-336s.
7. Ritter, A.M. Henry, M.F., Savage, W.F., 1984, High Temperature Phase Chemistries and Solidification Mode Prediction in Nitrogen-Strengthened Austenitic Stainless Steels, Metallurgical Transactions A, July, pp. 1339-1351.
8. Cieslak, M.J., Ritter, A.M, and Savage, W.F., 1982, Solidification Cracking and Analytical Electron Microscopy of Austenitic Stainless Steel Weld Metals, Welding Journal, January, pp 1s-8s.
9. Brooks, J.A., Williams, J.C., and Thompson, A.W., 1983, STEM Analysis of Primary Austenite Solidified Stainless Steel Welds, Metallurgical Transactions A, January, pp 23-31.
10. Takalo, T., Suutala, N., and Moisio, T., 1979, Austenitic Solidification Mode in Austenitic Stainless Steel Welds, Metallurgical Transactions A, August, pp 1173-1181.
11. Kokawa, H., Kuwana, T., and Yamamoto, A., 1988, Crystallographic Characteristics of Delta-Ferrite Transformations in Type 304L Austenitic Stainless Steel Weld Metal at Elevated Temperatures, IIW Doc IX-1529-88.
12. McCowan, C.N. and Siewert, T.A., 1989, The effect of Inclusions on the Fracture Toughness of 316L Stainless Steel Welds at 4 K, submitted to: Advances in Cryogenic Engineering - Materials.
13. Tobler, R.L. Read, D.T., and Reed, R.P., 1981, Strength/Toughness Relationship for Interstitially Strengthened AISI 304 Stainless Steels at 4 K, in Fracture Mechanics: Thirteenth Conference, Richard Roberts, Ed. ASTM STP-743, American Society for Testing and Materials, Philadelphia, pp. 250-268.

14. Read, D.T. and Tobler, R.L., 1982, Mechanical Property Measurements at Low Temperatures, in Advances in Cryogenic Engineering - Materials, Vol. 28, Plenum Press, New York, pp. 17-28.
15. Tobler, R.L., Shoji, T., Takahashi, and Ohnishi, K., 1986, Fracture, Acoustic Emission and Adiabatic Heating of Austenitic Stainless Steels at Liquid Helium Temperature, Yamaguchi, K, Aoki, K., and Kishi, T., Ed., in Progress in Acoustic Emission III, The Japanese Society of NDI, pp. 453-461.
16. Reed, R.P., Simon, N.J., Purtscher, P.T., and Tobler, R.L., 1986, Alloy 316 LN for Low Temperature Structures: A Summary of Tensile and Fracture Data, in Proceedings of the Eleventh International Cryogenic Engineering Conference, Kipping, G. and Kipping, I., Ed., Butterworth and Co. Surrey UK, pp. 786-793.
17. Lippold, J.C., Juhas, M.C., and Dalder, E.N.C., 1985, The Relationship between Microstructure and Fracture Behavior of Fully Austenitic Type 316L Weldments at 4.2 K, Metallurgical Transactions A, October, pp. 1835-1848.

# THE EFFECT OF INCLUSIONS ON THE FRACTURE TOUGHNESS OF 316L STAINLESS STEEL WELDS AT 4 K

C.N. McCowan and T.A. Siewert  
Fracture and Deformation Division  
National Institute of Standards and Technology  
Boulder, Colorado

The 4-K fracture toughness ( $K_{IC}(J)$ ) of a type 316L stainless steel weld composition increased significantly when the inclusion contents of the welds were decreased. For the three welds tested (Ni = 13 wt.%, 4 K yield strength  $\approx$  740 MPa), the fracture toughness increased from 132 to 150 to 179 MPa $\cdot$ m $^{1/2}$  as the inclusion contents decreased from 55,200 to 37,700 to 19,300 inclusions per mm $^2$ . Expressing the effect of inclusions on the toughness in terms of the inclusion spacing (inverse square root of the inclusion density), the fracture toughness of the 316L welds increased 18 MPa $\cdot$ m $^{1/2}$  per  $\mu$ m increase in the average inclusion spacing. Previous results from a 18Cr-20Ni stainless steel weld study are expanded on in this study and show a trend similar to the trend found for the 316L welds. For the 18Cr-20Ni welds (4-K yield strength  $\approx$  1000 MPa), the fracture toughness increased from 180 to 287 MPa $\cdot$ m $^{1/2}$  as the inclusion contents decreased over the range of 25,000 to 8,300 inclusions per mm $^2$ . Because the effects of yield strength and Ni content on the toughness of the two weld compositions were constant, the increases in toughness (35% for the 316L, 60% for the 18Cr-20Ni) are attributed solely to the reductions in weld metal inclusion contents. For the 316L welds, fractographic studies were conducted to characterize differences in the initiation of fracture as a function of the inclusion content. Measurements on fracture specimens loaded to only 85% of the estimated  $K_{IC}$  values revealed stable crack growth lengths of 0.1 to 0.25 mm crack growth occurs as voids which formed at inclusions link by microcracking, rather than coalescence.

## INTRODUCTION

Three variables that affect the fracture toughness of stainless steel welds and base materials at cryogenic temperatures are yield strength, Ni content, and inclusion content.<sup>1-3</sup> The toughness ( $K_{IC}(J)$ ) increases with increasing Ni content, and decreases with increasing strength and inclusion content. Therefore, it is not surprising that welds, which generally have higher inclusion contents than base materials, are typically found to have a



lower toughness than base materials of comparable strength and Ni levels. But the importance of inclusions in determining the toughness is not well defined for stainless steel welds and the quantitative dependence of the previously observed trends on the strength level, nickel content, and microstructure of an alloy has not been determined. This information is needed to help determine what increases in the toughness of welds at cryogenic can be expected by improved inclusion control.

The effect of inclusion content on the fracture toughness at 4 K has been studied in an 18Cr-20Ni weld composition.<sup>1</sup> In that study the fracture toughness ( $K_{Ic}(J)$ ) increased by 30 to 40% when inclusion contents were decreased from approximately 11,000 to 9,000 inclusions per mm<sup>2</sup>. This study adds to the work previously done on the 18Cr-20Ni GMA welds and evaluates the effect of inclusion content on the fracture toughness of type 316L stainless steel gas metal arc (GMA) welds.

## MATERIALS AND PROCEDURES

The chemical compositions supplied by the manufacturers of the two GMA electrodes used in this study are given in Table 1. The oxygen contents of the welds (Table 2) made for the study were measured with a fusion analysis technique using a thermal conductivity detector.

To produce welds having different inclusion contents, the oxygen content of the argon-oxygen shielding gas and the method of shielding used to make the welds were varied. Welds having inclusion contents most typical of commercially produced stainless steel GMA welds were made using an argon-2% oxygen (by volume) shielding gas and a conventional 16 mm (5/8 inch) gas nozzle. To attain higher inclusion content welds, an argon based shielding gas having approximately 8% oxygen was used. For low weld inclusion contents, a dual-gas-shielding configuration (Figure 1) was implemented using 100% argon for both the inner and outer shields. The shielding gas compositions were controlled during welding by using mass flow meters to mix commercial grade oxygen and argon. The total flow rate of the shielding gas was 14.2 L per min (30 cfh).

Table 1. The GMA electrode compositions in wt.%.

	C	Mn	Si	P	S	Cr	Ni	Mo	N	Cu
316L	0.02	1.73	0.35	0.008	0.009	19.2	13.1	2.15	NA	0.04
18Cr-20N	0.03	5.39	0.26	0.006	0.007	18.1	20.4	0.11	0.16	0.02

Table 2. The inclusion and  $O_2$  and contents of the welds. The D, Ro, and Ho suffixes stand for double Argon, Argon - 2% Oxygen, and Argon - 8% Oxygen shield respectively.

Weld	$O_2$	Inclusion Density	Inclusion Spacing
316L-D	0.0004	19,300	7.0
316L-Ro	0.048	37,700	5.0
316L-Ho	0.072	55,200	4.3
11	0.005	9,800	11.0
12	0.004	8,300	10.1
10	0.037	11,300	9.4
13	0.056	25,000	6.3

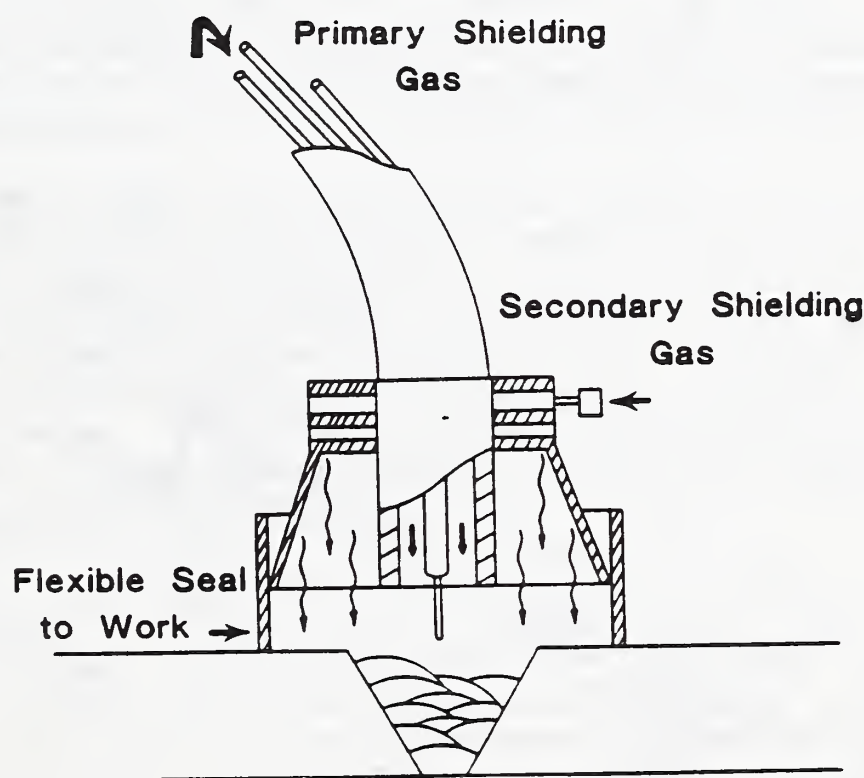


Figure 1. The dual-shield configuration used for this study to provide better shielding of the welding arc.

The specific welding parameters used for the welds are included in Table 3. In general, we tried to maintain the same heat input, contact tip-to-work distance and interpass temperature for all welds made with the same electrode. The exception was the 18Cr-20Ni number 11 weld that was made as part of a previous study.<sup>1</sup> For this weld, the welding parameters were altered to change the metal transfer mode from a spray to droplet type.

From each weld, a uniaxial tensile and two compact tension specimens were machined for testing at 4 K. The weld configuration and specimen locations are shown in Figure 2. The compact tension specimens were precracked in liquid nitrogen and then side grooved on each side to a depth of 10% of the specimen width prior to testing. The fracture toughness tests were conducted with the specimens submerged in liquid helium (4 K) using the single specimen compliance method. The uniaxial tensile tests were also conducted at 4 K: tensile specimens having diameters of 6.25 mm were strained at a rate of  $2 \times 10^{-4}$ , the percent elongation was measured over a 25.4 mm gauge length, and the yield strength was calculated using the 0.2% offset method. The details of the 4-K testing procedures are given elsewhere.<sup>4,5</sup>

Table 3. Welding and Testing Parameters used for the welds.

	Volts	Amperage	Electrode Extension (mm)	Electrode Diameter (mm)
316L-D-Ro-Ho	24	210	19	0.9
10*,12*,13	25	280	18	1.2
11*	20	175	12	1.2

\*Welded as part of a previous study.<sup>1</sup>

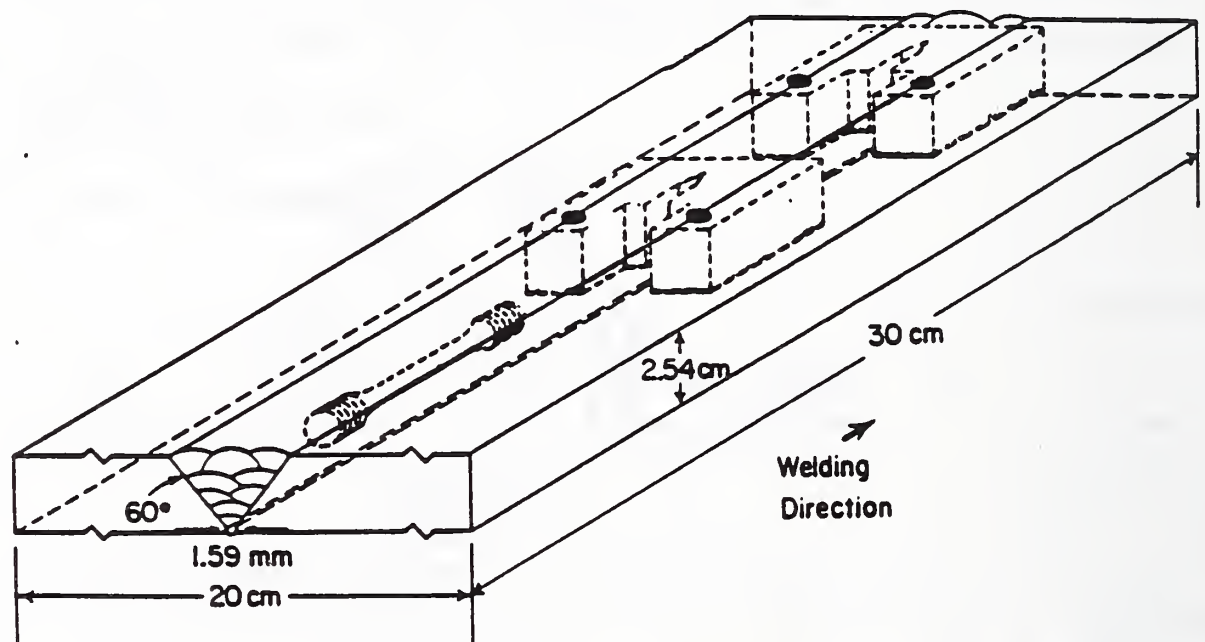


Figure 2. The welding configuration and specimen locations used for this study.



To estimate the inclusion densities, cross sections of the welds perpendicular to the welding direction were cut and polished for scanning electron microscope (SEM) evaluations. For each weld, 200 to 300 inclusions were counted at 2000x and then divided by the area scanned to determine the inclusion density. The average inclusion spacing was calculated as the inverse square root of the inclusion density.<sup>6</sup>

To evaluate damage to the weld microstructures near the onset of stable crack growth, the second fracture toughness test for each of the 316L welds was interrupted at 85% of the estimated  $K_{IC}(J)$  value so that the specimens could be removed and examined. Samples were prepared for light and scanning electron microscope evaluations as follows: (1) samples containing all of the fatigue crack and a reasonable volume of the crack front region were removed using an abrasive saw, (2) these samples were mounted in epoxy under vacuum, (3) by rough grinding, a plane perpendicular to the fatigue crack plane and parallel to the direction of crack growth was obtained at a depth of approximately 5  $\mu\text{m}$  from the original compact tension surface, and (4) following final polishing and observations on this plane, samples were reground and repolished numerous times to provide a series of sample planes from different depths within the specimens.

## RESULTS AND DISCUSSION

### Microstructure

The 316L and the 18Cr-20Ni welds had different solidification modes. The 18Cr-20Ni, because of the higher Ni and N content, solidified in a fully austenitic mode. The 316L welds solidified in a primary ferritic mode. The residual ferrite contents measured for the 316L welds using magnetic response techniques in accordance with ANSI/AWS Standard A4.2-74 ranged from 5 to 7 FN.

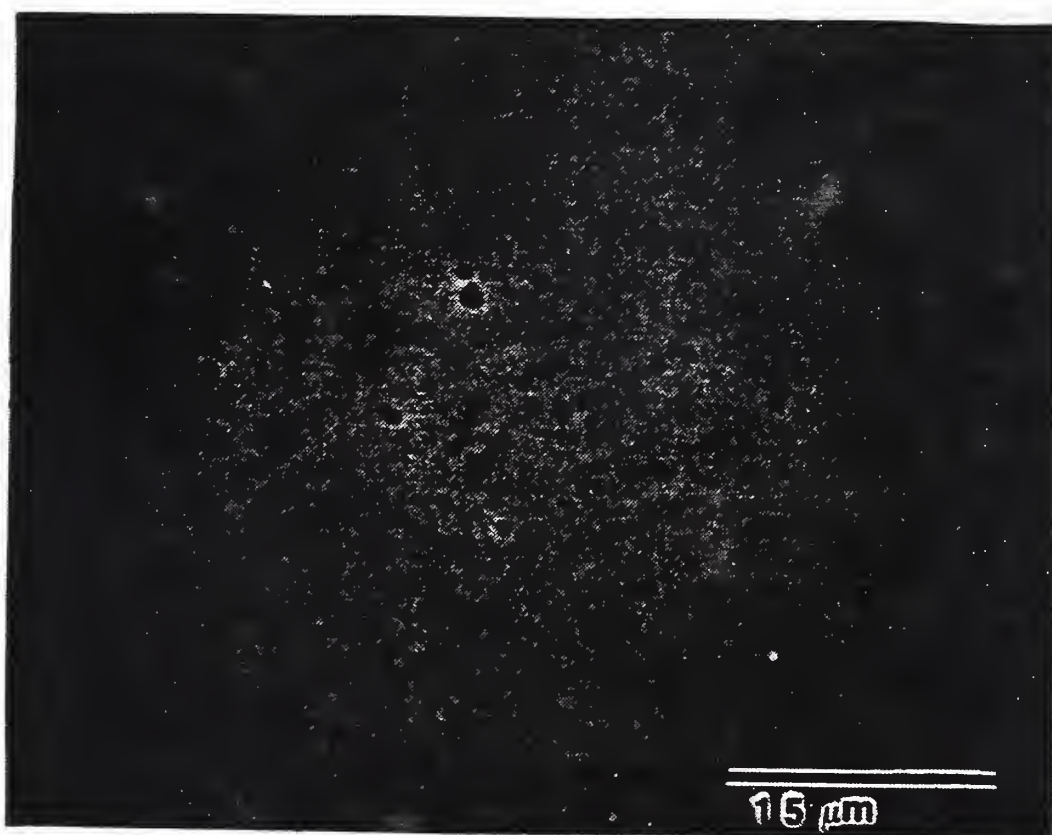
The variations in the inclusion contents observed for the 316L welds are shown in Figure 3 and estimated inclusion densities for all the welds are given in Table 2. Clearly a significant range in inclusion contents was achieved for both weld compositions: the percent increase in inclusions for the 316L and the 18Cr-20Ni welds over their respective ranges were 185 and 200%. The majority of the inclusions observed in the welds were spherical,  $\text{MnSiO}_3$  type inclusions. Occasionally, more angular inclusion shapes were observed that were determined during energy dispersive x-ray analysis to be rich in Cr, Ti, and sometimes Al.

### Mechanical Testing

The yield strength of the welds varied by less than 4% for a given electrode composition (Table 4) so the effect of strength and Ni on the toughness are essentially constant for the 316L and 18Cr-20Ni welds. The average yield strength was 742 MPa for the 316L welds and 1005 MPa for the 18Cr-20Ni welds. There was no correlation between the inclusion density and the yield strength of the welds.



(a)



(b)

Figure 3. The inclusion content range for the 316L welds: (a) 316L-D and (b) 316-H0. These SEM micrographs were taken on polish planes perpendicular to the welding direction.



Table 4. The mechanical properties of the weld at 4 K.

	$\sigma_y$	$\sigma_{TTS}$	%E	%R	$K_{Ic}(J)$
316L D	736	1343	47.9	46.6	179
316L Ro	747	1153	22.3	23.7	150
316L Ho	743	1122	10.2	13.1	132
10	991	1274	23.0		287
11	1027	1347	17.0	15	263
12	1015	1300	26.0	37.0	203
13	988	1209	7.7	16.6	180

The ultimate strength, elongation, and reduction in area for the tensile specimens are included in Table 4. Although there appears to be a trend of decreasing tensile ductility (as measured by elongation and reduction in area) with increasing inclusion content for the 316L welds, no such trend is evident for the 18Cr-20Ni welds. In part, this apparent difference in the tensile ductility of the welds is due to scatter in the data. Weld specimens, because of their coarse dendritic crystal structures, develop heavy surface textures during straining at 4 K that can result in stress concentrations which initiate failure. Therefore, variation in the tensile ductility data may not be due to the inclusion content. Alternately, microflaws in the weld specimens sometimes initiate premature failures.

The fracture toughness ( $K_{Ic}(J)$ ) increased as the inclusion content of the welds decreased (Table 4). For the type 316L stainless welds, the fracture toughness increased about 35% when the inclusion density was lowered from 55,200 to 19,300 inclusions per  $mm^2$ . This change in toughness with inclusion content is shown in Figure 4 to almost span the width of the strength-toughness trend band previously developed for type 316L and 308L stainless steel welds at 4 K.<sup>7</sup> The trend band was constructed using available stainless steel weld data and the width of the band were attributed to variations in weld inclusion contents between the different welding processes, which strongly supports this observation. The type 316L stainless steels welds tested in this study have an inclusion range that corresponds reasonably well to the range produced by common production welding processes and strongly supports this observation.



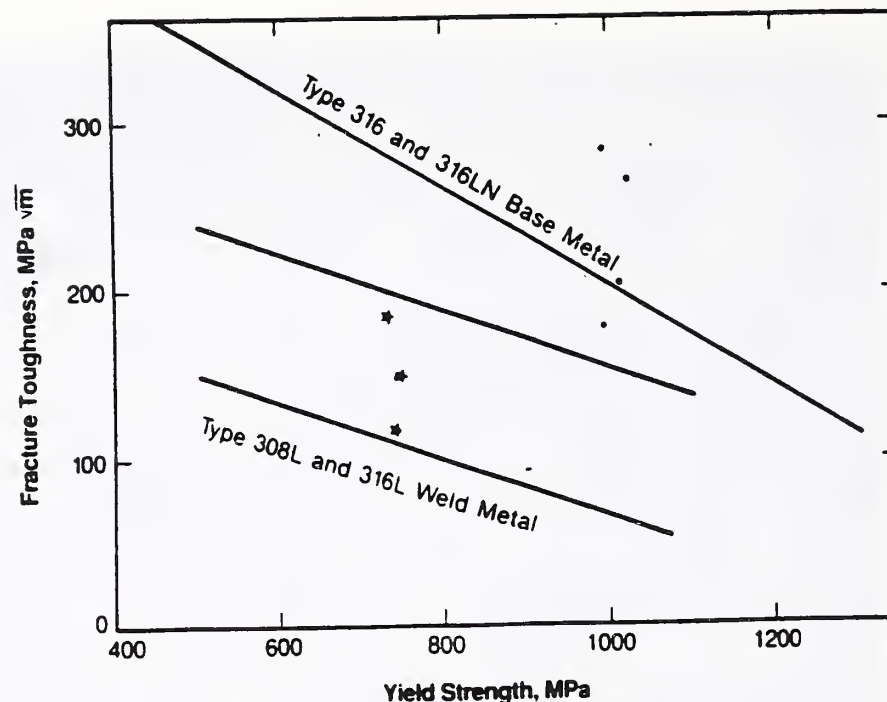


Figure 4. The 316L (stars and the 18Cr-20Ni (circles) weld data show increases in the toughness with decreasing inclusion contents. The changes in toughness are of a similar magnitude to the trend bandwidth determined for type 308 and 316 stainless steel welds made by a variety of commercial welding processes.

One way to express the effect of inclusions on toughness is in terms of the average inclusion spacing (inverse square root of the area density). This approach has been used to model fracture initiation. It provided a characteristic distance (inclusion spacing) over which a critical stress or strain must extend for the onset of stable crack growth.<sup>8</sup> The results of this study (Figure 5), as expected, show that the toughness increases significantly with inclusion spacing for both the 316L and the 18Cr-20Ni welds. Although the trends indicated by these data are not expected to be linear over a large range, the 316L weld data shows the fracture toughness at 4 K to increase by approximately  $18 \text{ MPa}\cdot\text{m}^{1/2}$  per  $\mu\text{m}$  increase in the inclusion spacing. A trend of similar magnitude is seen for the 18Cr-20Ni data. No differences in the trends for the two types of welds are due to differences in the inclusion spacing ranges, solidification mode, strength, and Ni content of the weld were resolved. As more data is collected for welds, these effects should become apparent.

In Figure 6, the effects of strength and Ni content on the toughness are normalized so that the effects of inclusion spacing indicated for the two weld compositions can be more fairly compared with each other and with type 316L stainless steel base materials at 4 K.<sup>9</sup> Considering that the base metal trend was developed at inclusion spacings greater than  $50 \mu\text{m}$ , the agreement of the extrapolated trend with the weld data is surprisingly good. All of the weld data is within the scatter band associated with the base metal trend.

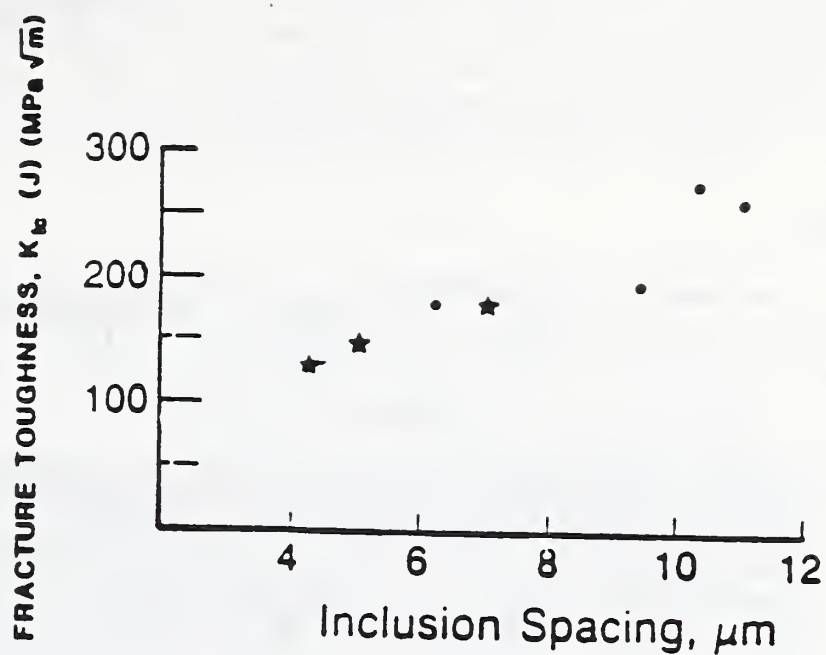


Figure 5. The increases in the toughness for the 316L (stars) and the 18Cr-20Ni (circles) welds are shown here in terms of increasing average inclusion spacing (inverse square root of the inclusion density).

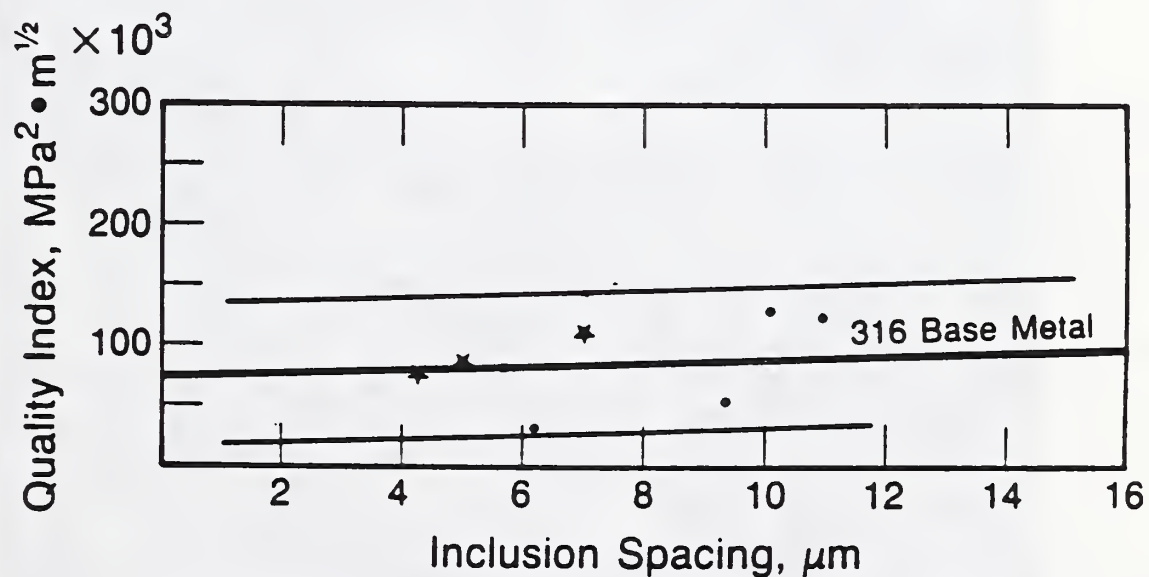


Figure 6. The Quality Index ( $K_{IC} \cdot \sigma_y$ ), normalized to a 12 wt.% nickel content, versus the inclusion spacings of the welds.



Although extrapolation of these weld data trends would indicate superior toughness for the welds compared to base materials at inclusion spacing greater than 12 to 15  $\mu\text{m}$ , inclusion size and morphology are not considered here, so such speculations are not appropriate. Perhaps the most interesting comparison to be made in Figure 6 is between the two types of solidification structures present for the welds. Unexpectedly, the fully austenitic structure of the 18Cr-20Ni welds does not appear to be inherently tougher than the 2-phase ferrite plus austenite structure of the 316L welds.

### Failure Analysis

All test specimens failed in a ductile manner with fracture surfaces exhibiting typical ductile dimple morphologies (Figure 7). Evaluations of the 316L specimens that were only loaded to 85% of their estimated  $K_{IC}(J)$  values showed more crack growth than expected (Figure 8). To examine the initiation of crack growth, we estimate that the fracture tests should have been interrupted at 70% of the respective  $K_{IC}(J)$  values. Still, there were several characteristic differences observed in the appearances of the 316L crack paths. The lower inclusion content specimen (316L-D) typically had an area of fracture out in front of the fatigue crack that appears to have formed first and then linked by microcracking to the fatigue crack tip. Sharp crack tips were commonly observed at the leading edges of these ductile fracture zones. For the 316L-R0 and -H0 specimens, a more continuous or shorter crack void-linking distance was observed ahead of the fatigue crack.

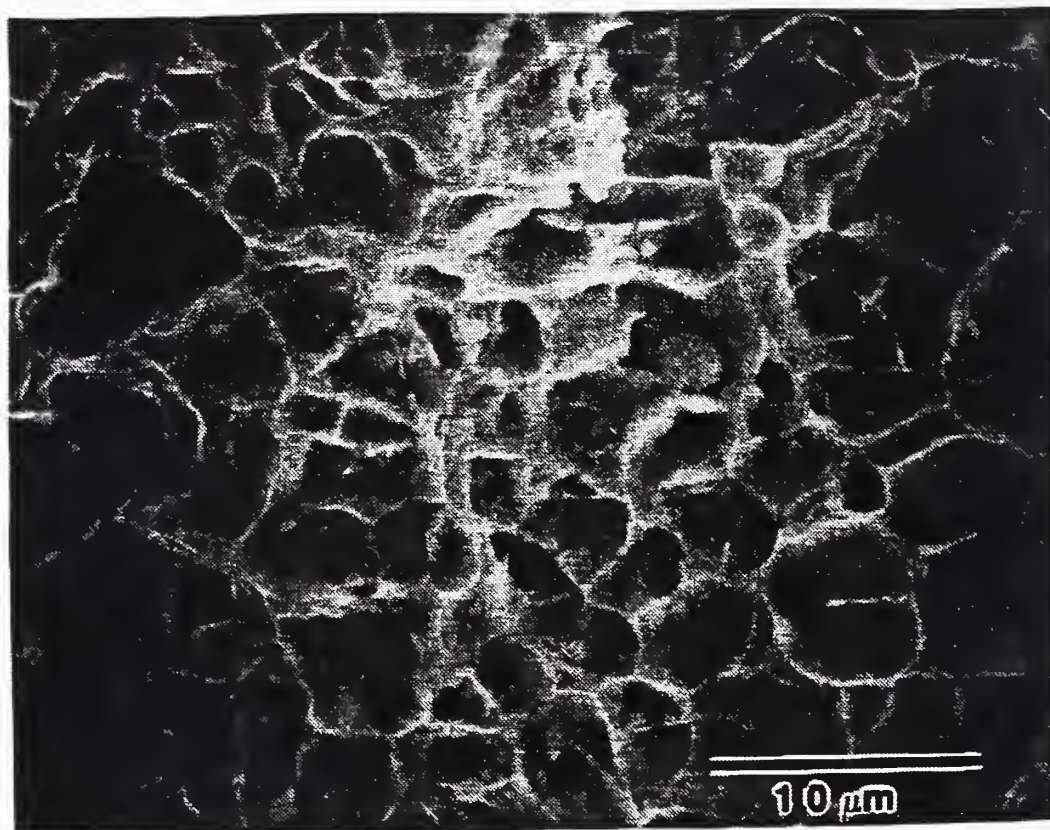


Figure 7. The fractures of the compact tension and uniaxial tensile specimens were dominated by ductile dimples (316L-H0 compact tension specimen).



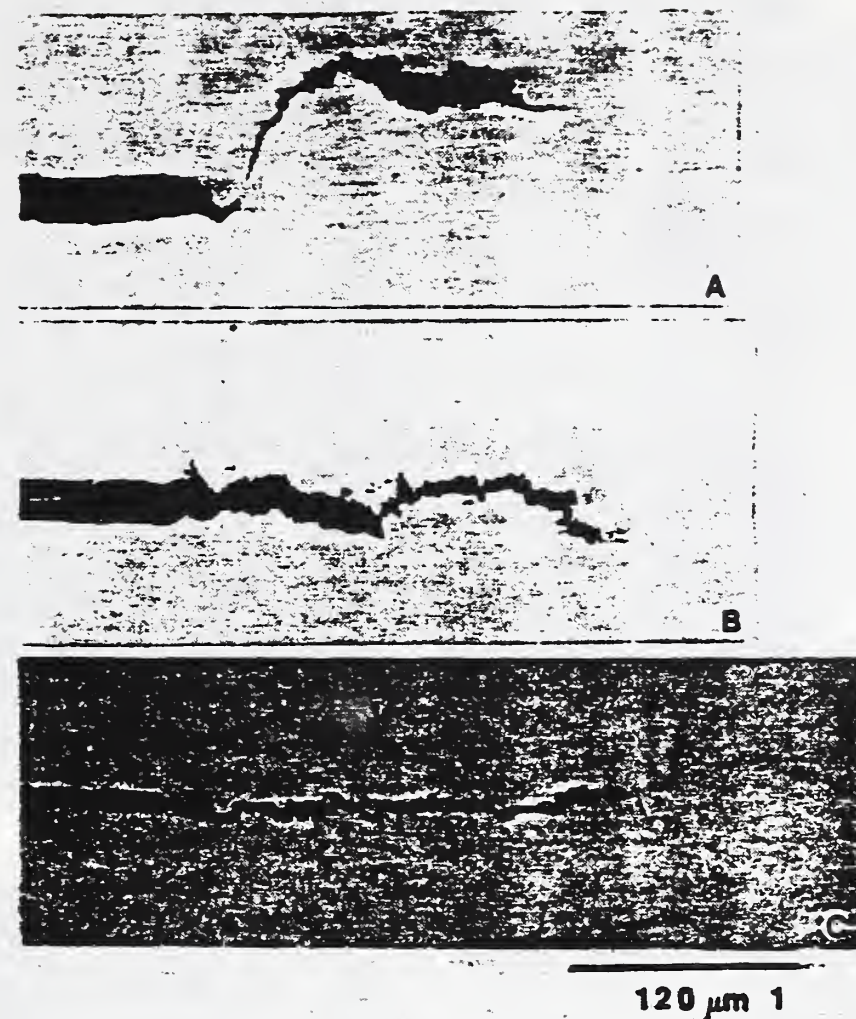


Figure 8. Stable crack growth was observed in each of the 316L fracture specimens at 85% of their estimated  $K_{IC}$  values. The SEM micrographs shown here are from the 316L-D (A), the 316L-R0 (B), and the 316L-H0 (C) compact tension specimens.

The void sizes observed on cross-sections of the tensile and compact tension samples are small compared with the ductile dimple sizes on the fracture surfaces (Figure 9). This implies that much of the dimple growth process is due to localized flow during fracture: voids do not appear to grow stably until impingement causes failure on a general basis. Most commonly, voids were observed to be linked by "microcracks" during the examination of the 316L crack profiles (Figure 10). Although the "microcracks" are sometimes closely associated with the ferrite phase (Figure 11), our observations indicate that this is due to a second order effect of the ferrite phase interrupting crack growth directions in the softer austenite, rather than the ferrite-austenite initiating cracks. Voids appear to nucleate at precipitates or inclusion associated with the ferrite phase. The ferrite phase, however, does serve as an effective barrier to plastic flow in the matrix (Figure 12), and this may be the principal cause of the increased strength and reduced toughness that has been attributed to the presence of ferrite in austenitic welds.



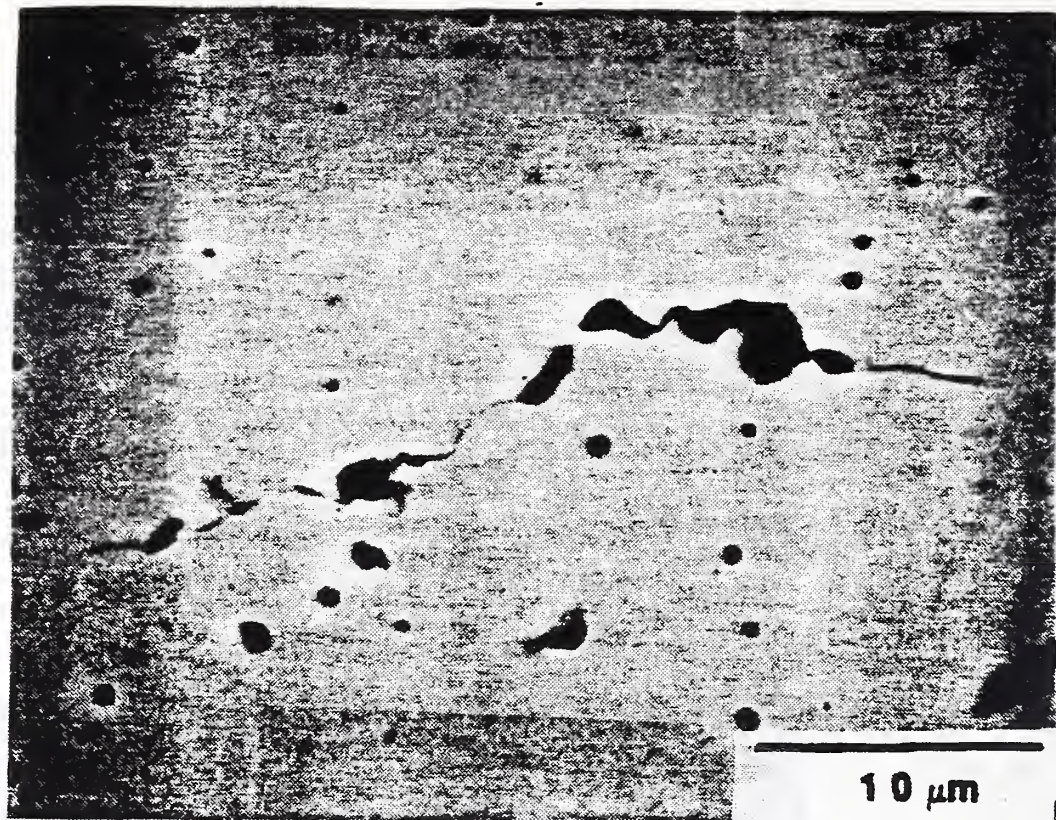


Figure 9. The voids that nucleated near the crack planes in the 316L fracture specimens typically showed only limited signs of growth (316L-H0 sample, 85%  $K_{Ic}$ ).

#### CONCLUSIONS

1. Improved gas shielding of the arc region during GMA welding results in welds of significantly increased toughness at 4 K.
2. Type 316L stainless steel welds already contain appreciable crack growth at 85% of their estimated  $K_{Ic}(J)$  values.
3. Stable crack growth appears to occur by the linking of voids via "micro-cracking" rather than the coalescence of voids.



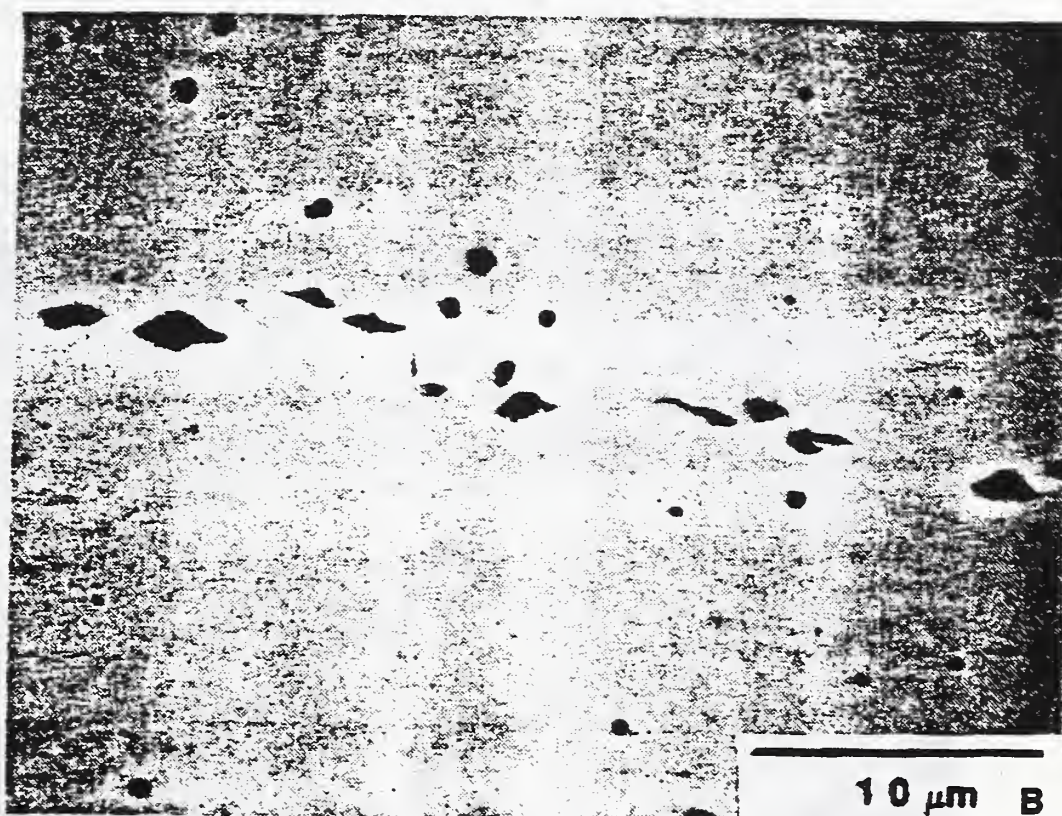
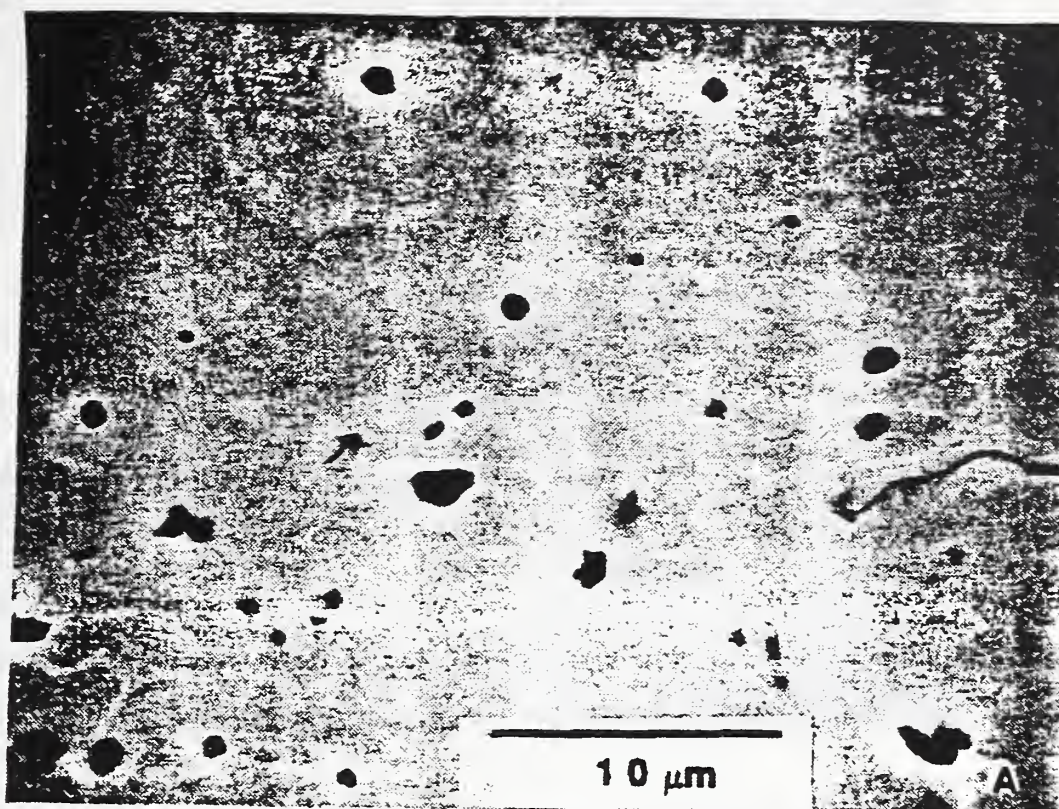


Figure 10. The crack tip region of the 316L-HO specimen (85% of  $K_{IC}$ ) shows voids to be linked by "microcracking" rather than void coalescence. For Figure 10A, a 20 ml HCl, 20 ml lactic acid, 5 ml  $HNO_3$  was etched.



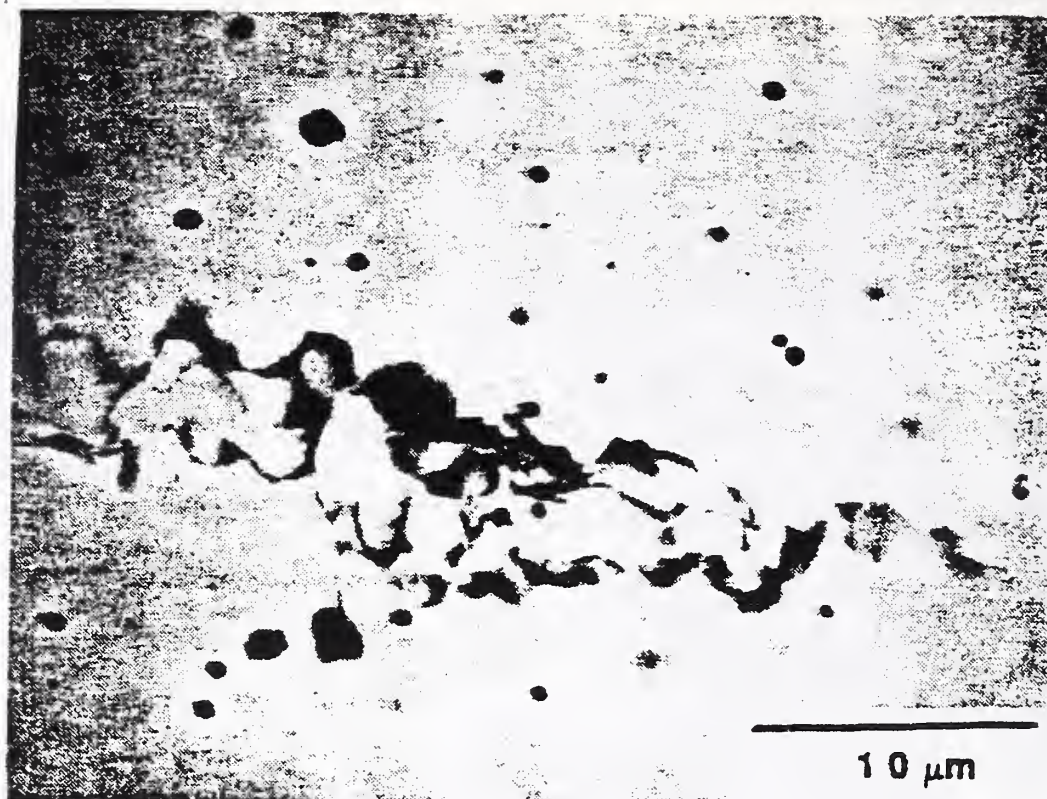


Figure 11. The ferrite phase (medium contrast, skeletal network) was sometimes found to be closely associated with the fracture path (316L-HO sample, 85% of  $K_{IC}$ ).



Figure 12. In the 316L-D tensile specimen (48% elongation), no fractured ferrite was observed. The etch (20 ml HCl, 20 ml lactic acid, 5 ml  $HNO_3$ ) shows ferrite (white) and plastic flow.



## REFERENCES

1. McCowan, C.N. and Siewert, T.A., Inclusions and Fracture Toughness in Stainless Steel Welds at 4 K, Advances in Cryogenic Engineering - Materials, Volume 32, 1986, Plenum Press, 335-342.
2. Morris, J.W., Structural Alloys for High Field Superconducting Magnets, Advances in Cryogenic Engineering-Materials, Volume 32, 1986, Plenum Press, 1-22.
3. Reed, R.P., Purtscher, P.T., and Yushchenko, K.A., Nickel and Nitrogen Alloying Effects on the Strength and Toughness of Austenitic Stainless Steels at 4 K, Advances in Cryogenic Engineering-Materials, Volume 32, 1986, Plenum Press, 43-50.
4. Tobler, R.L., Read, D.T., and Reed, R.P., Strength/Toughness Relationship for Interstitially Strengthened AISI 304 Stainless Steels at 4 K, Temperature, Fracture Mechanics: Thirteenth Conference, Richard Roberts Ed., ASTM STP 743, America Society for Testing and Materials, Philadelphia, 1981, 250-268.
5. Standard Test Method for  $J_{IC}$ , A Measure of Fracture Toughness, E813-81, in: Annual Book of ASTM Standards, Part 10, American Society for Testing and Materials, Philadelphia, 1982, 822-840.
6. Underwood, E.E., Quantitative Stereology, Addison-Wesley Publ. Co, Reading, MA, 1970.
7. Tobler, R.L., Siewert, T.A. and McHenry, H.I., Strength-Toughness Relationship for Austenitic Stainless Steel Welds at 4 K, Materials Studies for Magnetic Fusion Energy Applications at Low Temperatures - IX (NBSIR 86-3050), 1986, 239-246.
8. Ritchie, R.O. and Thompson, A.W., On Macroscopic and Microscopic Analyses for Crack Initiation and Crack Growth Toughness in Ductile Alloys, Metallurgical Transactions A (16A) 2, 1985, 233-247.
9. Reed, R.P., Simon, N.J., Purtscher, P.T., and Tobler, R.L., Materials Studies for Magnetic Fusion Energy Applications at Low Temperatures - IX (NBSIR 86-3050), 1986, 15-26.





# TEST STANDARDS



## UNITED STATES-JAPAN DEVELOPMENT OF TEST STANDARDS PROGRAM

PRINCIPAL INVESTIGATOR: R.L. Tobler

CONTRIBUTING ORGANIZATIONS: National Institute of Standards and Technology,  
Tohoku University,  
Japan Atomic Energy Research Institute,  
Kobe Steel,  
National Research Institute for Metals

### OBJECTIVES

- Establishment of a standard test method for tensile testing of structural alloys at 4 K
- Establishment of standard test methods for fracture testing at 4 K
- Administration of a round-robin test program to support the standards development
- Administration of experimental research to evaluate critical aspects of test standardization at 4 K
- Liaison with the American Society for Testing and Materials (ASTM) and its task group activities for the purpose of establishing the standards by voluntary consensus

### PROGRAM HIGHLIGHTS

- Cryogenic materials scientists were interviewed at government, industrial, and academic institutions in Japan. Their experience and advice were helpful in preparing the drafts of the test procedure standards.
- Six drafts of a proposed standard 4-K tensile test were written and submitted for review at domestic and international workshops. The sixth revision has been formally submitted to ASTM, and is being balloted.
- Five drafts of a proposed standard for 4-K fracture toughness testing were written and reviewed at Japanese domestic workshops. A sixth revision is being prepared for ASTM to begin due process for standardization.
- Round-robin tensile and fracture tests were conducted on a Fe-24Cr-15Ni alloy. A summary of results was presented at the 1988 United States-Japan International Workshop. A paper has been submitted for publication at the International Cryogenic Materials Conference to be held July 24-28, 1989 in Los Angeles.



- An experimental research program was completed by participants at NIST and four Japanese laboratories. From 70  $J_{IC}$  fracture toughness tests, the effects of specimen size, side grooves, test speed, and fatigue cracking on the test procedure were determined. Twelve papers describing the results have been published.

- Six workshops were an integral part of the program:

Standardization of Fracture Toughness Testing of Low-Temperature Structural Materials at Tohoku University, Sendai, Japan in March 1986.

Low-Temperature Structural Materials and Standards at Japan Atomic Energy Research Institute in Tokai-mura, Japan in August 1986

DOE-JAERI Low Temperature Structural Materials and Standards Workshop in Reno, Nevada in October 1986

United States-Japan Cooperative Research Program Review at Tohoku University in January 1987

United States-Japan Cooperative Research Program Review at the Japan Atomic Energy Research Institute, Tokai-mura in May 1988.

Workshop on 4-K Mechanical Testing at the National Institute of Standards and Technology, Boulder on April 4, 1989.

- At ASTM technical meetings, the draft standards are being reviewed by the task groups that will process these standards. The following meetings helped to advance these standards:

The E24 meeting on fracture testing held in Reno Nevada, April 16-17, 1988.

The E28 meeting on tensile testing held in Baltimore, Maryland May 16-17, 1988.

The E24 and E28 meetings held in Atlanta, Georgia, November 6-9, 1988.

The E24 and E28 meetings held in Kansas City, Missouri, May 22-25, 1989.

U.S. - JAPAN COOPERATIVE PROGRAM FOR THE  
DEVELOPMENT OF 4-K TEST STANDARDS  
Technical meetings (and follow-up discussions)

R.L. Tobler  
Fracture and Deformation Division  
National Institute of Standards and Technology  
Boulder, Colorado

## INTRODUCTION

With the American Society for Testing and Materials (ASTM), we are establishing standards for tensile and fracture toughness testing of alloys at 4 K. We are also interested in the status of standards for testing composite materials. In support of these activities, I participated in the following meetings:

1. The U.S. domestic workshop  
Colorado Springs, Colorado, October 18-19, 1988, and
2. ASTM Technical Committee Week,  
Atlanta, Georgia, November 7-10, 1988.

Since these meetings, several follow-up discussions have taken place. The purpose of this memorandum is to bring you up to date on the progress of all the related standards activities.

## THE 1988 U.S. DOMESTIC WORKSHOP

At this meeting I described some technical highlights from the U.S. - Japan international workshop held at JAERI May 27-28, 1988. I then presented a preliminary comparison of the second round robin results from the U.S. laboratories.

Four U.S. laboratories participated in the round robin testing of JN steel. Discussion focussed on the fracture toughness measurements because several problems were encountered. The data from two laboratories show unacceptable scatter in resistance curves and significant bias in  $K_{Ic}(J)$  measurements; the values from one lab are too low (about  $100 \text{ MPa}\cdot\text{m}^{1/2}$ ), and the values from another are too high (about  $300 \text{ MPa}\cdot\text{m}^{1/2}$ ).

All four laboratories used the unloading compliance technique. The system at NIST has been used since 1980. The other three systems were developed very recently, and two of them may still be bugged. Someone suggested that material variability could have contributed to the scatter, but there is no evidence of such variability in the Japanese results which are all very uniform.



In January 1989, JAERI and NIST agreed to publish the results of this round robin at the next meeting of ICMC (July 24-28, 1989). Therefore we have about five more months to resolve the U.S. results. After separate discussions with representatives of each lab (I. Hwang, MIT; L. Summers, LLNL; and J.W. Morris, LBL), I recommend the following actions to explain or improve the results:

1. Each U.S. participant will review their procedure and results to be sure no obvious mistakes were made.
2. Each participant will send fractured specimens to LBL for microscopic examination to verify that there are no anomalous fractographic features reflecting material variability.
3. The participants will consider a meeting of appropriate personnel to discuss programming and compare flow charts of their data acquisition and reduction methods.

Regarding the third point above, NIST can also benefit by upgrading its system to incorporate state-of-the-art advances. NIST is then the logical host for the technical meeting. The personnel involved with programming in each laboratory are: D.T. Read, NIST; I. Hwang, MIT; R. Riddle, LLNL; and J. Chan, LBL. A date has not yet been set, but all laboratories have agreed in principal to a meeting. In addition to the above, more compact specimens are requested from JAERI so that re-tests can be performed as necessary.

#### ASTM TECHNICAL COMMITTEE MEETINGS

##### Temperature Effects Subcommittee (ASTM E28.10).

This committee is processing our 4-K tensile standard. Mr. Thomas Wilmlink (Inco Alloys International, Huntington, West Virginia, 25720; telephone: 304-526-5690) has replaced R. McDemus as chairman.

Every standard must pass three ballots: the subcommittee, main committee, and society wide ballots. At this meeting the subcommittee ballot results for the tensile standard were made known. Our standard passed with 5 affirmatives, 5 abstentions, and 5 not returned. The standard now graduates to the second step, which is main committee ballot.

Regarding responses to our standard there were no negative criticisms, but a professional outside the subcommittee submitted some useful suggestions in writing. Also, at the 1988 U.S. - Japan workshop we agreed to define and add a new parameter,  $\sigma_1$ , the stress at the first serration. The subcommittee faced a choice of revising at this point or waiting for revisions until after the standard went through all the voting stages. At first it was decided to proceed without a revision, for the sake of expediency. Later, the chairman has reversed that decision because he discovered that a revision could be made without any substantial delay in processing at ASTM. Therefore I have agreed to provide a newly revised draft before the end of March. The subcommittee will have the revised draft at the next technical meeting (May 22, Kansas City). That draft will then be submitted to the main committee ballot in September, and any negatives



will be resolved at the technical meeting in November, 1989. According to this timetable the standard should be accepted in 1990.

Regarding developments on the other side, I learned recently from H. Nakajima that standardization of the tensile test is also proceeding in Japan. The original draft standard was revised slightly to simplify the requirements for alignment, and it is being processed as a Japanese Industrial Standard by a committee with Dr. H. Takahashi serving as chairman.

#### Fracture Initiation Concepts Task Group (ASTM E24.08.04).

This committee is processing our 4 K fracture toughness standard, among numerous other activities. At this meeting there were seven technical presentations, including my own summary of recent developments in 4-K testing, a talk highlighting data from the U.S. - Japan workshop (May, 1988).

In the presentation and the ensuing discussion, I emphasized that the austenitic steels at 4 K do not behave exactly like ferritic steels at room temperature. Evidence presented at the U.S. - Japan international workshop had indicated that the blunting behavior, regression line formalisms, and thickness requirements are different. In this way I reasoned to accept all of those modifications that the American and Japanese scientists agreed to at the international workshop.

Drs. Joyce and Hackett co-chair this task group, but Ed Wessel exercises main committee supervision. At Wessel's suggestion it was agreed to revise the format of our standard; instead of a separate new document, our standard will be re-written and included as an Annex to the existing method E813-87. Joyce is still somewhat concerned that our proposed modifications for cryogenic austenitic steels will conflict with the main text of E813-87. Therefore I must discuss and resolve the technical points with him by personal correspondence.

Regarding a schedule for progress, I agreed to write and distribute the Annex by April 1, 1989. This Annex must be acceptable to the co-chairmen and will be formally presented to the task group at the next technical meeting (May 22, 1989 in Kansas City). Balloting of the Annex should begin then.

According to the above, there must be a major change in our 4-K fracture standard. The present draft combines  $K_{IC}$  and  $J_{IC}$  testing, whereas the Annex will cover only  $J_{IC}$  testing at 4 K. NIST agreed to this change for several reasons. First, we believe that the existing  $K_{IC}$  standard (ASTM Methods E399-83), although it does not reference cryogenic apparatus, is fully satisfactory for 4-K testing in regard to its technical requirements (loading rate, precracking guidelines, etc). Also, the combination of test methods is already being pursued by another committee (ASTM E24.08.01). That group is working to establish a test procedure consisting of one large document covering and combining  $K_{IC}$ ,  $K_R$ ,  $J_{IC}$ ,  $J_R$ , and CTOD tests. They are exploring modifications of all test procedures in an attempt to achieve conformity between linear elastic, elastic-plastic, and fully plastic tests. Therefore it seems better for us to complete the 4-K  $J_{IC}$  test Annex now and benefit from the ASTM work in the future.

## Composite-Related Meetings

Committee D-30 (High Modulus Fibers and Their Composites) also held several meetings in Atlanta, but they conflicted with the metals meetings. I missed the Shear Testing Task Group (D30.03.01) and part of the Study Group on Compression Testing (part of D30.90). However, I attended the main committee meeting D-30 which provides an overview of all activities.

The status of standards for composites testing at room temperature is complicated. For example, ASTM now has three compression test standards and three more are in process. The question is: to what extent can we develop a single cryogenic test method that can address the various different design needs? One approach is to review the existing tests and relevant literature, and select a method with the features most relevant for cryogenic testing.

Committee D-20 (Plastics and Reinforced Plastics) did not meet in Atlanta, and generally there is little interaction between D-20 and D-30. Our main interest is glass reinforced plastics, but the methods of D-30 may prove better for us than those of D-20 because D-30 pays more attention to the problems of stress concentration effects which are of greater concern in cryogenic tests.

## CONCLUSION

The developments in cryogenic materials test standards may be summarized as follows: The 4-K tensile standard is well into the balloting process and may be published in 1990. The 4-K fracture standard has been reviewed by ASTM, but it must be re-formatted before balloting begins. I will send the revised drafts of the tensile and fracture standards to ASTM and to Japan according to the schedules indicated above. At present, there are no cryogenic standards for composites; we can begin by formulating a strategy for compression and shear tests based on what can be gained from experience at room temperature. A special session will be created at ICMC in July to gain background for standardization activities for composites.





UNITED STATES DEPARTMENT OF COMMERCE  
National Institute of Standards and Technology  
[formerly National Bureau of Standards]  
325 Broadway  
Boulder, Colorado 80303-3328

Reply to the attention of:

March 21, 1989

MEMORANDUM FOR: Dr. H.I. McHenry  
Chief, Fracture and Deformation Division

From: R.L. Tobler  
Fracture and Deformation Division

Subject: Trip Report - ASTM D30 Symposium and technical committee meetings related to development of standards for mechanical property tests of composites (Charlotte, NC, March 14-16, 1989)

I attended these meetings to gain contacts and information on the current activities of ASTM and other groups interested in the development of test standards for composites. Our goals for the DOE program include eventual development of test standards for composites at cryogenic temperatures.

#### I. SYMPOSIUM ON AUTOMOTIVE AND INDUSTRIAL COMPOSITES

This symposium ran into problems as 4 out of 8 papers were cancelled. However, the cancellations created extra time for informative discussion. The issues in this field unfold as follows:

- Accelerated testing - there is a need for tests enabling long term effects to be predicted from short-term measurements.
- Combined effects - there is a need for tests enabling the prediction of long-term durability of composites subject to combined effects of moisture, temperature, and stress.
- Fiber distribution effects - there is a need to account for fiber orientation distribution variations created by processing operations.

In automotive applications, the use of composites results in improved quality, durability, damage tolerance, and reduced costs or weight savings. Composites are already used in external body panels as well as some primary components: glass-epoxy is used in leaf springs and glass/graphite hybrid composites are used in drive shafts. Uses are expected to expand in the future.



An Automotive Composites Consortium (ACC) has been formed to improve America's international competitiveness by sponsoring general research of interest to the three participating manufacturers (Ford, GM, Chrysler). The ACC consists of a board of directors and three task groups: Materials, Processing, and Crash Energy. Their goal is to develop a textbook of composites technology including test methods and databases useful to all members and serving as a guide for their materials suppliers.

ACC's approach to standards is to adopt and adapt existing documents (ASTM, SACMA, and MIL standards), or create new standards as needed. At present structural components and processing are being emphasized. The automotive industry differs from the aerospace industry in that low cost, quick, and more specific tests are needed. Material variability is more of a problem because production techniques tend to create distributions of fiber orientations in contrast to the more highly oriented and well specified materials used in aerospace.

## II. COMPRESSION TESTING STUDY GROUP

Various aspects of compression testing were considered here in three presentations. Dale Wilson's description of SACMA and its cooperative interaction with ASTM was by far the most significant item.

SACMA (Suppliers of Advanced Composite Materials Association) is a trade association strongly pushing the development of test standards for commercial purposes. They have already drafted eleven standards and are submitting them for processing through appropriate committees in ASTM.

Wilson (Celion Carbon Fibers, Inc), an invited speaker for our next ICMC meeting, and active in both SACMA and ASTM, presented three of SACMA's draft standards for oriented fiber-resin composites to this D30 meeting and proposed prompt execution of round robin test programs supporting each standard.

Wilson described the materials to be tested, the fixtures to be used, and the test methodologies to be evaluated (compression, compression after impact, and open hole compression). Each methodology would be evaluated using 3-5 materials, and 5 tests per material. The study group voted in favor of his proposal, appointed specialists to review the draft documents, and agreed to respond formally to SACMA within one month. As a result, test results could be available at the next study group meeting (Orlando FL, November, 1989). Ten labs are needed for each type of test, and I placed NIST on the mailing list for possible participation.

## III. AUTOMOTIVE/INDUSTRIAL SHEAR TESTING

There were three items on the agenda for this meeting. These included comments on the automotive/industrial composites symposium (already discussed), an update on the task group's proposed V-notch shear test standard, and a presentation of a new method for in-plane shear measurements using a compact double-notched specimen.

As currently written, the proposed V-notch shear test standard recognizes both the Iosipescu and bend specimen geometries. This standard received some negative votes in recent balloting, and the equivalence of the two specimens became questionable because recent round robin results show some outliers for the bend specimen. Consequently, the task group at this meeting decided to omit the bend specimen from the document, proceed with standardization using only the Iosipescu specimen, and introduce the bend specimen later after additional study.

Post and Ifju (University of Virginia, Blacksburg) described a new specimen for in-plane shear measurements and presented preliminary experimental work using cross-ply specimens of graphite-epoxy. They find the new specimen geometry to be eminently suitable for routine determinations of stress-strain properties in shear, and for shear strength measurements at ambient temperatures.

The new specimen, a compact double-notched geometry, was 1.5 in long, 0.75 in wide, and 0.25 in thick, with opposing notches. Post claims from moire analysis that this specimen offers a state of nearly pure and uniform shear in the region between the notch tips, and that it may be superior in this respect to the popular Iosipescu specimen. The compact specimen is small, the fixtures are simple and inexpensive, and the tests are easy to perform. I assume the specimen can be scaled up or down in size a little more. Therefore, from our own perspective, it appears that this compact specimen may be the ideal choice for shear tests of irradiated composite materials at 4 K.

#### IV. CONCLUSION

The choice of specimen design is one of the critical steps in developing cryogenic test standards for shear and compression testing. Based on the information gained at these meetings, it appears that the problem of specimen geometry for 4-K shear testing of irradiated composites may be solved by using the new double-notched compact specimen. Laboratory tests of this specimen at cryogenic temperatures are needed to verify applicability and optimum specimen dimensions.





## CHARPY TESTS NEAR ABSOLUTE ZERO

R.L. Tobler and R.P. Reed  
Fracture and Deformation Division  
National Institute of Standards and Technology  
Boulder, Colorado 80303

Because the specimen warms up as it is transferred to the test machine and fractured, valid impact tests of alloys at 4 K can not be performed according to the standard procedure outlined in ASTM Methods E 23-86. This paper describes the problems of Charpy testing at extreme cryogenic temperatures, especially 4 K, including alternative methods of testing and calibration. We review previous experience, including observations of specimen temperatures during various phases of testing, and correlations of the Charpy impact energy (CVN) with quantitative toughness parameters such as  $J_{Ic}$  or  $K_{Ic}$ .

During Charpy tests at impact strain rates the temperature of austenitic steel specimens initially at a nominal temperature of 4 K rises over 100 K, and correlations between CVN and  $K_{Ic}$  or  $J_{Ic}$  do not necessarily show the desired 1:1 correspondence. Fracture does not occur at the intended temperature, or even at a constant temperature, since materials with different work hardening rates show different adiabatic heating behavior. Because of the temperature rise variability and data scatter in the measurements and property correlations, we conclude that it is not possible to accurately estimate the fracture toughness of ductile steels, or rank them exactly, using Charpy tests at 4 K.

### INTRODUCTION

Simple methods of fracture toughness evaluation are always desirable, especially at cryogenic temperatures where the tests are more expensive. Traditionally, the Charpy test has been used to evaluate the toughness of materials, especially ferritic steels, at temperatures as low as 77 K. For aerospace applications the temperature of interest is 20 K, and for superconducting machinery applications it is still lower at 4 K. Researchers have performed Charpy tests at these lower temperatures, but experience shows that special procedures and precautions regarding data interpretation are necessary when the test temperature approaches absolute zero.

The characterization of structural alloys for large superconducting magnets in fusion energy machines requires the evaluation of tough austenitic alloys at 4 K. Computerized J-integral fracture tests at slow loading rates provide a reliable quantitative measure of fracture toughness at 4 K; simpler Charpy tests have been used for screening purposes to develop new cryogenic alloys, and are sometimes proposed for quality control or acceptance tests. As argued in this paper, however, the meaning of impact test data at temperatures near absolute zero is questionable because of problems associated with temperature control.

The existing standard [1] does not mention it, but Charpy testing at 4 K requires departures from the conventional procedure because the specimen after being cooled to 4 K cannot be transferred through air to the test machine in the routine way. Instead, various methods of insulating the specimen on the anvil are used. The insulation is fractured with the specimen, necessitating a nonstandard calibration correction. Although specimen heating during transfer can be eliminated that way, the severe adiabatic heating of the specimen upon impact inevitably complicates any interpretation of the results. Adiabatic heating occurs in mechanical tests at any test temperature, including room temperature, but is much worse at extreme cryogenic temperatures because of the very low specific heats of the test materials.

Most laboratories that conduct impact tests rely on swinging pendulum type machines. A few labs have special facilities for nonstandardized tests, but little information on these other methods is available in the literature. As illustrated photographically by Novikov [2] and schematically by Verkin [3], a pneumatic device is used in the Soviet Union for impact tests at 4 K. Their device consists of an enclosed chamber with a vertically aligned and pneumatically driven hammer. Drop-weight impact tests [4] and instrumented impact test [5] at 4 K have also been conducted on a limited scale, but only conventional swinging pendulum tests are considered in this paper.

## PROCEDURE

### Conventional Testing

Conventional Charpy testing is conducted according to the ASTM Standard Methods for Notched Bar Impact Testing of Metallic Materials, Designation E 23-86 [1]. Within 5 s, a 10 x 10 x 55 mm notched bar specimen is quickly removed from a cooling bath, positioned on the anvil of an impact test machine, and fractured. The absorbed energy and the lateral expansion of the specimen at the notch plane are then measured to characterize fracture resistance. This procedure is quite satisfactory at temperatures down to 77 K, especially for the traditional characterization of ferritic steels, but for austenitic alloys at still lower temperatures it proves inadequate. Three problems are encountered: the temperature of the test specimen rises as it is transferred to the anvil, the specimen is susceptible to adiabatic heating as it fractures at impact strain rates, and the data scatter for replicate tests increases at cryogenic test temperatures.



## Cryogenic Testing

The most common temperatures in cryogenic research are the fixed bath temperatures of the liquid cryogens: 77 K (nitrogen), 20 K (hydrogen), and 4 K (helium). The principal means of verifying the adequacy of tests at these temperatures has been to instrument calibration specimens with thermocouples and record the specimen temperature throughout the various stages of testing.

Depending on purpose, the thermocouples can be attached to the specimen surface, or implanted in the center of the thickness by means of drilled holes. Chromel-versus-Gold + 0.07% iron thermocouples are preferred for maximum sensitivity below 20 K. Experimental observations confirmed that for specimens initially cooled to 77 K there is no appreciable temperature rise within the 5 s that it takes to transfer and fracture the specimen according to the ASTM procedure [6]. On the other hand, data for specimens cooled to 20 or 4 K show that the temperature begins to rise immediately after the specimen is removed from its Dewar [7,8]. Therefore different procedures are needed, depending on the intended initial test temperature: tests at 77 K or above can be conducted by the established procedure specified in ASTM Methods E 23, but to conduct tests at 20 or 4 K we must resort to special techniques. A number of approaches are described in the literature, but none are specified in the current standard.

In the quest to obtain satisfactory results at 4 K, almost every conceivable approach has been tried, including direct transfer of the specimen from the cryogenic bath through air to the anvil of the test machine, encapsulation of the specimen, and encapsulation of the entire test machine. Each method offers specific advantages and disadvantages, and none has come to predominate. A number of variations of each approach are considered below.

### Direct Transfer

Several researchers have tried to apply ASTM Methods E 23 while making no special provision for extreme cryogenic test temperatures. Their efforts show only that the conventional procedure fails.

For example, Lee and Dew Hughes [9] reported Charpy data for stainless steel castings at several temperatures as low as 77 K but they were forced to abandon Charpy testing at 4 K because "the problems of temperature control and scatter were unacceptable". To document the problem of temperature control quantitatively, Dobson and Johnson [8] recorded the thermal histories of AISI 304 specimens containing embedded thermocouples. Using pre-cooled tongs, they transferred bare specimens through air as quickly as possible but the specimen temperatures increased to 67-71 K before the specimens could be impacted. Yoshimura et al. [10] did better by covering their specimens during transfer; still, the temperature of their specimens rose to about 15 K before the hammer could strike them.

A rise to 15 K or more is of course unacceptable, since a temperature accurate to within one kelvin is required by the standard. Therefore significant efforts have been made to insulate the specimen, and sometimes the entire machine, to achieve a fixed initial test temperature. Several methods are reviewed below.



## Boating, Boxing, and Encapsulation

A paper boat method for tests at 20 K was first developed at Ohio State University [7]. As described by Zambro and Fontana [6], a standard Charpy specimen is glued to the bottom of a paper boat that has a perforated cover and is suspended by threads to paper tabs used for handling. After cooling in liquid hydrogen, the specimen is lifted out of its dewar and transferred through air to the anvil of the machine. During transfer, the container retains sufficient liquid to forestall specimen heating. Once the specimen is on the anvil, the threads are cut and the hammer released. A clever variation of the boating method can be used for tests at 5 or 6 K, as described by Long [11].

Although the paper boat method and its variants permit tests at 20 or lower, the method is disadvantageous in that hydrogen is hazardous, special precautions are necessary to avoid explosions. Therefore Jin et al. [12] developed a test using liquid helium and a plastic insulating box for specimens tested below 6 K.

To improvement on the method described by Jin et al., Ogata et al. [13,14] sought simpler types of encapsulation. In their system, the plastic box is replaced by a capsule made of grooved polystyrene foam which achieves better cooling efficiency and minimizes the calibration error.

Another recently developed technique, widely used in Japan, is the glass Dewar method [15]. The specimen is placed in an (open or closed) mouth vacuum-insulated glass tube capable of retaining liquid helium for several minutes. The tube containing the specimen is then placed on the anvil and fractured. This method assures an initial test temperature of 4.2 K, but the CVN measurement must be corrected to account for the significant energy absorbed in fracturing the glass container. Two methods of calibration correction have been suggested, as discussed in the next section.

In other work, the test machine as well as the specimen was encapsulated [7,16]. In general, the unique advantages of those methods are outweighed by the complexity of the apparatus required, and the methods haven't been used by anyone except the original experimenters.

## Calibration

Tests of encapsulated specimens require a nonstandard calibration correction to account for the energy absorbed in fracturing the insulation or container. Inevitably, assumptions are involved in arriving at a correction factor.

Usually, tests of encapsulated or insulated specimens are calibrated simply by subtracting the energy required to break the capsule from the total energy. The correction factor is deduced by comparing the results of tests performed on empty capsules versus the results for capsules with specimens. The comparison is sometimes made at 273 K [15], but usually at 77 K [17]. The calibration correction factor so determined is then used also at 4 K, assuming that the effect of the test temperature on the calibration factor is negligible. The underlying assumption, however, that the energy to break the capsule with a specimen is equal to the sum of the

energies required to break an empty capsule plus that to fracture a bare specimen, has not yet been experimentally verified.

Typical calibration factors for the various methods are listed in Table 1. The paper boat method has the advantage of the smallest correction factor. For the glass Dewar encapsulation technique, the correction factor is quite high and, for low toughness materials, it would amount to a significant fraction of the total impact energy. The glass Dewar method is therefore not suited for the low toughness alloys.

Another calibration technique is possible, but less commonly used. In Charpy testing it is customary to measure both the energy absorbed on impact (CVN) and the lateral expansion (LE). A number of researchers have shown that CVN and LE are approximately linearly related for certain conditions, and, as described by Mori and Kuroda [18], this relationship provides a basis for a second calibration procedure for tests at 4 K.

#### Adiabatic Heating

While specimen warming during transfer can be eliminated by boating, boxing, or encapsulation, the heat generated in the specimen during deformation and fracture at impact loading cannot be avoided.

Adiabatic heating depends on material and test variables, including the total quantity of plastic work consumed in fracturing the specimen, the rate of straining (heat production), the specific heat of the test material, and the efficiency of the cooling medium. Austenitic steels are more susceptible than other steels because they are usually tougher and have higher specific heats. In fact, adiabatic heating produces a measurable temperature rise in austenitic steel specimens during conventional tensile tests at room temperature [19]. The problem is worse at impact strain rates, and still worse at cryogenic test temperatures where the specific heats of the test materials are drastically reduced. For example, the specific heat of AISI 310S steel decreases by several orders of magnitude for a temperature change between 298 and 4 K.

Table 1. Typical calibration correction factors for Charpy tests methods at extreme cryogenic temperatures.

Method and type of insulation	Test temperature K	Calibration J	Reference
paper boat	20	0.3	[6]
polystyrene foam	5	1.5	[13]
plastic box	5-6	4.9	[12]
glass dewar	4.2	33	[15]



Adiabatic heating during fracture can be studied using specimens instrumented with thermocouples. In their impact tests of AISI 304 steel, Dobson and Johnson [8] recorded temperatures as high as 150 K. In future work, we intend to measure the temperature rises and compare them with numerical calculations based on the conversion of plastic work to heat.

### Data Trends

Typically, Charpy data for ferritic steels over a range of test temperatures show an abrupt decrease of energy at the transition temperature, whereas data for austenitic steels and alloys show a gradual increase or decrease of impact energy with test temperature. The same general trends have been observed in the extreme cryogenic range. For example, data for a 9% Ni steel and a high Mn austenitic steel were compared by [20]. The austenitic steel showed a gradual decrease of CVN at five temperatures between 4 and 295 K, whereas the ferritic steel showed a typical transitional behavior. There is one noteworthy feature regarding ferritic steel transitions: most mild steels have a transition temperature in the range 275–375 K, but in higher Ni steels the transition temperature is suppressed to 77 K or lower because Ni beneficially affects the resistance to cleavage.

### Data Scatter

Data scatter is a principal shortcoming of the Charpy test, and the old problem is magnified when Charpy tests are performed at temperatures approaching absolute zero. During the time it is being transferred, a bare test specimen warms continuously. Therefore the actual specimen temperature at the time of testing must vary with the transfer time, and this contributes to the data scatter of results.

Also, the scatter in data at extreme cryogenic temperatures increases relative to the level observed at room temperature because metallurgical and mechanical test variables have a greater influence on material properties at cryogenic temperatures. A third factor contributing to the increased scatter in Charpy measurements at 4 K is the added experimental uncertainty associated with the calibration correction factors required at 4 K.

### Data Correlations

In a large program sponsored by JAERI in cooperation with several Japanese steel companies, CVN data were used to screen newly developed cryogenic steels [20-21]. In this program, ninety alloy compositions were Charpy tested at 4 K, using the glass Dewar method. Alloys having CVN greater than 80 J were selected for further study. The selected alloys were then produced in greater quantities and subjected to quantitative  $J_{IC}$  tests. A 4-K fracture toughness of  $K_{IC} = 200 \text{ MPa}\cdot\text{m}^{1/2}$  or more was required to satisfy design constraints. In this way, six new alloy steel compositions were developed for superconducting machinery applications. After the  $J_{IC}$  values were measured, it was possible to compare the CVN and  $J_{IC}$  data for a number of alloys. The results, however, did not show a perfect 1:1 correlation [28, 29].



## DISCUSSION

We are sometimes tempted to avoid the extra effort involved in testing at 4 K by using 77 or 20 K data as a basis for making decisions about 4 K applications. Mazandarany et al. [30], in a presentation of data for an AISI 316LN base metal and several of its welds, demonstrated that this approach is inherently unreliable. They measured CVN at 77 K as well as  $J_{IC}$  at 4 K, but found no general correlation between the two parameters. Their data show that the problems of fracture characterization at 4 K cannot be resolved by Charpy tests at other temperatures. This is because the deformation mechanism at 4 K, is unique from that at 77 K or higher temperatures. At temperatures from ambient to 77 K, the load-displacement curves are regular, showing slow stable plastic deformation. At 4 K, however, the curves show instabilities which are due to increments of unstable (free-running) plastic deformations, each accompanied by temporary thermal spikes.

While general correlations between Charpy data and fracture toughness have been demonstrated at ambient temperature, there are several reasons to expect that CVN data should not correlate exactly with  $K_{IC}$  data at 4 K. First, the two tests do not measure exactly the same properties of materials. The Charpy test involves crack initiation from a notch, as well as crack propagation, whereas  $K_{IC}$  and  $J_{IC}$  pertain only to the initiation of fracture from a pre-existing crack.

Second, the tests are conducted at different strain rates, and the discontinuous plastic flow (serrated yielding) process that is a prominent feature of the 4-K tests is very sensitive to strain rate. Especially at nominal strain rates higher than about  $10^{-3}$ , the discontinuous deformation behavior and adiabatic temperature rise for most austenitic steels changes drastically [31].

Charpy impact data are used mainly in mechanical testing of steel products, in research, and in procurement specifications. As stated in the standard [1], the Charpy test is especially practical for tests of ferritic steels because it enables the ductile-to-brittle transition temperature to be determined; it is less informative when applied to austenitic alloys or face-centered cubic metals that typically do not exhibit transitional behavior. On these grounds, we conclude that the test is not ideally suited for austenitic alloys, or for the temperature of interest. Since the changes for austenitic alloys are not drastic, it is never clear to what extent the CVN changes with test temperature are due to material behavior or heating effects. Any test loses significance as the sensitivity of measurements approaches the property changes to be measured.

It seems that up to now the limitations of Charpy testing at liquid helium temperature have not been widely appreciated outside of the relatively small community of cryogenic researchers. For example, regulatory agencies today still require that helium storage tanks be designed according to the ASME boiler code which requires Charpy tests of materials of construction at 4 K. Although the value of Charpy tests at 4 K is questionable on technical grounds, the tests are nevertheless conducted because the code requires them. However, neither the code nor the Charpy test standard were originally written with 4-K applications or experience in view, and as emphasized in this paper, it is actually impossible to perform valid Charpy



tests at 4 K according to Methods E 23-86 as currently written, and as required by regulatory agencies.

Based on the facts reviewed in this paper, it may be appropriate to revise certain sections of Methods E 23 to recognize the problems of testing at extreme cryogenic temperatures. Revisions may include a temperature limitation for cryogenic testing to 77 or 20 K, or explicit recognition of special techniques appropriate for testing at 20 or 4 K.

## CONCLUSION

In this paper, we emphasize that it is impossible to perform Charpy tests at 4 K according to the procedure outlined in ASTM Methods E 23. After the specimen is removed from its dewar and before the hammer strikes it, the specimen temperature is continuously rising.

Charpy testing at 20 or 4 K entails a departure from the standard procedure of ASTM Methods E 23-86 because the specimen cannot be cooled and subsequently transferred to the test machine in the routine way. This paper describes the various alternative methods that have been used to perform impact tests at 4 K. Cryogenic researchers always employ some nonstandard procedure, and most prefer one of the various methods of insulating the specimen on the anvil. The insulation is fractured along with the specimen, requiring a nonstandard calibration correction. Each method has specific advantages and disadvantages, and none has gained predominance.

The Charpy test loses its simplicity in view of the extra efforts that must be taken to obtain data at 4 K. Consequently, the value of the Charpy test at 4 K is compromised. Perhaps some merit as a crude screening parameter for identifying brittle materials may be retained, in that a low CVN generally implies low toughness.

## REFERENCES

- [1] Standard Methods for Notched Bar Impact Testing of Metallic Materials, Designation E 23-86, in 1988 Annual Book of ASTM Standards, Section 3, Metals Test Methods and Analytical Procedures, Amer. Soc. Test. Mater., Philadelphia, 1988, pp 191-206.
- [2] Novikov, N.V., Mechanical Property Measurement Techniques of Structural Materials at Cryogenic Temperatures, in Adv. Cryo. Eng., Vol. 22, K.D. Timmerhaus, R.P. Reed, and A.F. Clark, Eds., Plenum, New York, 1977, pp. 113-118.
- [3] Verkin, B.I., The Development of Cryogenic Materials Science in the USSR, in Adv. Cryo. Eng., Vol. 26, Plenum, New York, 1980, pp. 37-47.
- [4] Nishijima, S., Takeno, M., and Okada, T., Impact Tests of Reinforced Plastics at Low Temperatures, in Adv. Cryo. Eng., Vol. 28, Plenum, New York, 1981, pp. 261-270.

- [5] Yoshida H., Kozuka, T., Miyata, K., and Kodaka, H., Instrumented Charpy Impact Tests at Low Temperatures, in Austenitic Steels at Low Temperatures, R.P. Reed and T. Horiuchi, Eds., Plenum, New York, 1983, pp. 349-354.
- [6] Zambrow, J.L., and Fontana, M.G., Mechanical Properties, Including Fatigue, of Aircraft Alloys at Very Low Temperatures, Trans. ASM, Vol. 41, 1949, pp. 480-518.
- [7] Kiefer, T.F., Keys, R.D., and Schwartzberg, F.R., Charpy Impact Testing at 20°K, in Adv. Cryo. Eng., Vol. 10, paper A7 Plenum, New York, 1965, pp. 56-62.
- [8] Dobson, W.G., and Johnson, D.L., Effect of Strain Rate on Measured Mechanical Properties of Stainless Steel at 4 K, in Adv. Cryo. Eng., Vol. 30, Plenum, New York 1984, pp. 185-192.
- [9] Lee, K.S., and Dew-Hughes, D., The Effect of  $\delta$ -ferrite Upon the Low Temperature Mechanical Properties of Centrifugally Cast Stainless Steels, in Austenitic Steels at Low Temperatures, R.P. Reed and T. Horiuchi, Eds., Plenum, New York, 1983, pp 221-242.
- [10] Yoshimura, H., Shimizu, T., Yada, H., and Kitajima, K., Tetsu-to-Hagane, Vol. 65, 1979, 681-686 (In Japanese).
- [11] Long, H.M., Union Carbide Corporation, in Adv. Cryo. Eng., Vol. 19, Plenum, New York, 1974, p. 378.
- [12] Jin, S., Horwood, W.A., Morris, Jr., J.W., and Zackay, V.F., A Simplified Method for Charpy Impact Testing Below 6 K, in Adv. Cryo. Eng., Vol. 19, Plenum, New York, 1974, pp. 373-378.
- [13] Ogata, T., Hiraga, K., Nagai, K., and Ishikawa, K., A Simplified Method for Charpy Impact Testing Near Liquid Helium Temperature, Cryogenics, Vol. 22, 9, 1982, pp. 481-482.
- [14] Ogata, T., Hiraga, K., Nagai, K., and Ishikawa, K., A Simple Method for Charpy Impact Test at Liquid Helium Temperature, Trans. Nat. Res. Inst. Metals., Vol. 26, No.3, 1984, pp. 238-242.
- [15] Takahashi, Y., Yoshida, K., Shimada, M., Tada, E., Miura, R., and Shimamoto, S., Mechanical Evaluation of Nitrogen Strengthened Stainless Steels at 4 K, in Adv. Cryo. Eng., Vol. 28, Plenum, New York, 1982, pp. 73-81.
- [16] DeSisto, T.S., Automatic Impact Testing to 8 K, Tech Report, 112/93 Watertown Arsenal Lab, 1958.
- [17] Matsumoto, T., Satoh, H., Wadayama, Y., and Hataya, F., Mechanical Properties of Fully Austenitic Weld Deposits for Cryogenic Structures, Welding Research Supplement, 1987, pp. 120-126s.



- [18] Mori, T., and Kuroda, T., Prediction of Energy Absorbed in Impact for Austenitic Weld Metals at 4.2 K, *Cryogenics*, Vol. 25, 1985, pp. 243-248.
- [19] Ferron, G., Influence of Heat Generation and Conduction on Plastic Stability under Uniaxial Tension, *Maters. Sci. Eng.*, Vol. 49, 1981, pp. 241-248.
- [20] Miura, R., Ohnishi, K., Nakajima, H., Takahashi, Y., and Yoshida, K., Mechanical Properties of 18Mn-5Cr Austenitic Steel at Cryogenic Temperatures, in *Austenitic Steels at Low Temperatures*, Plenum, New York, 1983, pp. 287-293.
- [21] Ogawa T., Masumoto, H., and Honma, H., The Weldability of 25 Mn Steel, in *Austenitic Steels at Low Temperatures*, R.P. Reed and T. Horinchi, Eds., Plenum, New York, 1983, pp. 339-348.
- [22] Tone, S., Shimada, M., Horiuchi, T., Kasamatsu, Y., Nakajima, H., and Shimamoto, S., in *Adv. Cryo. Eng.*, Vol. 30, Plenum, New York, 1984, pp. 145-152.
- [23] Masumoto, H., Suemune, K., Nakajima, H., and Shimamoto, S., Development of a High-Strength High-Manganese Stainless Steel for Cryogenic Use, in *Adv. Cryo. Eng.*, Vol. 30, Plenum, New York, 1984, pp. 169-176.
- [24] Horiuchi, T., Ogawa, R., and Shimada, M., Cryogenic Fe-Mn Austenitic Steels, in *Adv. Cryo. Eng.*, Vol. 32, Plenum, New York, 1986, pp. 33-42.
- [25] Sakamoto, T., Nakagawa, Y., and Yamauchi, I., Effect of Mn on the Cryogenic Properties of High Nitrogen Austenitic Stainless Steels, in *Adv. Cryo. Eng.*, Vol. 32, Plenum, New York, 1986, pp. 65-72.
- [26] Yamamoto, S., Yamagami, N., and Ouchi, C., Effect of Metallurgical Variables on Strength and Toughness of Mn-Cr and Ni-Cr Stainless Steels at 4.2 K, in *Adv. Cryo. Eng.*, Vol. 32, Plenum, New York, 1986, pp. 57-64.
- [27] Suemune, K., Sushino, K., Masumoto, H., Nakajima, H., and Shimamoto, S., Improvement of Toughness of a High-Strength, High-Manganese Stainless Steel for Cryogenic Use, in *Adv. Cryo. Eng.*, Vol. 32, Plenum, New York, 1986, pp. 51-56.
- [28] Tone, S., Ogawa, M., Yamaga, M., Kaji, H., Horiuchi, T., Kasamatsu, Y., Nakajima, H., Yoshida, K., Takahashi, Y., and Shimada, M., Preliminary Study on Structural Material Selection for Large Superconducting Magnets, in *Austenitic Steels at Low Temperature*, R.P. Reed and T. Horiuchi, Eds., Plenum, New York, 1983, pp. 263-275.
- [29] Nakajima, H., Yoshida, K., Okuno, K., Oshikiri, M., Tada, E., Shimamoto, S., Miura, R., Shimada, M., Tone, S., Suemune, K., Sakamoto, T., and Nohara, K., Fracture Toughness of Newly Developed Structural Materials for Superconducting coils of fusion experimental reactor, in *Adv. Cryo. Eng.*, Vol. 32, Plenum, New York, 1986, pp. 347-354.

- [31] Mazandarany, F.N., Parker, D.M., Koenig, R.F., and Read, D.T., A Nitrogen-Strengthened Austenitic Stainless Steel for Cryogenic Magnet Structures, in Adv. Cryo. Eng., Vol. 26, Plenum, New York, 1980, pp. 158-169.
  
- [32] Reed, R.P., and Walsh, R.P., Tensile Strain-Rate Effects in Liquid Helium, in Adv. Cryo. Eng., Vol 34, Plenum, New York, 1988, pp. 199-208.





WARM PRECRACKING AT 295 K AND ITS EFFECTS  
ON THE 4-K TOUGHNESS OF TWO AUSTENITIC STAINLESS STEELS\*

R.L. Tobler  
Fracture and Deformation Division  
National Institute of Standards and Technology  
Boulder, CO 80303

M. Shimada  
Iron and Steel Technology Center  
Kobe Steel, Ltd.  
Kobe, Japan

Experiments reported here show that some austenitic steels are toughened by warm prestress. We demonstrate this for Fe-17Cr-3Ni-13Mn-0.33N steel specimens that were warm precracked at 295 K and then fractured at 4 K where failure occurs by slip-band cracking. On the other hand, the toughness of Fe-13Cr-5Ni-22Mn-0.21N steel with a ductile fracture mechanism at 4 K was not affected by similar warm precracking. The behaviors of austenitic and ferritic steels are compared, and valid fatigue precracking procedures for standard 4 K fracture tests are considered.

## INTRODUCTION

Preloads applied to steel specimens or structures at a relatively high temperature  $T_1$  can influence the fracture toughness subsequently measured at a lower temperature,  $T_2$ . Either a single load or cyclic loading at  $T_1$  may increase the toughness at  $T_2$ . This, the warm prestress (WPS) effect, is common in ferritic steels when  $T_1$  is a temperature above the ductile-to-brittle transition and  $T_2$  is below the transition temperature. As shown in this paper, toughening from WPS also occurs in some austenitic steels if  $T_1$  is room temperature and  $T_2$  is near absolute zero.

Theories about WPS were advanced by Chell, Haigh, and Vitek [1], and by Curry [2]. Reviews were written by Nichols [3], and by Pickles and Cowan [4]. Previously, WPS effects were observed only in steels that had ferritic microstructures. Some examples include high-C spheroidized steel [1], medium strength steels [5], C-Mn steels [6], 0.36% C steel [7], A 533 B-1 steel [8], and free machining steel [9].

---



Our interest in austenitic steels began with questions about fracture test procedures at 4 K. Some investigators like fatigue-precrack their specimens at room temperature, for convenience, trusting that the toughness at cryogenic temperatures will not be affected. The supporting data are few and restricted in scope to Fe-Cr-Ni steels with ductile failure mechanisms at 4 K: in recent studies of the 300 series stainless steels, precracking at 76 K ( $K_{\max} = 60 \text{ MPa}\cdot\text{m}^{1/2}$ ) did not affect the toughness of AISI 310S at 4 K [10], precracking at 293 or 77 K ( $K_{\max} = 24 \text{ MPa}\cdot\text{m}^{1/2}$ ) did not affect the toughness of AISI 316 LN at 4 K [11], and precracking at 295 or 77 K ( $25 \leq K_{\max} \leq 43 \text{ MPa}\cdot\text{m}^{1/2}$ ) did not affect the toughness of SUS 304 steel at 4 K [12].

This paper contrasts two high-manganese austenitic stainless steels which have very different 4-K fracture characteristics. The effect of fatigue precracking at room temperature (RT) or liquid nitrogen temperature (LNT) on the fracture toughness at liquid helium temperature (LHeT) is investigated. We refer to room temperature fatigue precracking of 4-K test specimens as warm precracking and consider it a form of WPS. We find a toughening effect at 4 K after warm precracking for the relatively brittle steel, but not for the tough steel.

## MATERIALS

The two materials studied were a commercial heat of Fe-17Cr-3Ni-13Mn-0.33N steel (designated 13Mn) and a laboratory heat of Fe-13Cr-5Ni-22Mn-0.21N steel (designated 22Mn). The mill chemical compositions in weight percent are given in Table 1. Both materials have high manganese and nitrogen contents, and both are annealed.

The 13Mn steel is a high strength steel, selected because it has a cleavage-like failure mechanism at 4 K, and experience indicates that steels cleave are often susceptible to WPS effects. A 25.4 mm thick plate was obtained in the commercially annealed condition.

The 22Mn steel is a newly developed cryogenic steel which has high strength and toughness at 4 K [13]. This steel is a candidate for use in magnets for fusion energy devices at 4 K, and it represents a typical case of ductile fracture at 4 K. The test material was a 90 kg laboratory heat, vacuum-induction melted, forged (1200°C), hot-rolled (28 mm plate), solution-treated (1050°C), and water-quenched.

Table 1. Chemical compositions of the test materials.

Material	Fe	Cr	Ni	Mn	N	C	Si	S	P
13Mn	bal.	17.3	3.42	12.66	0.33	0.05	0.50	0.003	0.027
22Mn	bal.	12.92	4.93	21.9	0.212	0.02	0.50	0.004	0.003

## PROCEDURE

The 13Mn and 22Mn steels were tested at two different laboratories. Depending on the geographical elevation of the test laboratories, nitrogen boils at 76 or 77 K, and helium boils at 4 or 4.2 K, owing to the different atmospheric pressures. In the text, these test temperatures are designated by nominal values: 77 and 4 K, respectively.

The conventional tensile properties were measured using transversely oriented cylindrical specimens of diameter  $D$  and length of reduced section LRS. For 13Mn steel,  $D = 6.35$  mm and LRS = 38.1 mm. For 22Mn steel,  $D = 7$  mm and LRS = 39 mm. Table 2 shows the average tensile property measurements for two tests per condition.

Fracture toughness was measured using T-L oriented compact specimens 25.4 mm thick (B) and 50.8 mm wide (W). The procedure followed a fatigue-load, unload, cool to 4 K, and re-load to fracture sequence. A series of specimens of each steel were precracked at RT or LNT and then fractured at 4 K ( $T_1 > T_2 = 4$  K) by standard methods [14-16]. The results were compared with data for control specimens that were precracked and fractured at LHeT ( $T_1 = T_2 = 4$  K). Post-test examinations included scanning electron microscope (SEM) observations of the fractured surfaces at locations near the fatigue crack tip.

The 13Mn steel specimens were evaluated using ASTM Method E 399-83 [14] to measure the critical stress intensity factor,  $K_{IC}$ . The specimens were precracked in fatigue automatically [17]. Load cycling was performed with a sinusoidal waveform in load control at a frequency ( $f$ ) of 30 Hz while the crack length ( $a$ ) was monitored by compliance. The fatigue-stress-intensity-factor range ( $\Delta K$ ) varied from specimen to specimen, but was maintained constant during each test by periodic load reductions as a function of crack growth. After precracking, the specimens were fractured by a single loading at a crosshead displacement rate of 0.03 mm/s.

Table 2. Tensile properties of the tested steels (data are averages of two tests per temperature at strain rate of about  $2 \times 10^{-4}$  s $^{-1}$ ).

Material	Test Temperature (K)	Yield Strength (MPa)	Ultimate Strength (MPa)	Elongation (%)	Red. of Area (%)
13Mn	295	401	786	59	-
	76	1019	1489	20	-
	4	1401	1733	7	-
22Mn	298	306	640	78	75
	77	831	1315	59	43
	4.2	1188	1565	38	42



The high toughness 22Mn steel was evaluated using  $J_{IC}$  measurements, from which  $K_{IC}(J)$  values were derived. The specimens were precracked at room or cryogenic temperatures at  $f = 5, 10, \text{ or } 20 \text{ Hz}$ . For this steel the fatigue loads applied to each specimen were held constant, so the maximum stress intensity factor in fatigue ( $K_{max}$ ) increased with crack length. After precracking the specimens to similar relative crack lengths ( $a/W = 0.62$ ) using different final  $\Delta K$ , we fractured them using a computer-aided unloading compliance apparatus [18] and a methodology that defines  $J_{IC}$  at the intersection point of the blunting and regression lines [15, 18]. Systematically higher (10–15%)  $J_{IC}$  values would have been obtained using the revised methodology [16], but that would not change the conclusions of this study.

For both steels, the fatigue load ratio ( $R$ ) was 0.1. The magnitude of fatigue loading may be specified by either  $\Delta K$  or  $K_{max}$  since

$$R = (P_{min}/P_{max}) = (K_{min}/K_{max}) = 0.1, \text{ and} \quad (1)$$

$$\Delta K = K_{max} - K_{min} = 0.9K_{max}. \quad (2)$$

## RESULTS

### Linear Elastic 13Mn Steel

Load-displacement records for two 13Mn steel compact specimens are shown in Fig. 1. The loading response is linear elastic, as expected. Most of these tests satisfied the criteria of Method E 399-83, except where the fatigue load restrictions were intentionally violated to create WPS.

Table 3 lists the test results for three control specimens ( $T_1 = T_2 = 4 \text{ K}$ ), plus results for eight more tests where the fatigue precracking and fracture test temperatures were dissimilar. The average  $K_{IC}$  value for control specimens is  $83 \text{ MPa}\cdot\text{m}^{1/2}$ , with a spread of values between 81 and  $86 \text{ MPa}\cdot\text{m}^{1/2}$ . Higher toughness is observed for most of the warm precracked specimens, but this depends on the prestress temperature  $T_1$  and the fatigue stress.

The results for the 13Mn steel are plotted in Fig. 2 and summarized as follows. If precracking is performed at RT ( $T_1 = 295 \text{ K}$ ), a WPS effect is observed, and the measured toughnesses can be much higher than  $K_{IC}$ . In Table 3, the  $K_Q$  measurements that are affected by WPS are designated  $K_W$ . The highest  $K_W$  in Table 3 is  $114 \text{ MPa}\cdot\text{m}^{1/2}$ , 40% higher than  $K_{IC}$ . Still higher  $K_W$  could have been measured if the precracking loads were higher. As shown in Fig. 2,  $K_W$  decreases and becomes negligible at or below  $K_{max} = 17 \text{ MPa}\cdot\text{m}^{1/2}$ . This value, for 13Mn steel, may be a threshold. Actually, we did not demonstrate the existence of a threshold since we obtained no data below  $17 \text{ MPa}\cdot\text{m}^{1/2}$  (more than a million fatigue cycles per specimen would have been necessary); however, thresholds are observed in some ferritic steels [3, 6] and thresholds might be expected from the plastic zone size rationale discussed below.

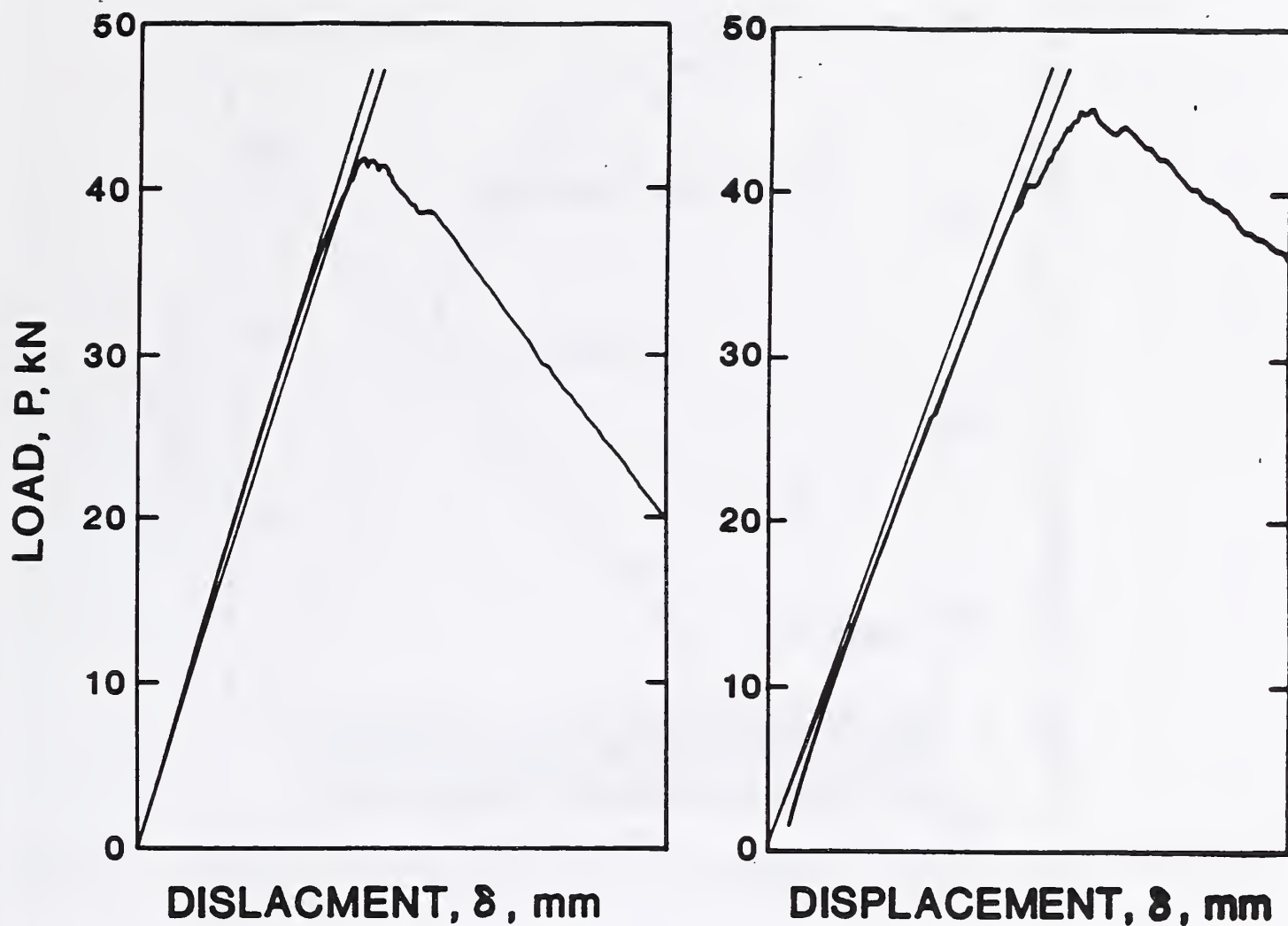


Figure 1. Load displacement curves for compact specimens of the 13Mn steel tested at 4 K: (a) normal loading behavior, and (b) abnormal behavior caused by inadequate precracking procedure ( $K_{max} < 0.6 K_{Ic}$ ).

Table 3. Precracking and 4-K toughness results for 13Mn steel.

Specimen No.	Precrack Temperature K	$\Delta K$ MPa·m <sup>1/2</sup>	$K_{max}$ MPa·m <sup>1/2</sup>	$K_Q$ MPa·m <sup>1/2</sup>	$K_W$ MPa·m <sup>1/2</sup>	$K_{Ic}$ MPa·m <sup>1/2</sup>
4	295	15.5	17	84.3	---	84.3
10	295	22.5	25	89.2	89.2	---
1	295	30.0	33	92.7	92.7	---
2	295	40.0	44	98.0	98.0	---
3	295	60.0	67	114.4	114.4	---
8	76	27.0	30	81.6	---	81.6
12	76	35.0	39	82.0	---	82.0
9	76	54.0	60	80.7	---	---
7	4	25.0	28	82.6	---	82.6
5	4	30.0	33	81.1	---	81.1*
6	4	30.0	33	85.5	---	85.5



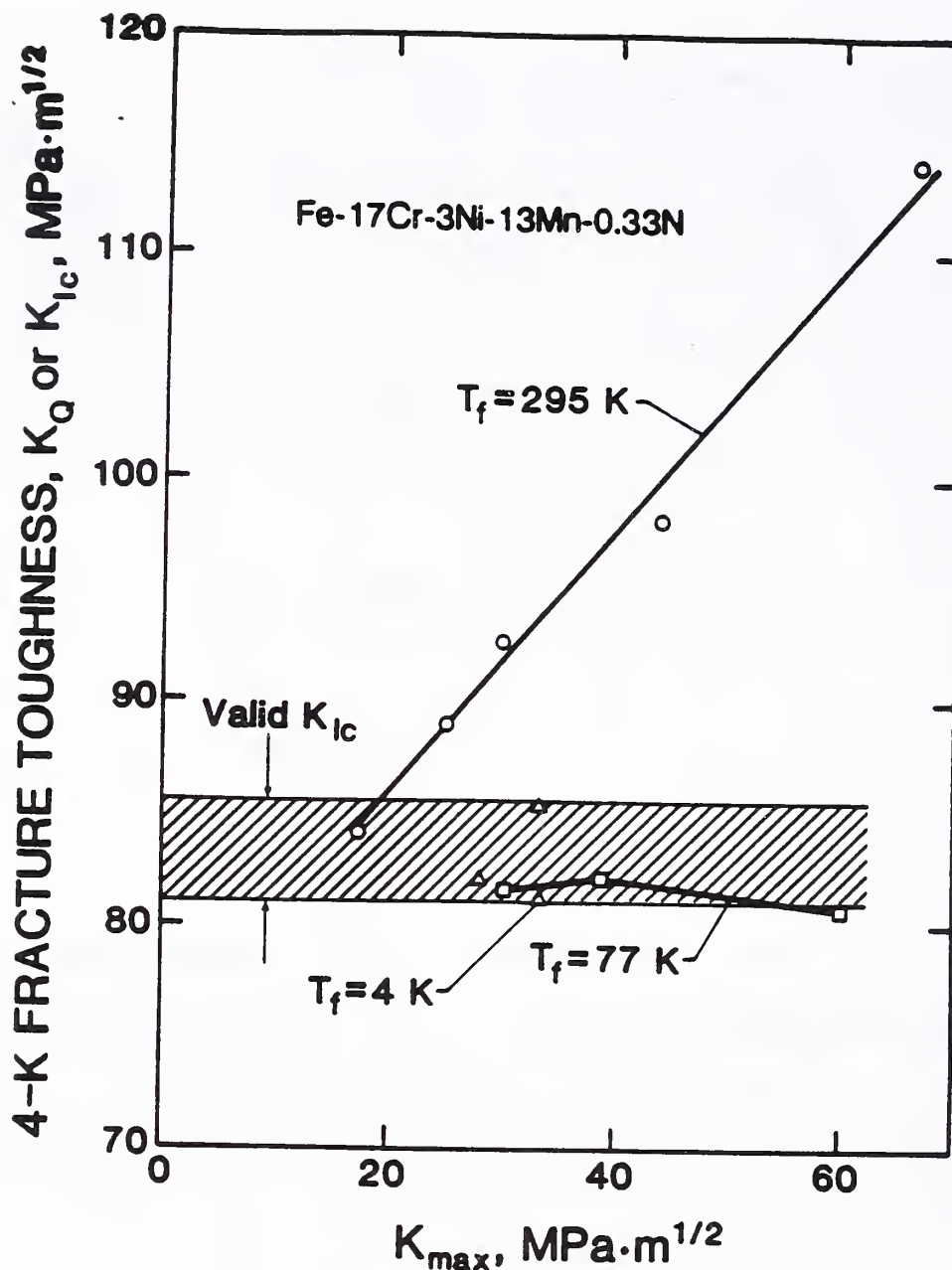


Figure 2. Fracture toughness of 13Mn steel at 4 K, showing the effects of fatigue precracking conditions.

Some specimens were precracked at LNT ( $T_1 = 76 \text{ K}$ ), but this did not toughen the 13Mn steel at 4 K. Two specimens were precracked at 76 K, at moderate  $\Delta K$ , and their toughnesses were equivalent to  $K_{IC}$  for control specimens. A third specimen was precracked at higher loads ( $K_{\max} = 60 \text{ MPa}\cdot\text{m}^{1/2}$ ) and the 4-K toughness that was in fact slightly lower than  $K_{IC}$ . As shown in Fig. 1(b), the test record in this case displays abnormal early pop-ins, attributable to a violation of the precracking rule,  $K_{\max} \leq 0.6K_{IC}$  (see Discussion).

#### Fully Plastic 22Mn Steel

Tests of the 22Mn steel revealed no WPS effects for any of the conditions investigated in this study. A typical 4-K load-displacement record is shown in Fig. 3, and typical 4-K J-resistance curves are shown in Fig. 4; the  $K_{IC}$  estimates as a function of  $T_1$  are shown in Fig. 5, and the fatigue precracking histories for all specimens are listed in Table 4.

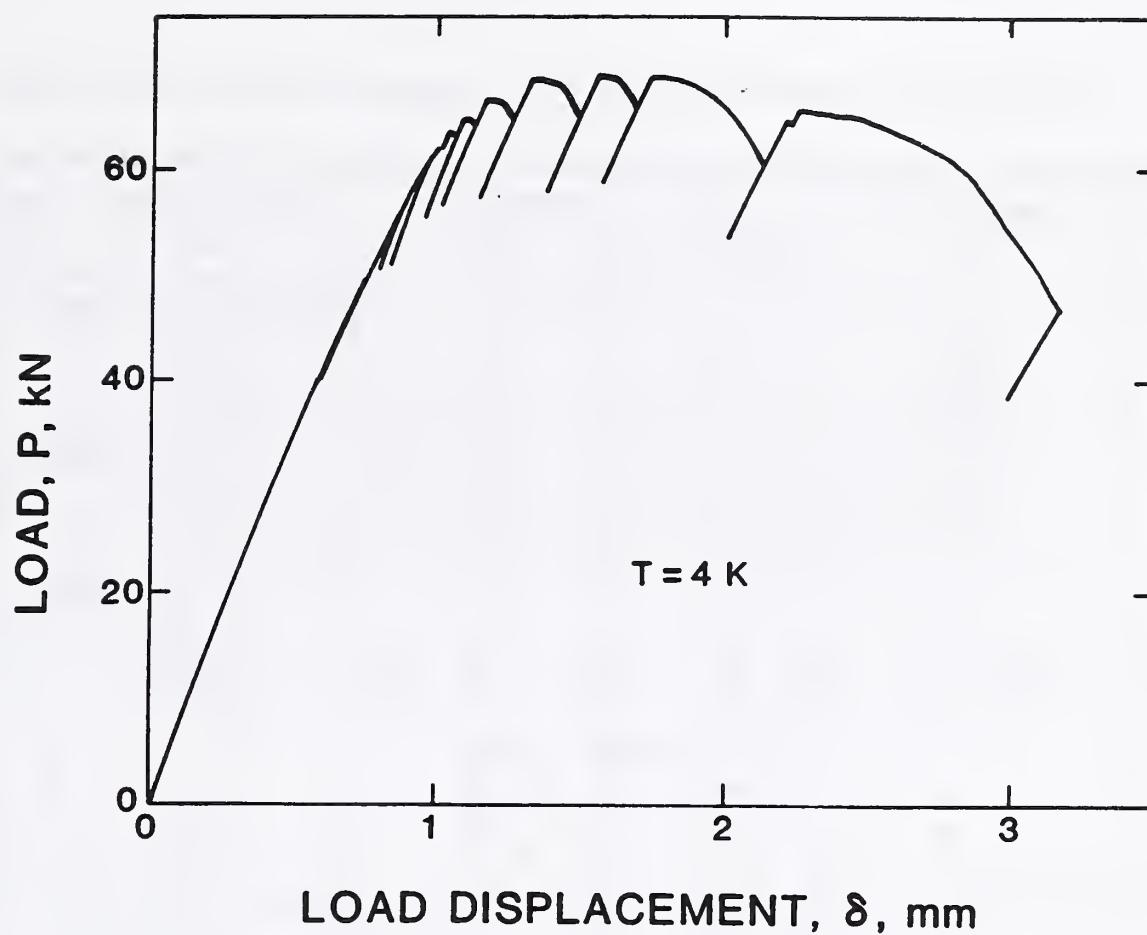


Figure 3. A load-displacement curve for a compact specimen of 22Mn steel.

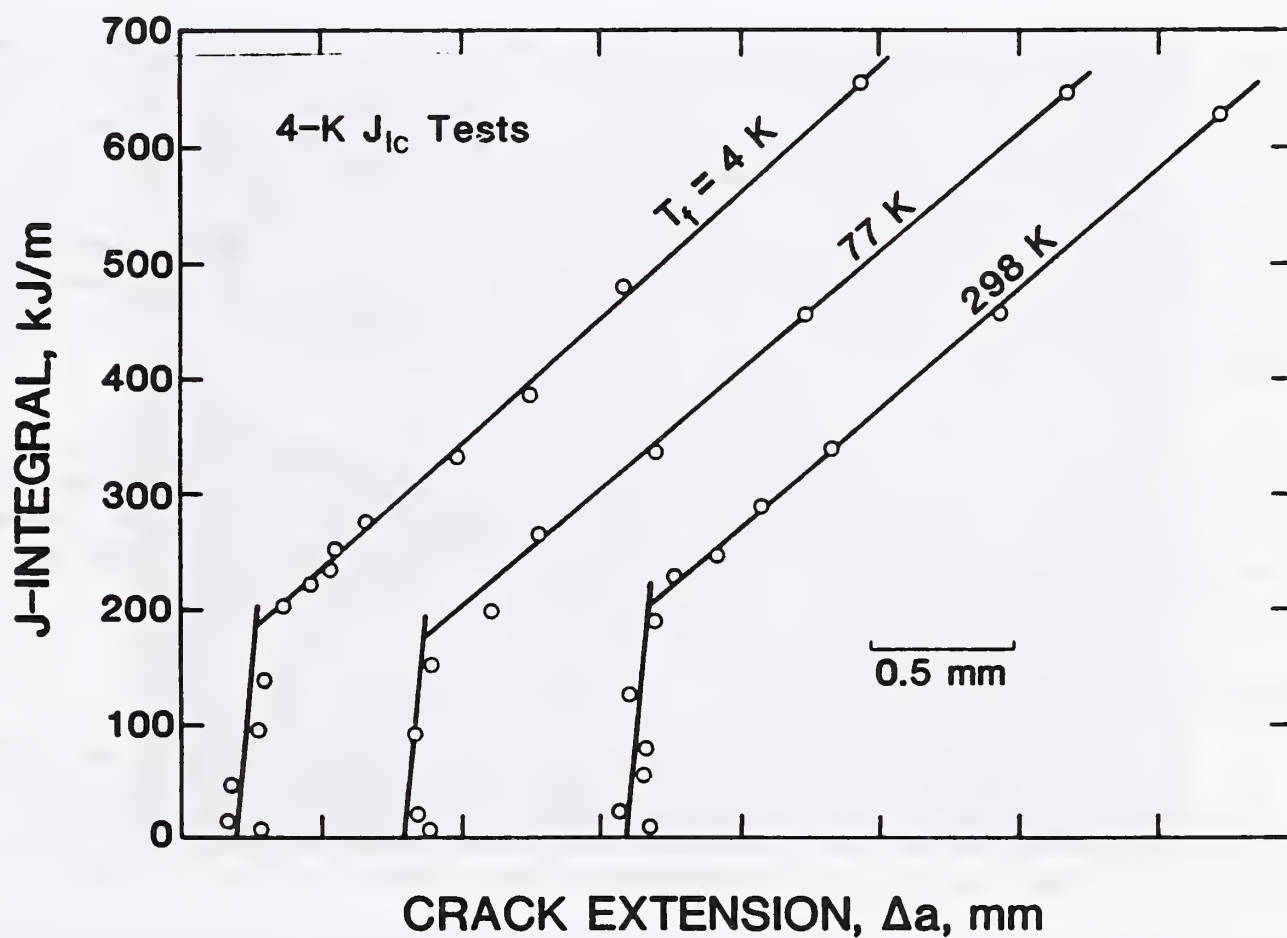


Figure 4. Resistance curves for 22Mn specimens precracked 298, 77, or 4 K.



Table 4. Precracking conditions and 4-K toughness results for 22Mn steel.

Specimen No.	Temperature K	$\Delta K$ MPa·m <sup>1/2</sup>	Frequency Hz	Crack Length mm	$K_{IC}(J)$ MPa·m <sup>1/2</sup>
22Mn-1	298	20.4	20	31.9	186
22Mn-2	298	35.2	20	31.0	185
22Mn-3	298	33.5	20	31.5	a
22Mn-4	298	41.5	20	31.2	204
22Mn-5	298	45.9	20	32.7	187
22Mn-6	298	32.2	20	31.4	209
22Mn-7	77	30.1	20	31.1	197
22Mn-8	77	41.0	20	31.9	190
22Mn-9	77	56.3	10	31.6	191
22Mn-10	77	56.6	10	31.1	a
22Mn-11	4	40.1	10	30.7	185
22Mn-12	4	30.6	10	30.6	199
22Mn-13	4	36.4	10	30.7	196
22Mn-14	4	59.3	5	31.9	208
22Mn-15	4	52.3	5	31.3	189

Note: <sup>a</sup>operator error terminated this test;

The load-displacement records (Fig. 3) for 22Mn steel are serrated, owing to repeated bursts of unstable plastic flow with sudden load drops and arrests [10]. Serration size increases towards the end of the test. Such behavior is typical of ductile steels tested in liquid helium at slow testing speeds. Our 22Mn steel specimens were nearly identical in crack size, so the serrations occurred at reproducible loads and displacements. Consequently, the J- $\Delta a$  data distributions within the exclusion intervals of the various resistance curves are nearly identical, independent of precracking temperature.

The fracture toughness data for 22Mn steel are plotted in Fig. 5. Within the range of specimen-to-specimen variability, the toughness  $K_{IC}(J)$  at 4 K is  $195 \pm 7\%$ , independent of the precracking conditions as far as they were explored in this study. There are no WPS effects, either on the resistance curve regression lines or  $J_{IC}$  values for this material.

#### Fractography

For both steels, SEM examinations of the fracture surfaces at locations near the fatigue crack tip failed to reveal any obvious difference in fracture morphology at  $T_2$  as a function of the precracking temperature (295, 76, or 4 K). Representative fractographs are shown in Figs. 6 and 7.

For 13Mn steel, the 4-K fracture surfaces consist of transgranular facets on (111) planes which are the active slip planes of the austenitic structure. The 4-K failure mechanism is slip-band cracking, a form of cleavage fracture [19]. Slip traces are visible on the transgranular

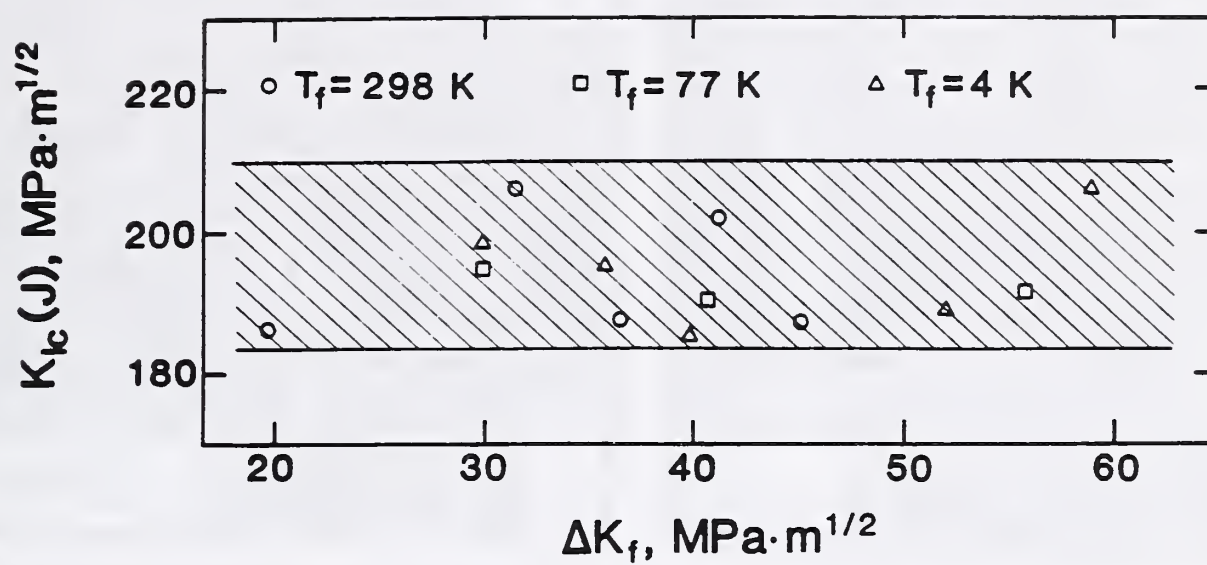


Figure 5. Fracture toughness values for 22Mn steel as a function of  $K_{\text{max}}$ .

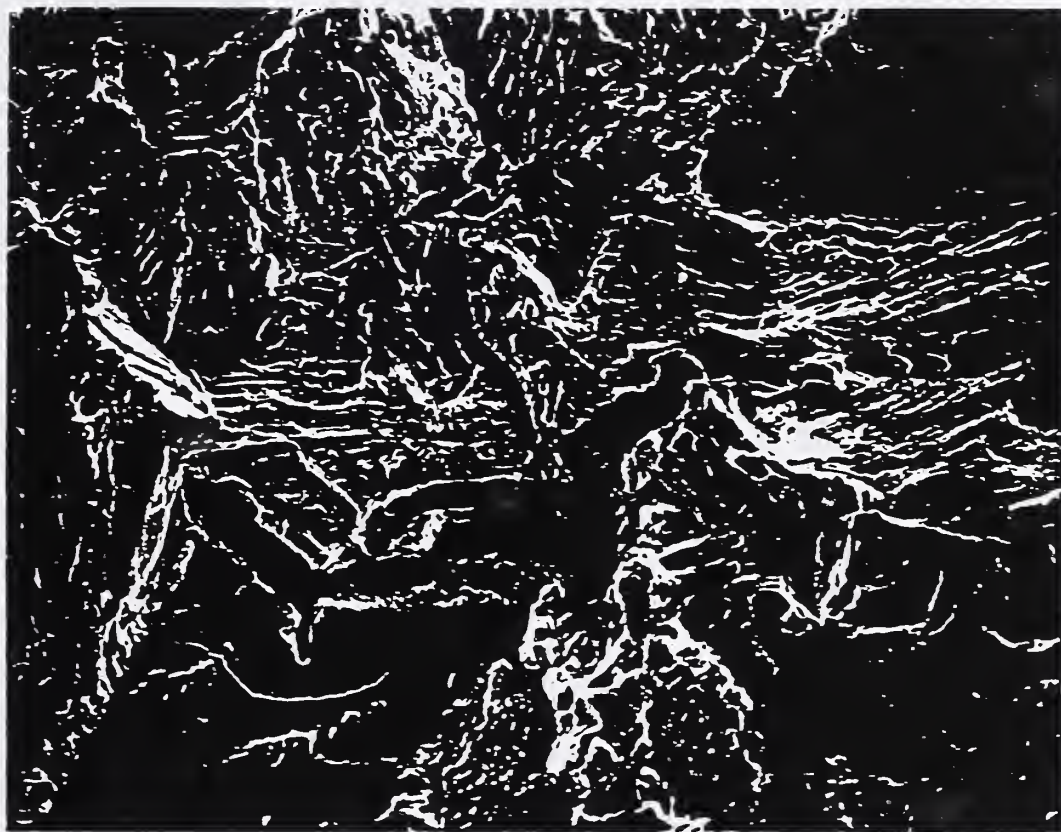


Figure 6. Fracture surface of the 13Mn austenitic stainless steel fractured at 4 K.



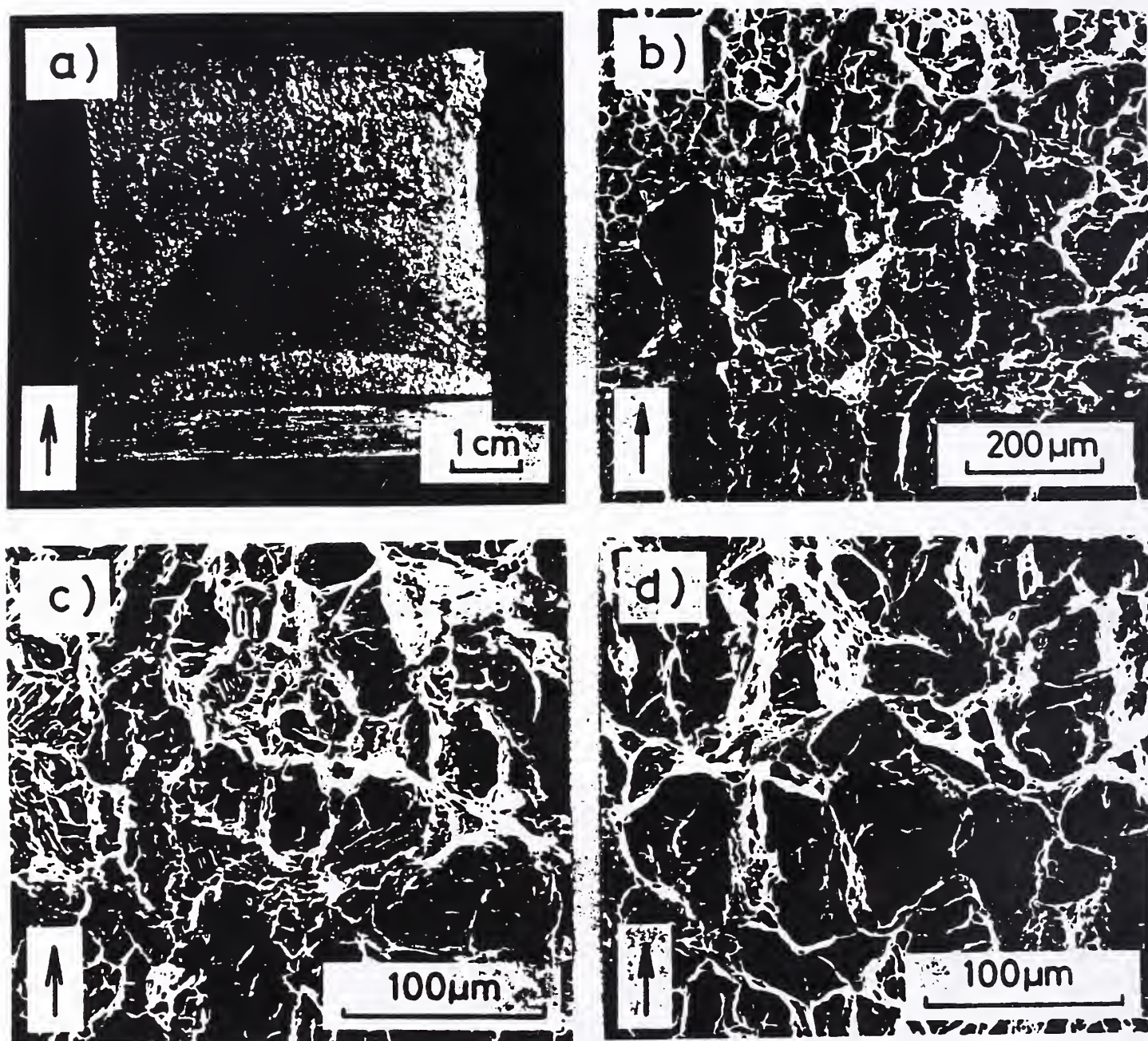


Figure 7. Fracture surfaces of a 22Mn steel fractured at 4 K.

facets, as shown in Fig. 6. This implies some microplastic deformation before fracture, even though the loading behavior (Fig. 1) is essentially linear, and the overall fracture morphology (Fig. 7) is brittle.

In contrast, the high-toughness 22Mn steel affords a completely ductile failure at 4 K. Figure 7 shows a specimen's fracture surface after  $J_{Ic}$  testing at 4 K. The surface is covered with dimples from void coalescence. Arrows in Fig. 7 indicate the direction of crack propagation. Figure 7(a) is a macrophotograph of the specimen. Figure 7(b) is an SEM of the fracture surface adjacent to the fatigue crack, and Fig. 7(c), an enlargement of the same area, shows a distinctive feather-like dimple pattern. Figure 7(d) shows the dimples at a distance 2 mm from the fatigue crack. As shown in Figs. 7(b-d), and for all 22Mn steel specimens tested in this study, the feather-like dimples exist only in a band adjacent to the fatigue crack tip. The band is 200-500  $\mu\text{m}$  wide, and is larger than the stretch zone.



Regarding the austenite stability of these alloys, X-rays of a previous heat of 13Mn steel indicated no detectable austenitic phase transformation (to bcc or hcp martensite), even after deformation and fracture at 4 K. However, small amounts of transformation may have gone undetected because the plastically deformed zone is extremely small. The present heat is quite similar in composition to the heat that was X-rayed, so we assume it has a similar level of austenite stability at 4 K. The 22Mn steel definitely transformed to  $\epsilon$  martensite, but not to  $\alpha'$  martensite, as determined by radiography and electron microscopy and summarized in Table 5.

Table 5. Volume fractions of phases detected in 22Mn steel plastic zones.

Temperature K	Fatigue stress intensity factor range, $\Delta K$ $\text{MPa}\cdot\text{m}^{1/2}$	austenite %	$\epsilon$ martensite %	$\alpha'$ martensite %
298	30	100	0	0
4	30-35	77	23	0

## DISCUSSION

WPS has implications both for design and for materials testing. In some designs with linear-elastic materials, WPS can be beneficial in that it supports a strategy of intentional overstressing at  $T_1$  to reduce the probability of fracture at  $T_2$  [4]. Our present interest, however, is valid test procedure for fracture toughness measurements at 4 K.

There are good reasons for wanting to precrack at room temperature before fracture testing at 4 K. Some laboratories are not equipped with 4-K fatigue capabilities, and most desire to conserve liquid helium and reduce cryogenic fluid costs. Since warm prestress effects may occur, it is necessary to understand this behavior and consider acceptable fatigue precracking criteria that will prevent warm precracking effects from interfering with standard toughness measurements.

### Comparison with Ferritic Steels

The behavior of the 13Mn austenitic steel of this study parallels ferritic steel behavior in some respects. Figure 8 compares the 13Mn steel and two ferritic steels which failed by cleavage at  $T_2$ . All three materials are ductile at  $T_1$  and brittle at  $T_2$ , and stress-controlled fracture mechanisms (slip-band cracking or cleavage) operate at  $T_2$ . All three steels were preloaded at room temperature, but there is a minor difference in that the 13Mn steel was preloaded in fatigue; the ferritic steels were preloaded monotonically.



As Fig. 8(a) shows, the 13Mn steel is tougher than the ferritic steels. One of the ferritic steels, a semi-killed Fe-0.19C-0.84Mn steel, was tested at  $T_2 = 77\text{ K}$  [6]; the other, a commercial free-machining Fe-0.17C-1.12Mn-0.2Ni steel, was tested at  $T_2 = 123\text{ K}$  [9]. Since the ferritic steels have very low toughnesses (23 and 26  $\text{MPa}\cdot\text{m}^{1/2}$ ) at these temperatures the affected toughness can be double, and the WPS effect seems relatively weak for the 13Mn steel in that a toughness increase of 40% was observed. The effects are similar, however, if the data are normalized to account for the different  $K_{Ic}$  values. The quantity  $K_{WPS} = K_Q - K_{Ic}$  is the increment of toughness added due to the WPS effect. As shown in Fig. 8(a),  $K_{WPS}$  is a similar function of  $K_{max}$  for all three steels.

### Significance of Plastic Zone Size

Toughness relates to the amount of energy absorbed in fracture which is governed by the crack-tip behavior. Therefore WPS effects may be related to plastic zone size effects, material composition and phase stability, and the mechanical (cold-worked [20,21]) state of the material locally.

A factor to consider is the ratio of plastic zone sizes at  $T_1$  and  $T_2$ . Irwin [22] estimated the plastic zone radius for plane strain conditions as

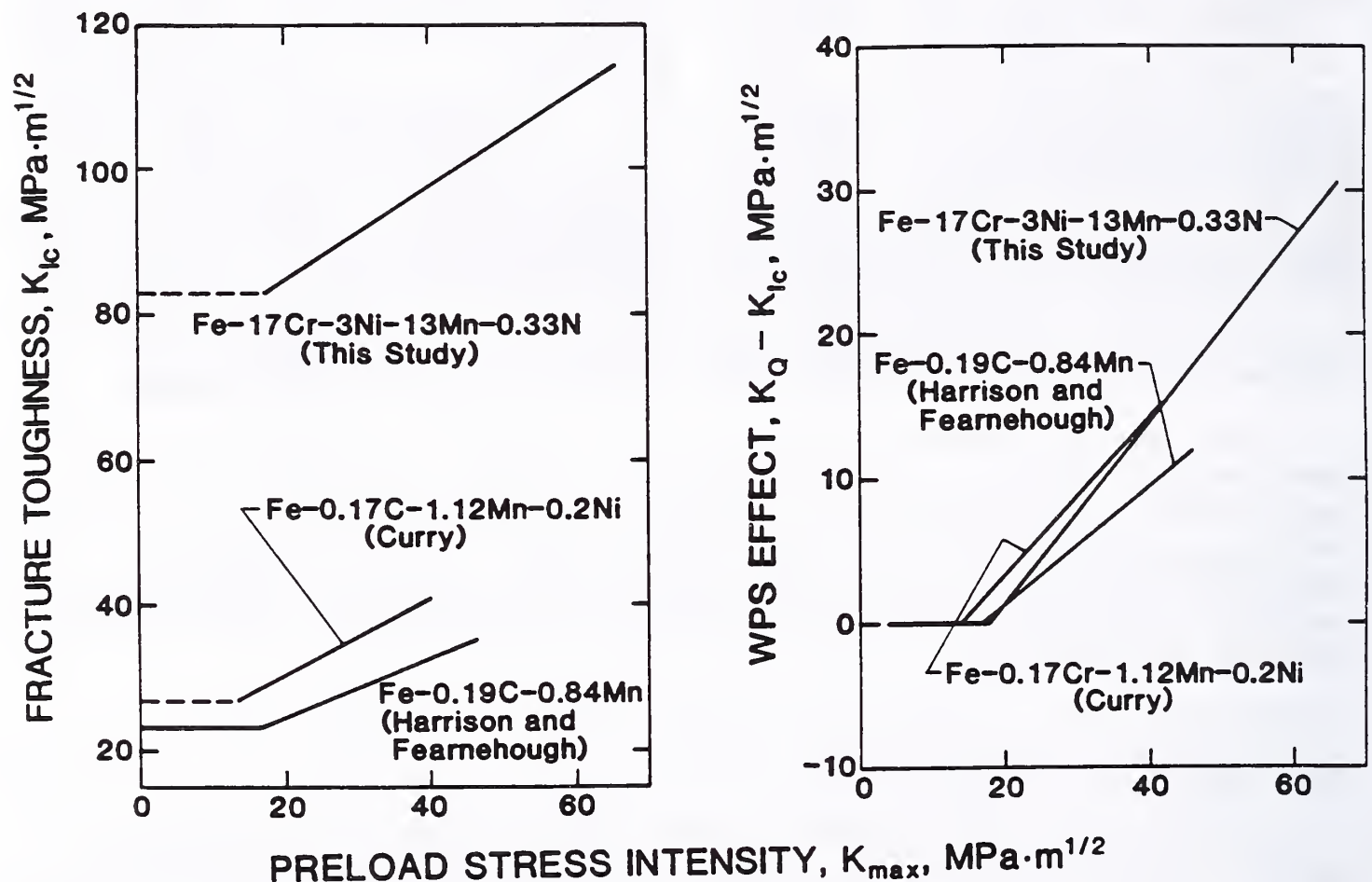


Figure 8. Comparison of WPS effects in austenitic and ferritic steels: (a) absolute data, and (b) normalized data.

$$R_Y = \frac{1}{6\pi} \left( \frac{K}{\sigma_{ys}} \right)^2. \quad (3)$$

This expression, although inexact [22], is often used to estimate zone sizes, and we use it here to estimate the magnitude of plastic deformation associated with various precracking conditions and with fracture at 4 K.

Figure 9, then, indicates that there are large variations in the fatigue plastic zone sizes developed at 295 and 4 K. In this figure,  $R_{Yf}$  is the radius of the plastic zone formed during the fatigue precracking, and  $R_{YF}$  is the maximum radius of the plastic zone formed in control specimens (those without warm prestress) at the point of fracture at 4 K. For 13Mn steel at a typical precracking level ( $K_{max} = 33 \text{ MPa}\cdot\text{m}^{1/2}$ ), the size of the zone formed during fatigue at 295 K ( $R_{Yf}$ ) is 12 times larger than that for identical loading at 4 K; it is also larger than  $R_{YF}$ . The ratio  $R_{Yf}/R_{YF}$  appears to be significant. Figure 9 shows, for the steels tested,  $K_W \approx K_{Ic}$  if this ratio approaches 1 or less. In other words, a WPS effect is likely if the plastic zone formed in fatigue at  $T_1$  exceeds that normally formed in control specimens during fatigue and fracture at  $T_2$ .

#### Significance of Fracture Mechanism

The literature suggests that WPS effects on toughness can be anticipated in steels with stress-controlled (brittle) mechanisms at  $T_2$ , and not in steels with strain-controlled (ductile) failure mechanisms at  $T_2$ .

In agreement, we find the effect in a 13Mn steel that is ductile at 295 K and brittle at 4 K, but not in the 22Mn steel nor other austenitic steels that remain ductile at 4 K [10-12]. Therefore we expect to find WPS effects in some other high strength austenitic steels, such as those of the Fe-Cr-Ni-Mn-N family, which have high N contents and some proportion of crystallographic faceting at cryogenic temperatures [24-29]. The 22Mn steel, which retains its dimpled-fracture mechanism at 4 K, shows no influence of WPS at 4 K and behaves similarly to AISI 316 LN and SUS 304 [11, 12]. These steels, in contrast to the 13Mn steel, are capable of extensive deformation at extreme cryogenic temperatures and the deformation begun at  $T_1$  is able to continue at  $T_2$ .

For 22Mn steel, feather-like dimples were observed on the fracture surfaces. Presumably, this reflects the steel's microstructure and stability. Neither  $\epsilon$  nor  $\alpha'$  martensite phases were induced by deformation at 295 K, but deformation at 4 K does induce some  $\epsilon$  (see Table 5). We suppose that transformation at 4 K generates a layered structure of  $\epsilon$  and austenite phases, that the  $\epsilon$  fractures first; then the austenite fractures in a more ductile fashion, producing a textured surface and the overall feather-like pattern. There is a change in fracture morphology, however, as the feathered pattern vanishes farther away from the fatigue crack (Fig. 7d). This too may be related to the transformation tendencies of 22Mn steel, since the  $\epsilon$  ceases to form at higher temperatures. From a previous study of fracture in liquid helium, we know that, along with serration size, the internal specimen temperature rises as testing progresses. Perhaps, after the crack extends 200 to 500  $\mu\text{m}$ , adiabatic heating associated with pronounced serrated



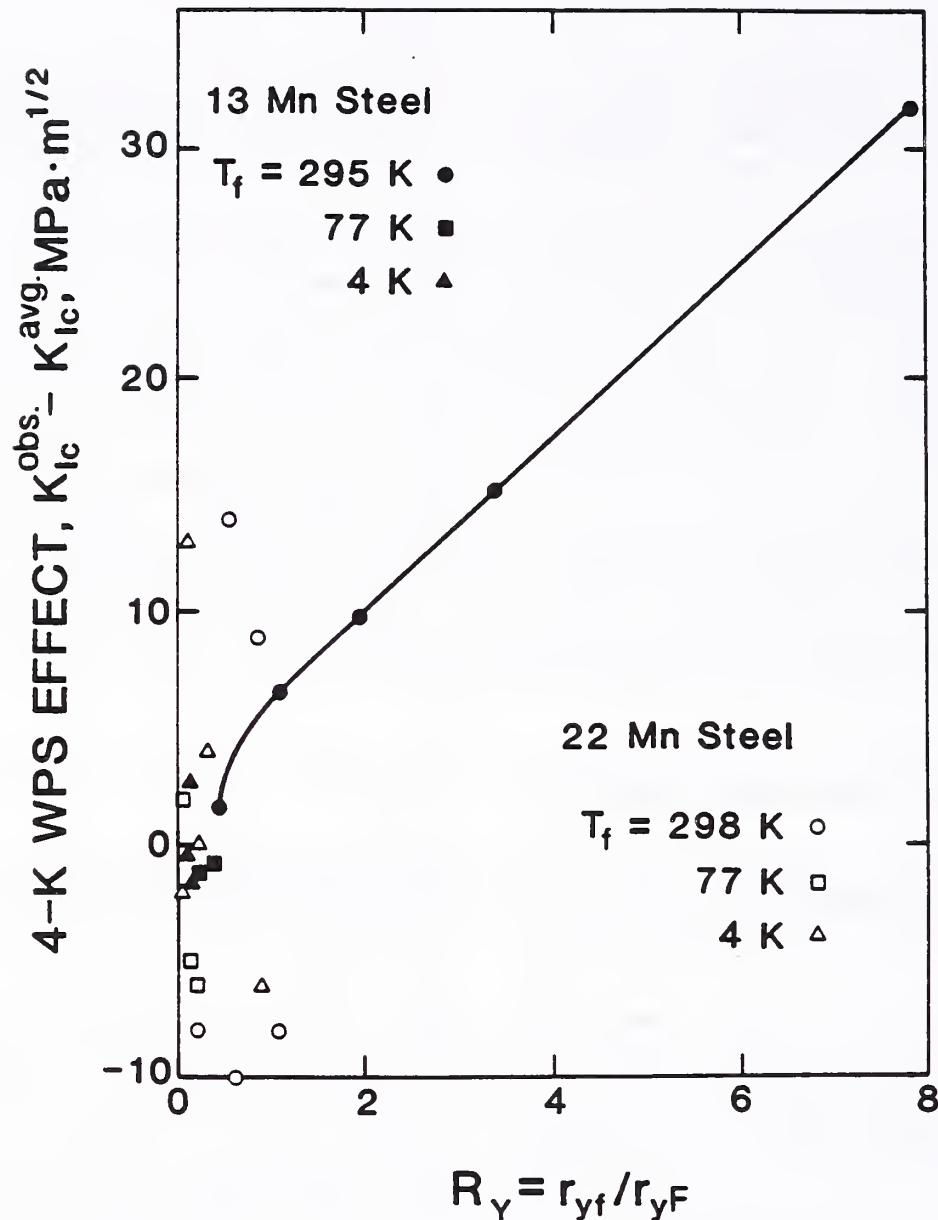


Figure 9. Fracture toughness at 4 K versus plastic zone size ratio.

yielding events is sufficient to suppress further transformation to  $\epsilon$  in this alloy. The feathered pattern then vanishes because it derives from fracture of a two-phase microstructure.

Unlike our high-Mn steels, many 300 series steels at 4 K readily transform to martensitic products, including  $\alpha$  phase. Martensitic transformations cause a volume expansion (2 or 3%) that depends on composition in the 300 series steels. During fatigue or monotonic loading at cryogenic temperatures, transformations occur in local plastic zones, but they occur less readily, or not at all, at 295 K. Since loading at 295 K may affect the phase transformation tendencies of steels like AISI 304 and AISI 316, it might be possible to discover WPS effects in such alloys. Although previous tests did not reveal any WPS effect in two of those alloys [11, 12], further studies on very lean alloy compositions are recommended.

## STANDARD CRYOGENIC TESTS

Test standards are designed to ensure valid fracture toughness measurements. For austenitic steels at 4 K, fatigue precracking restrictions are needed to prevent the effects of loading history on fracture toughness measurements. Guidelines should be simple and generally applicable. At present, there are no fatigue precracking guidelines for 4-K  $J_{IC}$  testing, and the published guidelines for  $K_{IC}$  tests have never been validated for extreme cryogenic temperatures.

### Precracking at Dissimilar Temperatures

Method E 399-83 for  $K_{IC}$  measurements allows precracking at a higher temperature  $T_1$ , followed by fracture testing at a lower temperature  $T_2$ , but only if  $K_{max}$  at  $T_1$  is not excessive. Section A2.4.4 of the standard sets this limit:

$$K_{max} \leq 0.6 \left[ \frac{\sigma_{ys1}}{\sigma_{ys2}} \right] K_Q, \quad (4)$$

where  $\sigma_{ys1}$  and  $\sigma_{ys2}$  are the yield strengths at  $T_1$  and  $T_2$  and  $K_Q$  is the toughness at  $T_2$ . Equation (5),

$$K_{max} = 0.6K_Q, \quad (5)$$

is a form of Eq. (4) where  $T_1 = T_2$  and  $\sigma_{ys1}/\sigma_{ys2}$  is 1. The intention is to restrict  $K_{max}$  to a fraction of  $K_Q$ , because if  $K_{max}$  approaches  $K_{IC}$  too closely, pronounced "pop-in" instabilities can affect the test records and toughness measurements [30], increasing [31] or decreasing [32, 33] the measured toughness. A decrease occurred for the affected test record shown in Fig. 1(b).

For 13Mn steel, Eq. (4) implies a negligible effect of warm precracking at 295 K on the toughness at 4 K if  $K_{max} < 14 \text{ MPa}\cdot\text{m}^{1/2}$ . This closely agrees with the experimental finding of  $K_{max} = 17 \text{ MPa}\cdot\text{m}^{1/2}$  (Fig. 4). These data confirm that some limitation on  $K_{max}$  is necessary for cryogenic tests and that Eq. (4) is sufficient to exclude WPS effects at 4 K when precracking is conducted at 295 K. These are the first data ever put forth supporting Eq. (4) for linear elastic tests near absolute zero.

Whereas Eq. (4) may be appropriate for  $K_{IC}$  tests, it is not useful for ductile fracture tests, and it does not apply to the 22Mn steel. In fact, the current standard for  $J_{IC}$  testing does not consider or recommended guidelines for warm precracking of test specimens.

### Limitations

The time consumed in precracking imposes a practical limitation. The number of cycles required to generate a crack depends on notch type, temperature, and technique (see section A2 of [14]), but the primary



variable is  $\Delta K$  or  $K_{\max}$ . For steels, a realistic time period for crack initiation and growth corresponds to  $10^4$  to  $10^6$  cycles. A typical  $K_{\max}$  to accomplish this is  $33 \text{ MPa}\cdot\text{m}^{1/2}$ .

Low  $K_{\max}$  may be favored to avoid load-history effects, but if  $K_{\max}$  is too low, the crack will not initiate quickly. These two requirements are in potential conflict, so it is impossible to properly precrack certain materials at specific temperatures.

Extremely brittle materials are among those that may be impossible to fatigue-crack in tension tests. Their  $K_{IC}$  values may be so low that  $K_{\max}$  from Eq. (4) approaches or falls below the thresholds required for crack initiation from the notch. This is common for ferritic steels tested at cryogenic temperatures, and it may account for the problems encountered by Stonesifer [34] in fatigue tests of A 533 B steel at 77 K. In some border line cases, tensile precracking may be possible, but the time required is prohibitive. For example, consider the 13Mn steel: for precracking at 295 K, Eq. (4) requires a  $K_{\max}$  lower than  $14 \text{ MPa}\cdot\text{m}^{1/2}$ , but values below  $14 \text{ MPa}\cdot\text{m}^{1/2}$  are too low to generate a crack in less than a million load cycles.

Problems can sometimes be resolved by precracking at an intermediate temperature. For the example of 13Mn steel, precracking at 77 K may be recommended. Precracking at 77 K is less conducive to a WPS effect at 4 K than precracking at 295 K; the material's yield strength is much higher at 77 than at 295 K, and  $K_{\max}/\sigma_{ys}$  is also higher.

In summary, for  $K_{IC}$  tests at 4 K, precracking at 4 K is reliable but costly. Precracking at 295 K is more convenient, but it will toughen some steels. A third alternative is precracking at an intermediate temperature. For tests of austenitic steels at 4 K, precracking at LNT works well because liquid nitrogen is inexpensive and 4-K test specimens must be precooled in liquid nitrogen anyway. For  $J_{IC}$  tests at cryogenic temperatures, there are no guidelines yet to ensure freedom from the warm precracking effect; therefore precracking at LNT or LHeT may be the best course to follow when in doubt about the behavior of specific alloys.

## CONCLUSIONS

1. Warm prestress effects do occur in some austenitic steels as well as ferritic steels. In our study, a toughening effect from warm precracking occurred in the relatively brittle Fe-17Cr-3Ni-13Mn-0.33N austenitic stainless steel at 4 K, but not in the higher toughness Fe-13Cr-5Ni-22Mn-0.21N steel at 4 K.
2. Precracking at room temperature is difficult or impossible for  $K_{IC}$  tests of some low toughness steels at 4 K because of the warm prestress effect. On the other hand, fatigue precracking at room temperature appears to be acceptable for tough steels, such as 22Mn steel, that are not susceptible to warm precracking effects when  $J_{IC}$  tests are performed at 4 K; more experience with other materials is needed.
3. Fatigue precracking at 77 K, using  $\Delta K$  less than  $36 \text{ MPa}\cdot\text{m}^{1/2}$ , appears to be a good general procedure; so far it proved to be satisfactory for

five austenitic steels that have been subjected to  $K_{IC}$  or  $J_{IC}$  tests at 4 K. In this study, precracking at 77 K completely suppressed the warm precracking effect in the susceptible 13Mn steel.

#### ACKNOWLEDGMENTS

This work was supported in the United States by the U. S. Department of Energy, Office of Fusion Energy. D. Shepherd (NIST) provided fractographs of the 13Mn steel.

#### REFERENCES

1. G.G. Chell, J.R. Haigh, and V. Vitek, A theory of warm pre-stressing, experimental validation and the implications for elastic-plastic failure criteria, C.E.R.L. Laboratory Note No. RD/L/N63/79 (1979).
2. D.A. Curry, A model for predicting the influence of warm prestress and strain ageing on the cleavage fracture toughness of ferritic steels, Int. J. Fract., 22, 145-159 (1983).
3. R.W. Nichols, The use of overstressing techniques to reduce the risk of subsequent brittle fracture, Parts 1 and 2, Brit. Weld. J., Jan-Feb, (1968).
4. B.W. Pickles, and A. Cowan, A review of warm prestressing studies, Int. J. Pres. Ves. & Piping, 14, 95-131 (1983).
5. A.J. Brothers and S. Yukawa, The effects of warm pre-stressing on notch fracture strength, J. Basic Eng., 85, 97-101, (1963).
6. T.C. Harrison and G.D. Fearnehough, The influence of warm prestressing on the brittle fracture of structures containing sharp defects, J. Basic Eng., 94, 373-376 (1972).
7. R.W. Nichols, W.H. Levine, A. Quirk, and E.A. Bevitt, A limit approach to the prevention of pressure vessel failure, Proc. First Int. Conf. on Fracture, Sendai, Japan, 1673-1678 (1966).
8. H. Nakamura, H. Kobayashi, T. Kodaira, and H. Nakazawa, On the effects of pre-loading on the fracture toughness of A 533B-1 steel, in: Advances in Fracture Research, Proc. ICF 5, 2, Pergamon, New York, 817-824 (1981).
9. D.A. Curry, A micromechanistic approach to the warm prestressing of ferritic steels, Int. J. Fract., 17, 335-343 (1981).
10. R.L. Tobler, Ductile fracture with serrations in AISI 310 S stainless steel at liquid helium temperature, in: Elastic-Plastic Fracture: Second Symposium, Vol. II - Fracture Resistance Curves and Engineering Applications, ASTM STP 803, C.F. Shih and J.P. Gudas, eds., Amer. Soc. Test. Maters., Philadelphia, 763-776 (1983).



11. T. Ogata, K. Ishikawa, T. Yuri, R.L. Tobler, P.T. Purtscher, R.P. Reed, T. Shoji, K. Nakano, and H. Takahashi, Effects of specimen size, side-grooving, and precracking temperature on J-integral test results for AISI 316 LN at 4 K, in: Adv. Cryo. Eng., 34, A.F. Clark and R.P. Reed, eds., Plenum, New York, 259-266 (1988).
12. M. Shimada, R.L. Tobler, T. Shoji, and H. Takahashi, Size, side-grooving, and fatigue precracking effects on the J-integral test results for SUS 304 stainless steel at 4 K, in: Adv. Cryo. Eng., 34, A.F. Clark and R.P. Reed, eds., Plenum, New York, 251-258 (1988).
13. T. Horiuchi, R. Ogawa, and M. Shimada, Cryogenic Fe-Mn Austenitic Steels, in: Adv. Cryo. Eng., 32, R.P. Reed and A. F. Clark, eds., Plenum, New York, 33-42 (1986).
14. Standard test method for plane strain fracture toughness of metallic materials, ASTM Designation: E 399-83, in: 1989 Annual Book of ASTM Standards, Section 3, Metals Test Methods and Analytical Procedures, 03.01, Amer. Soc. Test. Mater., Philadelphia, 487-511 (1989).
15. Standard test method for  $J_{Ic}$ , a measure of fracture toughness, ASTM designation: E 813-81, in; 1986 Annual Book of ASTM Standards, Section 3, Metals Test Methods and Analytic Procedures, 03.01, Amer. Soc. Test. Mater., Philadelphia, 968-990 (1986).
16. Standard test method for  $J_{Ic}$ , a measure of fracture toughness, ASTM designation: E 813-88, in: 1989 Annual Book of ASTM Standards, Section 3, Metals Test Methods and Analytical Procedures, 03.01, Amer. Soc. Test. Mater., Philadelphia, 698-712 (1989).
17. Y.W. Cheng and D.T. Read, An automated fatigue crack growth rate test system, in: Automated Test Methods for Fracture and Fatigue Crack Growth, ASTM STP 877, W.H. Cullen, R.W. Landgraf, L.R. Kaisand, and J.H. Underwood, eds., Amer. Soc. Test. Mater., Philadelphia, 213-223 (1985).
18. M. Shimada, R. Ogawa, T. Moriyama, and T. Horiuchi, Cryogenic Engineering, 21, 269-274 (1986), in Japanese.
19. R.L. Tobler and D.A. Meyn, Cleavage-like fracture in Fe-18Cr-3Ni-13Mn-0.37N austenitic stainless steel at liquid helium temperature, Metall. Trans., 19A, 1625-1631 (1988).
20. P.K. Liaw and J.D. Landes, Influence of prestrain history on fracture toughness properties of steels, Metall. Trans., 17A, 473-489 (1986).
21. J.L. Christian, J.D. Gruner, and L.D. Girton, Effects of cold rolling on the mechanical properties of type 310 stainless steel at room and cryogenic temperatures, Trans. ASM, 57, 199-207 (1964).
22. G.R. Irwin, Plastic zone near a crack and fracture toughness, in: Mechanical and Metallurgical Behavior of Sheet Materials, Proc. 7th Sagamore Ordnance Materials Research Conf., U.S. Army Office of Ordnance Research, 63-77 (1960).

23. T.M. Banks and A. Garlick, The form of crack tip plastic zones, Eng. Fract. Mech., 19, 571-581 (1984).
24. C.M. Hsiao and E.J. Dulis, Trans ASM, 52 855-877 (1960).
25. J.C. Shyne, F.W. Schaller, and V.F. Zackay, Trans. ASM, 52 848-854 (1960).
26. J.D. Defilippi, K.G. Brickner, and E.M. Gilbert, Trans. AIME, 245, 2141-2148 (1969).
27. G.R. Caskey, Jr., Report DP-MS-78-68, E.I. du Pont de Nemours and Co., Aiken SC, pp 1-21 (1978).
28. R.L. Tobler, R.P. Reed, and P.T. Purtscher, Linear elastic fracture of high nitrogen austenitic stainless steels at liquid helium temperature, J. Test. Eval. (1989).
29. T.A. Place, T.S. Sudarshan, C.K. Waters, and M.R. Louthan, Jr. Fractographic studies of the ductile-to-brittle transition in austenitic stainless steels, in: Fractography of Modern Engineering Materials: Composites and Metals, ASTM STP 948, Amer. Soc. Test. Mater., Philadelphia, 350-365 (1987).
30. W.F. Brown and J.E. Srawley, Plane Strain Crack Toughness Testing of High Strength Metallic Materials, ASTM STP 460, Amer. Soc. Test. Mater., Philadelphia, 1966, p. 51.
31. G. Clark, Significance of Fatigue Stress Intensity In Fracture Toughness Testing, Int. J. Fract., 15, R179-R181 (1979).
32. T. Yokobori and T. Aizawa, Reports of the Research Institute for Strength and Fracture of Materials, Tohoku University, 6, 19 (1970).
33. T. Kawasaki, T. Yokobori, Y. Sawaki, S. Nakanishi, and H. Izumi, Fatigue Fracture Toughness and Fatigue Crack Propagation in 5.5% Ni Steel At Low Temperature, in: Fracture 1977, Vol. 3, D.M.R. Taplin, Ed., University of Waterloo Press, Ontario, Canada, 1977.
34. F. Stonesifer, Effects of Grain Size and Temperature on Fatigue Crack Propagation in A 533 B Steel, Eng. Fract. Mech., 10, 305-314 (1978).





SIXTH DRAFT  
OCTOBER 1988a

NOTE: This is a working document of a standard being developed by the above committee for eventual submission to ASTM; it is intended for committee review purposes, but not for general distribution at this time.

Proposed Standard Method for

TENSILE TESTING OF STRUCTURAL ALLOYS AT LIQUID HELIUM TEMPERATURE

1. Scope

1.1 This standard describes the procedures to be used for the tensile testing of metals in liquid helium [4 or 4.2 K ( $-452^{\circ}\text{F}$ )]. The format is similar to that of other ASTM tensile test standards, but the contents include modifications for cryogenic testing, which requires special apparatus, smaller specimen size, and concern for serrated yielding, adiabatic heating, and strain-rate effects.

1.2 To conduct a tensile test by this standard, the specimen in a cryostat is fully submerged in normal liquid helium (He I) and tested using crosshead displacement control at a moderate strain rate. Tests that use load control or high strain rates are not considered in this standard.

1.3 This standard details methods for the measurement of yield strength, tensile strength, elongation, and reduction of area. The determination of the elastic modulus is treated in Method E 111.

1.4 Values stated in SI units are treated as primary; values stated in U.S. customary units are treated as secondary.

1.5 This standard does not address the issue of safety associated with cryogenic testing. It is the user's responsibility to learn and observe appropriate safety practices. Safety guidelines for handling liquid helium and other cryogens are available elsewhere (1).

NOTE 1—The boiling point of normal liquid helium (He I) at sea level is 4.2 K. This value decreases slightly with geographic elevation; it is 4.0 K at the National Institute of Standards and Technology in Boulder, Colorado, 1677 m (5500 ft) above sea level. In this standard, the test temperature is nominally designated 4 K.



## 2. Applicable Documents

### 2.1 ASTM Standards:

- A 370     Methods and Definitions for Mechanical Testing of Steel Products  
          (*Annual Book of ASTM Standards*, Vol. 01.04)
- E 4        Practices for Load Verification of Testing Machines  
          (*Annual Book of ASTM Standards*, Vols. 03.01, 04.02, 07.01, and 08.03)
- E 6        Definition of Terms Relating to Methods of Mechanical Testing  
          (*Annual Book of ASTM Standards*, Vols. 03.01 and 08.03)
- E 8        Methods for Tension Testing of Metallic Materials  
          (*Annual Book of ASTM Standards*, Vols. 01.02, 02.01, 02.02, 02.03, and 03.01)
- E 8M      Methods for Tension Testing of Metallic Materials, Metric  
          (*Annual Book of ASTM Standards*, Vol. 03.01)
- E 29      Recommended Practice for Indicating Which Places of Figures  
          Are to Be Considered Significant in Specified Limiting Values  
          (*Annual Book of ASTM Standards*, Vols. 02.03, 03.01, 03.03, 03.05, and 14.02)
- E 83      Practice for Verification and Classification of Extensometers  
          (*Annual Book of ASTM Standards*, Vol. 03.01)
- E 111     Method for Young's Modulus, Tangent Modulus, and Chord Modulus  
          (*Annual Book of ASTM Standards*, Vol. 03.01)

### 2.2 Japanese Industrial Standards (JIS):

- B 7721    Tensile Testing Machines
- B 7728    Load Calibration Devices for Verifying Material Testing Machines
- G 0567    Method of High Temperature Tensile Test for Steels and Heat-Resisting Alloys
- Z 2201    Test Pieces for Tensile Test for Metallic Materials
- Z 2241    Method of Tensile Test for Metallic Materials
- Z 8103    Glossary of Terms Used in Instrumentation
- Z 8401    Rules for Rounding Off of Numerical Values

NOTE 2—Japanese and English versions of these standards are published by the Japanese Standards Association, 1-24, Akasaka 4, Minato-ku, Tokyo, 107 Japan.

### 3. Definitions

3.1 The definitions of terms relating to tension testing that appear in ASTM Standard E 6 shall apply here. The following definitions also apply:

3.1.1 *tensile cryostat*—a test apparatus for applying loads to test specimens in cryogenic environments. A schematic illustration is shown in Fig. 1.

3.1.2 *Dewar*—a vacuum-insulated container for cryogenic fluids.

3.1.3 *adiabatic heating*—the internal heating of a specimen resulting from tensile testing under conditions such that the heat generated by plastic work cannot be quickly dissipated to the surrounding cryogen.

3.1.4 *reduced section*—section in the central portion of the specimen, which has a cross section smaller than the gripped ends.

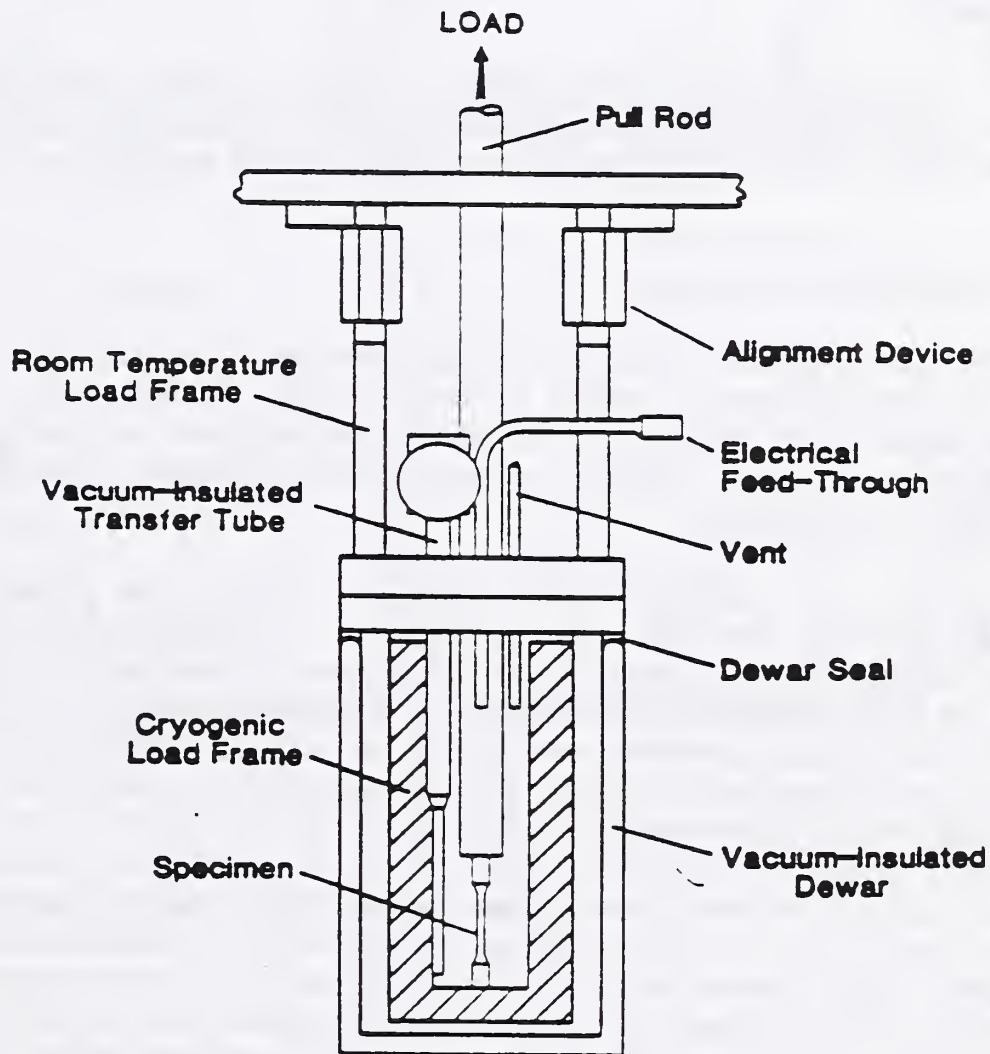


FIG 1 Example of a Cryostat with Double-Dewar Arrangement for Tensile Testing at 4 K



3.1.5 *length of the reduced section*—the distance between the tangent points of the fillets that bound the reduced section.

3.1.6 *adjusted length of the reduced section*—the length of the reduced section plus an amount calculated to compensate for strain in the fillet region.

3.1.7 *gage length*—the original distance between gage marks made on the specimen for determining elongation after fracture.

3.1.8 *axial strain*—the average of the strain measured on opposite sides of the specimen at equal distances from the specimen axis.

3.1.9 *bending strain*—the difference between the strain at the surface of the specimen and the axial strain. The bending strain varies from point to point around and along the reduced section of the specimen.

3.1.10 *maximum bending strain*—the largest value of bending strain in the reduced section of the specimen. It is calculated from strains measured at three circumferential positions, at each of two different longitudinal positions.

3.1.11 *discontinuous yielding stress,  $\sigma_i$* —the stress at the initiation of the first measurable serration on the load-deflection curve. The parameter  $\sigma_i$  is a function of test variables and is not a material constant.

#### 4. Significance and Use

4.1 In general, tensile tests provide information on the strength and ductility of materials under uniaxial tensile stresses. This information may be useful for alloy development, comparison and selection of materials, and quality control. Under certain circumstances, the information may also be useful for design.

4.2 At 4 K, the load-time and load-deflection record for metals tested in displacement control are serrated (2). Serrations are formed by repeated bursts of unstable plastic flow, followed by arrests. The unstable plastic flow (or discontinuous yielding) is a free-running process that occurs locally with sizable heat evolution at higher than nominal rates of strain. Typical stress-strain curves for an austenitic stainless steel with serrated yielding at 4 K are shown in Fig. 2.

4.3 Constant specimen temperature cannot be maintained at all times during tests in a liquid helium environment. Owing to adiabatic heat, the specimen temperature temporarily rises above 4 K during discontinuous yielding events (see Fig. 2). This behavior varies with specimen size and test speed, but altering the mechanical test variables cannot eliminate it completely (3). Therefore, tensile property measurements of alloys in liquid helium (especially ultimate strength, elongation, and reduction of area) lack the full significance of property measurements at higher temperatures where discontinuous yielding does not occur.

4.4 At 4 K, the stress-strain behavior of a material during unstable plastic deformation depends on whether load control or displacement control is used (4). Crosshead displacement control is specified because the goal of this standard is material characterization by conventional methods. This limitation must be taken into account when data are used for structural design in those applications where the actual circumstances may approach load-controlled conditions.

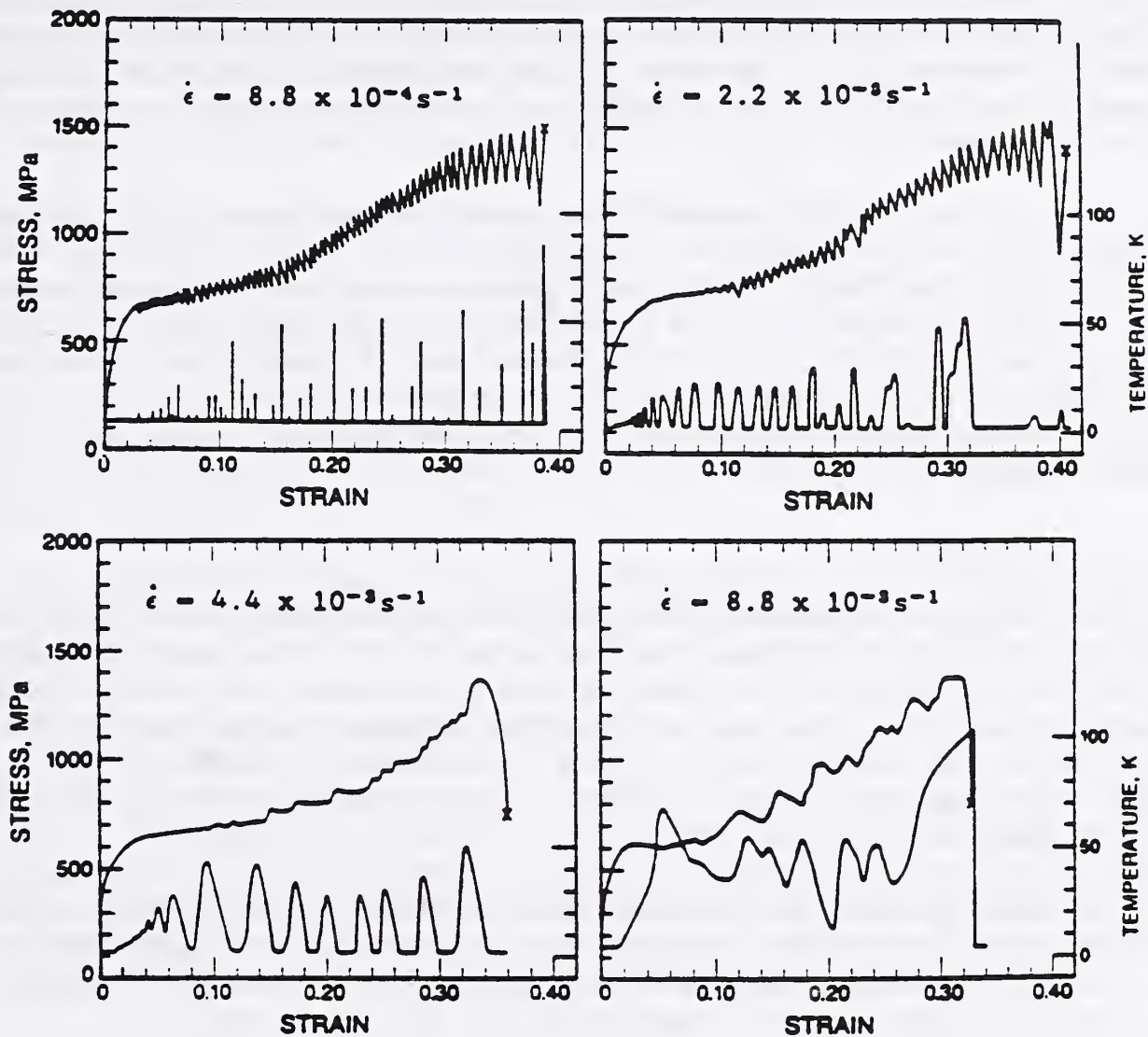


FIG. 2 Typical Engineering Stress-Strain Curves and Specimen Temperature Histories, at Four Different Nominal Strain Rates, for AISI 304L Stainless Steel Tested in Liquid Helium (Ref. 4).



## 5. Apparatus

5.1 *Test Machines*—Machines used for tensile testing shall meet the requirements of Practices E 4 regarding verification of load accuracy. The machine compliance (displacement per unit load of the apparatus itself) shall be measured. This can be done by removing the specimen from the load train, or by replacing the specimen with a rigid block.

5.2 *System Design*—Alloy strengths often double or triple between room temperature and 4 K. For the same specimen geometry, higher loads must be applied to the cryostat, test specimen, load train members, and grips at cryogenic temperatures. For most conventional test machines, which have a maximum load capacity of 10 tons, it is recommended that the apparatus be designed to accommodate one of the small specimens cited in section 7.2.2 of this standard.

5.3 *Construction Materials*—Many construction materials, including the vast majority of ferritic steels, are brittle at 4 K. To resist embrittlement, the grips and other load-train members must be fabricated using strong, tough, cryogenic alloys. Austenitic stainless steels (AISI 304LN), maraging steels (200, 250, or 300 grades, with nickel plating to prevent rust), and extra-low-interstitial (ELI) grade titanium alloys (Ti-6Al-4V and Ti-5Al-2.5Sn) have been used, with proper design, grips, pull rods, and cryostat frames.

### 5.4 Alignment:

5.4.1 *Single-Specimen Apparatus*—To avoid bending strains in the specimen, proper system alignment is essential. For a conventional single-specimen test apparatus, the machine and grips shall be capable of loading a precisely machined specimen so that the maximum bending strain does not exceed 10% of the axial strain. This calculation is based on the strain readings taken at zero load and at the highest load for which the machine is being qualified.

NOTE 3—This requirement will minimize contributions from the test apparatus to the bending strain. Tests performed with a qualified apparatus may still vary in percent bending strain owing to small variations in the specimens.

5.4.2 *Multiple-Specimen Apparatus*—For this type of cryostat, the alignment depends on the type of fixtures used. The maximum bending strain shall be measured and reported.

5.4.3 The testing apparatus may be qualified by axiality measurements at room temperature and at 4 K. To perform axiality tests of the apparatus, the specimen form should be the same as that used during cryogenic tests, the specimen concentricity should be as nearly perfect as possible, and no plastic strains should occur in the reduced section. In some cases, this may necessitate the use of a relatively stiff, high-strength calibration specimen.

5.4.3.1 For round bar specimens, the maximum bending strain, as defined in 3.1.10, is calculated from the strains measured at three circumferential positions, at each of two different longitudinal positions. The strains are measured with three electrical-resistance strain gages equally spaced around the reduced section of the specimen. The two longitudinal positions should be as far apart as possible, but not closer than one diameter to a fillet.

5.4.3.2 For specimens of rectangular cross section, strain may be measured at the center of each of the four sides, or in the case of thin strips, near the outer edges of each of the two broad sides.

5.4.3.3 To eliminate the effect of specimen bias, repeat the axially measurements with the specimen rotated 180 degrees, but with the grips and pull rods retained in their original positions. The maximum bending strain and strain at the specimen axis are then calculated as the average of the two readings at the same position relative to the machine.

5.4.4 *Strain Averaging Technique*—Nonaxiality of loading is usually sufficient to introduce errors in tensile tests at small strains when strain is measured on only one side of the specimen. To rectify this, two extensometers or strain gages may be attached to opposite sides of the specimen. The reported strain should be the average of the strains on both sides.

5.5 *Gripping Mechanisms*—The choice of gripping mechanism to be used at 4 K is influenced by specimen type. Any suitable mechanism described in Methods E 8 and E 8M may be used.

5.6 *Dimension-Measuring Devices*—Micrometers and devices used for measuring the dimensions of specimens shall be accurate and precise to at least one-half the smallest unit to which a given dimension must be measured.

## 5.7 *Cryostats and Support Apparatus*

5.7.1 *Cryostats*—A cryostat capable of retaining liquid helium is prerequisite. In general, cryostat load frames for existing test machines must be custom-built, but they may accommodate commercially available Dewars. The cryostat may employ adjustable load columns to facilitate alignment. Several practical designs, including turret-disc designs for multiple-specimen testing with a single cooling, are discussed in the literature (5-9).

5.7.2 *Dewars*—Stainless steel Dewars are recommended because they are safer than glass Dewars and less expensive than fiberglass Dewars. A single helium Dewar (see Fig. 1) is usually sufficient for short-term tests, but a double-Dewar arrangement, in which an outer Dewar of liquid nitrogen jackets the inner Dewar of liquid helium, is also possible.

5.7.3 *Ancillary Equipment*—Dewars and transfer lines for liquid helium must be vacuum insulated. Vacuum pumps, pressurized gas, and liquid nitrogen facilities are therefore required. After testing, the helium may be released to the atmosphere, recycled as a gas, or reliquefied. Recycling or reliquefaction requires large investments in purification and support systems.



## 5.8 Temperature Maintenance and Liquid-Level Indicators:

5.8.1 *Thermocouples*—The intended temperature of 4 K is ensured by maintaining a liquid helium environment. A thermocouple to measure the specimen temperature is not required for routine tests.

5.8.2 *Indicators*—Although a thermocouple attached to the specimen is not necessary, an indicator or meter is required to ensure that the specimen remains fully submerged for the duration of testing. On-off indicators of the carbon-resistor type may be used to verify that the liquid level always exceeds some reference point above the specimen, or the liquid level may be continuously monitored with superconducting wire sensors of appropriate lengths positioned vertically inside the cryostat.

## 5.9 Strain Gages:

5.9.1 *Selection*—Strain-gage films bonded directly to the specimen surface may be used to measure strain at 4 K (10). A satisfactory combination of gage active element, backing material, and bonding agent should be selected on the basis of experience and manufacturer's recommendations. One common choice is a Ni-Cr-alloy gage with a temperature-compensated active element (7,11).

5.9.2 *Characteristics*—Strain gages are typically wired to a dummy bridge using a three-wire temperature-compensating hookup, like that shown in Fig. 3. The gage resistance is typically 120 or 350  $\Omega$ . A low excitation voltage of about 1 to 2 V is recommended at 4 K to reduce Joule heating. Typical full-scale operating ranges are 1% at room temperature and 2% at 4 K.

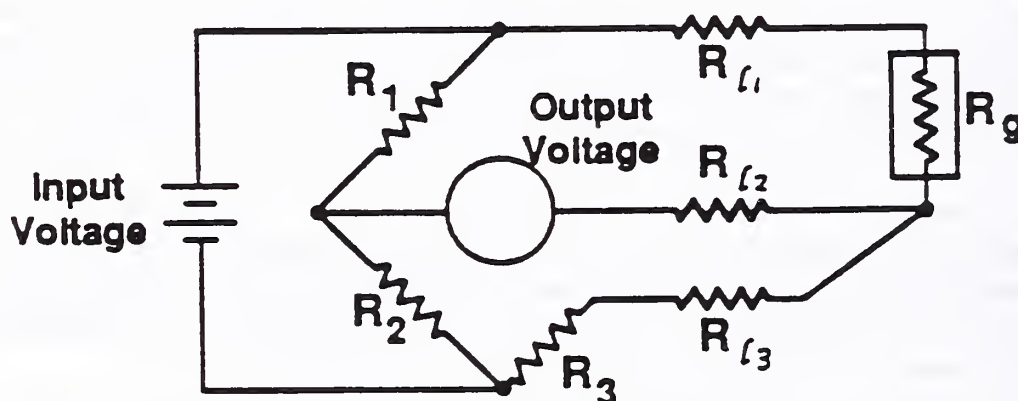


FIG 3 Method of Strain-Gage Wiring for Cryogenic Tests

5.9.3 *Calibration*—Strain-gage calibration at room temperature requires calibration of the electronics to changes in resistance. Calibration at 4 K requires consideration of the temperature dependence of the resistance in the electronic calibration. Gage factors as a function of temperature are provided by the manufacturers and in published research.

#### 5.10 *Clip-Gage Extensometers:*

5.10.1 *Types*—Detachable clip-gage extensometers for use at 4 K may be built or purchased. An example is the beam gage, which uses four strain-gage films bonded in a Wheatstone bridge arrangement (11). Extension within the specimen gage length is sensed by the extensometer, which is clipped to retaining pins that are fixed to the specimen reduced section.

5.10.2 *Characteristics*—To measure the 0.2% offset yield strength, a Class B-2 extensometer, as identified in Method E 83, may be used. The extensometer shall meet the sensitivity and accuracy requirements of Method E 83 and shall be tested to ensure accuracy at 4 K. Whenever possible, the extensometer should be mounted directly to the specimen reduced section.

5.10.3 *Calibration*—Extensometers should be calibrated at room temperature and at 4 K with a suitable device. For calibrations at 4 K, a micrometer with vertical extension tubes can be used with the extensometer(s) mounted at the lower end and immersed in liquid helium. Once the calibration is known and proven to be accurate, linear, and reproducible, room-temperature checks may be performed prior to each test series for indirect verification of the calibration at 4 K. Direct calibration at 4 K, however, must be performed periodically, when damage is suspected or repairs have been made.

5.11 *Capacitance Extensometers*—Extensometers that use capacitance measurement to monitor strain may be used (10). The type with overlapping concentric cylinders has an extended strain range, an output that is linear with displacement, and an adjustable sensitivity. The type with parallel plates has high sensitivity, but the output must be compensated for the hyperbolic dependence of the capacitance on displacement.

## 6. Sampling

6.1 Samples for tensile testing should be taken from the material in its final condition to ensure that the properties measured are representative of the end product. Allowance should be made for any superficial effects introduced by cutting operations.

6.2 Specimens should be cut from locations thought to be most representative of the stock material, realizing that test results for specimens taken from selected locations of a part or material may not be representative of the whole. The conventional locations should normally be used:

6.2.1 For products 40 mm or less in thickness, diameter, or distance between flats, the location should be at the center.



6.2.2 For products over 40 mm in thickness, diameter, or distance between flats, the location should be midway from the surface to the center.

6.3 The choice of specimen size and shape should be based on the requirements necessary to obtain representative samples of the material, and on test-machine load capability (section 5.2).

6.4 The orientation of the specimen axis relative to the principal working directions of the stock shall be specified using the notation in section 4 of Method A 370.

## 7. Test Specimens

### 7.1 General:

7.1.1 *Types and Specifications*—Any specimen configuration cited in Methods E 8 or E 8M may be used. The specifications for dimensions, tolerances, and surface finish are stated in sections 6.1 through 6.17 of those standards.

7.1.2 *Size*—Specimens from sheet or wire products having relatively small cross-sectional areas can be tested within the load limits of conventional apparatus. Specimens from thick plate or bar products, however, may need to be machined to a reduced cross-sectional area so the load capacity of the machine is not exceeded.

### 7.2 Round Bar Specimens:

7.2.1 *Standard Room-Temperature Specimens*—A 12.5-mm (0.5-in) diameter round bar specimen is the standard configuration for room-temperature tests according to Methods E 8 and E 8M. Specimens of such strong alloys, however, require excessive loads at 4 K. For example, 210 kN is required to test typical AISI 304LN steel at 4 K, whereas 100 kN or 10 tons is the limit for most machines.

7.2.2 *Standard 4-K Specimens*—To meet the load limitations of conventional test machines, the round bar specimens in sections 7.2.2.1 and 7.2.2.2 are recommended as standard for 4-K tests. The required dimensions and tolerances for these specimens are given in Table 1. Threaded or shouldered ends are common for gripping these specimens, and the requirement of section 5.4.1 can be met by precise machining.

7.2.2.1 *Standard, small metric specimens.* These specimens have a 7-mm diameter and a gage-length-to-diameter ratio of 5:1.

7.2.2.2 *Standard, small U.S. customary specimens.* These specimens have a 6.25-mm (0.25-in) diameter and a gage-length-to-diameter ratio of 4:1.

7.2.3 *Alternatives*—If the 4-K standard specimens recommended above are not appropriate, other sizes may be selected following the guidelines of Methods E 8 and E 8M. The proportions of such specimens should be similar to those of the standard specimens (see Fig. 4 of this standard and Fig. 8 of Methods E 8 and E 8M).

TABLE 1 Standard Specimens for Room-Temperature Tests and Recommended Proportionally Reduced, Standard Small Specimens for 4-K Tests<sup>1</sup>

(a)		
Metric Versions G/D ratio = 5 (dimensions, mm)	Standard Specimen (room temperature)	Standard Small Specimen (4 K)
Nominal Diameter	12.5	7
G, gage length	62.5 ± 0.1	35 ± 0.1
D, diameter	12.5 ± 0.1	7 ± 0.1
R, fillet radius	10	7
A, reduced section	75	42
(b)		
U.S. Customary Versions G/D ratio = 4 (dimensions, in)	Standard Specimen (room temperature)	Standard Small Specimen (4 K)
Nominal Diameter	0.5	0.25
G, gage length	2.000 ± 0.005	1.000 ± 0.005
D, diameter	0.500 ± 0.010	0.250 ± 0.005
R, fillet radius	0.375	0.1875
A, reduced section	2.25	1.25

<sup>1</sup>See also the notes to Fig. 8 in Methods E 8 and E 8M.

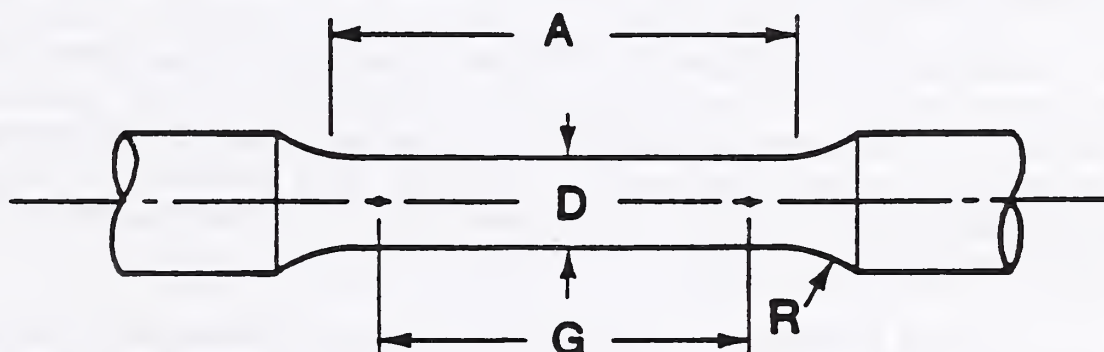


FIG 4 Round Bar Specimen Configuration (see Table 1)



7.2.4 *Subsize specimens*—Special care in fabrication and testing is required for specimens with diameters less than 6 mm. As the specimen size is reduced, factors such as machining, surface finish, alignment, and the number of grains per cross section are of increasing importance.

## 8. Procedures

### 8.1 *Marking and Measuring the Test Specimen:*

8.1.1 *Gage Length*—Gage length marks should be lightly punched, scribed, or inked at appropriate locations on the reduced section of the specimen, which is the conventional method. The gage length should normally be five times the diameter for metric specimens or four times the diameter for U.S. customary specimens. If another gage length is used, it must be described in the report. Measure the gage length to the nearest 0.05 mm.

NOTE 4—For metals of low ductility, gage marks punched or scribed on the reduced section may induce failure at those locations due to stress concentrations. To avoid this, it may be possible to coat the reduced section with layout ink, and then mark the gage length by rotating the specimen in a jig with knife edges scraping off the ink at the appropriate intervals. Alternatively, gage marks may be placed on the specimen shoulders, or the overall length of the specimen may be measured.

8.1.2 *Reduced Section*—Measure the length of the reduced section and the adjusted length of the reduced section, if applicable, to the nearest 0.05 mm.

8.1.3 *Cross Section*—Measure the cross-sectional area of the reduced section as specified in section 7.1.1 of Methods E 8 and E 8M.

8.2 *Specimen Installation*—Install the specimen in the cryostat, leaving sufficient slack for instrumentation wires so they will not be stretched or crimped during positioning of the Dewar and subsequent testing.

8.3 *Seating and Alignment*—If the gripping fixture involves loose-fitting components, such as spherically seated bearings, prevent friction or mismatch of the bearing surfaces at 4 K by first checking the seating and alignment at room temperature. During this process of alignment, the applied loads should be kept below one-third of the proportional limit of the test material.

8.4 *Cooling Procedure*—Remove any moisture from the apparatus prior to cooling by drying it thoroughly with a pressurized air jet or heat gun. Ice can block cryogenic transfer lines or cause erratic loading behavior if it forms between various parts of the specimen, clip gage, and load train.

Next, position the Dewar and precool the apparatus to 77 K by transferring liquid nitrogen into the cryostat. After attaining equilibrium at 77 K, remove all the liquid nitrogen from the cryostat, and transfer liquid helium into the cryostat until the specimen and grips are fully submerged. Testing may begin after the system has reached thermal equilibrium at 4 K. The specimen must remain fully submerged at all times during the test.

NOTE 5—The heat-transfer characteristics of gaseous helium are inferior to those of liquid helium; therefore, a liquid helium environment is required to minimize specimen heating effects during discontinuous yielding.

## 8.5 Testing Speed:

8.5.1 *Rate Control*—Owing to adiabatic heating, tensile property measurements at 4 K can be significantly affected by the testing speed. Therefore, the test procedure must include a means of measuring and controlling the rate of crosshead motion. A nominal strain rate must be specified, since the actual rate cannot be precisely controlled or maintained when discontinuous yielding occurs. The nominal strain rate is calculated by dividing the crosshead rate by the length of the reduced section. Alternatively, a pacing or indicating device may be used to monitor the strain rate or an average strain rate may be determined by observing the time required to effect a known increment of strain.

8.5.2 *Rate Limit*—The nominal strain rate at any time during the test shall not exceed  $1 \times 10^{-3} \text{ s}^{-1}$ . Higher rates may cause excessive specimen temperature rises and therefore are not satisfactory for determining the acceptability of materials.

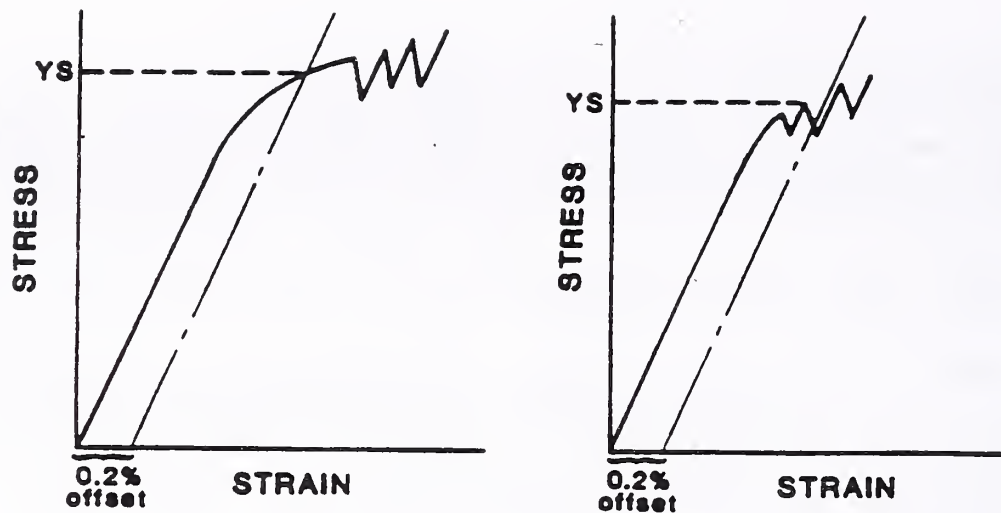
8.5.3 *Rate Change*—The strain at which discontinuous yielding begins usually increases with decreasing strain rate. If the first serration for a given material occurs near 0.2% plastic strain, it may be desirable to reduce the speed to prevent interference in the measurement of the yield strength (see Fig. 5). Then, a relatively low strain rate may be used to determine the yield strength, followed by a higher strain rate to complete the test. Any convenient crosshead speed may be used up to a stress of one-half the yield strength; after that, the crosshead speed must be such that the nominal strain rate does not exceed the  $1 \times 10^{-3} \text{ s}^{-1}$  limit.

## 8.6 Measurement of Mechanical Properties:

8.6.1 *Load-Extension-Curve Method*—To measure the yield strength, a record of load versus extension must be obtained, up to at least 0.2% plastic strain. The use of a strain measurement device for autographic recording is recommended.

Measure the yield strength via the 0.2% offset method, following Methods E 8 or E 8M, section 7.3.1. If the 0.2% offset line intersects the curve at a load drop owing to discontinuous yielding, then report the highest stress prior to that load drop as the yield strength.





A - Serrations after 0.2% strain      B - Serrations before 0.2% strain

FIG 5 Stress-Strain Diagram for Determination of Yield Strength by the Offset Method.

8.6.2 *Load-Time-Curve Method*—Yield strength measurements based on a 0.2% offset procedure applied to load-versus-time curves at 4 K are generally not recommended, but may be used for commercial test purposes with the agreement of all parties involved. If this method is used, it should be stated clearly in the report.

NOTE 6—Load-time curves for tests at 4 K are typically nonlinear at the start and less regular than load-extension curves. Also, the effective modulus of a thermally efficient load train may be low and dependent on the liquid helium level and the degree of temperature stabilization achieved throughout the system in the temperature range 295 to 4 K. As a result, yield strength data from load-time curves may be less accurate than those of the recommended method.

8.6.3 *Discontinuous yielding stress*—Calculate the stress corresponding to the point of initiation of discontinuous yielding by dividing the load at the first measurable serration by the cross sectional area of the specimen.

8.6.4 *Tensile Strength*—Calculate the tensile strength by dividing the maximum load carried by the specimen during the tensile test by the original cross-sectional area of the specimen.

8.6.5 *Elongation*—Calculate the percentage increase of elongation according to Methods E 8 or E 8M, section 7.6.

8.6.6 *Reduction of Area*—Calculate the percentage of reduction of area according to Methods E 8 or E 8M, section 7.7.

8.6.7 *Rounding Reported Test Data*—Round-off the calculated numerical test results according to Methods E 8 or E 8M, section 7.8.

8.6.8 *Replacement Specimens*—If necessary, discard any invalid data and test replacement specimens as per Methods E 8 or E 8M, section 7.9.

## 9. Report

### 9.1 General:

9.1.1 *Material Characterization*—Describe the test material, including manufacturing, processing, and metallurgical information.

9.1.2 *Specimen Characterization*—Describe the specimen location and its orientation relative to the principal working directions of the stock. Also report the specimen dimensions, including the cross-section dimensions, the fillet radius, the reduced section length, and the adjusted length of the reduced section (if used).

9.1.3 *Strain Rate*—Report the crosshead speed and the nominal strain rate during yielding and after yielding, if a rate change is used.

9.1.4 *Mechanical Property Measurements*—Report the yield strength, the ultimate strength, and the method of offset yield strength determination. Include the method of extension measurement and the location of extensometer attachment, if used. Also report the discontinuous yielding stress and the strain rate at which it was measured, the tensile elongation and its method of calculation, the gage-length-to-diameter ratio for round specimens, and the reduction of area.

9.2 *Optional Data*—Report any optional data, such as measurements of Young's modulus at 4 K, the mechanical properties at room temperature, and the average grain size of the test material. Report the compliance of the test machine with its cryostat.

9.3 *Replicate Tests*—If replicate specimens are tested, report the number of tests, the average values of all mechanical property measurements, and a measure of scatter.

9.4 *Subsize Specimens*—If subsize specimens are tested, state any precautions taken with respect to specimen machining, surface condition, or alignment, and report the grain size of the test material.

9.5 *Anomalies*—Report any anomalies in material behavior, test records, or failure type and location.

## 10. Precision and Bias

10.1 *Precision*—The precision of these methods is being established by a series of interlaboratory tests.



10.2 *Bias*—The bias of these methods includes quantitative estimates of uncertainties of the dimension-measuring devices, the calibration of test equipment, and the skill of the operators. At present, bias statements should be limited to the documented performance of individual laboratories.

#### REFERENCES

- (1) *Cryogenics Safety Manual*—A Guide to Good Practice, 2nd Ed., Mechanical Engineering Publications, London, 1982.
- (2) Basinski, Z. S., "The Instability of Plastic Flow of Metals at Very Low Temperatures," *Proceedings of the Royal Society*, Vol. A240, 1957, pp. 229-242.
- (3) Ogata, T., Ishikawa, K., and Nagai, K., "Effects of Strain Rate on the Tensile Behavior of Stainless Steels, Copper, and an Aluminum Alloy at Cryogenic Temperatures," *Tetsu-to-Hagane*, Vol. 71, No. 10, 1985, pp. 1390-1397.
- (4) Ogata, T. and Ishikawa, K. "Time-dependent Deformation of Austenitic Stainless Steels at Cryogenic Temperatures," *Cryogenics*, Vol. 26, 1986, pp. 365-369.
- (5) Schwartzberg, F. R., "Mechanical Property Testing Techniques for the Cryogenic Temperature Range," in: *Advances in Cryogenic Engineering*, Vol. 8, Plenum Press, New York, 1963, pp. 608-623.
- (6) Evans, D., Simmonds, G. E., and Stapleton, G. B., "Improved Facility for Determining Mechanical Properties of Materials in Liquid Helium," in: *Proceedings, Fourth International Cryogenic Engineering Conference*, IPC Science and Technology Press, Guildford, Surrey, England, 1972, pp. 331-337.
- (7) Hartwig, G. and Wuchner, F., "Low Temperature Mechanical Testing Machine," *Review of Scientific Instruments*, Vol. 46, 1975, pp. 481-485.
- (8) Novikov, N. V. "Mechanical Property Measurement Techniques of Structural Materials at Cryogenic Temperatures," in: *Advances in Cryogenic Engineering*, Vol. 22, Plenum Press, New York, 1977, pp. 113-118.
- (9) Horiuchi, T., Shimada, M., Fukutsuka, T., and Tokuda, S., "Design and Construction of an Apparatus for Testing Materials at Cryogenic Temperatures," in: *Proceedings, Fifth International Cryogenic Engineering Conference*, IPC Science and Technology Press, Guildford, Surrey, England, 1977, pp. 465-468.
- (10) Sparks, L. L., "Temperature, Strain, and Magnetic Field Measurements," in: *Materials at Low Temperatures*, R. P. Reed and A. F. Clark, eds., American Society for Metals, Metals Park, Ohio, 1983.

- (11) Read, D. T. and Tobler, R. L., "Mechanical Property Measurements at Low Temperatures," in: *Advances in Cryogenic Engineering—Materials*, Vol. 28, Plenum Press, New York, 1982, pp. 17-28.





# TECHNOLOGY TRANSFER





## TECHNOLOGY TRANSFER PROGRAM

LEADER: N.J. Simon  
CONTRIBUTORS: E.S. Drexler, R.P. Reed

### OBJECTIVES

- o Organization of workshops to promote interaction between designers and material specialists, to discuss issues related to low-temperature material needs of the fusion energy program, and to present new low-temperature data for structural alloys, composites, and weldments.
- o Preparation of an annual report, as well as monthly highlight reports to the Office of Fusion Energy, U.S. Department of Energy.
- o Evaluation of low-temperature mechanical and physical properties of insulator, conductor, and structural materials for cryogenic copper and superconducting magnets; preparation of handbook pages and supporting documentation; distribution of handbook pages to participants in the fusion energy program and to the Materials Handbook for Fusion Energy Systems.

### RESEARCH HIGHLIGHTS

- o The Eleventh Annual Cryogenic Structural Materials Workshop was organized; it was held October 8-9, 1988 in Colorado Springs, Colorado.
- o "Materials Studies for Magnetic Fusion Energy Applications - XI", (NBSIR 88-3082, 398 pages, 1988, editor R. P. Reed) was prepared, published, and distributed.
- o Data were collected for handbook pages on C10100-C10700 copper and C17000-C17510 beryllium copper. Over one thousand documents (reports and journal articles) were acquired, coded for property information, and entered into a data-base management system. Evaluation of documents pertaining to C10100-C10700 copper tensile, elastic, electromagnetic, fatigue, and thermal properties was completed; data were extracted and analyzed; handbook pages on these properties were prepared and distributed. Evaluation of documents for similar properties of C17000-C17510 beryllium copper was also completed; data were extracted and analyzed; handbook pages on tensile, elastic, electromagnetic, fatigue, and thermal properties were prepared and distributed.
- o Handbook pages on C50500-C52400 phosphor bronze tensile, elastic, fatigue, electro-magnetic, and thermal properties are in preparation. Documents (over 250) have been acquired, and preliminary data sets extracted and analyzed.





## ELEVENTH CRYOGENIC STRUCTURAL MATERIALS WORKSHOP

Clarion Hotel  
Colorado Springs, Colorado  
October 18-19, 1988

This workshop provided an opportunity for discussion of problems, advances, and goals in the development of low-temperature materials for cryogenic and superconducting magnets for fusion energy systems. The 1988 workshop emphasized:

- Cryogenic properties of copper alloys and laminates pertaining to design requirements for the compact ignition tokamak (CIT)
- Identification of materials needs for future magnet systems for the International Thermonuclear Experimental Reactor (ITER)
- New low-temperature materials developments in the United States and international research cooperation



# 11TH CRYOGENIC STRUCTURAL MATERIALS WORKSHOP

## PROGRAM

### TUESDAY, OCTOBER 18

8:00 a.m. Continental Breakfast

8:30 a.m. Introduction and Announcements

R. Reed, NIST

### GENERAL

8:40 a.m. DOE Overview and Perspectives

A. Opdenaker, OFE

9:00 a.m. CIT Design Overview and Materials Program

C. Bushnell, PPPL

9:30 a.m. Cryogenic Materials for the International  
Thermonuclear Experimental Reactor (ITER)

L. Summers, J. Mill  
LLNL

### WELDING

10:00 a.m. Cryogenic Material Properties of Stainless  
Steel Tube-to-Flange Welds

T. Siewert, C. McCow  
D. Vigliotti, NIST

10:25 a.m. Joining of Nonferrous Materials

G. Goodwin, ORNL

10:50 a.m. Role of Inclusions in the Fracture of  
Austenitic Welds

C. McCowan, T. Siew  
NIST

11:15 a.m. FN Predictive Diagram for Stainless Steel  
Welds

T. Siewert, C. McCow  
NIST, D. Olson, CSM

— Lunch Break

### INSULATORS

1:00 p.m. SSC Dipole Magnet Design and Performance Update

T. Nicol, Fermilab

1:30 p.m. Cryogenic Torsional Shear and Fracture Strength  
of Epoxy and Polyimide Composites

M. Kasen, N. Munshi,  
CTD

1:50 p.m. Radiation Effects in Structural Insulators

R. Reed, NIST

2:30 p.m. Discussion of U.S./Japan Efforts to Develop  
Radiation-Resistant Insulators

M. Kasen, CTD

2:50 p.m. Insulation Development for ITER

N. Munshi, M. Kasen,

3:10 p.m. CIT Insulation R & D Program

T. McManamy, Martin-  
Marietta, ORNL

3:45 p.m. Break

4:00 p.m. Discussion of CIT Program

6:00-7:30 Reception

# WEDNESDAY, OCTOBER 19

8:00 a.m. Continental Breakfast

## STRUCTURAL ALLOYS

8:30 a.m.	316LN Forgings for C-MOD-Metallurgical and Design Considerations	R. Ballinger, H. Becker, MIT
9:10 a.m.	Metallurgical Factors that Influence Fracture Toughness of Austenitic Steels	P. Purtscher, NIST
9:40 a.m.	Fracture Behavior of 304 Stainless in an 8 T Field	J. Chan, J. Glazer, and J. Morris, Jr., U. CA
10:10 a.m.	Creep of Copper and Austenitic Steels; 4 to 295 K	R. Walsh, N. Simon, C. King, R. Reed, NIST, J. Arvidson, MRE, Inc.
10:40 a.m.	Effect of Nitrogen on the LCF Properties of 316 Stainless Steel at 300 K and 77 K	J.-B. Vogt, J. Foct, U. Lille
11:10 a.m.	Load-Control Tensile Measurements on Austenitic Steels	H. Lee, J. Han, R. Reed, NIST
11:40 a.m.	Discussion of Load-Control Tensile Measurements in Terms of Magnet Design	R. Reed, NIST
—	Lunch Break	
1:30 p.m.	Review of International Cooperative Programs	R. Reed, NIST
2:00 p.m.	U.S.-Japan Program for Mechanical Property Test Standards - An Update	R. Tobler, NIST
2:30 p.m.	Fatigue Crack Growth in Metastable Austenitic Stainless Steels	Z. Mei, J. Morris, Jr., U. CA
3:00 p.m.	The Bureau of Mines Development Program for New Austenitic Stainless Steels and Cryogenic Characterization	J. Dunning, M. Glenn, USBM P. Purtscher, R. Walsh, T. Siewert, R. Reed, NIST
3:30 p.m.	The Cryogenic Mechanical Properties of Advanced Aluminum Alloys	J. Morris, Jr., J. Glazer, U. CA
4:00 p.m.	Fatigue Properties of High Strength Aluminum Alloys	J. Han, L. Ma, R. Tobler, NIST
4:30 p.m.	Handbook - Structural Materials for Superconducting Magnets - Progress Report	N. Simon, L. Delgado, C. King, R. Reed, NIST



## ELEVENTH CRYOGENIC STRUCTURAL MATERIALS WORKSHOP

### SUMMARY OF TECHNICAL PRESENTATIONS

#### GENERAL SESSION

A. Opdenaker from the DOE Office of Fusion Energy presented an overview of DOE perspectives on fusion. First, he outlined the overall budget for magnetically contained fusion energy systems. Over half of this budget goes to confinement system design, about one fourth to applied plasma physics and about one sixth to development and technology. The latter category includes the materials research for superconducting and cryogenic magnets that was the subject of this workshop. The current prototype reactor is the Compact Ignition Tokamak (CIT), which will have normal copper or copper alloy coils operating at 77 K to produce fields up to 16 Tesla. The next prototype, the International Thermonuclear Experimental Reactor (ITER), will have superconducting coils that operate at 4 K with fields of 11 - 12 Tesla. ARIES, a future design, may have fields as large as 24 - 30 Tesla. Priorities and future direction of the DOE fusion energy program will be 1) to understand confinement physics, since there is still a degree of skepticism due to uncertainty in confinement mechanisms; 2) base a practical research program chiefly on the Tokamak design; 3) since budgets will be level at best, old machines will have to be given up in favor of new ones and the next series of machines will have to be built with international cooperation and research assistance from universities; 4) safety and environmental concerns must be addressed.

C. Bushnell of PPPL gave an overview of the CIT design and materials program. There will be about 420 toroidal coil plates of Inconel 718 laminates, C17510 beryllium copper, or C15725 aluminum-dispersion strengthened copper. The latter material is also an alternative for the poloidal coils. The toroidal field pulse will have a 12 s rise, a constant ohmic heating period of 5 s, and an 8 - 12 s decay. Part of the system is expected to warm up nearly to room temperature during a pulse. The device is to be designed for a total of about 3000 pulses. A cooldown period of about one h is expected. Techniques for explosive bonding of copper to Inconel have been investigated. Coil development will take place through 1991, and the device is expected to be operational with plasma ignition in 1996.

The U.S., USSR, Japan and the European Community are involved in a three-year effort to design ITER. Materials design issues for the reactor were described by L. Summers of LLNL. ITER will be a very large machine, with each of 16 toroidal field coils weighing 350 tonnes, and a total cold mass of 10,000 tonnes of superconductor, sheathing and magnet case. A cable-in-conduit configuration with an Nb<sub>3</sub>Sn superconductor will be contained in a case of 304LN or 316LN stainless steel. The magnet will be pulsed, and therefore fatigue

problems are a serious materials issue. However, the magnet insulation will receive a total radiation dose of only about  $10^7$  Gy, which is 100 times smaller than the radiation dose predicted for earlier, more compact reactor designs such as TIBER II. Since vacuum impregnation of the coils with the insulating material is a requirement, an epoxy matrix rather than a polyimide or thermoplastic matrix is likely to be chosen. The problem of scrubbing of this insulation as the coils are pulsed will have to be investigated. Another important materials issue is the development of fabrication methods, including welding and inspection, for the conduit and superconductor. Conduit materials under consideration are Inconel 908, JBK 75, and A-286. Selection of this alloy is restricted by the requirement that it retain good properties after the  $\text{Nb}_3\text{Sn}$  heat treatment.

#### WELDING SESSION

The three reports given in the welding session were presented by NIST staff (T.A. Siewert and C.N. McCowan). They reported recent advances in predicting the ferritic phase content, solidification mode, fatigue life, and fracture toughness of stainless steel welds. The data generated by these programs are expected to be useful to fusion magnet designers. Data on increasing weld metal toughness by reducing the inclusion content of welds were of particular interest. From a practical standpoint, production welding processes must be used during the fabrication of fusion magnet structures and the NIST studies continue to address means to optimize the toughness of welds using modified production techniques.

#### INSULATOR SESSION

The session on structural composites, following the trends of all recent workshops, again emphasized the concern for magnet insulation in a radiation environment at low temperatures and the scarcity of appropriate data. The proposed closing of the Oak Ridge LTNIF facilities for the Bulk Shielding Reactor has completely frustrated the ongoing programs scheduled to use the ORNL facilities to develop radiation-resistant structural insulators. Past data on this subject were reviewed by R. Reed (NIST).

The CIT program to characterize structural insulators for the 77 - 300 K environment with a pulsed magnet was extensively discussed (T. McManamy, ORNL). Current plans for composite supports for the SCC program were presented by T. Nicol (Fermilab).

Generally, there are two types of composites using either 2- or 3- dimensional weaves of S-2 glass with either epoxy, bismaleimide, or polyimide resins. Since the cost varies by at least an order of magnitude, depending on the resin and reinforcement system, and since little or no useful data have been generated that simulates operating conditions, extensive research is required on this subject.



## STRUCTURAL ALLOYS - SESSION I

In the first session on structural alloys, mechanical property and metallurgical research from MIT, LBL, University of Lille in France, as well as from NIST was summarized. The talks demonstrated the diverse metallurgical/mechanical factors that affect material performance at cryogenic temperatures. There are still technical questions to answer before we can confidently build a safe magnet case to operate in liquid helium. Lee (NIST) described how loading rate affects the flow stress of different austenitic steels. The ultimate stress of the steels was reduced when the loading rate was increased to values that were similar to the loading rate a magnet might experience. This behavior may change the limiting design stresses for magnets. Chan from LBL described the results of their fracture toughness tests in the presence of high magnetic fields. No definite conclusions can be drawn from LBL's results at this point. The relatively low values of fracture toughness of 304 steel at 4 K would appear to be more significant than any effect due to the magnetic field. The global nature of the research effort in structural alloys was evident at this session. The large 316LN forgings for the C-MOD were made in West Germany because no company in the U.S.A. had the capability. Professor Foct from France showed some interesting effects of nitrogen additions on the deformation behavior of 316-type steels.

## STRUCTURAL ALLOYS - SESSION II

This session covered standards, alloy, and handbook developments. R. Reed, R. Tobler and N. Simon (NIST) described the handbook and standards related activities in the past year. Rapid progress has been made in the development of tensile and fracture toughness test standards because of the VAMAS and U.S. - Japan international programs. The official processing of draft standards through ASTM should be completed by 1990. Regarding steel developments, J. Dunning (U.S. Bureau of Mines) and P. Purtscher (NIST) described a cooperative program between the USBM and NIST to produce good, low cost austenitic stainless steels containing only 9%Cr. One of the four candidate materials (Fe-9Cr-14Ni-4Mn-2Mo) has 4-K yield strength and fracture toughness properties equivalent to commercial 304 steels, proving that the new low Cr alloys may be practical. Similarly, J.W. Morris (LBL) and J. Han (NIST) considered some new aluminum alloys. Previous data demonstrated that the Al-Li alloy 2090 in plate form surpasses conventional 2000 series alloys in strength-toughness properties at cryogenic temperatures. Now it appears that Al-Sc alloys surpass the Al-Li alloys in thin sheet tearing resistance at cryogenic temperatures. However, other data were presented, indicating that the superiority of 2090 versus alloys such as 2219 does not extend to thin sheet materials tested in notched tension or short term fatigue tests at cryogenic temperatures.



## BIBLIOGRAPHIC DATA SHEET

1. PUBLICATION OR REPORT NUMBER

NISTIR 89-3931

2. PERFORMING ORGANIZATION REPORT NUMBER

3. PUBLICATION DATE

November 1989

## TITLE AND SUBTITLE

Materials Studies for Magnetic Fusion Energy Applications at Low Temperatures -- XII

## AUTHOR(S)

R.P. Reed and R.L. Tobler, Editors

## PERFORMING ORGANIZATION (IF JOINT OR OTHER THAN NIST, SEE INSTRUCTIONS)

U.S. DEPARTMENT OF COMMERCE  
NATIONAL INSTITUTE OF STANDARDS AND TECHNOLOGY  
GAITHERSBURG, MD 20899

## 7. CONTRACT/GRANT NUMBER

## 8. TYPE OF REPORT AND PERIOD COVERED

## SPONSORING ORGANIZATION NAME AND COMPLETE ADDRESS (STREET, CITY, STATE, ZIP)

Department of Energy  
Office of Fusion Energy  
Washington, D.C. 20545

## 9. SUPPLEMENTARY NOTES

Previous reports in this series: NBSIR 88-3082, NBSIR 87-3067, NBSIR 86-3050, NBSIR 85-3025, NBSIR 84-3000, NBSIR 83-1690, NBSIR 82-1667, NBSIR 81-1645, NBSIR 80-1627, NBSIR 79-1609, NBSIR 78-884

☐ DOCUMENT DESCRIBES A COMPUTER PROGRAM; SF-185, FIPS SOFTWARE SUMMARY, IS ATTACHED.

## 11. ABSTRACT (A 200-WORD OR LESS FACTUAL SUMMARY OF MOST SIGNIFICANT INFORMATION. IF DOCUMENT INCLUDES A SIGNIFICANT BIBLIOGRAPHY OR LITERATURE SURVEY, MENTION IT HERE.)

This report contains the results of a research program to determine the properties of materials that may be used in cryogenic structures for the superconducting magnets of fusion energy power plants and prototypes. Its purpose is to facilitate their design and development. The program was developed jointly by the staffs of the National Institute of Standards and Technology and the Office of Fusion Energy of the Department of Energy; it is managed by NIST and sponsored by DOE. Research is conducted at NIST and at other laboratories through subcontracts with NIST.

Research results for 1988 are presented in technical papers under four headings that reflect the main program areas: Structural Alloys, Welding, Technology Transfer, and United States-Japan Development of Test Standards. Objectives and research highlights are summarized in the introduction to each program area.

## 12. KEY WORDS (6 TO 12 ENTRIES; ALPHABETICAL ORDER; CAPITALIZE ONLY PROPER NAMES; AND SEPARATE KEY WORDS BY SEMICOLONS)

austenitic steels; composites; cryogenic properties; elastic properties; low temperatures; mechanical properties; nonmetallics; stainless steels; structural alloys; welds

## 13. AVAILABILITY

XX

UNLIMITED

FOR OFFICIAL DISTRIBUTION. DO NOT RELEASE TO NATIONAL TECHNICAL INFORMATION SERVICE (NTIS).

ORDER FROM SUPERINTENDENT OF DOCUMENTS, U.S. GOVERNMENT PRINTING OFFICE,  
WASHINGTON, DC 20402.

XX

ORDER FROM NATIONAL TECHNICAL INFORMATION SERVICE (NTIS), SPRINGFIELD, VA 22161.

## 14. NUMBER OF PRINTED PAGES

277

## 15. PRICE

A13







